1988

Ultrafast pump-probe spectroscopy of electronic excitation transfer in random molecular systems and in photosynthetic antennae

Timothy P. Causgrove
Iowa State University

Order Number 8909132

Ultrafast pump-probe spectroscopy of electronic excitation transfer in random molecular systems and in photosynthetic antennae

Causgrove, Timothy P., Ph.D.

Iowa State University, 1988

U·M·I
300 N. Zeeb Rd.
Ann Arbor, MI 48106

Ultrafast pump-probe spectroscopy of electronic excitation transfer in random molecular systems and in photosynthetic antennae

by

Timothy P. Causgrove

A Dissertation Submitted to the
Graduate Faculty in Partial Fulfillment of the
Requirements for the Degree of
DOCTOR OF PHILOSOPHY

Department: Chemistry
Major: Physical Chemistry

Approved:

Signature was redacted for privacy.

In Charge of Major Work

Signature was redacted for privacy.

For the Major Department

Signature was redacted for privacy.

For the Graduate College

Iowa State University
Ames, Iowa

1988

TABLE OF CONTENTS

CHAPTER I. INTRODUCTION

Experimental and theoretical study of electronic excitation transport (EET) has been prompted at least in part by the role of this process in photosynthesis. It was first shown in 1932 [1,2] that a large number of chlorophyll (Chl) molecules act cooperatively in photosynthetic oxygen evolution. Using short, intense flashes of light, Emerson and Arnold [2] found that on the average, 2480 Chl molecules interact to produce one molecule of O_2. This result implied the existence of a photosynthetic unit, a group of closely associated Chl molecules which carries out the primary events in the photosynthetic chemical reaction (see Chapter V). This "cooperativity" was later explained [3] in terms of EET across a large array of Chl molecules (antennae) until the excitation reaches a trap (reaction center), where irreversible photochemistry takes place. The presence of the antenna increases the efficiency of photosynthesis in two ways: first, since the probability of absorption of the antenna molecules is approximately additive, the effective absorption of the trap is greatly increased. Second, the incorporation of different pigments (e.g., Chl *a*, Chl *b*, carotenoids) absorbing at different wavelengths allow the photosynthetic unit to use a greater portion of the solar spectrum. In order for an antenna system to be effective, each pigment molecule must be able to transfer its excitation to the reaction center before the excitation is lost to radiative or nonradiative processes. This requirement places severe demands on the efficiency, and therefore the organization of photosynthetic antennae.

The mechanism most often invoked for EET is the electrostatic dipole-

dipole interaction as described by Förster [4]. This theory predicts that the probability of EET between two molecules separated by a distance R is proportional to R^{-6} (see below). Therefore, the timescale of EET within the antenna is very sensitive to the separation of the Chl molecules. The aim of this work is to aid in the characterization of EET in random systems and then to apply the same techniques to photosynthetic antennae, which will provide insight into the chromophore organization and transfer dynamics in photosynthetic antennae.

Explanation of Dissertation Format

Chapters III and IV of this dissertation are published works pertaining to excitation transfer in systems of randomly oriented dye molecules on surfaces and in solution, respectively. Also, Chapters VI, VII and VIII are published works dealing with energy transfer in photosynthetic antenna systems. Each of these chapters contains a description of the experimental apparatus as it was used for the specific experiment; however, Chapter II contains a much more detailed description of the apparatus used to measure time-resolved absorption depolarization, with computer programs relevant to control of the experiment given in the Appendices. A survey of the literature pertinent to the photosynthetic systems studied appears in Chapter V, which also contains a section dealing with theoretical modeling of absorption depolarization. The remainder of Chapter I gives some necessary background in the theory of electronic energy transfer including a delineation of the strong coupling and weak coupling limits. Finally, the reader should note that each

Chapter contains a separate list of references; consult the table of contents for the page number of the appropriate list of references.

Review of Electronic Energy Transfer

Following absorption of a photon by a molecule, the resulting electronic excitation energy may be transferred to another molecule by radiative (i.e., fluorescence and reabsorption) or nonradiative interactions. It has been shown [5] that if the molecules are far apart ($R > \lambda\!\!\!^{-} = \lambda/2\pi n$, λ = fluorescence wavelength, n = refractive index of medium) then radiative transfer, although inefficient, is the only plausible mechanism; however, for molecules much closer together, ($R \leq \lambda\!\!\!^{-2/3}$) nonradiative transfer may become very efficient. The purpose of this section is to give a brief review of the theory of nonradiative excitation transfer as developed by Förster [6] since transition rates predicted by this theory will appear often in the remainder of this work.

Nonradiative excitation transfer arises from the Coulomb interaction of the electron clouds of the two molecules, which introduces a perturbation in the Hamiltonian $\hat{H}$ of the system

$$\hat{H} = \hat{H}_o + \hat{V}_{ab} \tag{1.1}$$

where $\hat{H}_o$ is the unperturbed Hamiltonian and $\hat{V}_{ab}$ is the intermolecular interaction potential. For a system of two molecules and one excitation, there are two quantum mechanical configurations, $\psi_a'\psi_b$ and $\psi_a\psi_b'$, where the prime denotes the excited state (i.e., the excitation on molecule a

and on molecule b, respectively). These configurations have energies $W_{a'b}$ and $W_{ab'}$, which are the total energies of the separated molecules. When the molecules are brought close together, there is a specific interaction energy U between the two configurations due to the presence of $\hat{V}_{ab}$

$$U = \langle \psi_{a'} \psi_b | \hat{V}_{ab} | \psi_a \psi_{b'} \rangle \tag{1.2}$$

This interaction has the effect of mixing the separated states of energy $W_{a'b}$ and $W_{ab'}$ so that two new states are formed with energies W_+, W_- given by [6]

$$W_\pm = \frac{1}{2}(W_{a'b} + W_{ab'}) \pm \frac{U}{\sin 2\alpha} \tag{1.3}$$

where

$$2\alpha = \tan^{-1} \frac{2U}{W_{a'b} - W_{ab'}} \tag{1.4}$$

Since the resonance integral U arises from the interaction of charges on the two molecules, it can be calculated from classical electrostatics. The electric field around a point charge e is inversely proportional to the square of the distance from the charge ($E = e/R^2$) or, written in vector notation,

$$\mathbf{E} = \frac{e\mathbf{R}}{R^3} \tag{1.5}$$

The electric field is related to a scalar potential ϕ by

$$\mathbf{E} = -\nabla\phi \tag{1.6}$$

so for a point charge

$$\phi = e/R \tag{1.7}$$

For the purpose of evaluating U, we are interested in the transition charge densities on each atom (charge in excited state minus charge in the ground state) of the molecule. This constitutes a system of charges e_i located at radius vectors $\mathbf{r}_i$, for which the electric field (and therefore the scalar potential) are additive. When summed over all charges e_i and written in vector notation, Eq. 1.7 becomes

$$\phi = \sum_i \frac{e_i}{|\mathbf{R} - \mathbf{r}_i|} \tag{1.8}$$

where $\mathbf{R}$ is the vector from the origin to the point at which the potential is to be measured, and $\mathbf{R} - \mathbf{r}_i$ is the vector from the charge e_i to the measuring point. If $\mathbf{R} \gg \mathbf{r}_i$, (the measurement is made at a large distance from the molecule) then $1/|\mathbf{R} - \mathbf{r}_i|$ may be expanded in a Taylor series

$$\frac{1}{|\mathbf{R} - \mathbf{r}_i|} = \frac{1}{\mathbf{R}} - \mathbf{r}_i \cdot \nabla\frac{1}{\mathbf{R}} \tag{1.9}$$

so that Eq. 1.8 becomes

$$\phi = \frac{\Sigma e_i}{R} - \Sigma e_i r_i \cdot \nabla \frac{1}{R} \tag{1.10}$$

For the case of transition charge densities $\Sigma e_i = 0$ because electrical charge must be conserved in the transition. The quantity $\Sigma e_i r_i$ is the dipole moment of the system of charges; stopping the expansion in Eq. 1.9 after the first order constitutes the dipole approximation. Substituting μ for the dipole moment and using $\nabla(1/R) = R/R^3$, Eq. 1.10 becomes

$$\phi = \frac{\mu \cdot R}{|R|^3} \tag{1.11}$$

Using the definition of the potential in Eq. 1.6, the electric field of the system of charges is

$$E = -\nabla \frac{\mu \cdot R}{|R|^3} = -|R|^{-3} \nabla(\mu \cdot R) - (\mu \cdot R) \nabla |R|^{-3} \tag{1.12}$$

Because μ is independent of R we may write $\nabla(\mu \cdot R) = \mu$, and using $\nabla(1/R^3) = -3R/R^5$, then

$$E = \frac{3(\mu \cdot R)R - |R|^2 \mu}{|R|^5} \tag{1.13}$$

so that the electric field intensity of a system of charges with $\Sigma e_i = 0$ falls off as R^{-3}. The energy of interaction between two systems is calculated by placing one system in the field of the other. Again using the dipole approximation

$$U = -\mu_a \cdot E_b \tag{1.14}$$

where the subscript denotes the system of charges (molecule a or molecule b). Substitution of Eq. 1.13 gives

$$U = \frac{(\mu_a \cdot \mu_b)R^2 - 3(\mu_a \cdot R)(\mu_b \cdot R)}{|R|^5} \tag{1.15}$$

which is often written as

$$U = \frac{|\mu_a||\mu_b|}{R^3} \kappa \tag{1.16}$$

where

$$\kappa = \cos\alpha - \cos\beta_a \cos\beta_b \tag{1.17}$$

Here, α is the angle between the dipoles, and β is the angle between a dipole and the vector connecting the two dipoles.

There are two limiting cases for the strength of the resonance interaction U. At one limit is the strong coupling case, where $2|U| >> |W_{a'b} - W_{ab'}|$, and the new system energies of Eq. 1.4 are approximated by

$$W_{\pm} = \frac{1}{2}(W_{a'b} + W_{ab'}) \pm U \tag{1.18}$$

This strong interaction mixes the separated states very much like atomic

orbitals interact to form a molecular orbital (see Fig. 1-1a); the new states are often called "exciton states". As a result, the absorption and circular dichroism spectra show two peaks separated by 2U, as shown in Fig. 1-1b and 1-1c. The intensity ratio of the two exciton absorption peaks depends on the geometry of the a-b dimer and may vary from zero to infinity. The total intensity, however, must be equal to that of the separated molecules (see Fig. 1-1b). Strong coupling can also produce a large increase in the magnitude of CD peaks (Fig. 1-1c), again depending on the geometry. When excitonic CD spectra do appear, the spectrum is conservative (i.e., the CD signal sums to zero).

It is possible, and not at all unusual, to have a situation where more than two molecules are strongly interacting. In this case, the problem is solved by diagonalization of the symmetric Hamiltonian matrix

$$\mathbf{A} = \begin{bmatrix} W_1 & U_{12} & \cdots & U_{1N} \\ U_{21} & W_2 & & \vdots \\ \vdots & & \ddots & \vdots \\ U_{N1} & \cdots & \cdots & W_N \end{bmatrix} \tag{1.19}$$

for the N-molecular system. The diagonalization gives a set of N eigenvalues, which are the energies of the N exciton states, and a set of N eigenvectors which describe the degree of mixing of the i^{th} molecular state in the K^{th} exciton state

$$\Psi_K = \sum c_{iK} \psi_i \tag{1.20}$$

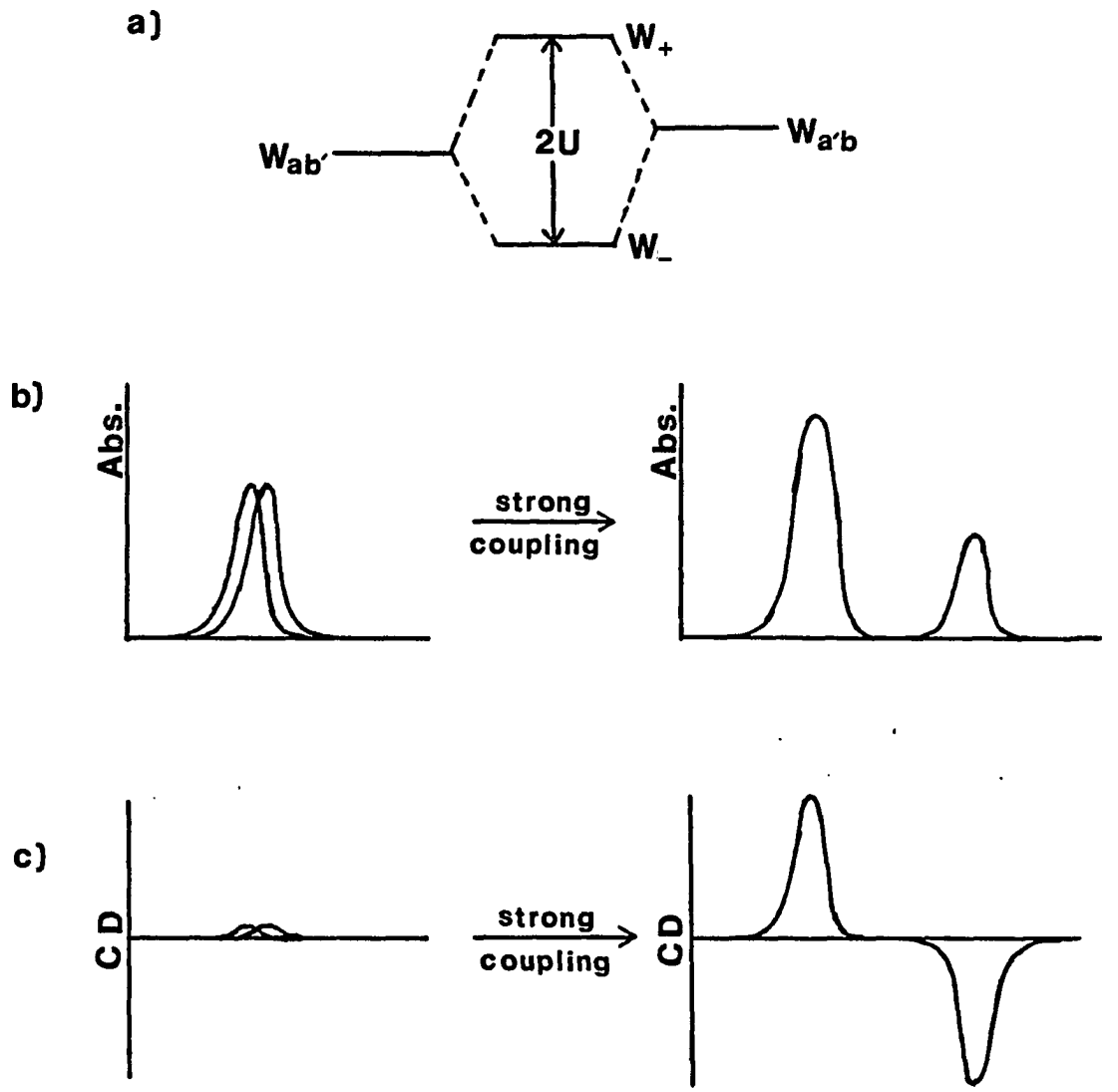

Figure 1-1. Effect of strong coupling in a two-molecule system a) Mixing of two molecular states ($W_{a'b}$ and $W_{ab'}$) to form two exciton states in the strong coupling limit. b) Effect of strong coupling of two molecules on absorption spectrum, and on c) circular dichroism (CD) spectrum.

Here, c_{iK} denotes the i^{th} component of the K^{th} eigenvector. The c_{iK} are useful in calculating the predicted absorption and CD spectra of the N-molecule complex. The absorption of the K^{th} exciton component A_K appearing at energy W_K is given by [7]

$$A_K = \sum_{i,j=1} c_{iK} c_{jK} \, \mu_i \cdot \mu_j \qquad (1.21)$$

using the dipole approximation and the CD intensity of this exciton component is

$$C_K = 1.7 \times 10^{-5} \omega_o \sum_{\substack{i,j=1 \\ i>j}}^{N} c_{iK} c_{jK} \, R_{ij} \cdot (\mu_i \times \mu_j) \qquad (1.22)$$

In Eqs. 1.21 and 1.22, μ_i is the dipole vector of the i^{th} molecule with magnitude in Debye (1 Debye = 10^{-18} esu-cm), R_{ij} is the distance vector from the dipole of molecule i to that of molecule j (in nm), and ω_o is the band center ($N^{-1} \Sigma W_N$). Knowing the position (eigenvalue) and intensity of each exciton component, the absorption and CD spectra are customarily generated by expanding each component in a gaussian of appropriate linewidth.

If two or more molecules are strongly interacting, they will mix to form exciton states as shown above, but the question of the location of the excitation has not been answered. In order to determine the excitation probability densities, time-dependent perturbation theory must be used. Returning to the two-molecule, one excitation system, solution

of the time dependent problem shows that under the strong interaction the excitation will show wavelike behavior with oscillations back and forth between the two molecules [6]. If molecule a is initially excited, then the first maximum in the probability that the excitation is on molecule b occurs at time

$$t = \frac{h}{4|U|} \sin 2\alpha \tag{1.23}$$

where h is Planck's constant. Since $\sin 2\alpha \approx 1$ for strong interaction (see Eq. 1.4), this defines a "quasi-transfer rate" of

$$n_{a \to b} = \frac{4|U|}{h} \tag{1.24}$$

As defined in Eq. 1.17, U is proportional to the inverse cube of the distance between molecules; the quantity $4|U|/h$ is therefore the "R^{-3} rate" often mentioned in the literature for strongly interacting molecules.

The second limiting case is where the interaction energy U is small, which defines the weak coupling case (this is called "very weak coupling" by Förster [6]; his "weak coupling" case does not apply for large molecules). If $2|U| \ll |W_{a'b} - W_{ab'}|$, then $\sin 2\alpha \approx 0$, and the system energy levels are given by $W_+ \approx W_{a'b}$ and $W_- \approx W_{ab'}$. Therefore, there is very little mixing of states, and the absorption (and CD) spectra are essentially unchanged from that of the separated molecules. In this limit, the excitation may be considered to reside on either molecule a or

molecule b, with a definite probability of transfer. This rate of transfer is again calculated using time-dependent perturbation theory, but now molecular vibrational states must be taken into account as well. In the strong coupling case, the effect of ignoring molecular vibrations was that a definite phase relationship was assumed between the vibrations of the unexcited and excited molecules. This implies that the strong coupling "transfer rate" of Eq. 1.24 is valid only for rates of greater than $1/T_2$, where T_2 is the chromophore dephasing time. In the weak coupling limit, the molecular vibrations are assumed to be completely thermalized in the excited molecule (as well as in the unexcited one). Femtosecond transient absorption experiments [8,9] have shown that thermalization occurs on a timescale of a few hundred femtoseconds in large organic dye molecules, independent of the solvent. Under the assumption of thermalized vibrations, the transfer probability acquires the form of

$$n_{a\to b} = \frac{U^2}{2}\int\left[\int g'(E'_a)\,S_a^2(E'_a, E'_a-h\omega)\,dE'_a\right]\left[\int g(E_b)\,S_b^2(E_b, E_b+h\omega)\,dE_b\right]\,d\omega \quad (1.25)$$

where $g'(E_a)$ and $g(E_b)$ are the Boltzmann factors for the molecules in the excited and unexcited states and S_a^2 and S_b^2 are vibrational overlap integrals (Franck-Condon factors) between ground and excited states of molecules a and b. The integrals in Eq. 1.25 are therefore closely related to the absorption and emission spectra, and the transition rate can be expressed as

$$n_{a \to b} = \frac{1}{\tau_o}\left[\frac{R_o}{R_{ab}}\right]^6 \tag{1.26}$$

where τ_o is the intrinsic lifetime of molecule a and the critical transfer distance R_o is given by

$$R_o^6 = \frac{9000\kappa^2(\ln 10)\phi}{128\ \pi^5\ n^4\ N} \int f_a(\omega)\varepsilon_b(\omega)\omega^{-4}d\omega \tag{1.27}$$

Here, n is the refractive index of the medium, ϕ is the quantum yield of fluorescence of molecule a, and N is Avogadro's number. The fluorescence spectrum $f_a(\omega)$ of molecule a and the molar extinction coefficient $\varepsilon_b(\omega)$ of molecule b are on a wavenumber (ω) scale, and the fluorescence spectrum is normalized to unity ($\int f_a(\omega)d\omega = 1$).

In comparing Eq. 1.24 and Eq. 1.26, one can see that in the strong coupling case the transfer rate varies as R^{-3} and in the weak coupling case the transfer rate is proportional to R^{-6}. Kenkre and Knox [10] have bridged the gap between these two regimes by using memory functions which decay exponentially with the time constant $1/T_2$. Knox has argued [11] that the decay time T_2 of phase information is $\sim 5\times10^{-15}$ s, based on the absorption bandwidth of (bacterio)chlorophyll monomers. As a result, there is a very brief time during which the excitation has the wavelike form of strong coupling, after which the excitation must be considered as localized on either molecule a or molecule b, and the R^{-6} rate applies.

In the weak coupling limit, two distinct types of EET may be distinguished: transfer between like molecules (D → D transfer) and

transfer betweeen unlike molecules (D → A transfer). While D → D transfer is reversible (it must be, due to symmetry), D → A transfer often is not due to the effect of the overlap integral in Eq. 1.27. This can be explained from the absorption and emission specta of the interacting molecules shown in Fig. 1-2. While the fluorescence of the donor f_D and the absorption of the acceptor ε_A have good overlap and therefore a large Förster parameter R_o, the opposite situation (f_A and ε_D) have very little overlap and almost no probability of transfer. In such a system, the excitation will become localized on the lower energy molecule with a low probability of back-transfer.

Electronic excitation transfer was first detected in D → A systems as sensitized luminescence, in which a "sensitizer" molecule absorbs light and transfers its energy to a "fluorescer" molecule, which is detected by its emission. Such a situation occurs often in photosynthetic systems; for example, in green plants, chlorophyll (Chl) b absorbs maximally at ~650 nm, but no Chl b emission is observed. Instead, emission from Chl a, which absorbs at ~680 nm, is observed. A contrasting type of situation is that in which the absorbing molecule transfers its excitation to a nonfluorescing "trap". This situation also exists in photosynthetic systems, where the donor is an antenna chromophore, and the trap is the reaction center, which due to its high efficiency in charge separation, shows little or no fluorescence.

When an excited molecule is able to transfer its excitation (in the weak coupling limit) to a nonfluorescent trap, an additional decay of rate k_T ($=n_{a\to b}$) is introduced into the system

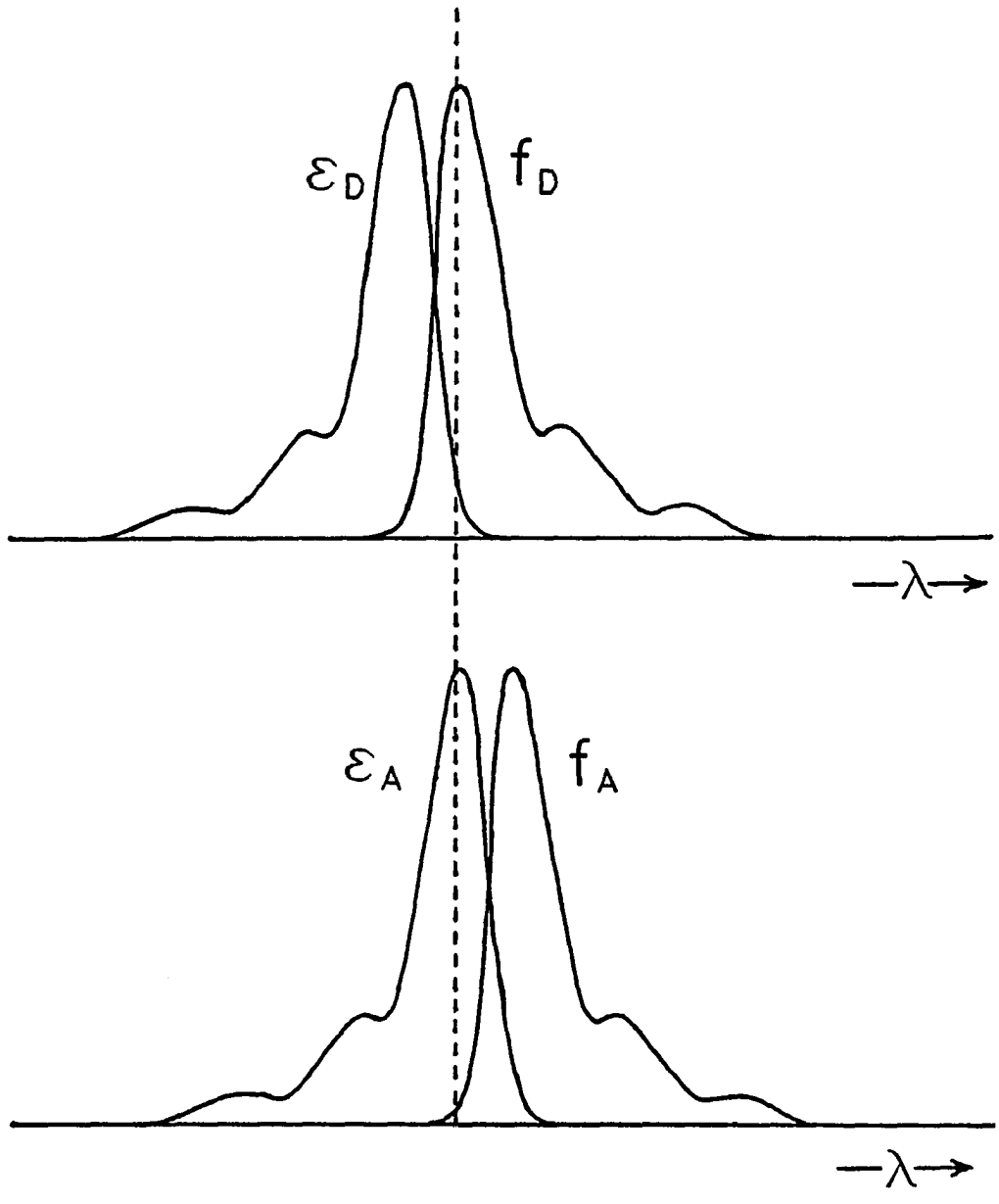

Figure 1-2. Relative position of absorption (ε) and fluorescence (f) spectra of donor (D) and acceptor (A) molecules. Note that donor emission and acceptor absorption show a large degree of spectral overlap.

$$\frac{1}{\tau_{obs}} = k_{obs} = k_o + k_T \tag{1.28}$$

where k_{obs} is the observed decay rate and k_o is the decay rate in the absence of a trap molecule. Therefore, the effect is a lowering of the observed lifetime, τ_{obs}. For a system with random molecular positions a range of lifetimes is observed due to variation in the distance R_{ab} between molecules. If we assume that traps far outnumber donor molecules ([T] >> [D]), and the molecules are randomly oriented ($\kappa^2 = 2/3$), the form of the excited state decay P(t) can be calculated analytically as

$$P(t) = \exp[-t/\tau - gC_T(3\pi t/2\tau)^{1/2}] \tag{1.29}$$

where the dimensionless reduced concentration of traps C_T is given by

$$C_T = \frac{4}{3}\pi R_o^3 \rho_T \tag{1.30}$$

Here, ρ_T is the trap number density (number of molecules per unit volume) and the factor $g = 0.8452$ arises from the static limit assumption that the molecules do not rotate during their excited state lifetime.

The condition under which Eq. 1.29 is valid is that [D] is small enough that the rate of transfer between donor molecules (D → D transfer) is negligible compared to the rate of excitation decay. Inclusion of D → D transfer complicates theoretical development considerably, since more than one hop per excitation becomes possible. In this case, the excitation probability function is given by a linked set of master

equations [12]

$$\frac{dp_j}{dt} = \sum_{k=1}^{N} w_{jk}(p_k - p_j) - \sum_{k=N+1}^{N+M} v_{kj}p_j - p_j/\tau_D \qquad j \leq N \qquad (1.31a)$$

$$\frac{dp_j}{dt} = \sum_{k=1}^{N} v_{jk}p_k - p_j/\tau_T \qquad N+1 \leq j \leq N+M \qquad (1.31b)$$

where donor molecules are numbered 1 through N and nonfluorescent (deep) trap molecules N+1 through N+M. $p_j(t)$ gives the probability that the excitation is on molecule j at time t, and w_{jk} and v_{jk} are the transfer rates given by Eq. 1.26 for D → D and D → T transfer, respectively. τ_D and τ_T are the measured lifetimes of donor and trap molecules in the absence of energy transfer. For a system with no trap molecules (only D → D transfer possible), Eq. 1.31 reduces to

$$\frac{dp'_j}{dt} = \sum_k w_{jk}(p'_k - p'_j) \qquad (1.32)$$

where the monomolecular decay term τ_D is eliminated by the substitution $p'_j(t) = p_j(t)\exp(-t/\tau_D)$. Eqs. 1.31 and 1.32 are valid in any system of weakly coupled molecules; if the system N (or N+M) is small enough, the set of master equations may be solved simultaneously and the probability distribution of excitation sites will be known at all times (for a given set of initial parameters). However, for larger systems such as random molecules in solution, the problem is intractable, and approximate solutions must be generated.

It is important to note that for the case of [T] → 0, no change in the excited state lifetime is observed ($k_T = 0$ in Eq. 1.29). For systems with only D → D transfer, EET is detected by depolarization techniques. Fluorescence depolarization (Fig. 1-3a) is a well-known technique in which a linearly polarized light pulse excites the sample and fluorescence components $I_{\parallel}(t)$ and $I_{\perp}(t)$ with polarization parallel and perpendicular to the excitation pulse are observed. For a system of molecules in three dimensions, these components are described by

$$\begin{aligned} I_{\parallel}(t) &= P(t)[1 + 0.8G^S(t)] \\ I_{\perp}(t) &= P(t)[1 - 0.4G^S(t)] \end{aligned} \tag{1.33}$$

where P(t) is the isotropic decay observed in the absence of energy transfer. The isotropic decay may be measured by placing a polarizer in the fluorescence at 54.7° from parallel; this effectively measures the weighted average $(2I_{\perp}(t) + I_{\parallel}(t))/3$, which from Eqs. 1.33 is P(t). Then $G^S(t)$ may be expressed as $2.5(I_{\parallel}(t) - I_{\perp}(t))/3P(t)$, or the time-dependent fluorescence anisotropy multiplied by 2.5. $G^S(t)$ normally ranges from 1.0 (maximum anisotropy) to 0.0 (fully depolarized).

The experimental configuration for pump-probe spectroscopy is shown in Fig. 1-3b. In this case, the absorption components $A_{\parallel}(t)$ and $A_{\perp}(t)$ are measured by using pump and probe pulses with parallel and perpendicular polarizations, respectively. The isotropic decay P(t) is measured with the probe beam polarization rotated 54.7° from the pump beam polarization. As it is drawn in Fig. 3, $I_{\parallel}(t)$ and $I_{\perp}(t)$ correspond to polarization along the x and y axes, respectively, while $A_{\parallel}(t)$ and

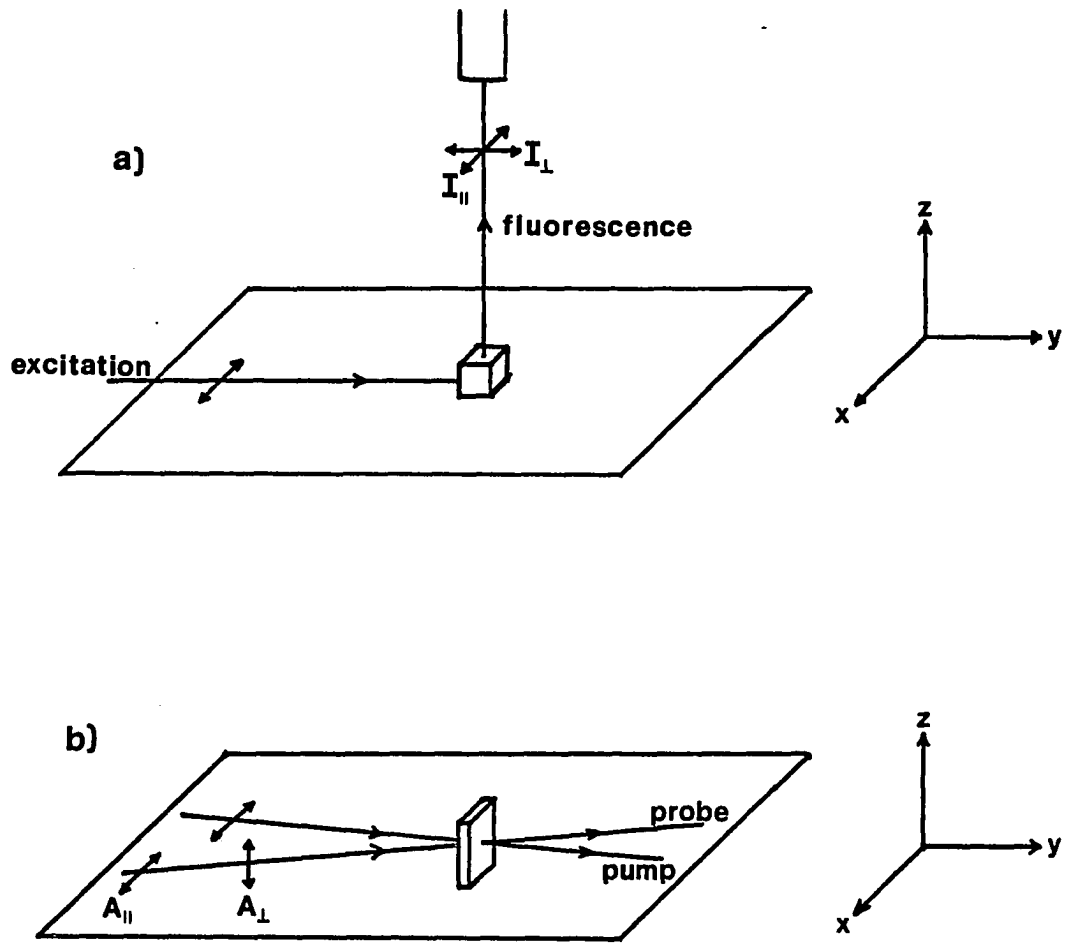

Figure 1-3. Schematic of energy transfer detected by a) fluorescence depolarization, and b) absorption depolarization. In both cases, excitation beams are linearly polarized; in a) polarized fluorescence is detected.

$A_{\perp}(t)$ correspond to polarizations along the x and z axes. It has been shown [13] that, assuming parallel absorption and emission dipoles, the components along the y and z axes are equivalent. Therefore, Eqs. 1.33 are valid for absorption components $A_{\parallel}(t)$ and $A_{\perp}(t)$ as well as the fluorescence components $I_{\parallel}(t)$ and $I_{\perp}(t)$.

Much theoretical work has been done on random systems of D → D electronic excitation transport in solution. Since Eq. 1.32 cannot be solved analytically for such a system, several theorists [14,15] have developed approximations to its solution of varying degrees of complexity. It has been shown experimentally [13] that a relatively simple approximation (the two-particle theory [14]) is accurate for a large range of concentrations of organic dye molecules in solution. The two-particle model predicts that in a 3-dimensional system the polarization will decay as

$$G^{s}(t) = \exp[-C_{D}(\pi t/2\tau_{D})^{1/2}] \qquad (1.34)$$

where C_D is the dimensionless reduced donor concentration analogous to C_T in Eq. 1.30. Again, the $\exp(-t^{1/2})$ behavior arises from dispersion in the distance between molecules; nonrandom systems will in general display different forms in the polarization decay (see Chapter V).

References

1. Emerson, R.; Arnold, W. J. Gen. Physiol. 1932, 15, 391.
2. Emerson, R.; Arnold, W. J. Gen. Physiol. 1932, 16, 191.
3. Gaffron, H.; Wohl, K. Naturwissenschaften 1936, 24, 81.
4. Förster, Th. Discuss. Faraday. Soc. 1959, 27, 7.
5. Knox, R. S. In "Bioenergetics of Photosynthesis"; Govindjee, Ed.; Academic Press: New York, 1975; p. 189.
6. Förster, Th. In "Modern Quantum Chemistry, Part IIIB: Light and Organic Crystals"; Sinanoglu, O., Ed.; Academic Press: New York, 1965; p. 93.
7. Pearlstein, R. M. In "Photosynthesis - Energy Conversion by Plants and Bacteria"; Govindjee, Ed.; Academic Press, New York, 1982; Vol. 1, p. 293.
8. Weiner, A. M.; Ippen, E. P. Chem. Phys. Lett. 1985, 114, 456.
9. DeSilvestri, S.; Weiner, A. M.; Fujimoto, J. G.; Ippen, E. P. Chem. Phys. Lett. 1984, 112, 54.
10. Kenkre, V. M.; Knox, R. S. Phys. Rev. Lett. 1974, 33, 803.
11. Knox, R. S. In "Primary Processes in Photosynthesis"; Elsevier: Amsterdam, 1977; Vol. 2, p. 73
12. Loring, R. F.; Anderson, H. C.; Fayer, M. D. J. Chem. Phys. 1982, 76, 2015.
13. Anfinrud, P. A. Ph. D. Dissertation, Department of Physical Chemistry, Iowa State University, 1987.
14. Huber, D. L.; Hamilton, D. S.; Barnett, B. Phys. Rev. B 1977, 16, 4642.
15. Gochanour, C. R.; Andersen, H. C.; Fayer, M. D. J. Chem. Phys. 1979, 70, 4254.

CHAPTER II. EXPERIMENTAL

The main experimental technique used in this work is transient absorption (pump-probe) spectroscopy. This consists of exciting the sample with a short pump pulse and some time later measuring the transmission through the sample of a short probe pulse. In experiments on strongly absorbing molecules such as in this work, transient photobleaching is detected; the pump pulse lifts a fraction of the sample to the excited state, where the absorption coefficient is less than in the ground state, and the probe pulse therefore experiences an increase in transmission. This "induced transmission", or photobleaching, is plotted as a function of the delay time t_d between pulses; as the delay time increases, a greater fraction of the molecules have returned to the ground state before the arrival of the probe pulse and the photobleaching curve tends toward zero. The plot of photobleaching vs. delay time therefore describes the ground state recovery of the ensemble of molecules absorbing at the probe wavelength. Note that this procedure does not rely on the speed of any electronic measuring device; time resolution of pump-probe experiments depends only on the temporal width of the optical pulses used.

Historically, there have been two rather distinct classes of pump-probe experiments: those using low repetition rates ($\lesssim$ 1000 Hz) and rather intense (microjoule to millijoule) pulses, and those using high repetition rates (>1 MHz) and weak (nanojoule or less) pulses. In the first type, the optical delay is often varied in discrete steps, with a number of laser shots averaged at each delay position. In the second type (including the experiments described in this work), the optical delay is

varied smoothly and the photobleaching signal is detected as a continuous function of the delay. The sections below describe the details of the picosecond laser system, pump-probe optical setup, detection electronics, and computer experimental control as used in Chapters IV, VI, VII, and VIII. An additional section discusses experimental artifacts common in pump-probe spectroscopy.

Passively Mode-Locked Dye Lasers

There are two basic ways of producing a mode-locked dye laser: synchronously pumping with an actively mode-locked pump laser [1], or adding a mode-locking dye to an otherwise completely continuous-wave system. Synchronous pumping has the advantage of stability and ease of use (as well as the ability to reduce the repetition rate by cavity dumping), while passive mode-locking is less expensive (since no acousto-optic mode-locker and drive electronics are required for the pump laser) and generally produces narrower pulses. (Synchronous pumping and passive mode-locking may be combined to produce hybrid mode-locking; all of these techniques have been qualitatively compared in the literature [2].) The narrowest pulses directly from a laser (27 fs) have been generated in a colliding pulse mode-locked (CPM) dye laser [3] which is a passively mode-locked laser in a ring configuration; however, CPM lasers suffer from low output power and little tunability. By using various combinations of gain and absorber dyes, pulses shorter than 1 ps have been generated over a large part of the visible wavelength range [4] in a simple two-jet linear cavity (Fig. 2-1) by passive mode-locking.

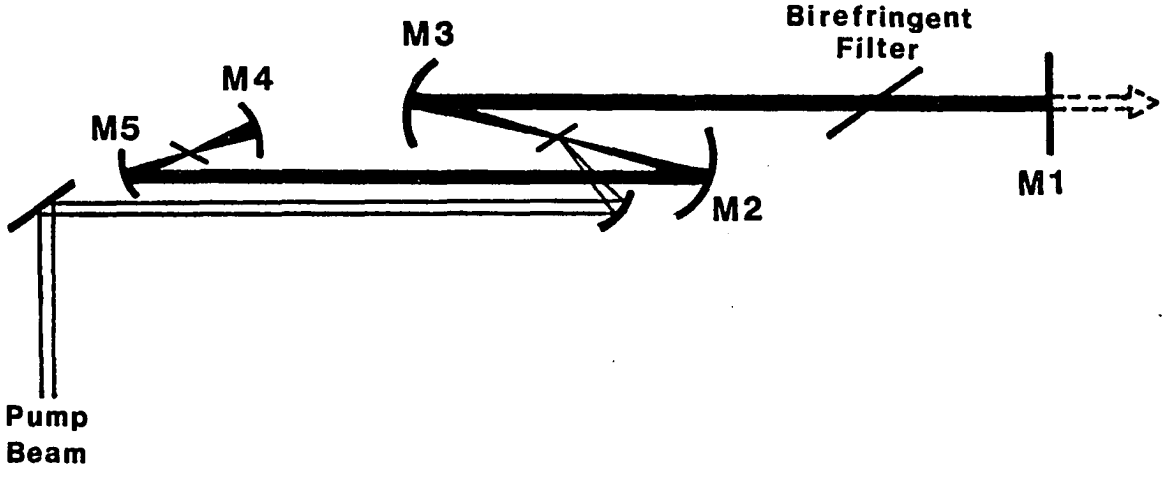

Figure 2-1. Schematic of linear-cavity passively mode-locked dye laser; overall length is not to scale.

Passive mode-locking arises from saturable absorption in the mode-locking dye and saturable amplification in the gain dye. The saturable absorber sharpens the leading edge of the intracavity pulse as shown in Fig. 2-2a; the solid line shows the pulse before passing through the saturable absorber jet, the dashed line after the jet. The leading edge is decreased in amplitude due to absorption by the mode-locking (absorber) dye, but at the peak the dye has become bleached; that is, the majority of the molecules are in the excited state and the optical density is very small. Therefore, the peak and trailing edge of the pulse pass through the jet nearly unhindered, and the result is a sharpening of the leading edge and an overall narrowing of the pulse. The trailing edge is shaped in a similar way by saturable amplification in the gain dye (see Fig. 2-2b). The leading edge and peak are amplified by the gain jet, but this returns most of the dye molecules to the ground state so that the trailing edge receives little or no amplification. In this way, the trailing edge is diminished as compared to the peak and the pulse full-width at half-maximum is reduced.

These pulse-shortening mechanisms have been examined theoretically [5,6] by injecting a Lorentzian pulse into a model cavity and calculating its shape evolution through many cavity round-trips. The conditions corresponding to stable mode-locking were a net round-trip loss on the leading and trailing edges of the pulse and a net round-trip gain at the peak. The calculations showed that these conditions could be met provided that: 1) the relaxation time of the gain medium is of the same order of magnitude as the cavity round-trip time; 2) the relaxation time of the absorber is less than the relaxation time of the gain medium; and

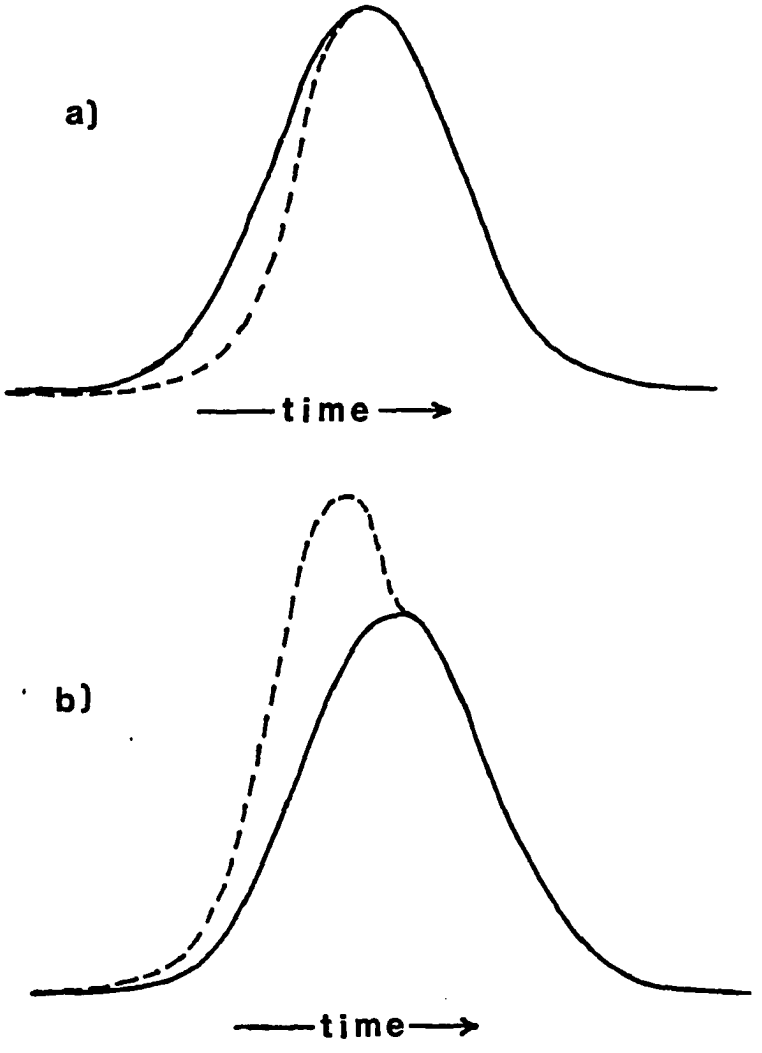

Figure 2-2. Idealized view of effect of a) saturable absorption and b) saturable gain in passively modelocked dye laser. Solid lines are laser pulse before passing through the respective element, dotted lines are after the element.

3) the s parameter defined by

$$s = \frac{A_g \sigma_a}{A_a \sigma_g} \qquad (2.1)$$

is large (≥ 2). In Eq. 2.1, σ_a is the absorber cross-section, σ_g is the stimulated emission cross-section, and A_a and A_g are the beam areas in the absorber and gain dyes, respectively. According to this theoretical development, the cavity pulse may be narrowed by as much as a factor of $\sqrt{2}$ for each cavity round-trip, and such narrowing continues indefinitely. In a real cavity, this narrowing is counteracted by dispersion and bandwidth restriction and an equilibrium pulse width is eventually reached.

The in-house built dye laser used in this work was of the design shown in Fig. 2-1, with R = 10 cm for M2 and M3 and R = 5 cm for M4 and M5. The output was transmitted through the flat mirror (M1), which was typically 95% reflecting. The overall length of the cavity was 120 cm, giving a repetition rate of 125 MHz, or one pulse every 8 ns. Tuning was accomplished with a 0.5 mm thick single-plate birefringent filter and the laser was pumped with 1.5 - 2.5 W of all-lines output of a continuous-wave argon ion laser. Combinations of gain dye/absorber dye used were rhodamine 6G (R6G)/DQOCI, DCM/DQTCI, and DCM/DDCI. Each of the three requirements for stable mode-locking was met in this cavity. The relaxation times of the gain dyes (~3.4 ns for R6G, ~2 ns for DCM) are of the order of the round-trip time of 8 ns; the relaxation time of the absorber dyes (each <1.5 ns) was less than that of the gain dyes, and using 2x shorter focal length mirrors for the absorber dye than for the

gain dye ($A_g = 4A_a$) assured that the s parameter of Eq. 2-1 was large. Pulse widths between 0.8 ps and 2.5 ps (autocorrelation width) were obtained at all wavelengths and typical output powers varied from 30 to 80 mW. The pulse width was most likely limited by the spectral bandpass of the single plate birefringent filter and by intracavity dispersion.

Multiple Modulation

The traditional method of detection in pump-probe experiments using high repetition rate lasers is by lock-in amplification. A mechanical chopper is placed in the pump beam path, which introduces a square-wave modulation on the beam at frequency f_{chop}. If transient photobleaching is detected, the transmission through the sample of the probe beam is smaller when the pump beam is blocked by the chopper than when the pump beam is unblocked. Therefore, the sample introduces a small modulation of frequency f_{chop} on the intensity of the probe beam; its amplitude is proportional to the excited state population. The output of a photodiode detecting the probe beam intensity is routed directly to a lock-in amplifier (LIA), which measures the amplitude of the modulation on the probe beam. The output of the LIA therefore measures the amount of photobleaching, which is recorded as a function of the delay between pump and probe pulses.

The major disadvantage to this approach to detection is that the amount of noise on the output of most continuous-wave modelocked dye lasers is orders of magnitude larger at low frequencies than at high frequencies. It has been shown [7] that at frequencies in the megahertz

range, the noise level approaches the shot noise limit (the theoretical limit due to random arrival of photons at the photodetector). This implies that if the pump beam were modulated at a frequency in the megahertz range, then the data quality would be much improved. Unfortunately, mechanical choppers cannot be operated at this speed; instead, acousto-optic modulation is used. In general, acousto-optic modulation acts as a voltage-controlled beam attenuator. The attenuation is produced by diffraction of the beam from a grating produced by areas of high and low index of refraction in the acousto-optic material, which are the crests and valleys of an acoustic wave. The acoustic wave is produced by a piezoelectric transducer on the material which is driven by a large amplitude radio frequency (RF) voltage. The fraction of the beam diffracted is proportional to the power of the RF signal. To produce a modulation on the pump beam at 4 MHz, for example, the RF signal is modulated at 4 MHz as shown in Fig. 2-3; also shown are the undiffracted (zero-order) beam intensity and the first-order beam intensity. Since the different diffraction orders are separated spatially, one of them can be blocked and the other used in the pump-probe experiment. In our system, Isomet 1206C modulators and 233A-1 drivers were used, and were typically driven by ~300 mV peak-to-peak (into 50 Ω) sine waves. The AOM drivers produced ~16 V p-p when modulated at the 110 MHz center frequency; this was sufficient to deflect ~80% of the beam into first order at the maximum (see Fig. 2-3).

Another improvement to the traditional chopper/lock-in technique is to modulate both pump and probe beams; in this case, the sample acts as a molecular mixer and a modulation at the sum and difference frequency is

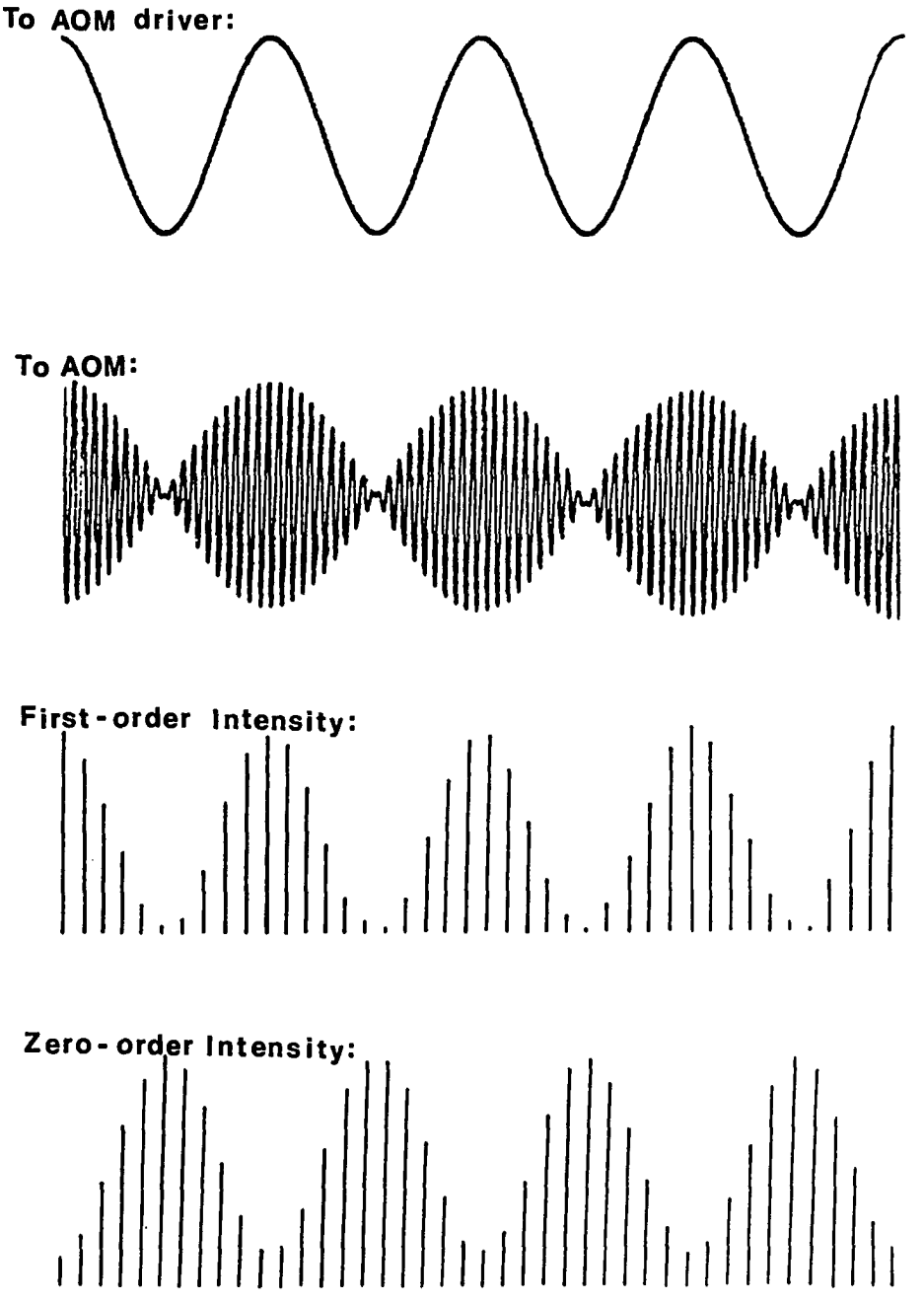

Figure 2-3. Signal applied to acousto-optic modulator driver, output from AOM driver to AOM, and resulting first-order and zero-order beam intensities as functions of time.

produced on the probe beam. This can be explained as follows: if the pump beam modulation is described by sin $\omega_1 t$, the transient photobleaching causes a modulation in optical density of the sample of Asin $\omega_1 t$. The intensity of the transmitted probe beam is the product of the incident intensity (sin $\omega_2 t$) and the fraction left unabsorbed by the sample, which is proportional to Asin $\omega_1 t$. Using the relation (sin $\omega_1 t$)(sin $\omega_2 t$) = $[\cos(\omega_1-\omega_2)t - \cos(\omega_1+\omega_2)t]$, one can see that sum and difference frequencies are produced. Demodulation at either the sum or difference frequency (but not both) constitutes single-sideband detection. Since the probe beam contains a large amplitude component at ω_2, it is best to set $\omega_1 >> \omega_2$; this avoids interference due to a large ω_2 very near in frequency to $\omega_1+\omega_2$ or $\omega_1-\omega_2$. The multiple modulation technique has the advantage that the detection system is immune to scattered pump light and to electrical interference from the modulators, since neither of these contain components at either the sum or difference frequency.

The frequency synthesis and detection scheme used in our laboratory has been described previously [8]; briefly, the system allows flexible modulation frequencies for both pump and probe beams with single-sideband detection from 0.01 to 30 MHz. The modulation frequency of the probe, ω_2, is controlled by f_{ext} from an external frequency synthesizer as $\omega_2 = |f_{ext} - 48.05\text{MHz}|$ and is generally held fixed at $\omega_2 \approx 0.5$ MHz. The pump beam modulation frequency ω_1 is determined by the detection frequency f_{det} set on the radio receiver as $\omega_1 = |f_{det} - f_{ext} + 48.05\ \text{MHz}|$ and is generally used between 4.0 and 7.0 MHz at a local minimum in the laser noise spectrum.

Optical Arrangement for Pump-probe Spectroscopy

The output of the passively modelocked dye laser was alternately routed to a real-time autocorrelator which has been previously described [9] or to the pump-probe optical arrangement shown schematically in Fig. 2-4. The system is basically a highly modified Michelson interferometer; the beamsplitter (BS in Fig. 2-4) divides the input into pump and probe beams, which traverse optical delay lines and are recombined in the sample. A 50% beamsplitter was used, resulting in nearly equal powers in pump and probe beams. Since only the relative delay between pump and probe and their relative polarization are important, either beam could be designated the probe with the other acting as pump; the choice of probe beam is made by placement of the photodiode (PD). That beam which is detected is automatically the probe and the other is the pump. In Fig. 2-4, it can be seen that the pump beam is variably delayed while the probe beam delay is constant. This choice was made because in the opposite arrangement, nonlinearity in the delay stage travel could possibly cause the probe beam to wander across the photodiode, adding noise or instability to the system.

The polarization of pump and probe beams are chosen by identical Glan-Thompson prisms, one of which is fixed at +45° to the input beam polarization, the other is variable from +45° (parallel) to -45° (perpendicular). The fixed polarizer was placed in the probe beam to avoid deviations in beam detection at the photodiode due to rotations of polarization; changing the pump beam polarization typically deviated the beam direction slightly so that re-optimization of the signal was

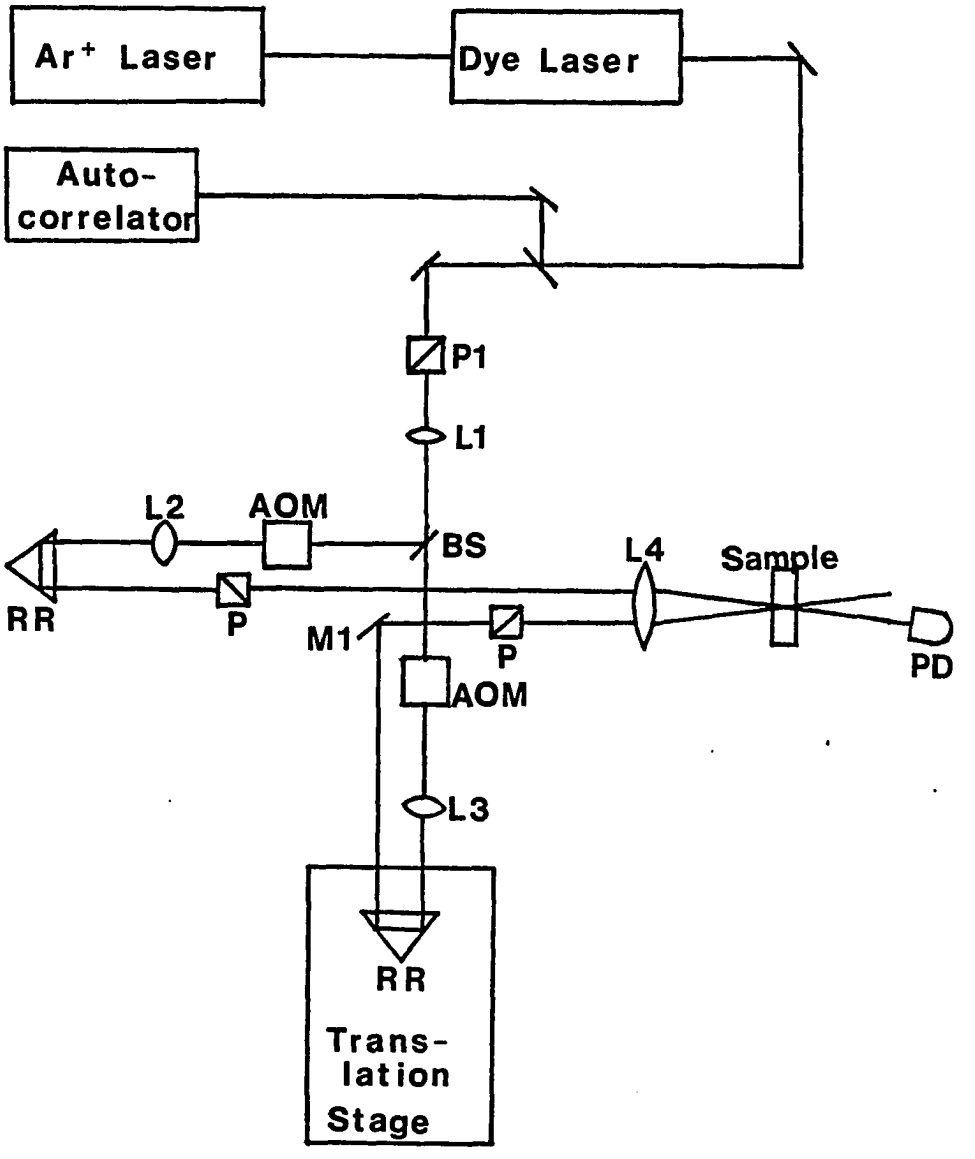

Figure 2-4. Schematic of optical arrangement for transient absorption (pump-probe) spectroscopy as used to study depolarization due to electronic energy transfer.

necessary by adjusting the angle of mirror M1.

Other than the variable delay and variable polarization, the pump and probe optical delay arms are very similar; each contains a corner cube prism (retroreflector, RR), an acousto-optic modulator (AOM), and collimating lens (L). Retroreflectors are useful because they have the property that the outgoing beam is parallel to the incoming beam, independent of the angular orientation of the retroreflector. This is particularly important for the variably delayed beam because a translation stage inevitably contains angular deviations from linearity of travel termed pitch and roll (see Fig. 2-5a). A retroreflector was used in the other arm of the arrangement in order to help reduce fluctuations in signal strength due to pointing instability of the dye laser. Fig. 2-5b shows how such instability can affect the signal if a rooftop prism is used in place of a retroreflector; an angular deviation of the input beam produces a large spatial deviation of the beam passing through the rooftop prism, but a small spatial deviation in the beam passing through the retroreflector. The two beams are then separated spatially in the sample and the signal is artificially decreased.

The acousto-optic modulators (AOMs) are used to produce an amplitude modulation on the pump and probe beams as discussed above. Focussing into the AOMs is required not only because of the small (1 mm diameter) aperture of the AOM, but also because high frequency modulation is inefficient for large beam diameters. This can be understood by realizing that since the acoustic wave travels at 3.63×10^6 mm/s in lead molybdate (the acousto-optic material), it would take 2.75×10^{-7} s to traverse a 1 mm beam; therefore, frequencies greater than $1/(2.75 \times 10^{-7}\ s)$ will

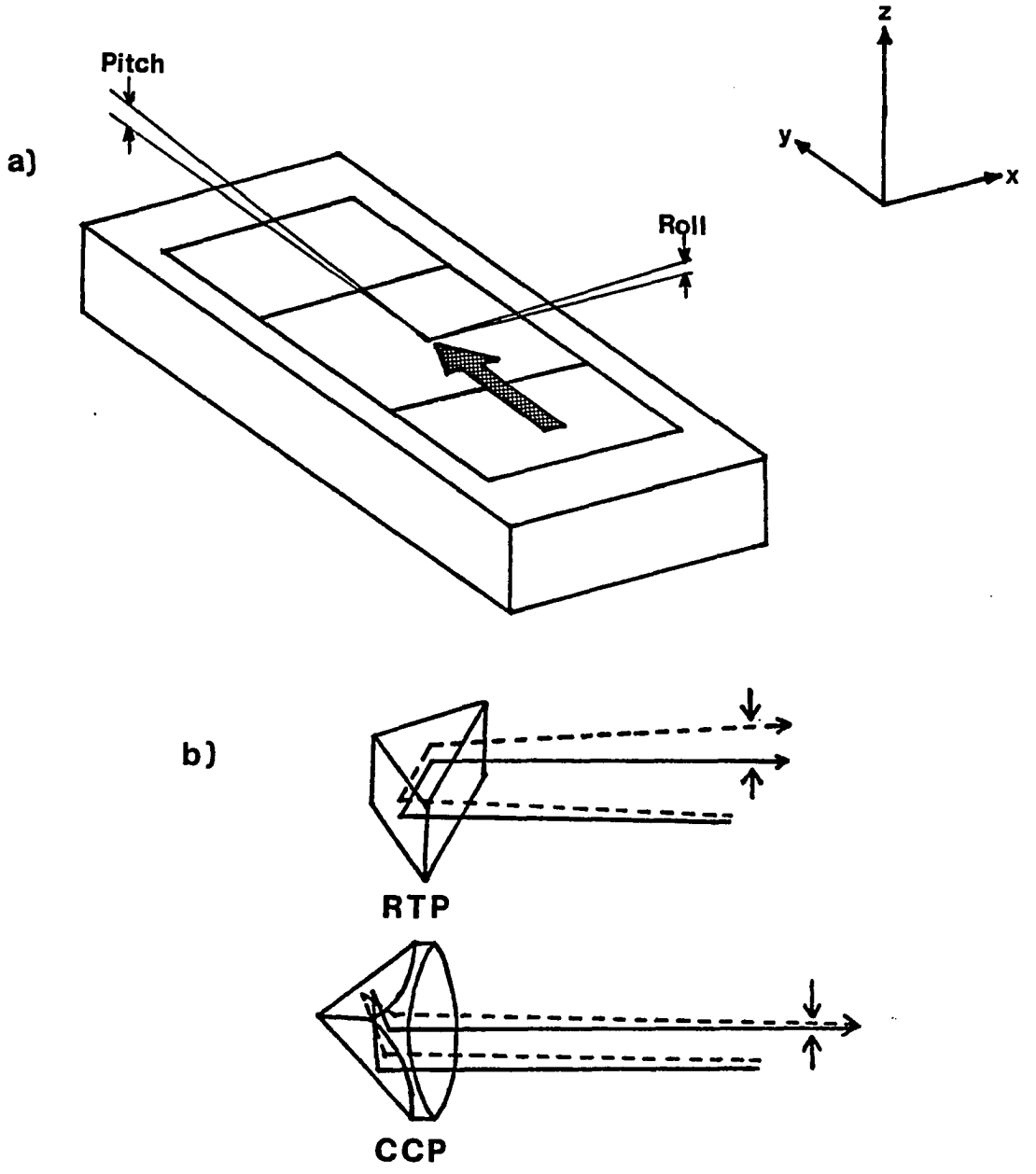

Figure 2-5. Possible error sources in pump-probe systems a) Deviations in linearity of translation stage travel in x-direction (pitch) and y-direction (roll). b) Displacement of beams due to variation in incoming angle upon reflection from rooftop prism (RTP) and retroreflector (CCP).

present areas of both high and low acoustic power to the optical beam, decreasing the modulation depth. However, very tight focussing limits the deflection efficiency because the beam intersects fewer acoustic wave cycles. Each of these effects were avoided to a large extent by using a focussing lens of 19.6 cm focal length, which produces an optical beam diameter of ~0.10 mm at the beam waist for an input diameter of 1 mm. Fig. 2-4 shows that a single lens (L1) focusses into both AOMs, but separate collimating lenses (L2,L3) are required for pump and probe beams.

The final lens before the sample (L4) is used to focus both pump and probe beams into the sample. Using a common lens rather than separate lenses has the advantage that spatial overlap of pump and probe beams can be assured (for a one-color experiment) by requiring that the beams be parallel to each other prior to entering the lens. The choice of focal length of lens L4 involves a trade-off between beam waist diameter and amount of spatial overlap of pump and probe beams. A short focal length lens causes a smaller spot size (which increases the signal strength due to greater power density), but causes pump and probe beams to converge at a greater angle, which decreases spatial overlap and hence the signal. It may be reasoned that the former effect is more important since the signal is proportional to the square of the photon flux; taking all factors (see the section on artifacts below) into account, a 7.3 cm focal length lens was chosen, giving a spot size of ~25 μm in the sample.

Samples were housed between fused silica plates using spacers of 100 μm to 800 μm in thickness depending on the optical density of the sample. Thick spacers are generally preferred so that positioning of the sample is not a critical parameter; however, for concentrated solutions a

thick sample transmits very little of the probe beam and the signal is attenuated. Therefore, it is advantageous to adjust either the sample concentration or spacer thickness for an absorbance of ~0.2 at the laser wavelength.

The transmitted probe intensity is detected by an EG&G FOD-100 photodiode, which produces ~0.3 amperes per watt of optical power at the wavelengths used here. The output of the photodiode (with 2 kΩ internal termination) was routed directly to the input (nominally 50 Ω) of a modified Drake R-7A receiver [8] and the transient signal detected as described above. An additional FOD-100 photodiode sampled the relative laser intensity using a stray reflection from the surface of one of the optical components (P1). The output of this photodiode went to an in-house built current-to-voltage converter and RC filter, which supplied a voltage from 0 V to 10 V (linearly proportional to laser power) to a spare analog-to-digital converter on the SR510 lock-in amplifier, which was read by the data collection program (see the section on computer control below).

Computer Control of Experiment

The pump-probe experiments of Chapters IV, VI, VII, and VIII were performed under completely computerized control of optical delay scanning and data collection. Digital control of the experiment reduces possible errors in time-delay position, allows ramping up and down of the rate of movement of the delay stage (necessary at higher speeds), and offers ease of use. Computerized data collection eliminates possible loss of data

while transferring from an external device, and supplies data in a convenient form for fitting to various mathematical models. A schematic diagram of the computer control and data collection system is shown in Fig. 2-6. Two computers were used in the system; a dedicated Commodore 64 (C64) provided control of the translation stage stepper motor and recorded its position, while a DEC MINC 23 operating in a TSX-Plus multiuser environment read experimental data from the lock-in amplifier, normalized it to the laser power, and stored it in a disk file.

Two user-programmable chips onboard the C64 computer are shown explicitly in Fig. 2-6; the signals used to control the stepper motor are derived from these two chips. One is a 6581 Sound Interface Device (SID), which is designed to produce audio waveforms. The other is a 6526 Complex Interface Adapter (CIA), which provides access to an 8-bit parallel input/output register and two independent, linkable 16-bit interval timers/counters. The C64 computer actually contains two CIA chips, one of which (CIA#1) is used by the computer operating system; the other, CIA#2, is available to the user and is accessed via the user port.

The source code of the program used on the C64 to control the optical delay translation stage is listed in Appendix A, along with a description of the program logic. This program was written in BASIC with machine language subroutines used in situations where greater speed is required. As shown in Fig. 2-6, three output signals are generated by the C64; two (STEP, DIR) are used to control the translation stage stepper motor, the other is sent to the MINC computer. STEP consists of a series of square pulses generated by the SID, with each pulse corresponding to one step of the stepper motor (0.1 μm for the translation stage used here). The DIR

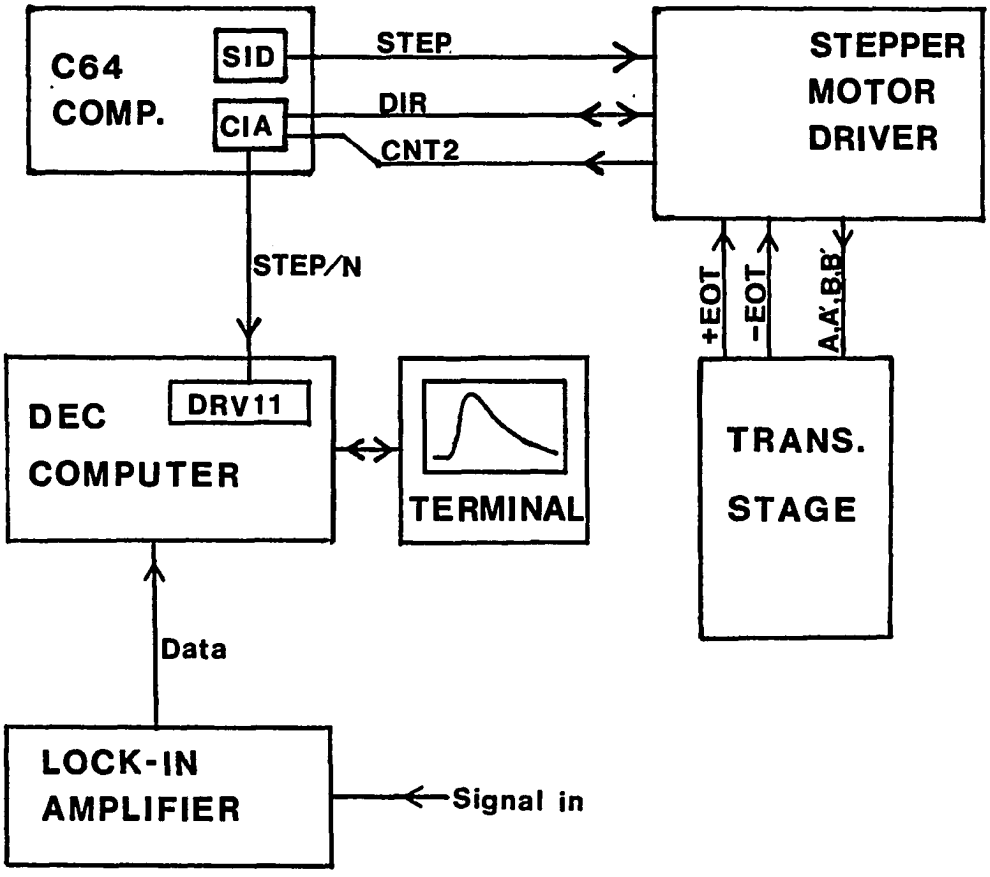

Figure 2-6. Schematic of experimental apparatus used for computer control of pump-probe measurements.

output is a TTL logic level sent from CIA#2, and is used to control the direction of travel ("positive" or "negative") of the translation stage. The third output, STEP/N, is a TTL pulse occurring at a frequency of the STEP rate divided by an integer N. This signal synchronizes translation stage movement with data acquisition by commanding the MINC computer to record one data point per STEP/N pulse.

Each of these three signals are sent to the Stepper Motor Driver box, which consists of a set of logic circuits and a high-voltage, constant-current driver for the stepper motor. (Note that although the Fig. 2-6 shows STEP/N being sent to the MINC computer, it actually passes through the Stepper Motor Driver box.) Since STEP is the only input which is not a TTL signal, it is routed through a comparator to remove any noise spikes and create a TTL-compatible logic level. The logic circuits are shown in Fig. 2-7; lines marked STEP, DIR, and CNT2 are connected to the C64, and EOT signals are from the stepper motor. The "driver" output goes to the stepper motor driver circuitry (see below). The two inputs from the stepper motor are end-of-travel (EOT) warning signals (one for each direction of travel), which are open-circuited in normal operation but grounded when the translation stage nears the respective limit. The logic circuit is designed so that the stepper motor cannot be driven past the EOT signal, but can be driven in the opposite direction while an EOT warning is active (the hysteresis in the signal is ~1 mm of translation stage travel). Since it is possible for the C64 to be sending STEP pulses while the stepper motor is not moving (i.e., EOT reached or driver box not switched on) a separate line is used to send active STEP pulses back to the C64. These pulses are routed to the counter input of CIA#2 (labelled

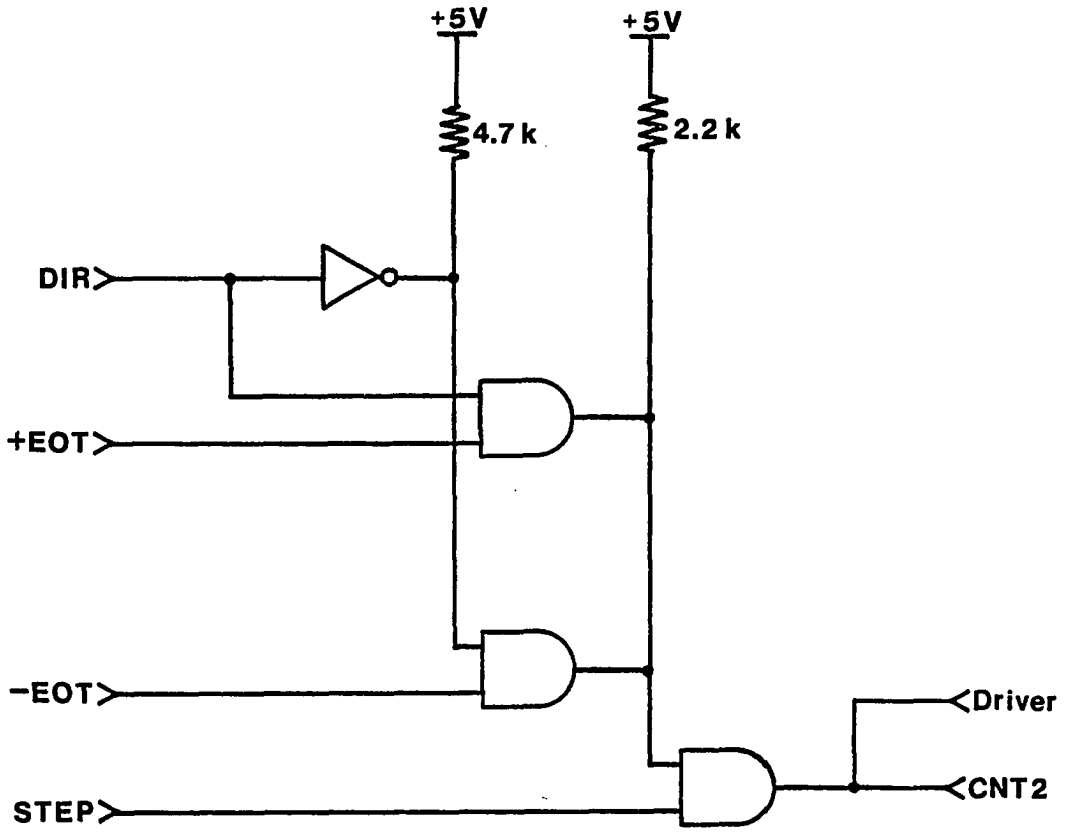

Figure 2-7. Logic circuits contained in Stepper Motor Control Box shown in Fig. 2-6; see text for explanation of input and output signals.

CNT2) which records the actual number of steps taken. Likewise, the DIR logic level is sent back to the C64 and is used to determine the direction of travel. The STEP/N signal is sent through a pulse stretcher (since the C64 output is only 1 μs in duration) and a 50-ohm line driver before being routed to the MINC computer.

In addition to being sent back to the C64 computer, the STEP output is also sent to an Ames Laboratory-built logic board which produces from it four separate signals (A, A′, B, B′) with the correct phase relationship required by the stepper motor. Each of the four phases is supplied to the stepper motor by a separate constant-current amplifier (designed by Ames Laboratory, Fig. 2-8a). Since the stepper motor itself consists of coils of large inductance, the voltage across any one of the four phases during a step cycle will appear as a large spike (up to -60 V) decaying to a non-zero level (Fig. 2-8b). The current level is set by R_F, which was set at 680 Ω, for a current of 125 mA. Use of a constant-current type amplifier allows operation at higher speeds than with a conventional amplifier because greater torque is applied in the early stages of the waveform.

As mentioned above, the C64 supplies a signal to the MINC computer at a rate of the STEP frequency divided by an integer N. During a normal experimental scan, a single data point is recorded for each STEP/N pulse received; therefore, the time calibration of the data scan is set by the integer N. This parameter is entered into the C64 by the user at the "Number of Steps/Channel" prompt; the number of femtoseconds between data points K_{ch} is related to N by $K_{ch} = 2N/3$; the factor 3 is due to the speed of light (three 0.1 μm steps per femtosecond), and the 2 arises from the fact that the the laser beam traverses the step delay distance twice. The

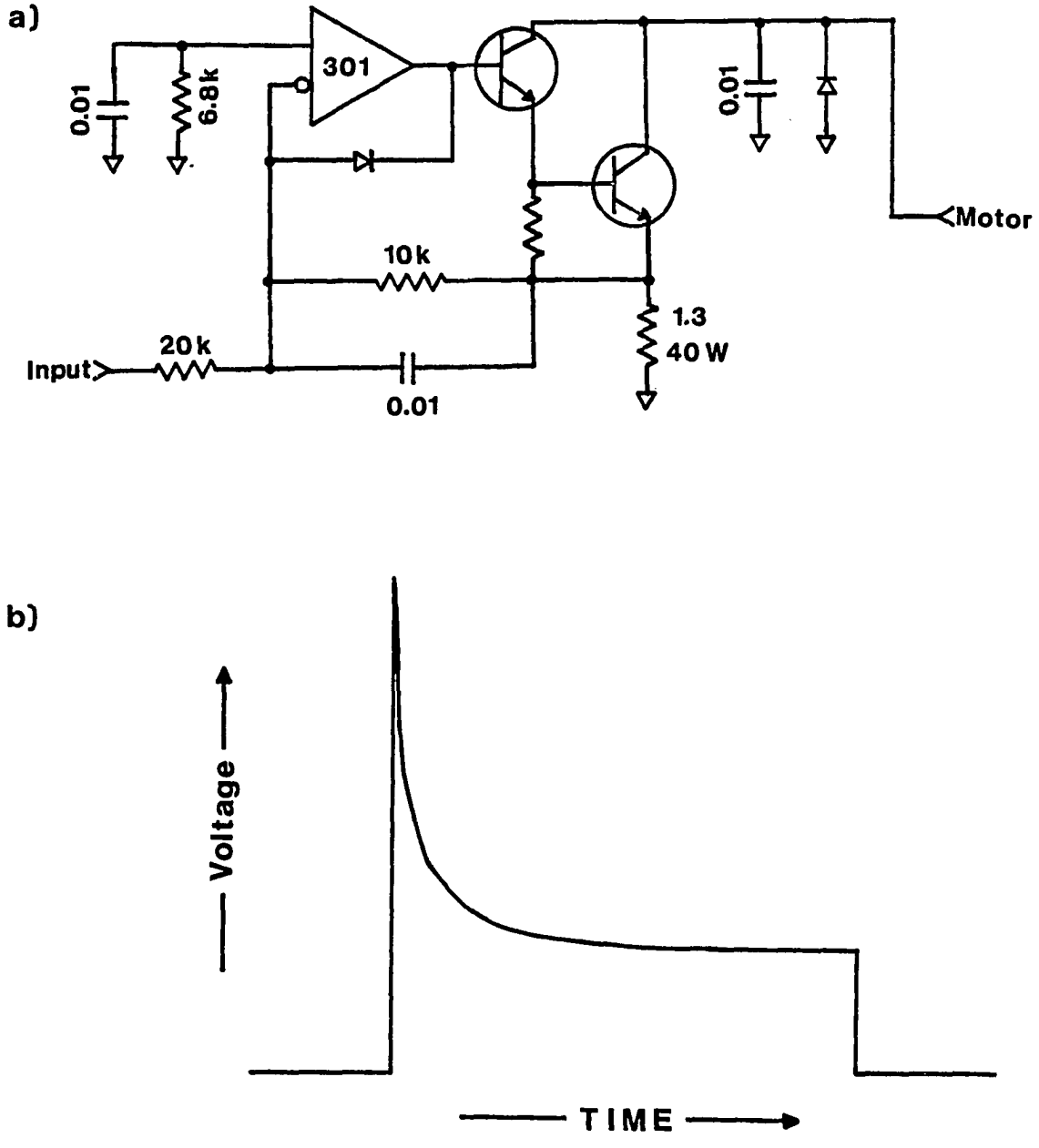

Figure 2-8. Function of stepper motor driver circuits a) Constant current amplifier used to send current pulses to stepper motor; b) voltage signal across inductive load of motor windings.

STEP/N signal is received by the data collection program LOCKIN (see Appendix B) running on the MINC computer. The logic of LOCKIN is rather simple; it enters a wait state until it receives an interrupt (STEP/N pulse), at which time it reads a data point via RS232 from the lock-in amplifier, plots it on the screen, and waits again. This wait/data cycle is repeated until 512 data points have been recorded. The program then normalizes the data to the square of the laser power (if this option has been chosen), and writes the data to a disk file. The laser power is detected as described above and is also read via the RS232 port.

Experimental Artifacts

Pump-probe experiments are prone to a several types of artifacts, some of which are avoidable and others unavoidable. This section will describe several of the most common types of artifacts, their causes, and where applicable, their elimination from the data.

The most obvious artifact in single-color pump-probe experiments is one which cannot be avoided, the coherent coupling artifact or "coherence spike". It appears as a narrow spike superimposed on the data centered about zero delay. The coherence spike arises from an interferometric interaction between pump and probe pulses, and therefore only occurs when the pump and probe are derived from the same laser. The coherent coupling artifact was originally described [10] as due to a transient grating formed by interference of pump and probe pulses when they are simultaneously present in the sample. This grating could then scatter some pump light into the probe beam path, causing a spike in the detected

intensity. According to this explanation, the coherence spike would be expected to disappear if one used collinear, copropagating pump and probe beams of orthogonal polarization and detected the total transmitted intensity. Heinz et al. [11] tested this assertion and found that the coherence spike did not disappear. They offered an alternative explanation for the origin of coherent coupling as a "cooperative bleaching" of the sample while the pump and probe pulses are present in the sample. Mathematically, they showed that the photobleaching signal $S(\tau)$ consisted of three terms

$$S(\tau) = \beta(\tau) + \beta'(\tau) + \gamma(\tau) \tag{2.2}$$

where $\beta(\tau)$ and $\beta'(\tau)$ arise from coherent interaction of pump and probe pulses, and $\gamma(\tau)$ is an incoherent term describing the rise of the desired signal (for which the decay is to be measured). The mathematical form of each term can be written explicitly for orthogonal pump and probe pulses if the sample consists of isotropically distributed molecules having a definite transition dipole moment and a fixed orientation on the timescale of interest. If the pump pulse is described as $E(t)\exp(i\omega t)$, then the probe pulse (being derived from the same laser) can be written as $E(t-\tau)\cdot\exp(-i\omega\tau)$, which is simply a delayed copy of the pump pulse. The incoherent term $\gamma(\tau)$ is then given by

$$\gamma(t) = \mathrm{Re}\left[\int_{-\infty}^{+\infty} dt\ A(\tau-t) \int_{-\infty}^{+\infty} dt'\, |E(t')|^2 |E(t'-t)|^2 \right] \tag{2.3}$$

which is the impulse response of molecular absorption A(t) convoluted with the intensity autocorrelation function $\rho_I(\tau)$. On the timescale of interest, A(t) may be approximated as a step function; in this case, the incoherent term $\gamma(\tau)$ rises as the autocorrelation of pump and probe pulses. The two coherent coupling terms can be written as

$$\beta(\tau) = \mathrm{Re}\left[\int_{-\infty}^{+\infty} dt \int_{-\infty}^{+\infty} dt' \; E^*(t-\tau)E(t)E^*(t')E(t'-\tau)A(t-t') \right] \qquad (2.4)$$

$$\beta'(\tau) = \mathrm{Re}\left[e^{-2i\omega t} \int_{-\infty}^{+\infty} dt \int_{-\infty}^{+\infty} dt' \; E^*(t-\tau)E(t)E^*(t'-\tau)E(t')A(t-t') \right] \qquad (2.5)$$

The term $\beta'(\tau)$ oscillates at twice the optical frequency ω, and therefore averages out to zero unless the probe delay is scanned extremely slowly, much more slowly than in the current experiments. The $\beta(\tau)$ term describes the coherence spike and varies as the square of the electric field autocorrelation function $|\rho_E(\tau)|^2$, not the intensity autocorrelation function $\rho_I(\tau)$. This means that the width of the coherence spike depends not on the pulse width Δt but on the spectral width $\Delta\omega$. For transform limited pulses $\rho_I(\tau)$ and $|\rho_E(\tau)|^2$ will coincide, but for nontransform limited pulses (such as those used in this work) the coherence spike will be narrower than the intensity autocorrelation.

In order to correctly fit experimental data over the entire scan range, it is necessary to remove the effects of the coherent coupling artifact term $\beta(\tau)$. Since Eqs. 2.3 and 2.4 predict that the terms $\beta(\tau)$ and $\gamma(\tau)$ are equal at zero delay, it is possible to remove the coherence spike by subtracting the experimentally measured electric field

autocorrelation normalized to half the signal at zero delay. For transform limited pulses, one may use the intensity autocorrelation function rather than the electric field autocorrelation. However, in practice this procedure is only applicable for perpendicular pump and probe polarizations; when using other polarizations, a thermally enhanced coherence spike occurs which is variable in size and often much larger than the incoherent term. When this happens, it is impossible to accurately subtract the $\beta(\tau)$ term.

Another method is to remove the coherent coupling term $\beta(\tau)$ through data antisymmetrization [12]. This relatively simple procedure takes advantage of the fact that $\beta(\tau)$ is predicted to be symmetric about zero delay. The antisymmetrized signal $S_a(\tau)$ is given by

$$S_a(\tau) = [S(\tau) - S(-\tau)]/2 = [\gamma(\tau) - \gamma(-\tau)]/2 \qquad (2.6)$$

where the $\beta'(\tau)$ term is assumed to average out to zero and the $\beta(\tau)$ term disappears because $\beta(\tau) = \beta(-\tau)$. After antisymmetrizing the data, it may be fit as usual using a convolute-and-compare program by antisymmetrizing the fitted curve between the convolute and compare steps. This procedure was used in Chapter III to remove not only the coherent coupling artifact, but also a residual artifact due to two-photon absorption in ZnO.

Although the antisymmetrization procedure removes any artifact symmetric about zero delay, there is one caveat to its use. In the derivation of the form of the $\beta(\tau)$ term in Eq. 2.4, it was inherently assumed that the electric field autocorrelation width $|\rho_E(\tau)|^2$ was much longer than the material dephasing time T_2. It has been shown [13] that

for transform limited pulses if $5T_2 > \rho_I(\tau)$, the coherent coupling term $\beta(\tau)$ may not be symmetric. If this is the case, then data antisymmetrization would not remove the artifact. The exact effect of $T_2 \approx \rho_I(\tau)$ is dependent on the pulse shape and other factors, and is rather difficult to determine for a particular experimental situation.

Aside from the coherence spike, the artifacts discussed here manifest themselves as gradual deviations from the "true" decay over the length of the data scan. Such deviations can arise from purely mechanical sources; as mentioned above, the signal strength in pump-probe experiments depends critically on the overlap of pump and probe beams in the sample. Obviously, any type of movement of the two beams relative to one another will cause artificial changes in the amplitude of the signal. As discussed above, the beam directions are stabilized by the use of retroreflectors, but proper alignment is still important. In particular, it is desirable to have the incoming beam to the variable delay be parallel to the direction of travel of the translation stage. If these are not parallel, the position (although not the direction) of the outgoing beam will depend on the delay position as shown in Fig. 2-9. Theoretically, such a parallel displacement of the emergent beam would not cause a change in the position of the focussed beam spot, but due to aperturing on other optical components and lens aberrations, artifacts could in practice occur.

In addition to assuring that the beam spot does not move during the experiment, the size of the spot must be independent of the delay position as well. The size of the spot can change if the incoming beam to the translation stage is convergent or divergent; the spot size at the focus

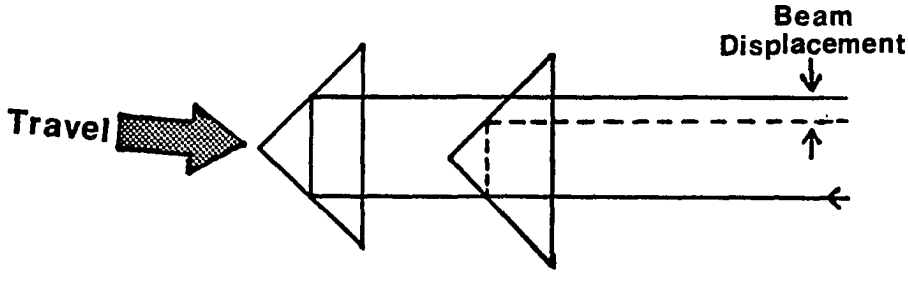

Figure 2-9. Effect of nonparallelicity between translation stage travel and incoming beam to retroreflector; note that the position of the outgoing beam but not the direction is affected.

w_3 is related to the beam size at the focussing lens w_1 by [14]

$$w_3 = \frac{f\lambda}{w_1 n} \tag{2.7}$$

Here, f is the focal length of the lens, n is its refractive index, and λ is the laser wavelength. The spot size at the focus is therefore inversely proportional to the size of the beam at the focussing lens. Given a typical laser beam divergence of 1 mrad (full angle), over 10 cm of optical delay the beam size would grow by 0.1 mm, a change of ~10% for the beam sizes used here. In view of Eq. 3, such unchecked beam divergence would cause a noticeable deviation in the signal. Therefore, it is necessary to adjust the distance between lenses L1 and L3 in Fig. 2-3 for the best possible beam coherence. This may be done by directing the output of L3 over a long distance and moving L3 until the beam size is the same in the near and far field.

Some types of artifacts may appear in pump-probe experiments on photosynthetic antennae systems which do not occur in simpler systems (such as randomly distributed dye molecules). One of the most common is singlet-singlet annihilation, which is seen as an intensity-dependent absorption decay (i.e., shorter lifetimes at higher laser intensities). The mechanism of singlet-singlet annihilation is shown in Fig. 2-10. Panel a) shows a domain of four (B)Chl molecules, two of which have become photoexcited. Through energy transfer, the excitations may migrate to two chromophores in close proximity to one another, as in panel b). Then it is possible for molecule 2 to transfer its excitation energy to molecule 3, which rises to the S_2 state. In following with Kasha's rule, molecule

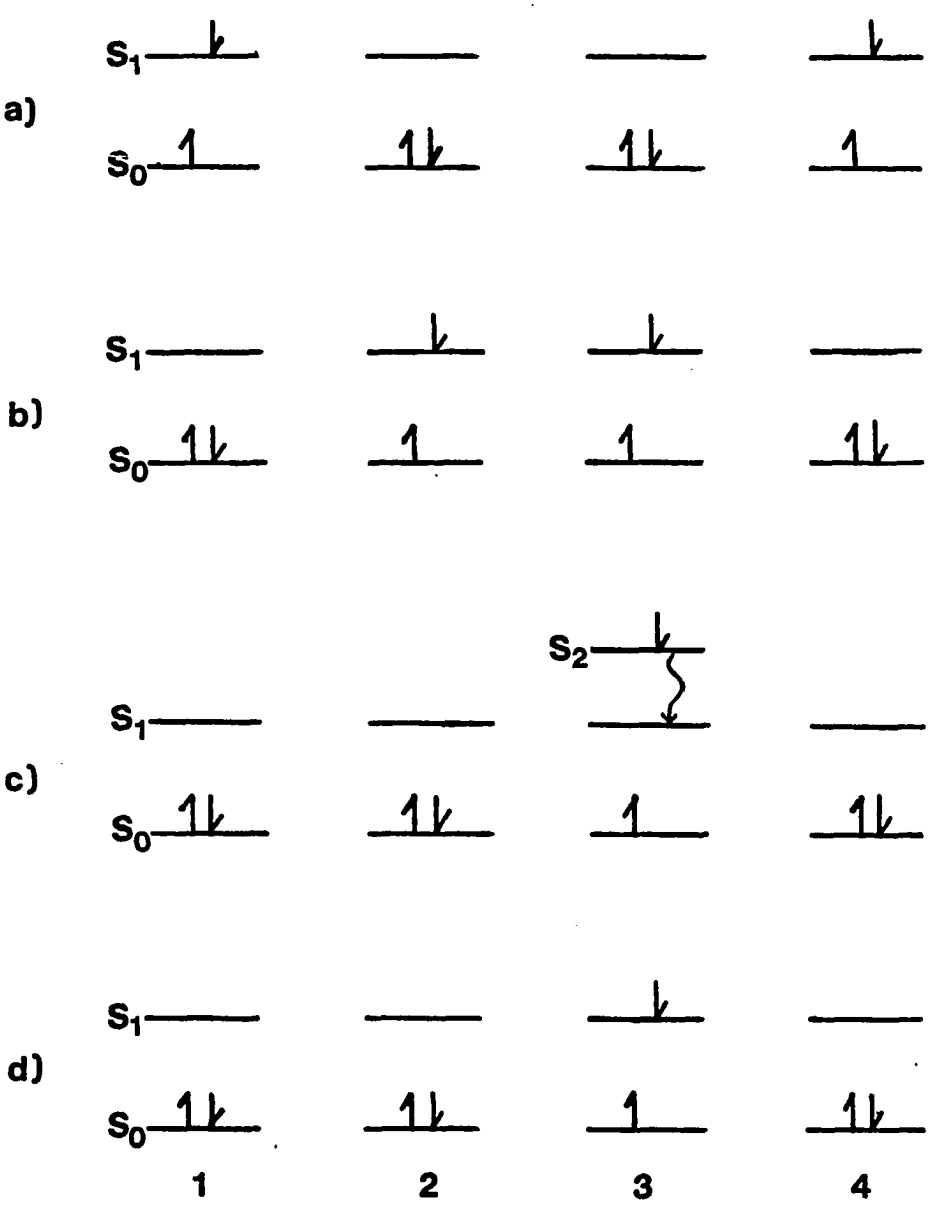

Figure 2-10. Mechanism of singlet-singlet annihilation within an energy transfer domain. a) Two excitations are initially present in the domain; b) the excitations migrate close to one another; c) energy transfer to an already excited molecule followed by internal conversion reduces the number of excitations by one, as in d).

3 then undergoes very fast internal conversion to S_1 (panel c)). The overall process from Fig. 2-10a to Fig. 2-10d is the loss of one excitation due to the presence of another, and may be summarized as

$$(B)Chl^* + (B)Chl^* \xrightarrow{\gamma_2} (B)Chl + (B)Chl^* \qquad (2.8)$$

The rate constant γ_2 is the overall two-excitation decay rate, which includes contributions from EET across the domain and from the probability that annihilation will occur when two excitations meet. (Note that other processes are possible as well, such as singlet-triplet annihilation, or singlet-singlet annihilation resulting in the loss of both excitations or the formation of triplet states; however, the process in Eq. 2.8 is usually dominant, especially for very short pulses [15].) For the purposes of pump-probe experiments, it is necessary to keep the laser pulse energy density low enough that annihilation does not compete with the single-excitation decay. The maximum allowable laser pulse energy depends on the rate constant γ_2, which in turn depends in a complicated way on several molecular parameters. One of the most important is domain size; in general, larger domains will show effects of annihilation at lower pulse energies. In addition to molecular parameters, the allowable pulse energy depends on experimental parameters such as the size of the beam in the sample and the sample optical density at the laser wavelength. In practice, one usually checks for these effects by repeating the experiment with successively lower laser powers until the observed decay no longer changes. It has been shown [16] that annihilation processes begin in BChl a-protein at about 10^{14} photons/cm^2; excitation densities in

the studies of Chapters VI, VII, and VIII were $<10^{13}$ photons absorbed/cm^2.

Another concern in pump-probe experiments on photosynthetic systems is the formation of long-lived triplet states in the sample. When using high repetition rate lasers, triplet states can accumulate from pulse to pulse to eventually become the dominant species. The relevant decay processes and their associated rates are shown in Fig. 2-11: the intersystem crossing rate k_{ISC}, the phosporescence decay rate k_{ph}, and the $S_0 \leftarrow S_1$ decay rate k_f. If these are known, then a simple calculation can determine whether triplets accumulate in the sample. The calculation is based on the rate of formation of the triplets; if the rate of formation is greater than their rate of decay, then accumulation would occur. The rate of formation depends on the number of photons absorbed per chromophore per pulse I_{abs}, the intersystem crossing quantum yield ($q_{ISC} = k_{ISC}/[k_f + k_{ISC}]$ as depicted in Fig. 2-11), and the laser repetition rate f_R. If these satisfy

$$I_{abs}\, q_{ISC}\, f_R > k_{ph} \tag{2.9}$$

then triplet accumulation will occur. Fig. 2-11a shows the usual case where the inequality of Eq. 2.9 is not satisfied, and the population of triplet states is negligible. Here, the observed decay k_{obs} is due to $S_0 \leftarrow S_1$ ground state recovery, as has been assumed above. In Fig. 2-11b, however, Eq. 2.9 is satisfied and triplet states are the dominant species. In this case, the observed decay may occur in the triplet manifold, rather than in the singlet manifold as desired. The ratio of singlet to triplet signal in k_{obs} also depends on the relative absorption coefficients of S_0

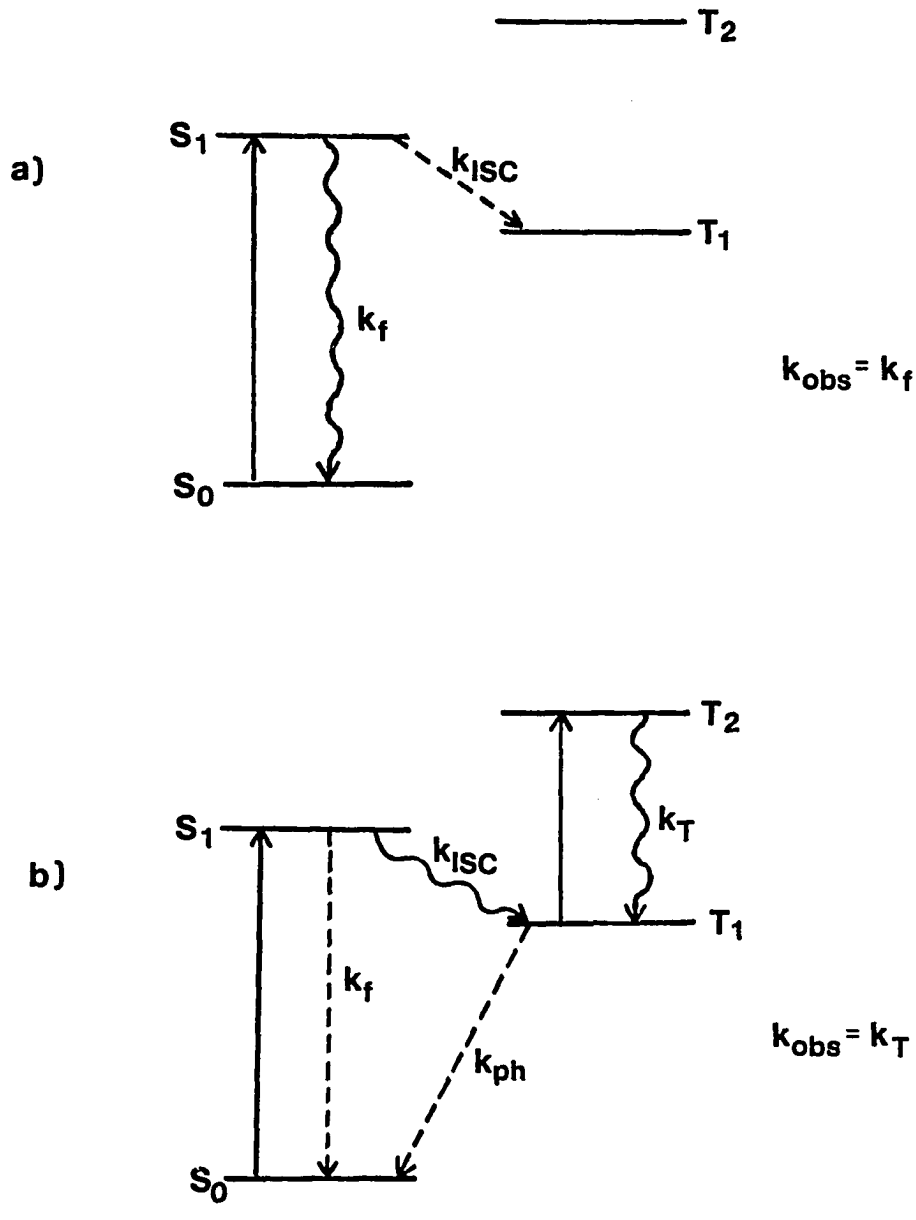

Figure 2-11. Energy levels and decay rates pertinent to formation of triplet states. a) Decay rates are such that triplet states do not accumulate in the sample, and transient absorption occurs in the singlet manifold; b) decay rates allow triplet states to accumulate, and the measured decay is $T_1 \leftarrow T_2$.

and T_1 at the laser wavelength; however, the triplet absorption coefficients for antenna systems are largely unknown. It is unlikely that absorption from T_1 is stronger than the intense $S_0 \rightarrow S_1$ absorption, but at some wavelengths they could become nearly equal. It is difficult to determine what the effect on the decay would be for $k_{obs} = k_T$; the best way to check for such effects would be to vary the laser repetition rate over a large range and look for changes in the observed decay.

When dealing with very long-lived triplet states, it is important to take into account the details of the experimental apparatus. For example, in our experiments the sample was rotated at 12 Hz. If the radius of the circle exposed to the laser beams is ~3 mm, then the ratio of exposed area to beam spot size is ~1200. At 12 Hz rotation, the rate at which new sample is exposed would then be ~1.5×10^4 s^{-1}. This rate could easily be greater than k_{ph} (phosphorescence lifetimes of >1 ms are common in vivo [17]), and the relevant "rate of decay" of triplets in Eq. 2.9 would then be 1.5×10^4 s^{-1}, rather than the actual k_{ph}. By using large spinning radii and a cavity-dumped dye laser, it may be possible to approach the regime where each laser pulse impinges upon an area of fresh sample.

References

1. Hedstrom, J. F. Ph. D. Dissertation, Department of Chemistry, Iowa State University, 1987.

2. Couillard, B.; Fossati-Bellani, V. Lasers & Applications 1985, 4, 91.

3. Valdmanis, J. A.; Fork, R. L.; Gordon, J. P. Opt. Lett. 1985, 10, 31.

4. French, P. M. W.; Taylor, J. R. In "Ultrafast Phenomena V", Fleming, G. R.; Siegman, A. E., Eds.; Springer-Verlag: Berlin, 1986; p. 11.

5. New, G. H. C. Opt. Commun. 1972, 6, 188.

6. New, G. H. C. IEEE J. Quant. Electron. 1974, QE-10, 115.

7. Baer, T. M.; Smith, D. D. In "Ultrafast Phenomena IV", Austin, D. H., Eisenthal, K. B. Eds.; Springer-Verlag: Berlin, 1984; p.96.

8. Anfinrud, P.; Struve, W. S. Rev. Sci. Instrum. 1986, 57, 380.

9. Yasa, Z. A.; Amer, N. M. Opt. Commun. 1981, 36, 406.

10. Ippen, E. P.; Shank, C. V. In "Ultrashort Light Pulses", Shapiro, S. L., Ed.; Springer-Verlag: Berlin, 1977; p. 110.

11. Heinz, T. F.; Palfrey, S. L.; Eisenthal, K. B. Opt. Lett. 1984, 9, 359.

12. Engh, R. A.; Petrich, J. W.; Fleming, G. R. J. Phys. Chem. 1985, 89, 618.

13. Balk, M. W.; Fleming, G. R. J. Chem. Phys. 1985, 83, 4800.

14. Siegman, A. E. "An Introduction to Lasers and Masers"; McGraw-Hill: New York, 1971; p. 316

15. van Grondelle, R. Biochim. Biophys. Acta 1985, 811, 147.

16. van Grondelle, R.; Hunter, C. N.; Bakker, J. G. C.; Kramer, H. J. M. Biochim. Biophys. Acta 1983, 723, 30.

17. Hoff, A. J. In "Light Emission by Plants and Bacteria"; Govindjee; Amesz, J.; Fork, D. C., Eds.; Academic Press: New York, 1986; p. 243.

PICOSECOND PUMP-PROBE EXPERIMENTS ON SURFACE-ADSORBED DYES: GROUND STATE-RECOVERY OF RHODAMINE 640 ON ZNO AND FUSED SILICA

Timothy P. Causgrove, Philip A. Anfinrud,

and Walter S. Struve

Department of Chemistry and Ames Laboratory - USDOE

Iowa State University, Ames, Iowa 50011

CHAPTER III. PICOSECOND PUMP-PROBE EXPERIMENTS ON SURFACE-ADSORBED DYES: GROUND-STATE RECOVERY OF RHODAMINE 640 ON ZNO AND FUSED SILICA

Introduction

Solar photochemistry workers have been concerned with the fate of electronic excitation in visibly absorbing dyes adsorbed on wide-bandgap semiconductors. When used in liquid-junction solar cells, single-crystal semiconductors coated with such dyes exhibit low quantum efficiencies ($\lesssim 10^{-2}$) for conversion of dye-absorbed photons into conduction-band electrons [1]. The mechanistic question which arises is whether these low quantum yields are a consequence of efficient back-transfer of electrons to the dye following electron injection into the semiconductor or whether they are due to rapid nonradiative decay of dye excitation into substrate surface modes [2], interband excitation in the semiconductor [3], or surface states.

Time-correlated photon counting was recently used [4] to demonstrate that the fluorescence lifetime of cresyl violet (CV) separated from a TiO_2 single crystal surface by a variable number of organized arachidic acid monolayers depends on the dye-surface separation d for 80Å < d < 509Å in a manner which is consistent with a classical electromagnetic theory for nonradiative excitation decay in a molecule near a dielectric surface [5]. At such large separations, the theory predicts that the excited state lifetime depends on the substrate's bulk properties largely through the real part n of its refractive index $\tilde{n}$ at the dye fluorescence wavelength.

Since both n and d could be characterized for CV above TiO_2 at separations > 80Å, meaningful comparisons between theory and experimental lifetimes were possible at these separations. For directly adsorbed CV ($d \lesssim 5$Å), a controlling parameter in the theoretical lifetime is the imaginary (absorptive) part κ of $\tilde{n}$, a quantity whose order of magnitude is uncertain [6] at visible wavelengths for many wide-bandgap semiconductors like TiO_2. Since κ and the effective adsorption distance d are unknown for directly adsorbed dye, the ultrafast fluorescence dynamics could not be used to infer the nature of competition between electron injection and nonradiative decay at such small distances.

In this work, ground-state recovery is monitored in rhodamine 640 adsorbed directly onto ZnO using picosecond pump-probe spectroscopy. For radiationless mechanisms involving direct decay of S_1 state dye into ground state dye, the ground state recovery dynamics will be commensurate with dye fluorescence profiles [4] observed on semiconductors. Populations of mobile charge carriers generated in TiO_2 by electron injection from a photoexcited adsorbed dye decay over millisecond timescales [7], and hence appreciably slower ground-state recovery dynamics can be expected if electron injection is an important excited state decay route. Ground-state recovery on ZnO is contrasted at several coverages with that on $\lambda/4$ fused silica. Photobleaching recovery on ZnO proves to be ultrafast and essentially independent of dye coverage over the studied range. The recovery dynamics on silica are considerably slower; they accelerate with increased dye coverage, because excited state decay on silica is dominated by excitation trapping by dye aggregates whose surface number density increases with coverage. Our results support

the occurrence of efficient nonradiative dye → surface excitation decay on semiconductors.

Experimental

Optically flat (λ/4) silica substrates were precleaned with chromosulfuric acid, and rendered hydrophobic for homogeneous dye coating by treatment with 20% $Si(CH_3)_3Cl$ solution in $CHCl_3$ followed by rinsing in methanol and distilled water. Rhodamine 640 (used as received from Exciton) was adsorbed onto silica from aqueous solution by immersing substrates for 5 - 10 min. Single-crystal ZnO substrates cut and polished normal to the c-axis (Airtron, Morris Plains, NJ) were inherently hydrophobic and were coated similarly. Absorption spectra of aqueous rhodamine 640 solutions obtained on a Perkin-Elmer 320 spectrophotometer at concentrations higher than 10^{-5}M showed, in addition to the monomer $S_1 \leftarrow S_0$ band near 570 nm, a secondary peak at ~540 nm due to dimerization. The dimer peak was not resolved at lower concentrations. The monomer peak position varied with solution concentration: ~572 nm at 10^{-4} and 10^{-5}M and ~565 nm at 10^{-6}M. Since rhodamine 640 (like rhodamine B) exhibits a free carboxyl group, this position shift arises from an acid-base equilibrium [8] between protonated and unprotonated dye. This equilibrium is mirrored in absorption spectra of rhodamine 640 coatings on silica, which closely resemble the aqueous solution spectra apart from spectral shifts (λ_{max} ~ 581 and ~ 572 nm for silica coated with 10^{-5} and 10^{-6}M solutions). On ZnO, the monomer peak position (~ 576 nm) on surfaces coated with solutions over the same concentration range was nearly

independent of coverage. Acidic and basic rhodamine B exhibit contrasting fluorescence lifetimes in ethanol (2.48 vs. 3.01 ns [9]). However, ground-state recovery of rhodamine 640 on ZnO proves to be more than an order of magnitude faster than its fluorescence decay in water, and the recovery dynamics are found to be independent of coverage (following section). Hence, the nonradiative decay on ZnO is immaterially influenced by the carboxyl acid-base equilibrium.

Optical densities of coated ZnO and silica surfaces at the dye monomer peak wavelength vary nonlinearly with coating solution concentration between 10^{-6} and 10^{-5}M (Table I). Unlike CV (which dimerizes nearly quantitatively in water and on silica [10]), rhodamine 640 exists predominantly as monomers on both ZnO and silica, and excitation trapping by aggregates is far slower for rhodamine 640 than for CV adsorbed at the same coverage. Adsorption measurements such as those reported in Table I require caution, because dye adsorption onto coating vessel walls and previously coated surfaces can deplete the coating solution concentration below its nominal value, particularly at the lower concentrations. For this reason, the nominal difference between the minimum and maximum coating solution concentrations used in the picosecond transient series on both ZnO and silica is a lower limit to the true difference; the nominal and true solution concentrations can differ by factors up to ~2 at 10^{-6}M and by less at the higher concentrations. The lowest rhodamine 640 optical densities used in pump-probe experiments corresponded to $\lesssim$0.1 monolayer adsorption.

The synchronously pumped rhodamine 6G laser system has been described previously [4,10]; it produced 590 nm pulses with ~12 ps fwhm at 96 MHz

Table I. Rhodamine 640 adsorption onto ZnO and fused silica

Surface	Coating Solution Concentration, M	Monomer Optical Density at $S_1 \leftarrow S_o$ Peak
Fused Silica	2.0×10^{-7}	0.0017
	4.0×10^{-6}	0.0049
	4.0×10^{-5}	0.0074
ZnO	2.0×10^{-7}	0.0012
	4.0×10^{-6}	0.0036
	4.0×10^{-5}	0.0105

repetition rate and ~90 mW average power. The vertical laser polarization was continuously rotatable using a Fresnel double rhomb; the resulting beam was split into orthogonally polarized pump and probe beams of comparable intensity using a calcite Glan-Thompson prism. The two beams were focussed into Isomet Model 1206C acoustooptic modulators operated with ~80% modulation depth at 6.5 and 0.5 MHz respectively.

The pump-probe beam geometry was similar to that of Ippen et al. [11]. The probe beam was subjected to a variable delay using a right-angle BK-7 prism (±30 arc-s) mounted on a Micro Controle UT10050PP computer-controlled translation stage (0.1 μm/step, 5 cm range). Both beams were condensed to ~10 μm spot diameter on the dye-coated substrate using a common 7.3 cm f.l. precision-optimized achromatic lens. The average incident laser power at the surface was ~10 mW in each beam. The probe beam was detected with an EG&G FOD-100 photodiode, and phase-locked single-sideband detection was achieved at 7.0 MHz in a Drake R-7A radio receiver which was modified and augmented with auxiliary frequency-mixing circuitry to provide flexible modulation frequencies in both beams [12]. At the 7.0 MHz multiple-modulation sum frequency, signal detection was essentially shot noise-limited.

Scattered pump light and dye sample photooxidation introduce more severe complications in surface experiments than in solution work. When parallel pump and probe beam polarizations were used, interference between surface-scattered pump light and the probe beam at the photodiode surface created a large fluctuating noise signal at 7.0 MHz when the time delay between pump and probe pulses was small enough for their profiles to overlap. Such a spurious signal can arise from spatial inhomogeneity in

photodiode response, which enables the fluctuating interference pattern between pump and probe pulses to contribute noise at the sum frequency. This noise was largely eliminated with orthogonally polarized beams. Effects of adsorbed dye photooxidation were minimized by rotating 10 mm x 10 mm ZnO or silica substrates at 12 Hz about the surface normal while translationally cycling them at 1 Hz over a 2 mm range with the laser beam intersection near the sample edge, generating a raster over a 0.4 cm^2 annular region of the surface.

Uncoated ZnO and TiO_2 substrates exhibited a pulse-limited negative-going absorptive transient, which was symmetric about t = 0 and resembled zero-background autocorrelation traces obtained using a Type I KDP crystal rotated 45° about its surface normal from the optimum orientation for SHG for either pump or probe polarization. This transient (which is likely due to two-photon absorption in ZnO) was small on an absolute scale, but it was considerably more intense than the photobleaching transient of dye adsorbed at submonolayer coverage (Fig. 3-1). The semiconductor transient could be removed by data antisymmetrization [13], but it contributed excessive noise to the antisymmetrized optical density transient near zero delay. Improved S/N ratios were obtained by coating half of the rotating ZnO substrate with dye and by demodulating the resulting 12 Hz signal output from the Drake R7A receiver using a Stanford Research Systems SR510 lock-in amplifier (LIA) for cancellation of the ZnO transient. (This procedure was unnecessary on silica, which exhibited no such transient.) The LIA output was filtered with ~1 s time constant and routed through a voltage-controlled oscillator to a Canberra Series 30 multichannel analyzer (MCA) operating in the multichannel scaling mode with 1 s dwell

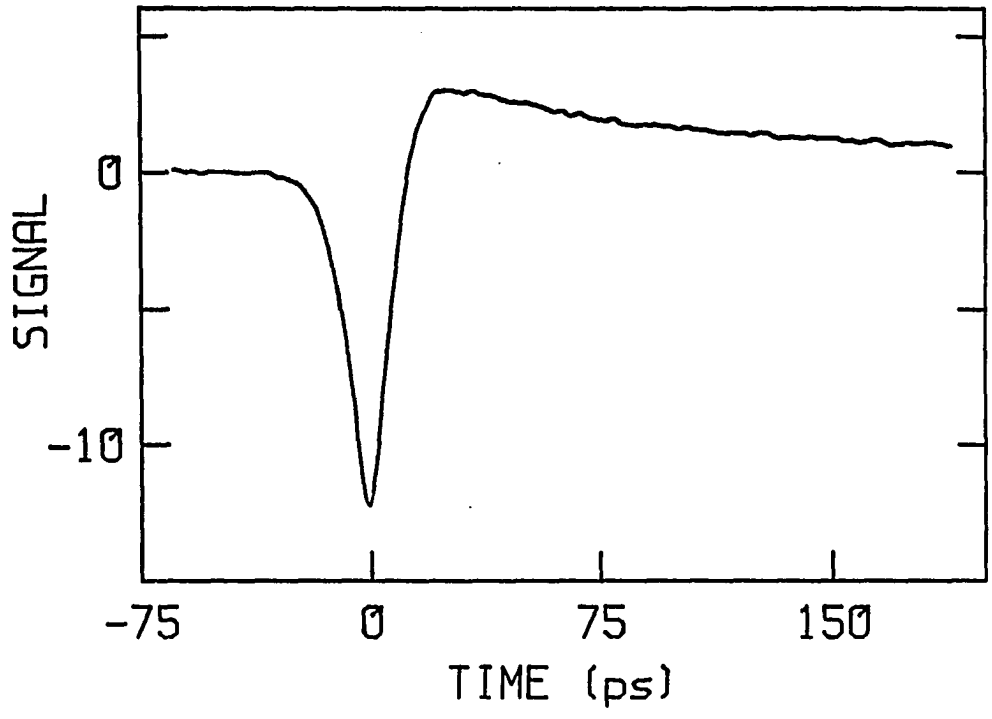

Figure 3-1. Transient response signal for rhodamine 640 on TiO_2 obtained with rastered surface uniformly covered by dye. Negative-going transient is TiO_2 response; positive-going transient for t>0 is dye photobleaching.

time. Since some dye photooxidation occurred despite sample rastering, this dwell time was matched to the 1 Hz raster frequency for signal averaging over the annular region (larger transients were exhibited at the outer edge of the ring, where more rapid sweeping and hence slower photooxidation occurred). The probe pulse delay was translated at 0.5 ps/s.

Raw time-resolved optical density profiles were transferred to a DEC MINC-23 minicomputer system equipped with Winchester disk drive operating in a TSX-Plus multiuser environment. Photooxidation decay caused substantial distortion in the profiles; its kinetics were characterized at all coverages on rastered ZnO and silica substrates by monitoring the real-time dye optical density for fixed 30 ps delay time between pump and probe pulses. A typical calibration profile so obtained for rhodamine 640 adsorbed with ~0.009 initial optical density at 581 nm on silica is shown in Fig. 3-2a, where photooxidation caused the optical density to decline ~50% over the 480s sweep time. Such calibration profiles were fitted with biexponential decay laws on silica and with triexponential decay laws on ZnO using a Marquardt nonlinear least-squares program. Raw time-resolved profiles (obtained with probe delay scanned from -66 to +190 ps using identically prepared samples) were then normalized to the fitted calibration profiles, with the result shown in Fig. 3-2b for the sample whose calibration profile is given in Fig. 3-2a. The validity of this normalization technique was confirmed by obtaining similar rhodamine 640 ground-state recovery dynamics on ZnO and silica for both directions of probe pulse scanning.

Normalized transient profiles were antisymmetrized using the method of

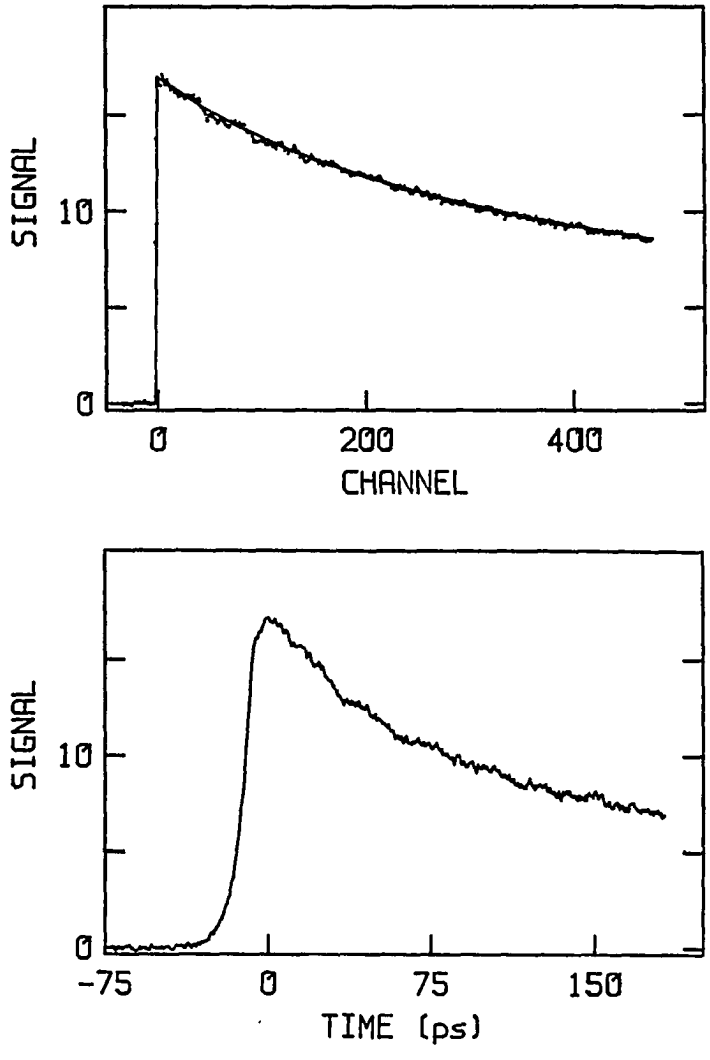

Figure 3-2. Photooxidation and transient decay curves for rhodamine 640 on a fused silica substrate. a) Photooxidation decay curve for a sample exposed to pump and probe beams with 30 ps delay, turned on at t=0. Channel calibration is 1.0 s per channel; silica surface is coated with 10^{-5} M aqueous dye solution. Continuous curve is fitted biexponential, 0.74exp(-t/1180s) + 0.26exp(-t/148s). b) Transient decay of identically prepared sample, normalized to the fitted decay in a).

Engh et al. [13] and deconvoluted from the laser autocorrelation function with a nonlinear convolute-and-compare analysis [10] using a biexponential decay law as model function for ground-state recovery.

Results

Antisymmetrized response functions are shown in Fig. 3-3 for rhodamine 640 coated onto silica using aqueous solutions with 10^{-6} and 10^{-5}M nominal concentrations. The continuous curves are discrete convolutions C_n in channel n of the laser pulse autocorrelation function x(t) with optimized antisymmetrized biexponential decay functions,

$$C_n = \sum_{i=-\infty}^{n} x(i)A(n-i) \tag{3.1}$$

with

$$\begin{aligned} A(t) &= A_1\exp(-t/\tau_1) + A_2\exp(-t/\tau_2), \quad t > 0 \\ &= -A_1\exp(t/\tau_1) - A_2\exp(t/\tau_2), \quad t < 0 \end{aligned} \tag{3.2}$$

For $t \geq 15$ ps (i.e., positive times beyond the range of the autocorrelation function), the antisymmetrized response function coincides with the dye photobleaching component of the total response function. The ground-state recovery is clearly more rapid on the silica surface with higher dye coverage, in consequence of excitation trapping by aggregates whose surface number density increases with total dye coverage. This

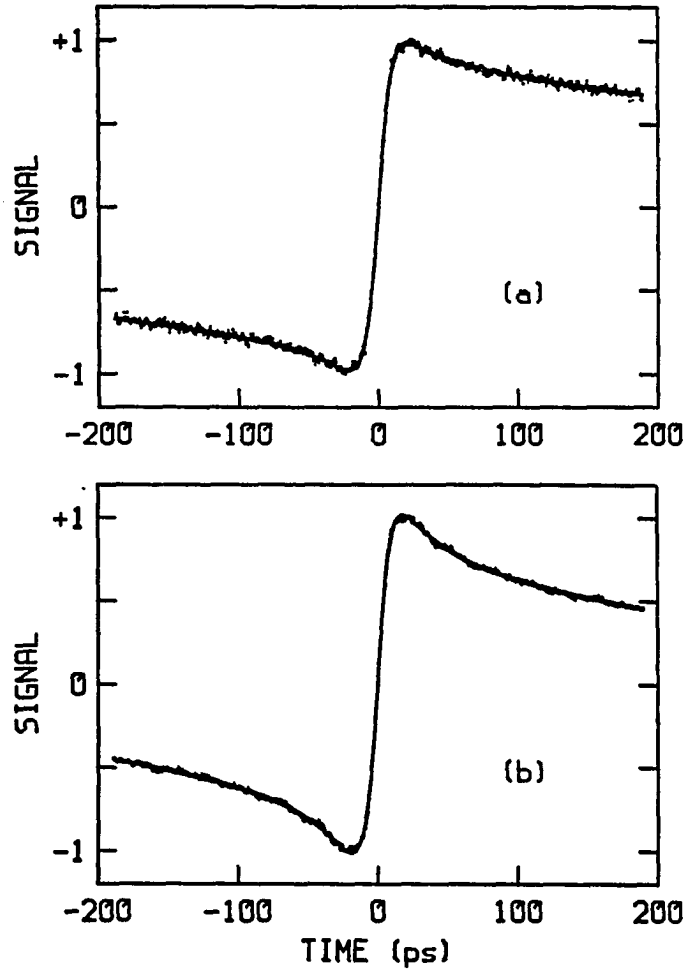

Figure 3-3. Antisymmetrized response signals for silica coated using a) 10^{-6} M and b) 10^{-5} M rhodamine 640 solutions. Continuous curves are convolutions of laser autocorrelation function with optimized biexponential decay law in Eqs. 3.1 and 3.2.

behavior qualitatively parallels the coverage dependence of cresyl violet fluorescence decay on silica [10]. Since rhodamine 640 monomers are the dominant species on the present surfaces, excitation transport typically passes from monomer to monomer several times prior to trapping at an aggregate. Ground-state recovery therefore generally occurs in a monomer other than the photoexcited one. Polarization effects then render the response function decays in Fig. 3-3 slower than the true ground-state recovery, since excitation transport to monomers with transition moments randomly oriented in the azimuthal angle about the surface normal [14] increases the mean projection of absorption transition moments along the probe pulse polarization when the pump and probe polarizations are orthogonal. These effects can be analyzed to extract the trapping dynamics on silica. We omit such an analysis here because the silica data in Fig. 3-3 are included primarily for contrast with the ground-state recovery dynamics on ZnO.

Antisymmetrized response functions for rhodamine 640 coated onto ZnO using 10^{-6}, $3x10^{-6}$, and 10^{-5}M solutions are shown in Fig. 3-4. Similar dye coverages were obtained on ZnO and silica with coating solution concentration over this range (Table I), and the coverages on the first and third ZnO surfaces in Fig. 3-4 were comparable to those on the first and second silica surfaces in Fig. 3-3, respectively. The ground-state recovery on ZnO is markedly faster at all coverages than on silica, with antisymmetrized response functions (normalized to 1.0 at the peak observed signal in Figs. 3-3 and 3-4) decaying to 0.1 at 200 ps. The decay dynamics on ZnO are very similar at all three coverages; the normalized response functions in Fig. 3-4 differ primarily in their S/N ratios, which

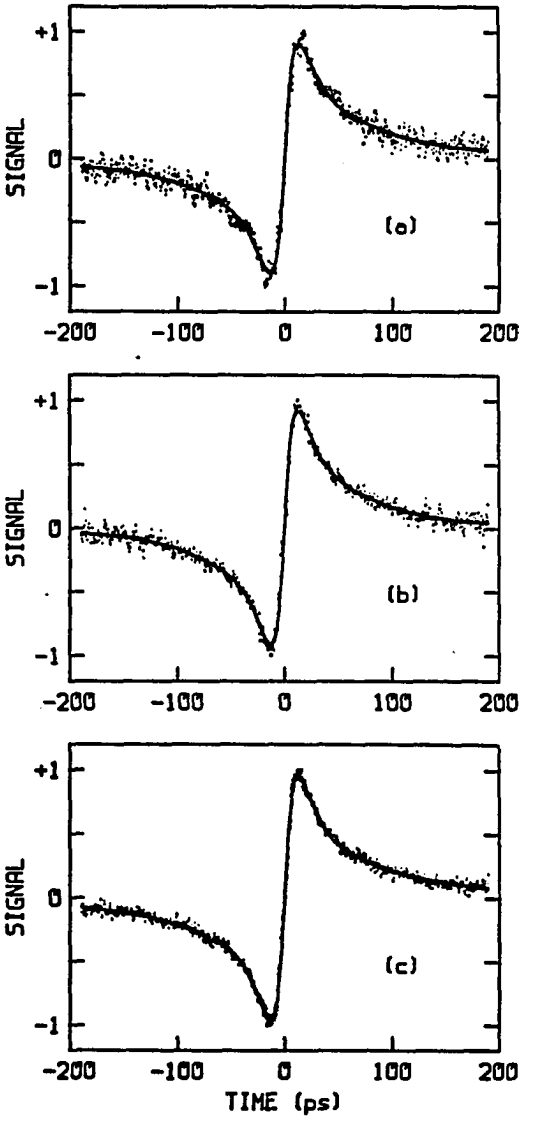

Figure 3-4. Antisymmetrized response signals for ZnO coated with a) 10^{-6} M, b) $3x10^{-6}$ M, and c) 10^{-5} M rhodamine 640 solutions. Continuous curves are convolutions of laser autocorrelation function with optimized biexponential law.

increase with coverage. Optimized biexponential parameters are listed in Table II for fits to the antisymmetrized profiles using Eqs. 3.1 and 3.2 for all studied coverages on silica and ZnO. On silica, the decay is dominated by a coverage-dependent long-component lifetime in the hundreds of picoseconds; on ZnO, an essentially laser pulse-limited short-component lifetime (denoted τ_1 in Table II) dominates. Since ground-state recovery is independent of coverage on ZnO, it occurs primarily at the laser-excited site, and polarization effects are unimportant in evaluating the ground-state recovery dynamics from the data in Fig. 3-4 and Table II. The biexponential decay law in Eq. 3.2 does not consider the possibility of irreversible photobleaching (e.g., photooxidation and/or electron injection) occurring in parallel with ground-state recovery. The quantum yield ϕ for irreversible decay is given in terms of the dye response function A(t) by $\phi = A(\infty)/A(0)$. An order-of magnitude upper limit for ϕ can be obtained by approximating $A(\infty)$ with the response signal averaged over the last 20 channels in Fig. 3-4, and by extrapolating the optimized biexponential fit to A(t) back to t = 0 to obtain A(0). This procedure yields $\phi \leq 0.05$, 0.02, and 0.05 for the response signals in Fig. 3-4, parts a, b, and c. While these estimates are sensitive to errors in fitting the antisymmetrized short-time response function, ϕ is clearly small, and rapid ground-state repopulation occurs efficiently on ZnO. However, ϕ is not negligible, as evidenced by the effects of photooxidation on the real-time transient decay observed on both ZnO and silica.

Table II. Biexponential fitting parameters for antisymmetrized profiles

Surface	Coating Solution Concentration, M	A_1	τ_1(ps)	A_2	τ_2(ps)
Fused Silica	10^{-6}	0.73	584	0.27	19.7
	10^{-5}	0.62	290	0.38	23.0
ZnO	10^{-6}	0.66	13.3	0.34	78.6
	3×10^{-6}	0.66	9.3	0.34	61.3
	10^{-5}	0.71	12.5	0.29	87.4

Discussion

The ground-state recovery on ZnO may be compared with fluorescence profiles of dyes on ZnO. Photon-counting measurements of time-resolved fluorescence from rhodamine 3B adsorbed at low coverage on ZnO [15] indicated that the fluorescence decay is nonexponential; a triexponential fit to a typical rhodamine 3B/ZnO profile yields the optimized fluorescence decay law $I(t) = 0.55\exp(-t/79\text{ps}) + 0.32\exp(-t/337\text{ ps}) + 0.13\exp(-t/1221\text{ ps})$. The dominant short-component lifetime of 79 ps is probably limited by the ~80 ps instrument function width of the photon-counting apparatus, in which fluorescence photons are detected by a microchannel plate phototube; similar short-component lifetimes are obtained for rhodamine 3B on TiO_2. Hence, the ground-state recovery of rhodamine 640 on ZnO and the fluorescence decay of rhodamine 3B on ZnO are commensurate in that the dominant short-component dynamics of both measurements are instrument-limited. Since the rate of ultrafast ground-state recovery in Fig. 3-4 exceeds that of population decay of photogenerated charge carriers in semiconductors [7] by several orders of magnitude, the present experiments furnish strong evidence of rapid, efficient, nonradiative dye → surface excitation decay.

With their comparatively low S/N ratios, our pump-probe results do not elucidate the actual mechanism of the nonradiative decay. For molecules separated from metal and semiconductor surfaces by distances larger than ~50 Å, the excited state decay appears to be well described [2-4] by the classical electromagnetic theory [5]. The asymptotic behavior of the predicted single-exponential lifetime τ for small d is

$$\frac{1}{\tau} = \frac{3q\lambda^3\theta}{32\pi^3\tau_o} \cdot \frac{n\kappa d^{-3}}{(1 + n^2 - \kappa^2)^2 + 4n^2\kappa^2} \qquad (3.3)$$

where q is the fluorescence yield, λ is the fluorescence wavelength, τ_o is the isolated-molecule lifetime, and $\theta = 1(2)$ for fluorescence transition moments parallel (normal) to the surface. This equation predicts femtosecond decay for visibly fluorescent dyes directly adsorbed on metals like Au ($n = 0.22$, $\kappa = 3.22$ at 6200Å [16]) and considerably slower decay on ZnO ($n = 1.8$, $\kappa \sim 5 \times 10^{-6}$ at 6000Å [17]) owing to the small absorption coefficient of the semiconductor. However, the classical theory breaks down [18] at very short distances. Considerable theoretical (but little experimental) work has focussed on decay of molecules separated from metals by $\lesssim$ 10Å [19,20]. We are not aware of any theory for excitation decay in molecules adsorbed directly onto semiconductors.

The marked nonexponentiality observed in both our pump-probe transients and photon-counting profiles is difficult to explain on the basis of Eq. 3.3, even by postulating that the dye is adsorbed over a distribution of separations d. An alternative decay mechanism is Förster dipole-dipole excitation trapping [21] by bulk impurity or surface states in the semiconductor. Such trapping will be efficient for states with excitation energies which overlap the dye fluorescence spectrum [22] and thus lie significantly below the energies of allowed transitions in the pure bulk semiconductor. When the trap density greatly exceeds the dye number density, averaging of the dipole-dipole transition rate over randomly distributed traps leads to the nonexponential decay law [21]

$$N(t) = N_o \exp[-t/\tau_o - \alpha(t/\tau_o)^{d/6}] \qquad (3.4)$$

where τ_o is the isolated-molecule lifetime, α is a dimensionless number proportional to the trap density, and d is the dimensionality of the trap distribution. Nonlinear least-squares analysis of photon-counting profiles from rhodamine 3B on ZnO [15] with variable α and τ_o in Eq. 3.4 yields excellent fits; τ_o converges to 2.54 ns and 19.4 ns, respectively for d = 2 and 3. Since the first of these lifetimes is commensurate with those measured in rhodamine 3B solutions and 19.4 ns is unphysically long, the trap distribution appears to resemble a 2-dimensional more than a 3-dimensional one. Similar results have been obtained in fluorescence profiles from rhodamine 3B on TiO_2. The nonexponentiality in the decay law of Eq. 3.4 arises from the disorder in the trap distribution, as each excited dye molecule experiences a different set of nearest-trap distances.

Identification of the surface states responsible for trapping requires independent characterization of the surface composition, which is unlikely to have been $Zn_{1.00}O_{1.00}$ prior to coating under our conditions. Auger measurements of oxygen/metal atomic ratios on TiO_2 surfaces untreated by Ar^+ ion bombardment and heating cycles generally yield nonstoichiometric values [23]. The concomitant local variations in surface electronic structure may create surface states. Commonly adsorbed impurities may provide additional trapping sites. Molecular excited-state decay on semiconductors is likely to be sensitive to surface treatment, and experiments on surfaces cleaned under ultrahigh-vacuum conditions may yield results contrasting with those reported here.

Acknowledgements

The Ames Laboratory is operated for the U.S. Department of Energy by Iowa State University under Contract No. W-7405-Eng-82. This work was supported by the Office of Basic Energy Sciences.

References

1. Spitler, M. T. "Proceedings of the Eighth Department of Energy Solar Photochemistry Research Conference", Lake Geneva, WI, June 11-14, 1984.

2. Drexhage, K. H.; Kuhn, H.; Schaefer, F. P. Ber. Bunsen-Ges. Phys. Chem. 1968, 72, 329.

3. Whitmore, P. M.; Alivisatos, A. P.; Harris, C. B. Phys. Rev. Lett. 1983, 50, 1092.

4. Crackel, R. L.; Struve, W. S. Chem. Phys. Lett. 1985, 120, 473.

5. Chance, R. R.; Prock, A.; Silbey, R. Adv. Chem. Phys. 1978, 37, 245.

6. Cardona, M.; Harbeke, G. Phys. Rev. 1965, 137, A1467.

7. Fessenden, R. W.; Kamat, P. V. "Proceedings of the Ninth Department of Energy Solar Photochemistry Research Conference", Lake Mohonk, NY, June 2-6, 1985.

8. Faraggi, M.; Peretz, P.; Rosenthal, I.; Weinraub, D. Chem. Phys. Lett. 1984, 103, 310.

9. Sadkowski, P. J.; Fleming, G. R. Chem. Phys. Lett. 1978, 57, 526.

10. Anfinrud, P.; Crackel, R. L.; Struve, W. S. J. Phys. Chem. 1984, 88, 5873.

11. Ippen, E. P.; Shank, C. V.; Bergman, A. Chem. Phys. Lett. 1976, 38, 611.

12. Anfinrud, P.; Struve, W. S. Rev. Sci. Instrum. 1986, 57, 380.

13. Engh, R. A.; Petrich, J. W.; Fleming, G. R. J. Phys. Chem. 1985, 89, 618. See also: Palfrey, S. L.; Heinz, T. F.; Eisenthal, K. B. "Ultrafast Phenomena IV", Auston, D. H.; Eisenthal, K. B., Eds.; Springer-Verlag: Berlin, 1984; Vol. 4, p 216.

14. DiLazzaro, P.; Mataloni, P.; DeMartin, F. Chem. Phys. Lett. 1985, 114, 103.

15. Crackel, R. L. Ph. D. Dissertation, Department of Physical Chemistry, Iowa State University, 1986.

16. Johnson, P.; Christy, R. Phys. Rev. B: Solid State 1973, B6, 4370.

17. Burgiel, J. C.; Chen, Y. S.; Vratny, F.; Smolinsky, G. J. Electrochem. Soc. 1968, 115, 729. The absorption spectrum of our ZnO samples was measured on a Perkin-Elmer 320 spectrophotometer.

18. Persson, B. N. J. J. Phys. C 1978, 11, 4251.

19. Maniv, T.; Metiu, J. J. Chem. Phys. 1980, 72, 1996.

20. Waldeck, D. H.; Alivisatos, A. P.; Harris, C. B. Surf. Sci. 1985, 158, 103.

21. Förster, Th. Ann. Phys. (Leipzig) 1948, 6, 55.

22. Förster, Th. Discuss. Faraday Soc. 1959, 27, 7.

23. Vannice, M. A.; Odier, P.; Bujor, M.; Fripiat, J. J. ACS Symp. Ser. 1985, No. 288, 98.

EXCITATION TRANSPORT IN GLYCEROL SOLUTIONS OF RHODAMINE 640: ABSENCE OF ORIENTATIONAL CORRELATION

Timothy P. Causgrove, Sandra M. Bellefeuille,

and Walter S. Struve

Department of Chemistry and Ames Laboratory - USDOE

Iowa State University, Ames, Iowa 50011

CHAPTER IV. EXCITATION TRANSPORT IN GLYCEROL SOLUTIONS OF RHODAMINE 640: ABSENCE OF ORIENTATIONAL CORRELATION

Introduction

Time-resolved fluorescence depolarization has been employed in our laboratory as a quantitative dynamic probe of electronic excitation transport (EET) among molecules in disordered systems [1-5]. When due attention is accorded to artifacts such as self-absorption [6], solvent reorganization [3,4], and fluorescence profile distortions arising from excitation trapping by aggregates [1,2], this technique can provide a sensitive test of current EET theories [7-10]. In our program, molecules are excited by weak, linearly polarized laser pulses, and the ensuing fluorescence profiles $I_{\parallel}(t)$, $I_{\perp}(t)$ polarized parallel and perpendicular to the laser polarization are accumulated using time-correlated single photon counting. For molecules which rotate freely in three dimensions, these intensity components are related to the time-dependent probability $G^S(t)$ that the excitation resides on the laser-excited molecule by

$$I_{\parallel}(t) = P(t)[1 + 0.8r(t)G^S(t)]$$
$$I_{\perp}(t) = P(t)[1 - 0.4r(t)G^S(t)] \qquad (4.1)$$

when residual polarization [11] is neglected. (Recent work by Fredrickson [12] has shown that the effects of rotational diffusion are described only approximately by Eqs. 4.1. The rotational diffusion timescale for dye molecules in glycerol is so slow (following section) that minimal error is

incurred in the present analysis.) The isotropic decay function P(t) is ideally single-exponential in a dilute, homogeneous solution; solvent organization normally endows the measured decay in P(t) nonexponential at early times [3,4]. The rotational anisotropy function r(t), initialized to unity at zero time in Eqs. 4.1, has the single-exponential form

$$r(t) = \exp(-6Dt) \tag{4.2}$$

in the spherical rotor approximation [13] if the absorption and fluorescence moments are parallel. We showed that EET in ethylene glycol solutions of 3,3′-diethyloxadicarbocyanine iodide (DODCI) is well represented for times $t \lesssim 5\tau$ and DODCI concentrations up to ~5 mM by the two-particle theory of Huber et al. [7], in which

$$G^S(t) = \exp[-C(\pi t/2\tau)^{1/2}] \tag{4.3}$$

Here τ is the intrinsic S_1 state lifetime in the absence of transport, and C is the dimensionless reduced concentration

$$C = \frac{4}{3}\pi R_o^3 \rho \tag{4.4}$$

which depends on the molecule number density ρ and the Förster parameter R_o [14]. At such times and concentrations, the two-particle theory for $G^S(t)$ essentially coincides with the more complicated (but analytic) GAF three-body theory [8] for three-dimensional disordered systems.

This situation contrasts markedly with the fluorescence depolarization

observed for DODCI in glycerol, a solvent frequently used in earlier EET experiments [1,14] because its large viscosity (954 cp at 25° C) freezes out rotational contributions to depolarization. Significant discrepancies emerged between the observed fluorescence depolarization and that predicted by the two-particle theory (Eqs. 4.1,4.3) for randomly oriented chromophores; these discrepancies increased with DODCI concentration. Unlike most alcohols (including ethylene glycol [16]), glycerol at 25° C exhibits coherence in its radial correlation function (i.e., crystalline ordering) out to distances as large as 25 Å [17]. It was hypothesized that the rodlike DODCI geometry (Fig. 4-1) facilitated its substitution into the glycerol "lattice" in such a way that two DODCI molecules separated by distances shorter than the ordered domain size were preferentially aligned with parallel transition moments [4]. No fluorescence depolarization accompanies EET between such a pair of chromophores; this hypothesis is therefore consistent with the fact that the apparent reduced concentration parameter C in the observed Green's function $G^S(t)$ becomes increasingly depressed relative to its true value at higher concentrations [3]. The magnitudes of these discrepancies were analyzed under the ad hoc assumption that DODCI chromophores separated by distances less than an orientational correlation length R_c exhibited parallel transition moments, but were uncorrelated for separations $R \geq R_c$. The resulting correlation length R_c - 40 Å (comparable to, but somewhat larger than the the radial correlation length from x-ray scattering in liquid glycerol [17]) also supported orientational correlation as the origin of the discrepancies.

Such orientational correlation requires marked anisotropy in the

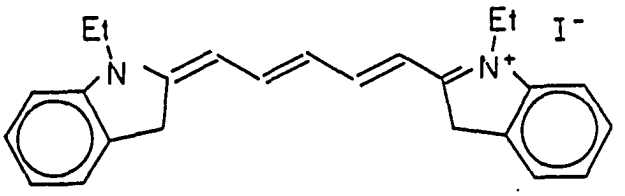

DODCI

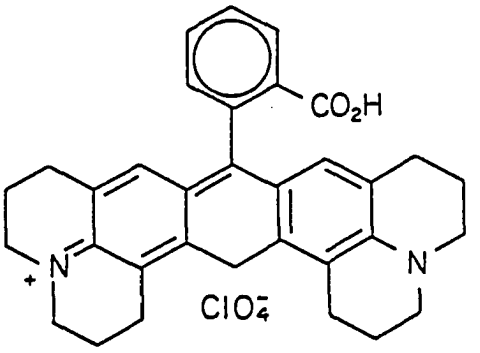

RHODAMINE
640

Figure 4-1. Structures of 3,3'-diethyloxadicarbocyanine iodide (DODCI) and rhodamine 640 (rh 640).

interactions between chromophore and solvent as well as local ordering in the solvent structure. In this work, we have repeated the fluorescence depolarization studies for rhodamine 640 (hereafter rh 640) in glycerol. While far from spherical, the rh 640 chromophore (Fig. 4-1) is considerably less eccentric than DODCI. We correspondingly find that the EET in this system conforms closely to Eqs. 4.1, with $G^s(t)$ modeled by the two-particle function of Eq. 4.3; there is no evidence for orientational correlation of rh 640 molecules in glycerol. We have also monitored EET in this system through polarized pump-probe spectroscopy [18] in order to compare this technique with fluorescence depolarization as a means of studying transport. In pump-probe spectroscopy, the sample $S_1 \leftarrow S_0$ transition is excited by a weak, linearly polarized pump pulse; the subsequent $S_1 \leftarrow S_0$ photobleaching decay is interrogated by a variably delayed probe pulse at the same wavelength. The occurrence of EET between nonparallel rh 640 molecules does not influence the isotropic part of the ground-state recovery, but it affects the polarization of the photobleaching transient in a manner which mirrors fluorescence depolarization. The optical densities $A_{\parallel}(t)$, $A_{\perp}(t)$ experienced by probe pulses polarized parallel and perpendicular to the pump polarization prove to be exactly analogous to Eqs. 4.1 for the fluorescence intensity components $I_{\parallel}(t)$, $I_{\perp}(t)$. Pump-probe techniques do not easily match the superb data statistics accessible through photon counting [19], but their laser pulse-limited time resolution is far superior to our photon counting instrument function of ~47 ps. Polarized pump-probe spectroscopy is therefore preferable to fluorescence depolarization for studying EET in green plant antennae, where subpicosecond single-site hopping times have

been inferred [20]. Since pump-probe techniques (unlike fluorescence) are not inherently S_1 state-selective, the present calibration of pump-probe techniques against fluorescence depolarization is an essential first step in assessing whether artifacts such as triplet-triplet absorption influence their applicability to photosynthetic antenna systems.

Experimental

The tunable picosecond excitation laser system and time-correlated photon counting electronics have been described previously [2-4]. A rhodamine 590 dye laser with 3-plate birefringent filter was synchronously pumped by a mode-locked argon ion laser and cavity-dumped at 4.8 MHz to generate linearly polarized 570 nm pulses with ~7 ps FWHM. Rhodamine 640 was obtained from Exciton. Emission from glycerol solutions of rh 640 was analyzed by a Promaster Spectrum 7 linear polarizer, passed through two Schott OG-590 filters, collected with a 10 cm f.l. lens, and focussed through a variable rectangular aperture onto a Hamamatsu R1564U microchannel plate phototube (MCP).

The rh 640 monomer-dimer equilibrium in glycerol was characterized by obtaining rh 640 absorption spectra at several concentrations in this solvent. The dimerization equilibrium constant $K_d = [M_2]/[M]^2$, computed from the monomer and dimer absorbances at 580 and 540 nm, depends on the values of peak absorption coefficients $\varepsilon_{max}(M)$ and $\varepsilon_{max}(M_2)$. The former (~1.03×10^5 l/mol. cm) was evaluated from a spectrum taken at low concentration. According to the simple exciton theory [21], $\varepsilon_{max}(M_2)$ lies between $\varepsilon_{max}(M)$ and $2\varepsilon_{max}(M)$. The nominal rh 640 concentrations in our

transport experiments ranged from 0.246 to 5.61 mM. In the worst case where $\varepsilon_{max}(M)$ is assumed to be equal to $\varepsilon_{max}(M_2)$, the total rh 640 concentration [T] = [M] + 2[M_2] and the rh 640 monomer concentration [M] are 5.61 and 5.55 mM, respectively, in the most concentrated solutions used. Hence, the monomer-dimer equilibrium has minimal effect on [M] for rh640 in glycerol, in contrast to DODCI in glycerol [4].

The isotropic decay function P(t) was measured at each concentration by obtaining a magic-angle profile with the analyzing polarizer aligned 54.7° from the laser polarization. These were fitted with a biexponential decay law using a Marquardt nonlinear least-squares algorithm [22]. The isotropic decay is dominated at all concentrations by a long component whose lifetime increases by 6% from ~3840 ps to 4090 ps between 3.4 μM and 2.70 mM; this trend, due to self-absorption, resembles the behavior shown by rh 6G [1] and DODCI [3,4] in alcohols. Excitation trapping by rh 640 aggregates abbreviated the lifetimes at the two highest concentrations. The short component arises principally from solvent reorganization at lower concentrations. In separate experiments, magic-angle profiles were obtained at 3.4 μM using a 2 nm bandpass ISA monochromator. The short component preexponential factors a_2 resulting from biexponential fits to these profiles are plotted against transmission wavelength in Fig. 4-2, which clearly demonstrates the dynamic spectral shifts accompanying solvent reorganization during the first several hundred ps following excitation. Maroncelli and Fleming [23] have analyzed the solvation dynamics of polar liquids around the asymmetric dye coumarin 153 in terms of differential S_1 - S_0 charge distributions obtained from MNDO calculations. Like DODCI, the unperturbed rh 640 chromophore has no

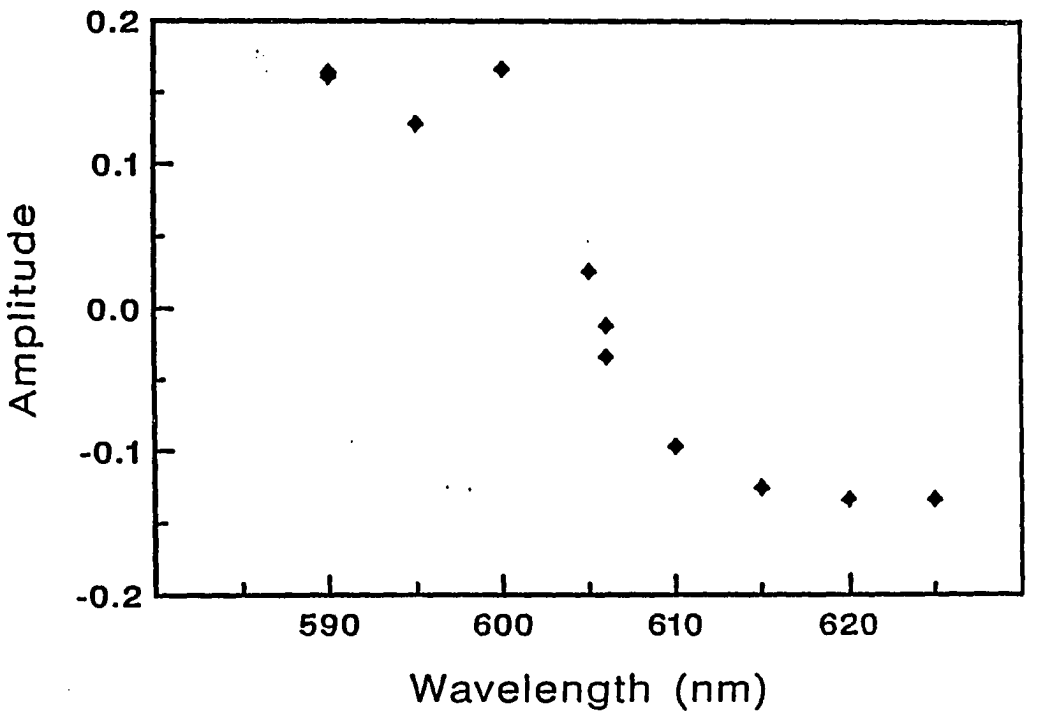

Figure 4-2. Plot of short-component preexponential factors a_2 yielded by biexponential fits of magic-angle fluorescence profiles from 3.4 μM rh 640 in glycerol, versus detected fluorescence wavelength λ.

dipole moment (Fig. 4-1) and so the nature of the charge shifts responsible for solvation must be fundamentally different in our systems.

The rotational anisotropy function r(t) was determined by obtaining the polarized fluorescence profiles $I_{\parallel}(t)$, $I_{\perp}(t)$ at a concentration so low (3.4 μM) that negligible transport occurs during the ~9 ns photon counting time window. These profiles were fitted using Eqs. 4.1 with $G^s(t) = 1.0$ and r(t) given by Eq. 4.2; the rotational diffusion parameter D in r(t) was allowed to float, while the isotropic functions P(t) were expressed as biexponential functions with parameters fixed at the values determined from the 3.4 μM magic angle profiles. The average values of $\tau_{rot} = 1/6D$ = 100.9 ns obtained from three trials exceeded the rh 640 fluorescence lifetime by a factor of ~25 owing to the large viscosity of glycerol. Rotational diffusion therefore contributes little to the total fluorescence depolarization for rh 640 at most concentrations in glycerol. The measured rotational diffusion time appears to be sensitive to water impurity in the glycerol; τ_{rot} ~20 ns was obtained for rh 640 in glycerol which had been exposed to the air for six days.

The polarized profiles $I_{\parallel}(t)$, $I_{\perp}(t)$ obtained at higher concentrations were fitted with Eqs. 4.1 in a linked deconvolution which simultaneously minimizes the combined χ_r^2 of both profiles [1,3,4]. The biexponential parameters in the isotropic profiles P(t) were held at the values obtained from magic-angle profiles, while the rotational diffusion time τ_{rot} in the anisotropy function r(t) was maintained at 100.9 ns. The two-particle $G^s(t)$ in Eq. 4.3 was used with the intrinsic lifetime τ held at 3.85 ns (vs. the long-component lifetimes in the isotropic decay at 3.4 μM). The only variable parameter in the Green's function $G^s(t)$ is therefore the

dimensionless reduced concentration C.

The laser system used in the pump-probe experiments was a passively mode-locked dual jet rhodamine 590-DQOCI laser, pumped by a multiline argon ion laser with 6W plasma tube. It produced vertically polarized 605 nm laser pulses with ~50mW average power at 125 MHz repetition rate; real-time autocorrelation [24] traces exhibited 1.8 ps FWHM. Our pump-probe beam geometry [25] and multiple modulation detection scheme were similar to an apparatus described previously [26,27]. The probe beam polarization was fixed at 45° from the laser polarization using a calcite Glan-Thompson prism polarizer; the variable pump beam polarization was selected with an identical, rotatable polarizer. Both beams were focussed by a common 7.3 cm f.l. lens to ~10 μm spot diameter at the rh 640/glycerol solution, which was housed between fused silica optical flats separated by a spacer (0.1 mm thick for rh 640 concentrations higher than 1.77 mM, 0.4 mm thick for the more dilute solutions). The average incident laser power was ~5 mW in each beam.

Pump-probe sweeps were accumulated for ten rh 640 concentrations from 0.409 to 5.60 mM for parallel, perpendicular, and magic-angle polarizations. Convolutions of Eqs. 4.1 with the laser autocorrelation function were fitted to the polarized profiles $A_{\parallel}(t)$, $A_{\perp}(t)$ in a procedure analogous to that followed in the fluorescence data analysis. The magic-angle profiles were fitted with triexponential decay laws. In analyzing the anisotropic profiles $A_{\parallel}(t)$ and $A_{\perp}(t)$, the rotational anisotropy function r(t) was fixed at 1.0 throughout, since the rotational period of rh 640 in glycerol encompasses some 400 pump-probe scan intervals in our geometry.

Figure 4-3, which shows magic-angle fluorescence and pump-probe profiles for rh 640/glycerol solutions at concentrations near 0.4 mM, illustrates the comparative qualitites of data achieved in the two experiments. The fluorescence profile, accumulated with ~25,000 counts in the peak channel, exhibits noticeably larger S/N than the pump-probe transient. The 10 ns photon counting time window enables isotropic decay monitoring over ~2.5 lifetimes, while only the first 200 ps of the photobleaching decay are accessible in a pump-probe experiment using a 5 cm translation stage. These differences account for the contrasting levels of noise exhibited by the final data plots extracted from analyses of the polarized fluorescence and pump-probe profiles (cf. Fig. 4-4 in the following Section).

Results and Discussion

Results of convolute-and-compare analyses of the anisotropic fluorescence profiles using Eqs. 4.1 as model functions with the two-particle Green's function for $G^S(t)$ are summarized in Figure 4-4a. The optimized reduced concentrations C_D are related to the parameter C which enters $G^S(t)$ in Eq. 4.3 by $C_D = C/0.846$; this factor arises from orientational averaging of the dipole-dipole transition probability in Förster transport [14]. When plotted versus the true rh 640 concentration as shown in Fig. 4-4a, these C_D values fall very nearly on a straight line, as predicted by Eqs. 4.3 and 4.4. The Förster parameter R_o yielded by a linear least-squares fit of these points using Eq. 4.4 is 54.5 Å. The agreement between our data and the two-particle theory for $G_s(t)$,

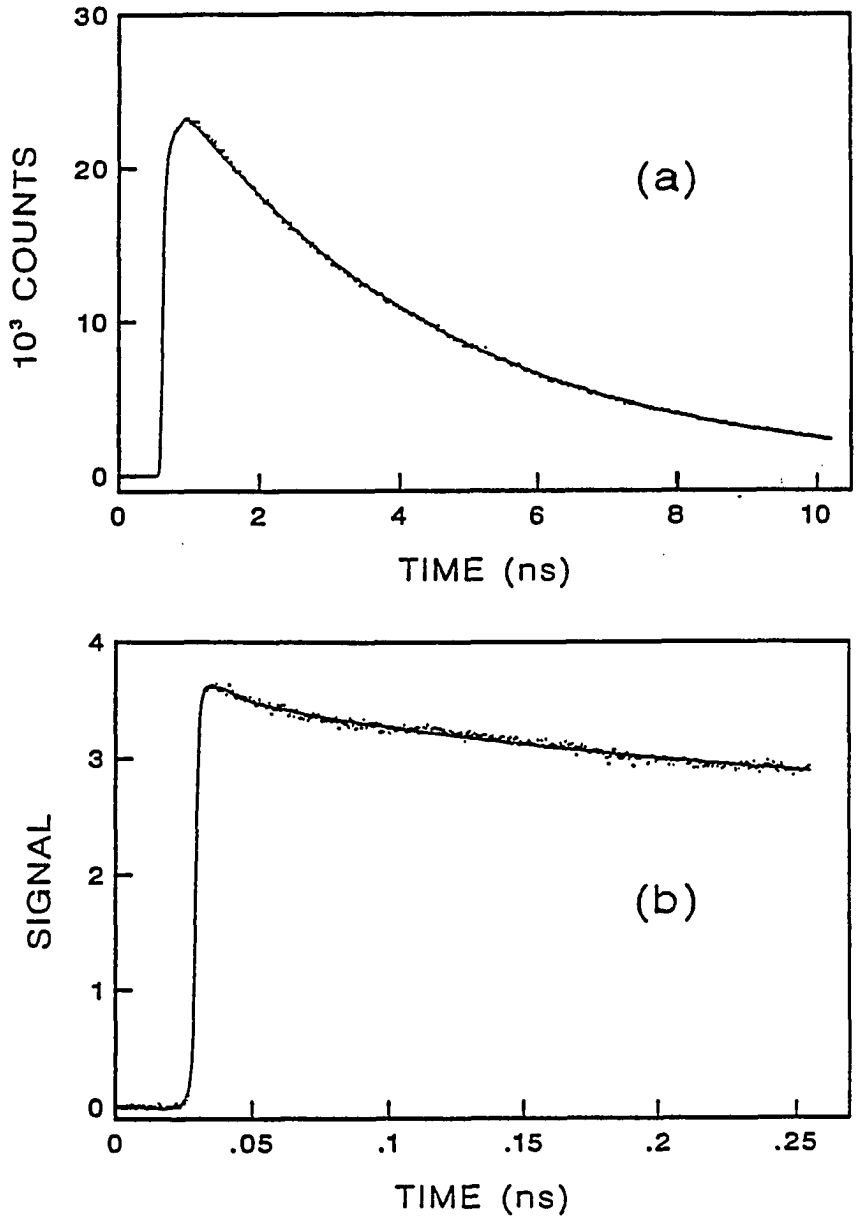

Figure 4-3. Isotropic decay of rh 640 in glycerol a) Magic-angle fluorescence profile from 0.494 mM solution b) magic-angle photobleaching decay of 0.409 mM solution. Note the difference in time windows (~10 ns and ~200 ps, respectively).

which was developed on the premise that the chromophores are randomly oriented, is far closer than for DODCI in glycerol [3,4]. There is no evidence for significant orientational correlation between rh 640 chromophores in glycerol even at the highest concentration studied (-5.6 mM), at which the most probable nearest-neighbor separation becomes -36 Å. The chromophore-solvent interactions for rh 640 in glycerol are clearly not sufficiently anisotropic for preferential alignment of this dye within the ordered domains of the glycerol liquid structure. Our earlier work [1] did not exhibit sufficient S/N and freedom from self-absorption to establish a similar conclusion for rhodamine 6G in glycerol.

We show in Fig. 4-4b the optimized C_D parameters from similar convolute-and-compare analyses of the anisotropic pump-probe profiles. These are displayed in a format which allows direct comparison with the analogous plot derived from the fluorescence depolarization experiments, Fig. 4-4a. The pump-probe data plot in Fig. 4-4b is considerably the noisier of the two, particularly at the lower rh 640 concentrations where depolarization is slow. The straight line in Fig. 4-4b corresponds to R_0 = 50 Å; the Förster parameters derived from the fluorescence experiments agree to within scatter in the pump-probe data points. The principal origin of the noise in Fig. 4-4b is the far narrower time window in the pump-probe experiments (200 ps versus 10 ns in Fig. 4-3); the depolarization here is monitored only in its earliest stages, where differences between the transients $A_{\parallel}(t)$ and $A_{\perp}(t)$ remain subtle. Nevertheless, the locus of pump-probe data points for rh 640 concentrations $\gtrsim$1 mM overlaps closely with the fluorescence data plot in Fig. 4-4a, indicating that pump-probe techniques offer an equally valid method

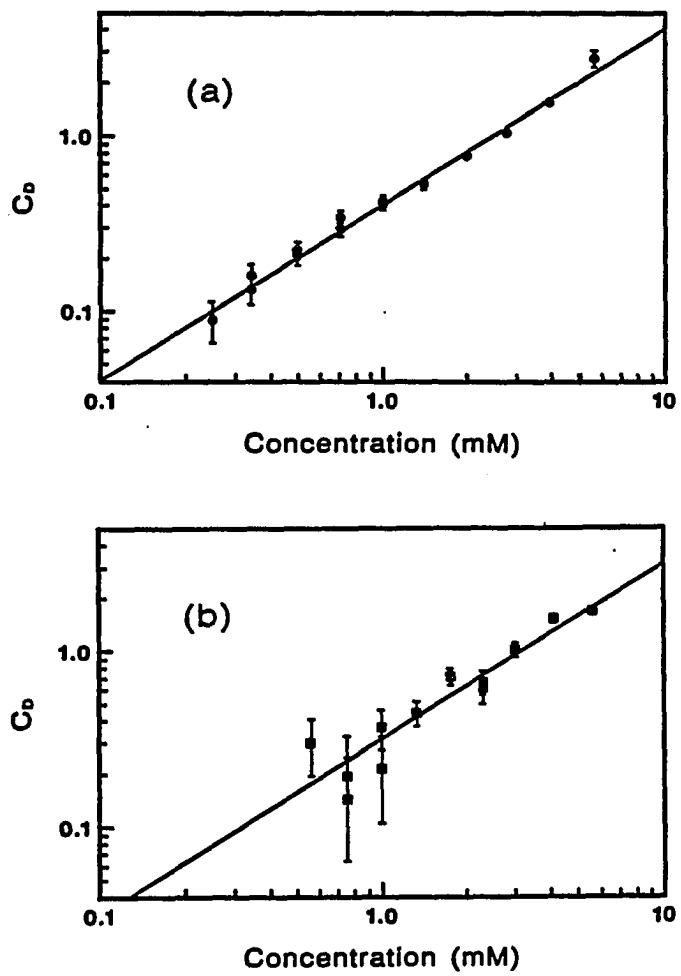

Figure 4-4. Optimized reduced concentrations C_D versus true rh 640 monomer concentration, obtained by fitting a) anisotropic fluorescence profiles and b) anisotropic pump-probe profiles with $G^S(t)$ given by the two-particle theory in Eqs. 4.1. The error bars show propagated standard deviations based on the standard deviations in the anisotropic profiles.

for monitoring EET depolarization. The agreement between the fluorescence and pump-probe experiments is interesting because the T_1 state lifetimes of rhodamines in alcohols (~250 ns for rhodamine 6G in air-saturated ethanol [28]) are far longer than our 8 ns laser pulse spacing. Our 605 nm probe wavelength was some 10^3 cm^{-1} lower in energy than the 570 nm absorption peak for rh 640 in glycerol. At such energies, xanthene dyes exhibit triplet-triplet absorption coefficients of ~10^4 l/mole-cm [29], which is comparable to the rh 640 $S_1 \leftarrow S_0$ absorption coefficient at the wavelength at which photobleaching was monitored. (This probe wavelength was mandated by the limited operating regime of the saturably mode-locked rhodamine 590-DQOCI laser.) The low intersystem crossing yields in rhodamines (typically ~10^{-2}), combined with the small ratios (~10^2) of pulse photons to irradiated molecules, enabled the present pump-probe experiment to tolerate a repetition rate as high as 125 MHz. In recent experiments, the technique has been applied to EET depolarization in the bacteriochlorophyll a-protein complex from Prosthecochloris aestuarii [30] and in PS I-60 enriched photosystem I particles from spinach chloroplasts [31].

Acknowledgements

We are grateful to W. E. Catron for supporting one of us (T. P. C.) through a Research Fellowship, and to P. A. Anfinrud for helpful discussions. The Ames Laboratory is operated for the U. S. Department of Energy at Iowa State University under Contract No. W-7405-Eng-82. This work was supported by the Office of Basic Energy Sciences.

References

1. Anfinrud, P. A.; Hart, D. E.; Hedstrom, J. H.; Struve, W. S. J. Phys. Chem. 1986, 90, 2374.

2. Anfinrud, P. A.; Hart, D. E.; Hedstrom, J. H.; Struve, W. S. J. Phys. Chem. 1986, 90, 3116.

3. Hart, D. E.; Anfinrud, P. A.; Struve, W. S. J. Chem. Phys. 1987, 86, 2689.

4. Anfinrud, P. A.; Struve, W. S. J. Chem. Phys. 1987, 87, 4256.

5. Anfinrud, P. A.; Hart, D. E.; Struve, W. S. J. Phys. Chem. 1988, 92, 4067.

6. Hammond, P. R. J. Chem. Phys. 1979, 70, 3884.

7. Huber, D. L.; Hamilton, D. S.; Barnett, B. Phys. Rev. B. 1977, 16, 4642.

8. Gochanour, C. R.; Andersen, H. C.; Fayer, M. D. J. Chem. Phys. 1979, 70, 4254.

9. Fedorenko, S. G.; Burshtein, A. I. Chem. Phys. 1985, 98, 341.

10. Baumann, J.; Fayer, M. D. J. Chem. Phys. 1986, 85, 4087.

11. Anfinrud, P. A.; Struve, W. S. J. Phys. Chem. 1987, 91, 5058.

12. Fredrickson, G. H. J. Chem. Phys. 1988, 88, 5291.

13. Chuang, T. J.; Eisenthal, K. B. J. Chem. Phys. 1972, 57, 5094.

14. Förster, Th. Discuss. Faraday Soc. 1959, 27, 7.

15. Gochanour, C. R.; Fayer, M. D. J. Phys. Chem. 1981, 85, 1989.

16. Podo, F.; Nemethy, G.; Indovina, P. L.; Radics, L.; Viti, V. Mol. Phys. 1974, 27, 521.

17. Soltwisch, M.; Steffen, B. Z. Naturforsch. Teil A, 1981, 36, 1045.

18. Fleming, G. R. "Chemical Applications of Ultrafast Spectroscopy"; Oxford University Press: New York, 1986.

19. O'Connor, D. V.; Phillips, D. "Time-correlated Single Photon Counting"; Academic Press: London, 1984.

20. Owens, T. G.; Webb, S. P.; Mets, L.; ALberte, R. S.; Fleming, G. R. Proc. Natl. Acad. Sci. USA 1987, 84, 1532.

21. Chambers, R. W.; Kajiwara, T.; Kearns, D. R. J. Phys. Chem. 1974, 78, 380.

22. Marquardt, D. W. Commun. ACM 1970, 13, 47.

23. Maroncelli, M.; Fleming, G. R. J. Chem. Phys. 1987, 86, 6221.

24. Yasa, Z. A.; Amer, N. M. Opt. Commun. 1981, 36, 406.

25. Ippen, E. P.; Shank, C. V.; Bergman, A. Chem. Phys. Lett. 1976, 38, 611.

26. Anfinrud, P. A.; Causgrove, T. P.; Struve, W. S. J. Phys. Chem. 1986, 90, 5887.

27. Anfinrud, P.; Struve, W. S. Rev. Sci. Instrum. 1986, 57, 380.

28. Webb, J. P.; McColgin, W. C.; Peterson, O. G.; Stockman, D. L.; Eberly, J. H. J. Chem. Phys. 1970, 53, 4227.

29. Buettner, A. V.; Snavely, B. B.; Peterson, O. B. In "Molecular Luminescence"; Lim, E. C., Ed.; Benjamin: New York, 1969.

30. Causgrove, T. P.; Yang, S.; Struve, W. S. J. Phys. Chem. 1988, 92, 6121.

31. Causgrove, T. P.; Yang, S.; Struve, W. S.; Golbeck, J. H. J. Phys. Chem., in press.

CHAPTER V. ELECTRONIC ENERGY TRANSPORT IN PHOTOSYNTHETIC SYSTEMS

Literature Review of BChl a-protein from P. aestuarii

In Chapter I, the concept of a "photosynthetic unit" consisting of a trap (reaction center) and a large set of antenna molecules was introduced. The antenna molecules act as both a light-harvesting apparatus and excitation energy pathway to the reaction center (RC), where photochemistry occurs. When an excitation reaches the reaction center, charge separation takes place; the electron donated by the RC is stored to be used in the basic reaction of photosynthesis. Much progress has been made in determining the structure and dynamics of RCs, particularly in the purple photosynthetic bacteria [1]. However, the experiments described in this work deal only with excitation energy transfer (EET) between antenna molecules, and the reaction center will generally be modeled as a simple excitation quencher (deep trap).

Several models of the photosynthetic unit (PSU) have been proposed, often based on a 1-, 2-, or 3-dimensional regular lattice in order to simplify mathematical modeling of transport and trapping properties. A 2-dimensional lattice is often assumed for antenna systems of green plants because the pigment molecules are known to lie within the thylakoid membrane [2]. Two different types of 2-dimensional lattices are shown in Fig. 5-1, where circles represent antenna chlorophyll (Chl) molecules and squares represent traps (reaction centers). Fig. 5-1a corresponds to a "lake" model, in which traps are randomly interspersed in an antenna array, while Fig. 5-1b is an example of the "isolated puddles" model,

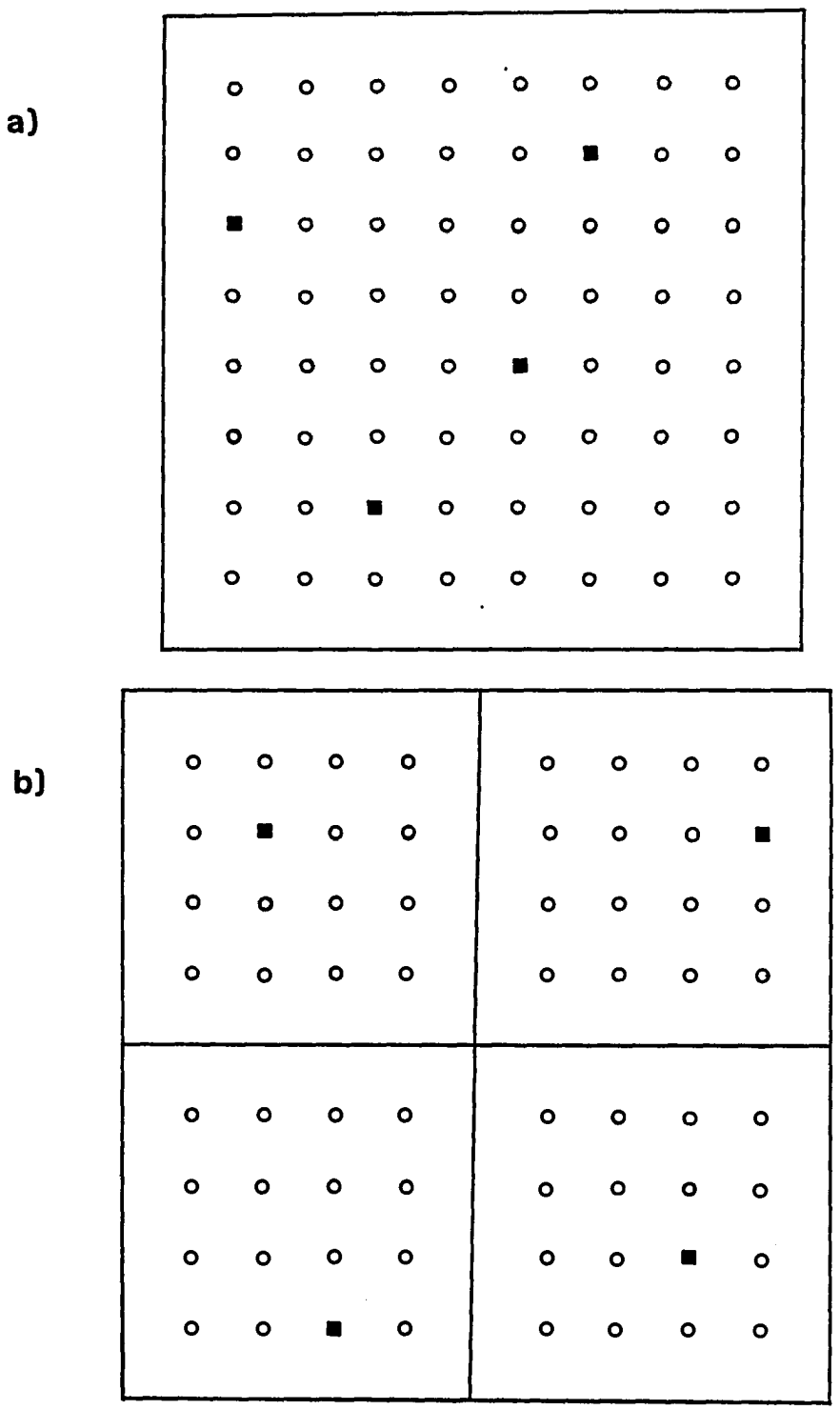

Figure 5-1. Schematic diagrams of a) lake and b) puddle models of chromophore organization in photosynthetic antenna systems.

where each separate PSU contains a single trap. In addition some models have assumed that antenna chromophores nearer to the trap absorb at longer wavelength, leading to an energy funnelling effect (Fig. 5-2). This downhill transfer (as opposed to near-resonant transfer) has been shown to increase trapping rates by as much as a factor of 10 [3]. Sauer's "pebble mosaic" model [4] suggests a different type of organization consisting of an array of clusters of Chl molecules (Fig. 5-3). The chromophores within a cluster are strongly interacting (form exciton states) and Förster hopping occurs between clusters. This model is supported by the isolation of pigment-protein complexes containing a small number (<7) of closely-spaced chromophores [5,6]. Very little theoretical work has been done on energy transfer between clustered pigments, but similar trapping times have been reported for regular-lattice and clustered models with the same chromophore density [7].

Much is known about the organization of the PSU for the green sulfur bacteria Chlorobium limicola and Prosthecochloris aestuarii. (In much of the early literature, these organisms are referred to as Chloropseudomonas ethylica, which was identified in 1972 as a mixed culture of the green sulfur-oxidizing bacterium Chlorobium limicola and a colorless sulfate-reducing bacterium, Desulfuromonas acetoxidans. However, in 1976 the green bacterium of the mixed culture designated strain 2K, which was used in Chapter VI, was discovered to be P. aestuarii, not C. limicola. The N2 strain does, however, contain C. limicola [8].) Both of the green bacteria are members of the Chlorobiaceae group, and because they grow at lower depths of lakes and ponds, they have developed extensive light-harvesting systems. Electron micrographs of thin-section and negative-

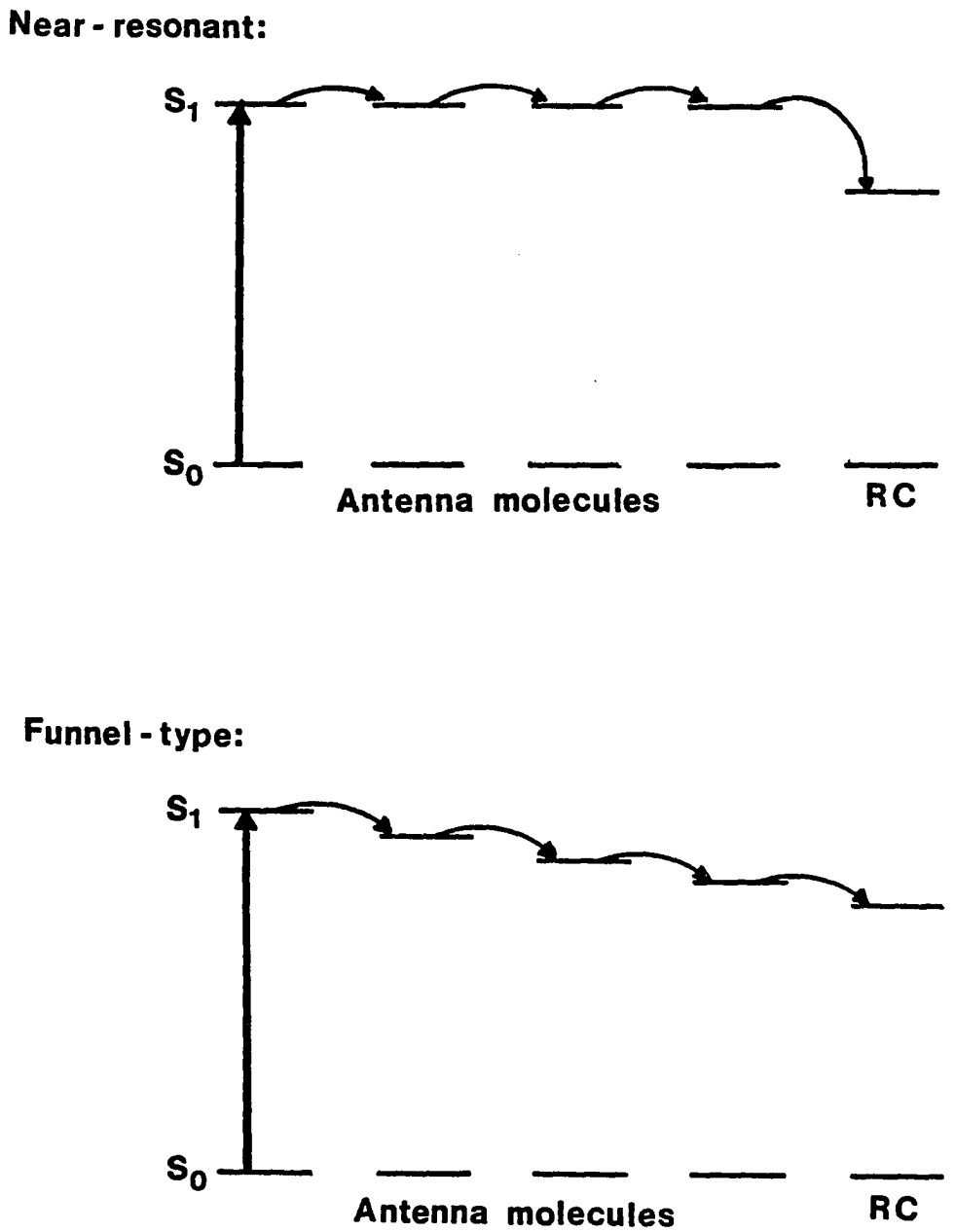

Figure 5-2. Energy levels for near-resonant energy transfer and "funnel"-type antenna systems.

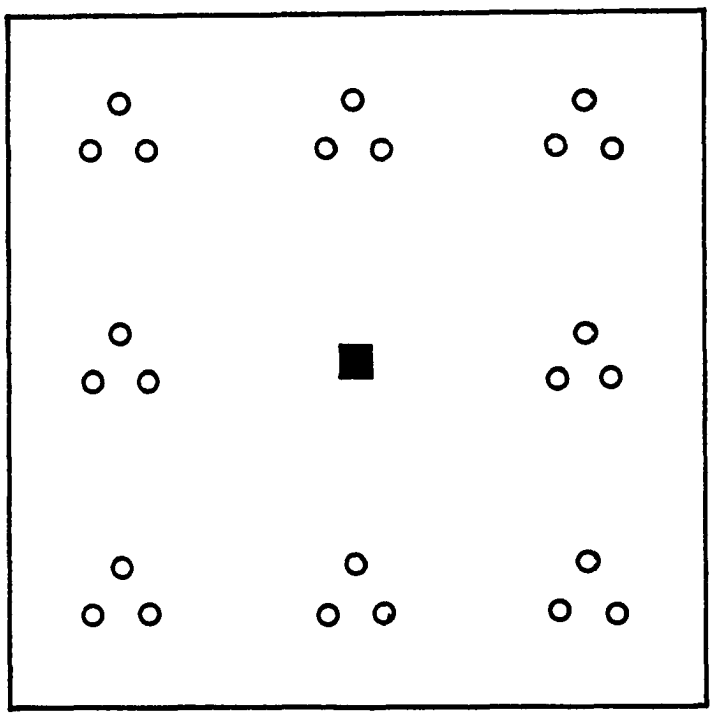

Figure 5-3. Pebble mosaic model of an antenna system, in which pigments are clustered in small groups forming strong interactions.

stained P. aestuarii [9] and C. limicola [10] show oblong bodies called chlorosomes attached to the inside of the cell wall. The chlorosomes (formerly called "chlorobium vesicles") vary in size from 100 to 300 nm in length and from 50 to 100 nm in width. Based on freeze-fracture micrographs (as well as available biochemical and biophysical data) Staehelin et al. [11] proposed a model for the chlorosome as shown in Fig. 5-4a. The chlorosome contains 10-30 rod-shaped elements (~10 nm in diameter) of BChl c-protein complex which serve as the primary light-harvesting apparatus. The BChl c are very closely spaced, with 12-14 chromophores per 15 kDa protein [12]. The BChl c-protein rods are most likely surrounded by a monogalactolipid layer, which separates the cytoplasm from the hydrophobic interior of the chlorosome. These rods are separated from the cytoplasmic membrane by a crystalline "baseplate", which is clearly seen in the freeze-fracture micrographs [11]. The baseplate, which contains a BChl a-protein complex, is ~5 nm thick and shows a periodicity of ~6 nm. This complex will be described in greater detail below. The reaction centers (~30 per chlorosome) as well as non-crystalline BChl a-protein are located in large (~10-14 nm diameter) particles embedded in the cytoplasmic membrane. Reaction center particles retaining photochemical activity have been isolated [13] with either 75 or 35 BChl a per RC (~350 kDa and ~600 kDa, respectively). The particles are comprised largely of BChl a and an as yet unidentified pigment [14]. In later work, Gerola and Olson [15] found that there is another BChl a-protein located in the chlorosome envelope between the BChl c rods and the crystalline baseplate. This small (~5 kDa) protein contains at least 2 BChl a molecules and apparently functions as an intermediary in electronic

a)

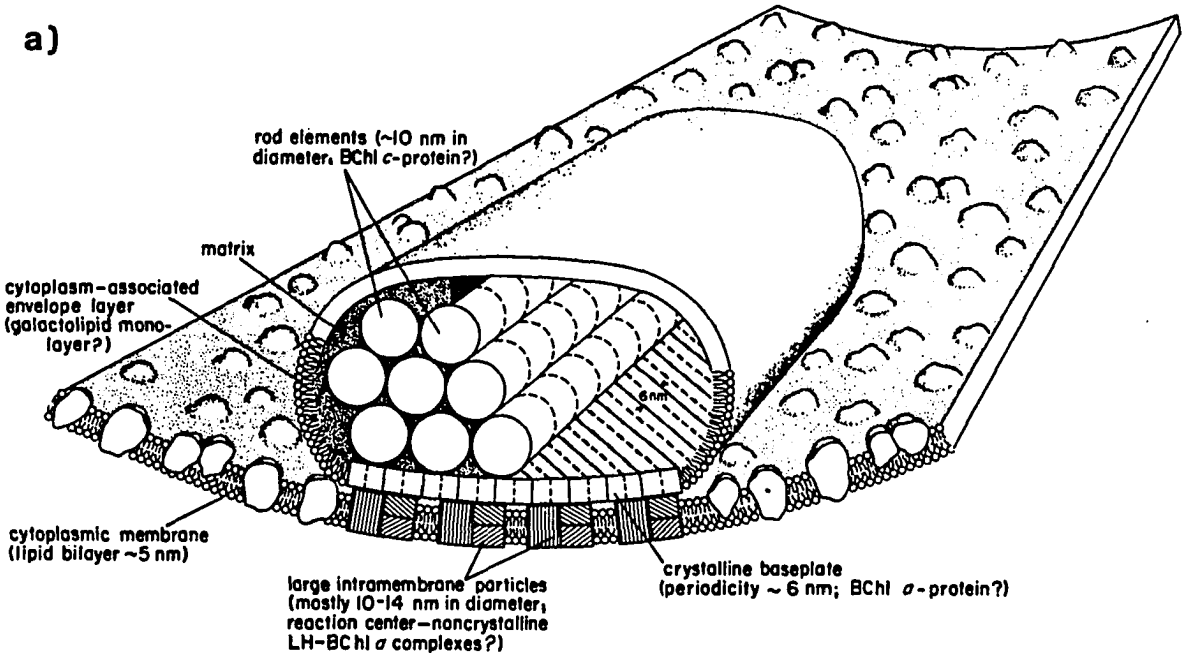

b)

Abs. Max.:	750 nm	794 nm	810 nm	840 nm
	BChl c ⟶	BChl a (5 kDa) ⟶	BChl a (45 kDa) ⟶	RC complex
Abundance:	1500	16	80	1

Figure 5-4. Photosynthetic apparatus of green sulfur bacteria. a) Model of a chlorosome of C. limicola based on freeze-fracture micrographs. From ref. [11]. b) Apparent energy transfer order, with absorption maximum and relative abundance of each complex in terms of number of BChl per reaction center.

excitation transfer between BChl c and the baseplate. The apparent transfer order for the chlorosome system, the absorption maximum of each complex and its abundance in terms of number of BChl per reaction center are given in Fig. 5-4b.

The BChl a-protein from the baseplate of P. aestuarii is unusual in that it is water-soluble and can therefore be easily separated and purified [16]. Furthermore, under proper conditions the protein can be crystallized [17]. Using crystals grown by J. M. Olson, Matthews and Fenna [18] determined the structure of the complex using x-ray crystallography at 2.8 Å resolution. The basic unit of the protein is a trimer with identical subunits related by a three-fold symmetry axis (Fig. 5-5). Each subunit consists of a protein "bag" surrounding seven BChl a molecules which are held in place by hydrogen bonds to the protein. Five of the chromophores also have histidine side chains as the fifth ligand to the Mg atom. The x-ray studies yield a molecular weight of 45 kDa per subunit (38.6 kDa due to protein, 6.4 kDa for 7 BChl a molecules), in agreement with gel electrophoresis measurements [19]. The protein of each subunit contains ~360 amino acids [20] which form extensive β-sheets and protect the hydrophobic BChl core from the solvent. There are extensive interactions between the protein chains of different subunits in a trimer; this is consistent with observations that the trimer cannot be split into subunits without denaturing the protein [19] and supports the belief that the trimer exists in vivo. The seven BChl a molecules within a subunit have no obvious symmetry, but all lie within 40° of an average plane [18]. The nearest-neighbor Mg - Mg separations within a subunit are 11 - 14 Å [21] and there are extensive contacts among BChl molecules as well as

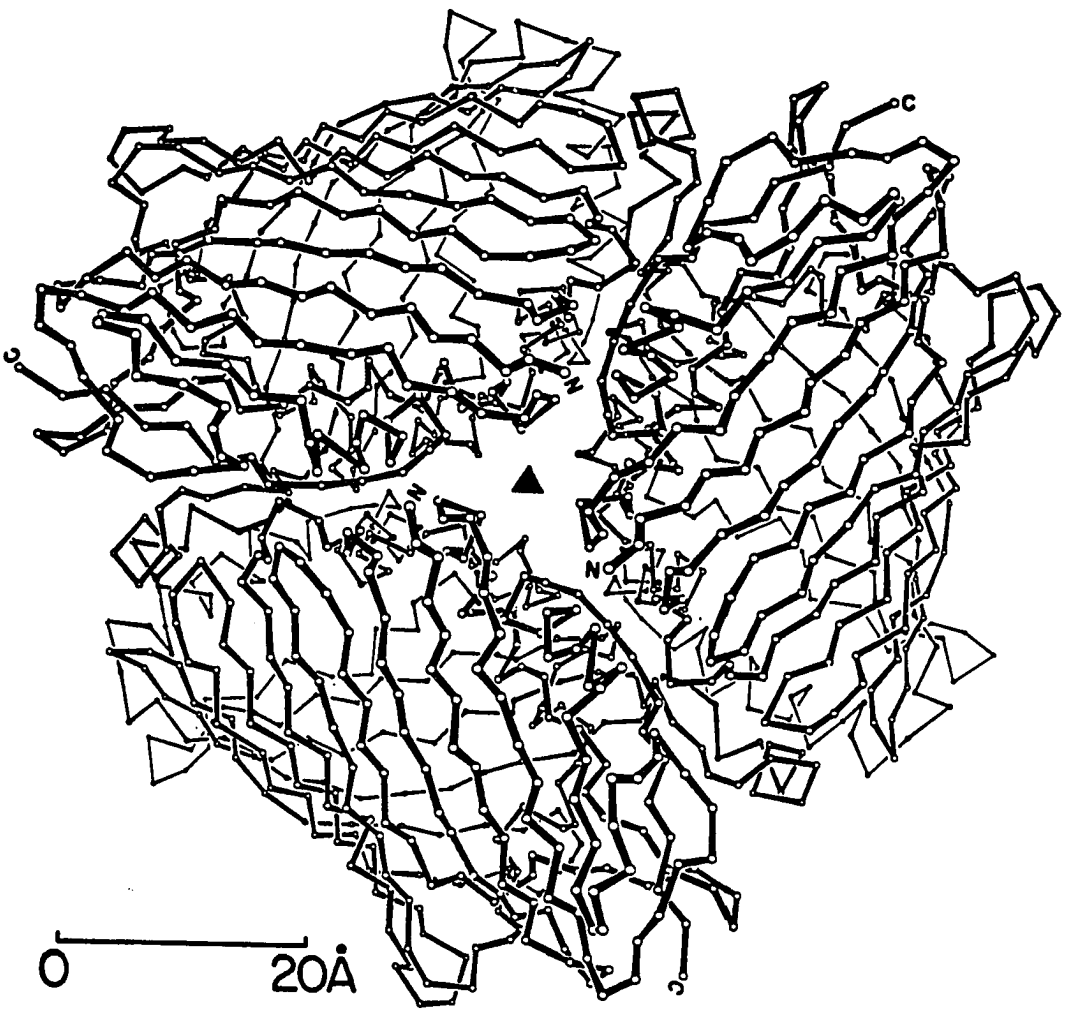

Figure 5-5. BChl a-protein trimer showing three-fold symmetry axis. The BChl a chromophores have been excluded for clarity. From ref. [18].

between BChl molecules and protein.

Under slightly different conditions, the protein forms crystals of $P6_1$ or $P6_3$ symmetry [22]. The complete structure determination was done on crystals of $P6_3$ symmetry, but the former has also been shown to consist of trimers [23]. In the $P6_3$ crystals, each trimer is related to another by a 2_1 screw axis (Fig. 5-6). The combination of the screw axis and three-fold symmetry axes forms large (63 Å diameter) solvent channels which are readily seen in electron micrographs of sectioned crystals [24]. Subunits related by three-fold axes are separated by ~33.1 Å (based on the average Mg positions) while subunits related by 2_1 axes are separated by ~61.5 Å, including 49.3 Å (one-half the unit cell dimension) along the c-axis.

Since the position and orientation of each of the seven BChl *a* molecules within a subunit are known [21], this system provides an excellent opportunity to test models of excitation energy transport. Based on the separations of the chromophores, it is expected that the molecules will be strongly interacting to form exciton states (see Chapter I). Much spectroscopic evidence has been assembled to show that this is indeed the case. First, low temperature absorption spectra of the Q_y region [25-27] show several subbands of unequal magnitude which are narrower than that of BChl *a* in solution. Using fourth and eighth derivatives of low temperature absorption spectra, seven peaks have been identified in the Q_y absorption band [28]. Second, the circular dichroism (CD) spectrum [25,26] is conservative (sums to zero over the Q_y region) and much larger in magnitude than that of monomeric BChl *a*. Such features of CD spectra have been shown to be a consequence of excitonic interaction [29]. Third, the low-temperature emission spectrum is a mirror image of

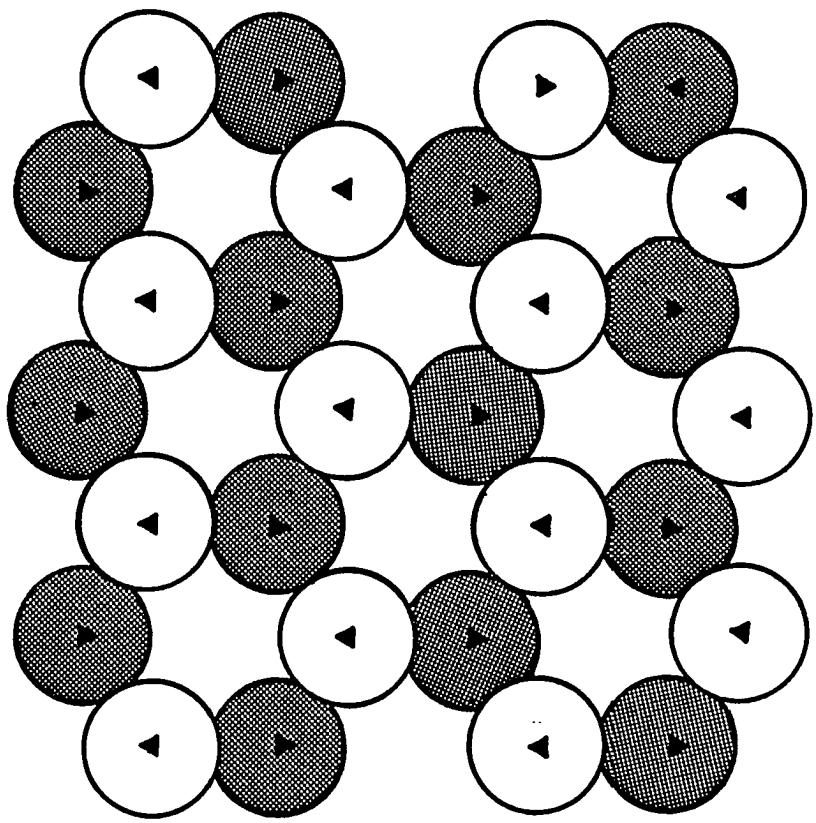

Figure 5-6. Orientation of BChl a-protein trimers in crystals of $P6_3$ symmetry (each circle represents one trimer). Shaded trimers are displaced from unshaded trimers by 49.3 Å perpendicular to the page.

only the lowest energy absorption subband [30,31], not the entire absorption band. This behavior is indicative of very fast transfer to the lowest-energy subband, though not necessarily excitonic interaction. Finally, the overall width of the Q_y absorption band is consistent with interacting dipoles 11 - 14 Å apart [25].

Assuming that all seven BChl a molecules are strongly interacting, it should be possible to calculate the position and intensity of the seven features of the Q_y absorption and CD spectra. Such calculations were performed by Pearlstein and Hemenger [32] using simple exciton theory in the point monopole [33] approximation and more advanced DGS (degenerate ground state) theory [34-36], but with little success. Qualitative agreement with experimental spectra was seen only under the assumption that the lowest energy transition is Q_x rather than Q_y polarized. This assumption is contrary to resonance Raman spectra [37] which support the liganding and hydrogen-bonding assignments from x-ray crystallographic data [30]. A possible reason for such disagreement is that much larger perturbations on the BChl a molecules are present as a consequence of their interaction with the protein. For example, the centroid of the BChl a Q_y band in the protein from P. aestuarii is shifted by 600 cm^{-1} from that in solution [27] as compared to a maximum exciton interaction of 250 cm^{-1}. An understanding of such spectral shifts, which occur in nearly all pigment-protein complexes, would greatly aid theoretical modeling of chlorophyll interactions in vivo.

As stated above, it is believed that trimers of BChl a-protein exist in vivo and mediate energy transfer from the light-harvesting BChl c complex to the reaction center. In such a role, the orientation of the

trimer is crucial in understanding the transfer of energy between different pigment-protein complexes. Olson [38] has suggested that the trimer three-fold axis makes an angle of ~25° with the plane of the cytoplasmic membrane, which would explain the pattern seen in freeze-fracture micrographs [11]. This contrasts with linear dichroism spectra of samples oriented in a pressed gel [39] which indicate that the three-fold axis is approximately perpendicular to the membrane. However, this assignment hinges on the assumption that free trimers exist in the gel; experiments on electric-field oriented samples [40] indicate that small crystallites containing several tens of trimers exist in solution.

Modeling of Energy Transport in BChl a-protein

In spite of the failure of exciton theory to correctly predict the absorption and CD spectra of the BChl a-protein, it is generally accepted that the molecules within a subunit are strongly interacting to form exciton states, but there is no strong interaction between molecules in different subunits. This view of EET in the BChl a-protein (which is essentially the same as Sauer's pebble mosaic model) stems from the fact that the maximum interaction energy calculated for molecules in different subunits is ~27 cm^{-1}, as compared to ~250 cm^{-1} for molecules in the same subunit. Under the conditions of this assumption, light absorption into one of the seven exciton subbands would be followed by rapid internal conversion to the lowest energy exciton state, which could then undergo EET to the same state of a nearby trimer. The rate of transfer would then depend upon the transition dipole moment direction of the lowest-energy

exciton state through the orientation factor κ^2. (Population of higher-energy exciton states is possible, and is governed by the Boltzmann distribution. At room temperature, $kT \approx 209\ cm^{-1}$, and substantial population of higher levels is expected. In this case, the factor κ^2 would be a weighted average of the seven Q_y levels.) In view of the R^{-6} dependence of Förster transport, two types of intersubunit transfer are most likely to occur as shown in Fig. 5-7. The first type is between subunits in the same trimer, such as A → B or C → A, and occur with rate w_{AB}. The second type is between subunits related by the 2_1 screw axis, such as A → D or B → H, which have rate w_{AD}. The ratio of these rates w_{AB}/w_{AD} can vary from zero to infinity depending on the transition dipole moment direction of the lowest exciton state (or states), which is at this point unknown. The purpose of this section is to develop kinetic models to predict the observable time-dependent anisotropy function for arbitrary w_{AB}/w_{AD} using EET domain sizes up to 27 trimers.

Calculation of the time-dependent parallel and perpendicular absorption probabilities $A_{\parallel}(t)$ and $A_{\perp}(t)$ can be divided into two distinct parts: derivation of the time-dependent population of each subunit and the orientation of each subunit with respect to the laser polarization. To provide an example of each of the two contributions, consider first the simplified case where $w_{AD} = 0$ (i.e., the excitation is limited to one trimer). The time-dependent population probabilities A(t), B(t), and C(t) for subunits A, B, and C are then related by the kinetic equations

$$-\frac{dA}{dt} = 2w_{AB}A - w_{AB}B - w_{AB}C$$

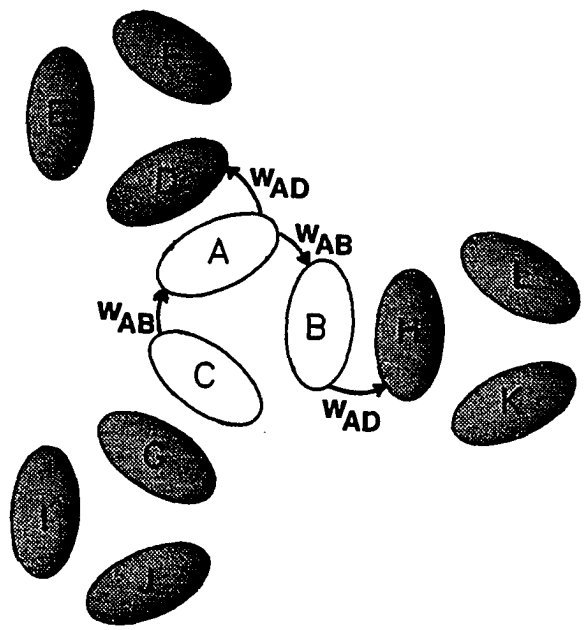

Figure 5-7. Relative orientation of trimers showing transfer types with rates w_{AB} and w_{AD}.

$$-\frac{dB}{dt} = -w_{AB}A + 2w_{AB}B - w_{AB}C \qquad (5.1)$$

$$-\frac{dC}{dt} = -w_{AB}A - w_{AB}B + 2w_{AB}C$$

If we assume that at t=0 subunit A is excited to population A_o then the initial conditions are $A(0) = A_o$, $B(0) = C(0) = 0$. The populations B(t) and C(t) then become equivalent by symmetry and the population A(t) will be given by $A = A_o - 2B$ (for this discussion of EET the isotropic decay will not be considered, as it does not affect derivation of the anisotropic components). Under these conditions each of Eqs. 5.1 reduces to

$$-\frac{dB}{dt} = -w_{AB}(A_o - 3B) \qquad (5.2)$$

This can be rearranged and integrated

$$-\int_0^B \frac{dB'}{3B'-A_o} = \int_0^t w_{AB}dt' \qquad (5.3)$$

which yields

$$B(t) = C(t) = \frac{A_o}{3}\left[1 - \exp(-3w_{AB}t)\right] \qquad (5.4)$$

and therefore

$$A(t) = \frac{A_0}{3}\,[1 + 2\exp(-3w_{AB}t)] \tag{5.5}$$

The contribution of each of these populations to the parallel and perpendicular absorption depends on the orientation of its transition dipole moment $\boldsymbol{\mu}$ with respect to the laser polarization. For light polarized along the laboratory x-axis, the absorption of subunit A is proportional to $(\boldsymbol{\mu}\cdot\mathbf{x})^2 = \mu_{Ax}^2$. Similar factors can be written for subunits B and C and for y-polarization. If we assign the pump polarization as the x-direction and the perpendicular probe polarization as the y-direction, the transient absorption expressions are

$$\begin{aligned} A_{\parallel}(t) &= \mu_{Ax}^4 A(t) + (\mu_{Ax}^2\mu_{Bx}^2 + \mu_{Ax}^2\mu_{Cx}^2)B(t) \\ A_{\perp}(t) &= \mu_{Ax}^2\mu_{Ay}^2 A(t) + (\mu_{Ax}^2\mu_{By}^2 + \mu_{Ax}^2\mu_{Cy}^2)B(t) \end{aligned} \tag{5.6}$$

Recall that subunit A is excited by x-polarized pump light at t=0; therefore each term carries a μ_{Ax}^2 coefficient to account for the probability of this occurrence. Other μ^2 (such as μ_{By}^2) factors correspond to the absorption of probe light. In order for Eqs. 5.6 to be useful, the transition moment projections must be written in terms of the crystallographic a,b,c axes. The three components of the transition moment $\mathbf{r}_A$ in subunit A can be assigned α, β, γ along the a, b, c axes. The transition moments $\mathbf{r}_B$ and $\mathbf{r}_C$ for subunits B and C are then rotations by 120° and 240° about the c-axis:

$$\mathbf{r}_A = \begin{bmatrix} \alpha \\ \beta \\ \gamma \end{bmatrix} = \begin{bmatrix} a_1 \\ b_1 \\ c \end{bmatrix} \tag{5.7a}$$

$$\mathbf{r}_B = \begin{bmatrix} -\alpha/2 - \sqrt{3}\beta/2 \\ \sqrt{3}\alpha/2 - \beta/2 \\ \gamma \end{bmatrix} = \begin{bmatrix} a_2 \\ b_2 \\ c \end{bmatrix} \tag{5.7b}$$

$$\mathbf{r}_C = \begin{bmatrix} -\alpha/2 + \sqrt{3}\beta/2 \\ -\sqrt{3}\alpha/2 - \beta/2 \\ \gamma \end{bmatrix} = \begin{bmatrix} a_3 \\ b_3 \\ c \end{bmatrix} \tag{5.7c}$$

The notation a_i, b_i, c has been introduced for compactness of expressions to appear below; the subscripts 1, 2, 3 will be used to refer to subunits A, B, C. The relationship between the laboratory-fixed x,y,z coordinate system and the crystallite a,b,c axes may be taken into account by the Euler angles [41]. The transformation for the coordinate system $\mathbf{x}'$ to the coordinate system $\mathbf{x}$ can be represented in matrix notation as

$$\mathbf{x} = \boldsymbol{\lambda}\, \mathbf{x}' \tag{5.8}$$

For the current purpose, $\mathbf{x}'$ represents the trimer-fixed a,b,c axes and $\mathbf{x}$ is the laboratory x,y,z frame. The Euler angles ϕ, θ, χ give the rotation of the a,b,c axes with respect to the x,y,z set as shown in Fig. 5-8. With the angles so defined, the transformation matrix $\boldsymbol{\lambda}$ is

$$\boldsymbol{\lambda} = \begin{bmatrix} \cos\phi\cos\chi - \sin\chi\cos\theta\sin\phi & \cos\chi\sin\phi + \sin\chi\cos\theta\cos\phi & \sin\chi\sin\theta \\ -\sin\chi\cos\phi - \cos\chi\cos\theta\sin\phi & -\sin\chi\sin\phi + \cos\chi\cos\theta\cos\phi & \cos\chi\sin\theta \\ \sin\theta\sin\phi & -\sin\theta\cos\phi & \cos\theta \end{bmatrix} \tag{5.9}$$

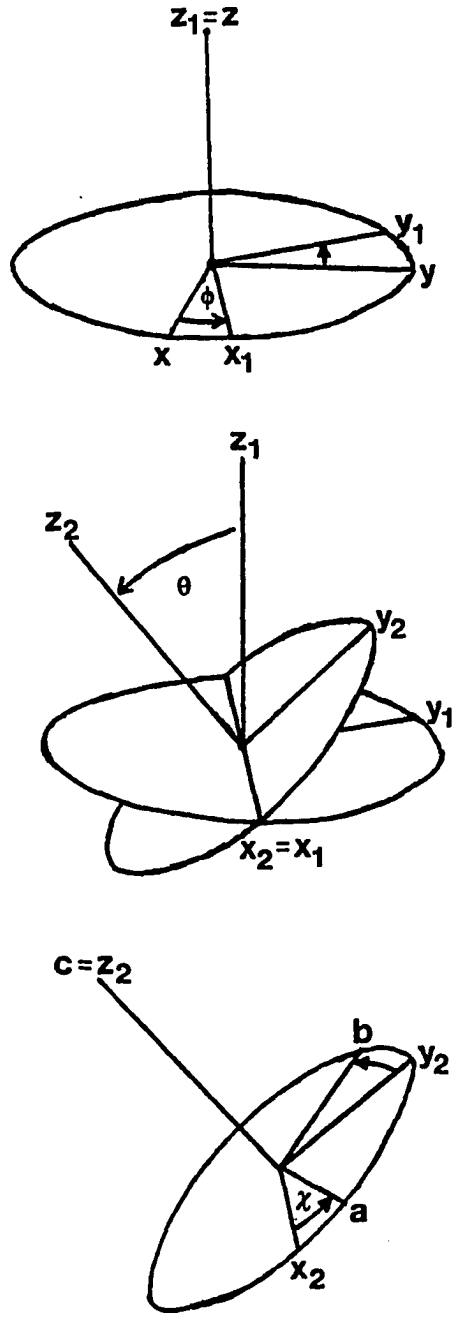

Figure 5-8. Definition of Euler angles θ, ϕ, and χ relating laboratory-fixed x,y,z axes and trimer-fixed a,b,c axes.

Eq. 5.8 can then be used to transform the vectors of Eqs. 5.5 as

$$\begin{aligned} \mu_A &= \lambda \cdot r_A \\ \mu_B &= \lambda \cdot r_B \\ \mu_C &= \lambda \cdot r_C \end{aligned} \tag{5.10}$$

If the λ matrix is denoted as

$$\lambda = \begin{bmatrix} \lambda_{xa} & \lambda_{xb} & \lambda_{xc} \\ \lambda_{ya} & \lambda_{yb} & \lambda_{yc} \\ \lambda_{za} & \lambda_{zb} & \lambda_{zc} \end{bmatrix} \tag{5.11}$$

then using the a_i, b_i, c notation from Eq. 5.7, the first of Eqs. 5.10 can be expanded as

$$\begin{aligned} \mu_{Ax} &= \lambda_{xa}a_1 + \lambda_{xb}b_1 + \lambda_{xc}c_1 \\ \mu_{Ay} &= \lambda_{ya}a_1 + \lambda_{yb}b_1 + \lambda_{yc}c_1 \end{aligned} \tag{5.12}$$

Similar expressions can be written for subunits B and C by changing to subscript 2 and 3, respectively, on the right-hand side of Eq. 5.12. The z-component is not listed since it is not required by Eq. 5.6 (polarization along the z-axis is not detected). Next, terms such as $\mu_{Ax}^2\mu_{Bx}^2$ must be generated from Eq. 5.12 by polynomial multiplication. The expansion of $\mu_{Ax}^2\mu_{Bx}^2$ contains 21 terms

$$\mu_{Ax}^2\mu_{Bx}^2 = \lambda_{xa}^4 a_1^2 a_2^2 + \lambda_{xb}^4 b_1^2 b_2^2 + \lambda_{xc}^4 c^4 + 2\lambda_{xa}^2\lambda_{xb}^2 a_1 a_2 b_1 b_2 + 2\lambda_{xa}^2\lambda_{xb}^2 (a_1 b_2 + a_2 b_1)^2$$
$$+ \lambda_{xa}^2\lambda_{xc}^2 c^2 (a_1+a_2)^2 + 2\lambda_{xa}^2\lambda_{xc}^2 c^2 a_1 a_2 + \lambda_{xb}^2\lambda_{xc}^2 c^2 (b_1+b_2)^2$$
$$+ 2\lambda_{xb}^2\lambda_{xc}^2 c^2 b_1 b_2 + \lambda_{xa}^3\lambda_{xb} a_1 a_2 (a_1 b_2 + a_2 b_1) + 2\lambda_{xa}^3\lambda_{xc} c a_1 a_2 (a_1+a_2)$$
$$+ 2\lambda_{xb}^3\lambda_{xc} c b_1 b_2 (b_1+b_2) + 2\lambda_{xa}^2\lambda_{xb}\lambda_{xc} c (a_1+a_2)(a_1 b_2 + a_2 b_1)$$
$$+ 2\lambda_{xa}^2\lambda_{xb}\lambda_{xc} c a_1 a_2 (b_1+b_2) + 2\lambda_{xa}\lambda_{xc}^3 c^3 (a_1+a_2)$$
$$+ 2\lambda_{xa}\lambda_{xb}^3 b_1 b_2 (a_1 b_2 + a_2 b_1) + 2\lambda_{xa}\lambda_{xb}\lambda_{xc}^2 c^2 (a_1+a_2)(b_1+b_2)$$
$$+ 2\lambda_{xa}\lambda_{xb}^2\lambda_{xc} c b_1 b_2 (a_1+a_2) + 2\lambda_{xa}\lambda_{xb}^2\lambda_{xc} c (b_1+b_2)(a_1 b_2 + a_2 b_1)$$
$$+ 2\lambda_{xa}\lambda_{xb}\lambda_{xc}^2 c^2 (a_1 b_2 + a_2 b_1) + 2\lambda_{xb}\lambda_{xc}^3 c^3 (b_1+b_2) \qquad (5.13)$$

To account for the random orientation of BChl a-protein crystallites in solution, Eq. 5.13 (as well as each of the other orientational coefficients) must be integrated over all possible Euler angles ϕ, θ, χ. For example, the first term of Eq. 5.13 gives

$$\langle\lambda_{xa}^4\rangle = \int_0^{\pi}\int_0^{2\pi}\int_0^{2\pi} \lambda_{xa}^4 \sin\theta \, d\theta \, d\phi \, d\chi \qquad (5.14)$$

$$\langle\lambda_{xa}^4\rangle = \int_0^{\pi}\int_0^{2\pi}\int_0^{2\pi} (\cos\theta\cos\chi - \sin\chi\cos\theta\sin\phi)^4 \sin\theta \, d\theta \, d\phi \, d\chi$$

$$\langle\lambda_{xa}^4\rangle = 1/5$$

Here, the angle brackets indicate a quantity averaged over all possible orientations. This integration must be repeated for the remaining 20 terms of Eq. 5.13; fortunately, the last 12 terms (all those containing

odd powers) integrate to zero. The first 9 terms are non-zero when integrated and yield the results

$$\langle \lambda_{xa}^4 \rangle = \langle \lambda_{xb}^4 \rangle = \langle \lambda_{xc}^4 \rangle = \frac{1}{5} \tag{5.15a}$$

$$\langle \lambda_{xa}^2 \lambda_{xb}^2 \rangle = \langle \lambda_{xa}^2 \lambda_{xc}^2 \rangle = \langle \lambda_{xb}^2 \lambda_{xc}^2 \rangle = \frac{1}{15} \tag{5.15b}$$

Equation 5.13 therefore reduces to

$$\langle \mu_{Ax}^2 \mu_{Ay}^2 \rangle = \frac{1}{5}[a_1^2 a_2^2 + b_1^2 b_2^2 + c^4] + \frac{1}{15}[(a_1 b_2 + a_2 b_1)^2 + 2(a_1 a_2 b_1 b_2) + 2c^2 a_1 a_2 + c^2 (b_1 + b_2)^2 + 2c^2 b_1 b_2 + c^2 (a_1 + a_2)^2] \tag{5.16}$$

Each of the a_i, b_i, c in Eq. 5.16 are then replaced by their definition in terms of α, β, γ as given in Eq. 5.7. When simplified, this gives

$$\langle \mu_{Ax}^2 \mu_{Bx}^2 \rangle = \frac{1}{10}[(\alpha^2 + \beta^2)^2 + 2\gamma^4] \tag{5.17}$$

The subscript 2 in Eq. 5.16 can be replaced by a 1 and a 3 to yield μ_{Ax}^4 and $\mu_{Ax}^2 \mu_{Cx}^2$ (recall the numbering scheme introduced in Eq. 5.7). These are expanded in terms of α, β, γ as above to give

$$\begin{aligned} \langle \mu_{Ax}^4 \rangle &= \frac{1}{5}(\alpha^2 + \beta^2 + \gamma^2)^2 \\ \langle \mu_{Ax}^2 \mu_{Cx}^2 \rangle &= \frac{1}{10}[(\alpha^2 + \beta^2)^2 + 2\gamma^2] \end{aligned} \tag{5.18}$$

Since the oscillator strength of each subunit is identical (by symmetry), the transition dipole moments may be written as unit vectors, i.e., $\alpha^2 + \beta^2 + \gamma^2 = 1$. Then, using $\alpha^2 + \beta^2 = 1 - \gamma^2$, the dipole moment projections of Eqs. 5.18 become

$$\langle \mu_{Ax}^4 \rangle = \frac{1}{5}$$

$$\langle \mu_{Ax}^2 \mu_{Bx}^2 \rangle = \langle \mu_{Ax}^2 \mu_{Cx}^2 \rangle = \frac{1}{10}(1 - 2\gamma^2 + 3\gamma^4) \tag{5.19}$$

Eq. 5.19, along with the time-dependent population probabilities of Eqs. 5.4 and 5.5, can be substituted into Eq. 5.6 to give the transient absorption expected for parallel pump and probe polarization

$$A_{||}(t) = \frac{A_0}{15}\left[(1 + 2\exp(-3w_{AB}t) + (1-2\gamma^2+3\gamma^4)(1 - \exp(-3w_{AB}t))\right] \tag{5.20}$$

or

$$A_{||}(t) = \frac{A_0}{15}\left[(2-2\gamma^2+3\gamma^4) + (1+2\gamma^2-3\gamma^4)\exp(-3w_{AB}t)\right] \tag{5.21}$$

The time-dependent transient absorption for perpendicular pump and probe polarization can be calculated in a manner exactly analogous to the parallel contribution. The counterpart of Eq. 5.13, the expansion of $\mu_{Ax}^2 \mu_{By}^2$, contains 46 terms since no collection of terms is possible. Twelve of these terms are non-zero when integrated over all possible ϕ, θ, and χ; their coefficients are

$$\langle \lambda_{xa}^2 \lambda_{ya}^2 \rangle = \langle \lambda_{xb}^2 \lambda_{yb}^2 \rangle = \langle \lambda_{xc}^2 \lambda_{yc}^2 \rangle = \frac{1}{15} \tag{5.22}$$

$$\langle \lambda_{xa}^2 \lambda_{yb}^2 \rangle = \langle \lambda_{xa}^2 \lambda_{yc}^2 \rangle = \langle \lambda_{ya}^2 \lambda_{xb}^2 \rangle$$
$$= \langle \lambda_{xb}^2 \lambda_{yc}^2 \rangle = \langle \lambda_{ya}^2 \lambda_{xc}^2 \rangle = \langle \lambda_{yb}^2 \lambda_{xc}^2 \rangle = \frac{2}{15} \tag{5.23}$$

$$\langle \lambda_{xc} \lambda_{yc} \lambda_{xb} \lambda_{yb} \rangle = \langle \lambda_{xc} \lambda_{yc} \lambda_{xa} \lambda_{ya} \rangle = \langle \lambda_{xa} \lambda_{ya} \lambda_{xb} \lambda_{yb} \rangle = -\frac{1}{30} \tag{5.24}$$

These reduce the 46-term expansion to

$$\langle \mu_{Ax}^2 \mu_{By}^2 \rangle = \frac{1}{15}\Big[a_1^2 a_2^2 + b_1^2 b_2^2 + c^4 - 2c^2(a_1 a_2 + b_1 b_2) - 2a_1 a_2 b_1 b_2 +$$
$$2(a_1^2 b_2^2 + a_2^2 b_1^2) + 2c^2(a_1^2 + a_2^2 + b_1^2 + b_2^2)\Big] \tag{5.25}$$

This can be expressed in terms of α, β, γ from Eq. 5.7 as before to give

$$\langle \mu_{Ax}^2 \mu_{By}^2 \rangle = \frac{1}{30}\left[\frac{7}{2} + 3\gamma^2 - \frac{9}{2}\gamma^4 \right] \tag{5.26}$$

using $\alpha^2 + \beta^2 + \gamma^2 = 1$. Replacement of subscript 2 in Eq. 5.25 by 1 and 3 gives $\langle \mu_{Ax}^2 \mu_{Ay}^2 \rangle$ and $\langle \mu_{Ax}^2 \mu_{Cy}^2 \rangle$, respectively

$$\langle \mu_{Ax}^2 \mu_{Ay}^2 \rangle = \frac{1}{15}$$
$$\tag{5.27}$$
$$\langle \mu_{Ax}^2 \mu_{Cy}^2 \rangle = \frac{1}{15}\left[\frac{7}{2} + 3\gamma^2 - \frac{9}{2}\gamma^4 \right]$$

These relations along with the population probabilities A(t), B(t) are inserted into the $A_\perp(t)$ expression in Eq. 5.6 to give

$$A_\perp(t) = \frac{A_o}{45}[1 + 2\exp(-3w_{AB}t) + (\frac{7}{2} + 3\gamma^2 - \frac{9}{2}\gamma^4)(1 - \exp(-3w_{AB}t))]$$

$$= \frac{A_o}{45}[(\frac{9}{2} + 3\gamma^2 - \frac{9}{2}\gamma^4) + (-\frac{3}{2} - 3\gamma^2 + \frac{9}{2}\gamma^4)\exp(-3w_{AB}t)] \qquad (5.28)$$

Both of Eqs. 5.21 and 5.28, the expressions for $A_\parallel(t)$ and $A_\perp(t)$, have a time-dependent term and a time-independent term, and are of the same form as Eqs. 1.33 if $P(t) = A_o/3$ (recall that the isotropic decay has been excluded). Also, the quantity $2A_\parallel + A_\perp$ is a constant (independent of both t and γ) showing that the magic angle of 54.7° is valid for this system. As expected, the time dependence disappears for $\gamma = 1$; in this limit the transition dipoles of subunits A, B, and C are parallel and no depolarization will be observed. With the anisotropy defined as $2.5(A_\parallel - A_\perp)/(2A_\perp + A_\parallel)$, the residual anisotropy $\underline{a}$ as $t \to \infty$ can be written in terms of γ as

$$a = \frac{1}{4}(3\gamma^2 - 1)^2 \qquad (5.29)$$

In general, the anisotropy (see Eqs. 1.33) can be written in the form of

$$G^s(t) = (1-a)\exp(-t/\tau) + a \qquad (5.30)$$

where $\underline{a}$ is defined as above and $\tau = (3w_{AB})^{-1}$.

It is now desirable to expand the calculation to the more general case $w_{AD} \neq 0$. In order to write kinetic equations, a finite domain size of EET must now be assumed. Consider first two trimers ABC and DEF arranged as in Fig. 5-7. If A is again the initially excited subunit ($A(0) = A_o$, all other terms initialized to zero), symmetry demands that $B(t) = C(t)$ and $E(t) = F(t)$. There are then four unique populations $A(t)$, $B(t)$, $D(t)$, and $E(t)$ which are linked by the set of differential equations

$$-\frac{dA}{dt} = 2w_{AB}A - 2w_{AB}B + w_{AD}A - w_{AD}D \tag{5.31a}$$

$$-\frac{dB}{dt} = -w_{AB}A + w_{AB}B \tag{5.31b}$$

$$-\frac{dD}{dt} = -w_{AD}A + 2w_{AB}D + w_{AD}D - 2w_{AB}E \tag{5.31c}$$

$$-\frac{dE}{dt} = -w_{AB}D + w_{AB}E \tag{5.31d}$$

Unlike the single-trimer calculation these cannot be reduced to a single variable in a single differential equation. It is then advantageous to take the Laplace transform of each of Eqs. 5.31, which gives

$$-s\mathbf{A} + A_o = (2w_{AB} + w_{AD})\mathbf{A} - 2w_{AB}\mathbf{B} - w_{AD}\mathbf{D} \tag{5.32a}$$

$$-s\mathbf{B} = -w_{AB}\mathbf{A} + w_{AB}\mathbf{B} \tag{5.32b}$$

$$-s\mathbf{D} = -w_{AD}\mathbf{A} + (2w_{AB} + w_{AD})\mathbf{D} - 2w_{AB}\mathbf{E} \tag{5.32c}$$

$$-s\mathbf{E} = -w_{AB}\mathbf{D} + w_{AB}\mathbf{E} \tag{5.32d}$$

where s is the Laplace transform variable and bold type denotes a transformed function. This set of linear equations can be rewritten in

matrix form as

$$\begin{bmatrix} A_o \\ 0 \\ 0 \\ 0 \end{bmatrix} = \begin{bmatrix} 2w_{AB}+w_{AD}+s & -2w_{AB} & -w_{AD} & 0 \\ -w_{AB} & w_{AB}+s & 0 & 0 \\ -w_{AD} & 0 & 2w_{AB}+w_{AD}+s & -2w_{AB} \\ 0 & 0 & -w_{AB} & -w_{AB}+s \end{bmatrix} \begin{bmatrix} A \\ B \\ D \\ E \end{bmatrix} \tag{5.33}$$

Since this matrix equation is of the form

$$\mathbf{b} = \mathbf{M}\,\mathbf{x} \tag{5.34}$$

the solution is obtained by inverting the 4x4 matrix

$$\mathbf{x} = \mathbf{M}^{-1}\mathbf{b} \tag{5.35}$$

Because only one term of **b** is nonzero, the multiplication is simple

$$\begin{aligned} A &= (M^{-1})_{11}\, A_o \\ B &= (M^{-1})_{12}\, A_o \\ D &= (M^{-1})_{13}\, A_o \\ E &= (M^{-1})_{14}\, A_o \end{aligned} \tag{5.36}$$

In practice, a value of t (and therefore s) was chosen, the matrix inverted numerically by Gauss-Jordan method, and the inverse Laplace transforms taken using the Stehfest algorithm [42]. The four population probabilities A(t), B(t), D(t), E(t) were traced as a function of time by

choosing successive values of t.

With the population probabilities (numerically) known, the orientational factors must be calculated. With six subunits now involved, the transient absorption expressions become

$$A_{\parallel}(t) = \langle\mu_{Ax}^4\rangle A(t) + \langle\mu_{Ax}^2\mu_{Bx}^2 + \mu_{Ax}^2\mu_{Cx}^2\rangle B(t) + \langle\mu_{Ax}^2\mu_{Dx}^2\rangle D(t) + \langle\mu_{Ax}^2\mu_{Ex}^2 + \mu_{Ax}^2\mu_{Fx}^2\rangle E(t) \quad (5.37a)$$

$$A_{\perp}(t) = \langle\mu_{Ax}^2\mu_{Ay}^2\rangle A(t) + \langle\mu_{Ax}^2\mu_{By}^2 + \mu_{Ax}^2\mu_{Cy}^2\rangle B(t) + \langle\mu_{Ax}^2\mu_{Dy}^2\rangle D(t) + \langle\mu_{Ax}^2\mu_{Ey}^2 + \mu_{Ax}^2\mu_{Fy}^2\rangle E(t) \quad (5.37b)$$

The terms $\langle\mu_{Ax}^4\rangle$, $\langle\mu_{Ax}^2\mu_{Bx}^2 + \mu_{Ax}^2\mu s_{Cx}^2\rangle$, $\langle\mu_{Ax}^2\mu_{Ay}^2\rangle$, and $\langle\mu_{Ax}^2\mu_{By}^2 + \mu_{Ax}^2\mu_{Cy}^2\rangle$ are the same as given earlier (Eqs. 5.19, 5.22, 5.23, 5.24); the others must now be determined. Since subunits A, B, C are related to subunits D, E, F by 180° rotation about the c-axis, the transition moment directions are given by

$$\mathbf{r}_D = \begin{bmatrix} -\alpha \\ -\beta \\ \gamma \end{bmatrix} = \begin{bmatrix} a_4 \\ b_4 \\ c \end{bmatrix} \quad (5.38a)$$

$$\mathbf{r}_E = \begin{bmatrix} \alpha/2 + \sqrt{3}\beta/2 \\ -\sqrt{3}\alpha/2 + \beta/2 \\ \gamma \end{bmatrix} = \begin{bmatrix} a_5 \\ b_5 \\ c \end{bmatrix} \quad (5.38b)$$

$$\mathbf{r}_F = \begin{bmatrix} \alpha/2 - \sqrt{3}\beta/2 \\ \sqrt{3}\alpha/2 + \beta/2 \\ \gamma \end{bmatrix} = \begin{bmatrix} a_6 \\ b_6 \\ c \end{bmatrix} \quad (5.38c)$$

The rotational averaging is performed exactly as before; for example, $\langle \mu_{Ax}^2 \mu_{Dy}^2 \rangle$ is generated from Eq. 5.16 by replacing subscript 2 with subscript 4, then replacing a_i, b_i, and c with their α, β, γ expressions and simplifying. This is repeated for subunits E and F with the result

$$\langle \mu_{Ax}^2 \mu_{Dx}^2 \rangle = \frac{1}{15}(3 - 8\gamma^2 + 8\gamma^4) \tag{5.39a}$$

$$\langle \mu_{Ax}^2 \mu_{Ex}^2 \rangle = \langle \mu_{Ax}^2 \mu_{Fx}^2 \rangle = \frac{1}{30}(3 + 2\gamma^2 + \gamma^4) \tag{5.39b}$$

The process is identical for y-polarization probe light using Eq. 5.25, giving the expressions

$$\langle \mu_{Ax}^2 \mu_{Dy}^2 \rangle = \frac{1}{15}(1 + 4\gamma^2 - 4\gamma^4) \tag{5.40a}$$

$$\langle \mu_{Ax}^2 \mu_{Ey}^2 \rangle = \langle \mu_{Ax}^2 \mu_{Fy}^2 \rangle = \frac{1}{30}\left(\frac{7}{2} - \gamma^2 - \frac{1}{2}\gamma^4\right) \tag{5.40b}$$

These expressions are then combined with the time-dependent populations as in Eq. 5.37 and the transient absorptions $A_{\parallel}$ and $A_{\perp}$ are calculated for a given value of t and γ. Fig. 5-9 shows the effect of including A → D transfer in the calculation by plotting $A_{\parallel}(t)$ and $A_{\perp}(t)$ for $w_{AB} = 1$, $w_{AD} = 0$ (one-trimer calculation) and $w_{AB} = w_{AD} = 1$ (two trimers) for $\gamma = 0.9$. Note that the convergence is faster for the latter case since there are three pathways for the depopulation of subunit A (A→B, A→C, A→D) as compared to two pathways when $w_{AD} = 0$ (A→B, A→C).

In principle, the method used for the two-trimer calculation could be extended to arbitrary EET domain sizes for BChl a-protein crystallites.

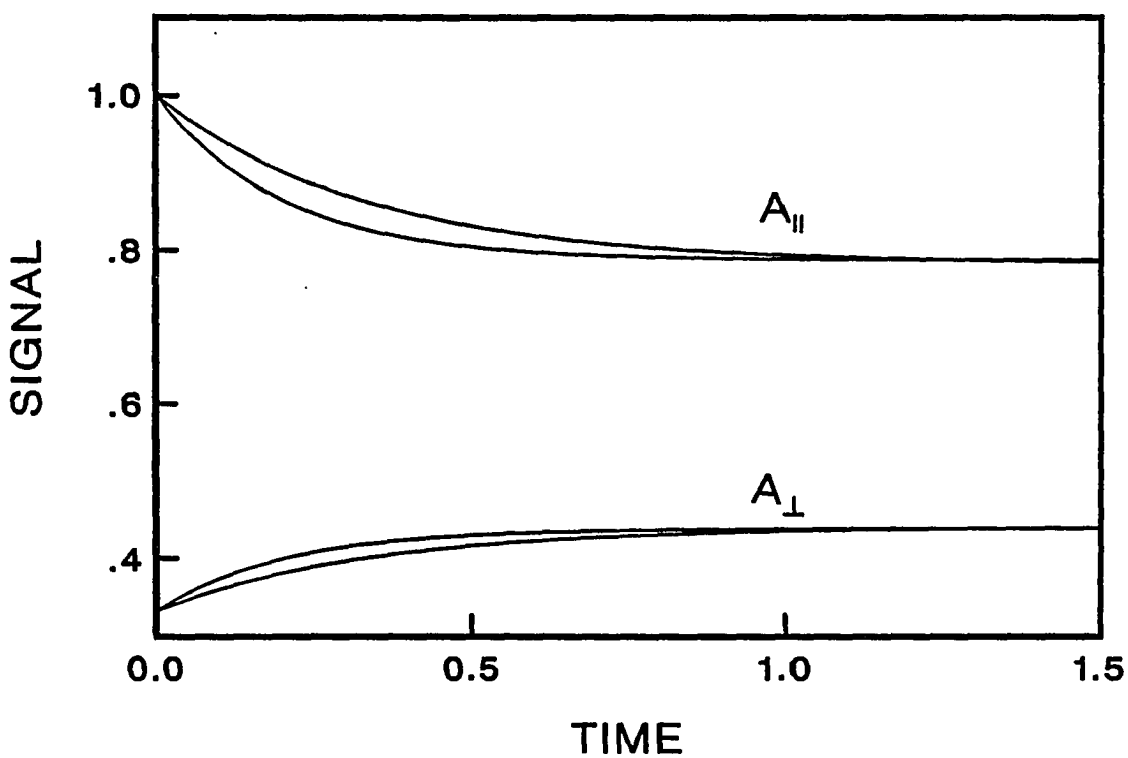

Figure 5-9. Plot of $A_{\parallel}(t)$ and $A_{\perp}(t)$ vs. time showing the effect of including A → D transport in calculations. The slower curves are for $w_{AB} = 1$, $w_{AD} = 0$; faster depolarization is seen when $w_{AB} = w_{AD} = 1$.

In practice, the domain size is limited only by available computer time to perform the matrix inversion and inverse Laplace transform for large numbers of variables. Increasing the domain size is relatively simple because there are only six unique subunit orientations in the BChl a-protein crystal, so no additional orientational terms need be calculated.

For solutions containing crystallites of BChl a-protein, the two-trimer calculation, although useful for demonstration, is arguably invalid. This is because subunits A and D lie along a 2_1 screw axis; therefore, subunit A is equidistant from two subunits which could be designated D, one 49.8 Å above the plane of the ABC trimer (along the c-axis) and one 49.8 Å below the plane. Rather than considering two trimers, then, three should be included. The subunits of these trimers are labelled ABC, $D_1E_1F_1$, and $D_2E_2F_2$. Subunits sharing the same letter are related by translation by 1 unit cell (98.6 Å) along the c-axis. In this three-trimer model, subunits (D_1,D_2) and (E_1, E_2, F_1, F_2) are equivalent by symmetry, so no additional variables for population probability are required. The modification of the kinetic equations result in the new Laplace transform matrix equation

$$\begin{bmatrix} A_o \\ 0 \\ 0 \\ 0 \end{bmatrix} = \begin{bmatrix} 2w_{AB}+2w_{AD}+s & -2w_{AB} & -2w_{AD} & 0 \\ -w_{AB} & w_{AB}+s & 0 & 0 \\ -w_{AD} & 0 & 2w_{AB}+w_{AD}+s & -2w_{AB} \\ 0 & 0 & -w_{AB} & -w_{AB}+s \end{bmatrix} \begin{bmatrix} \mathbf{A} \\ \mathbf{B} \\ \mathbf{D} \\ \mathbf{E} \end{bmatrix} \qquad (5.41)$$

which is solved numerically as before, and populations obtained through inverse Laplace transformation.

Other models considered include domain sizes of 7 trimers and 27

trimers. Included in the 7-trimer calculation were subunits A-L in Fig. 5-10 (enclosed by a dashed line) and two "levels" for subunits D-L, which are shaded. If subunit A is initially excited, by symmetry the time-dependent populations must follow

$$B = C$$

$$D_1 = D_2$$

$$E_1 = E_2 = F_1 = F_2$$

$$G_1 = G_2 = H_1 = H_2$$

$$I_1 = I_2 = J_1 = J_2 = K_1 = K_2 = L_1 = L_2$$

There are therefore six independent populations, A, B, D, E, G, and I, and the Laplace transform matrix equation will be

$$\begin{bmatrix} A_o \\ 0 \\ 0 \\ 0 \\ 0 \\ 0 \end{bmatrix} = \begin{bmatrix} 2w_{AB}+2w_{AD}+s & -2w_{AB} & -2w_{AD} & 0 & 0 & 0 \\ -w_{AB} & w_{AB}+2w_{AD}+s & 0 & 0 & -2w_{AD} & 0 \\ -w_{AD} & 0 & 2w_{AB}+w_{AD}+s & -2w_{AB} & 0 & 0 \\ 0 & 0 & -w_{AB} & w_{AB}+s & 0 & 0 \\ 0 & -w_{AD} & 0 & 0 & 2w_{AB}+w_{AD}+s & -2w_{AB} \\ 0 & 0 & 0 & 0 & -w_{AB} & w_{AB}+s \end{bmatrix} \begin{bmatrix} A \\ B \\ D \\ E \\ G \\ I \end{bmatrix} \tag{5.43}$$

As mentioned above, only six distinct orientations exist in BChl a-protein crystals. In the 7-trimer model, the following sets of trimers share the same orientation: (D_1, D_2, K_1, K_2, J_1, J_2); (G_1, G_2, F_1, F_2, L_1, L_2); and (H_1, H_2, E_1, E_2, I_1, I_2). Then, knowing the population and orientation of each subunit the transient absorption probabilities are calculated numerically with an expression analogous to Eq. 5.37.

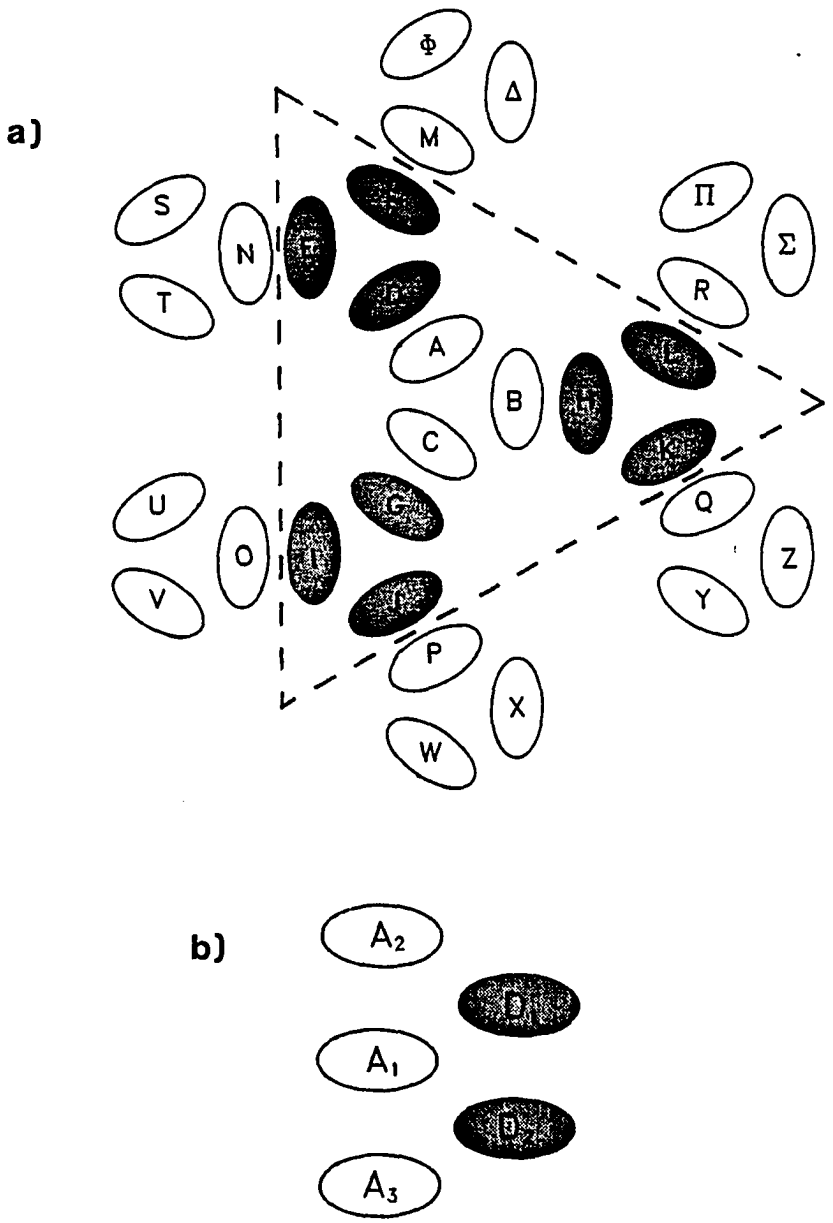

Figure 5-10. Schematic of crystalline aggregate of BChl a-protein trimers showing lettering scheme used in multiple trimer calculations. a) View down along c axis; shaded subunits are displaced by ±49.6 Å along the c axis. b) View perpendicular to the c axis of A and D subunits only, showing numbering according to c axis displacement.

The 27-trimer model includes each of the subunits pictured in Fig. 5-10, with 2 levels of shaded subunits and 3 levels of unshaded subunits considered. The subscript numbering assignment is shown in Fig. 5-10b. The 81 subunits reduce to 16 variables based on the following equivalences from the crystal symmetry

$$A_1$$

$$B_1 = C_1$$

$$A_2 = A_3$$

$$B_2 = B_3 = C_2 = C_3$$

$$D_1 = D_2$$

$$E_1 = E_2 = F_1 = F_2$$

$$G_1 = G_2 = H_1 = H_2$$

$$I_1 = I_2 = J_1 = J_2 = K_1 = K_2 = L_1 = L_2$$

$$N_1 = N_2$$

$$O_1 = P_1 = Q_1 = R_1$$

$$M_2 = N_2 = M_3 = N_3$$

$$O_2 = O_3 = P_2 = P_3 = Q_2 = Q_3 = R_2 = R_3$$

$$S_1 = T_1 = \Delta_1 = \Phi_1$$

$$U_1 = V_1 = W_1 = X_1 = Y_1 = Z_1 = \Sigma_1 = \Pi_1$$

$$S_2 = T_2 = \Delta_2 = \Phi_2 = S_3 = T_3 = \Delta_3 = \Phi_3$$

$$U_2 = V_2 = W_2 = X_2 = Y_2 = Z_2 = \Sigma_2 = \Pi_2$$
$$= U_3 = V_3 = W_3 = X_3 = Y_3 = Z_3 = \Sigma_3 = \Pi_3$$

If we assume that subunit A_1 is initially excited then the 16 independent variables (listed on the far left of the preceding equations) are linked

by the Laplace transformed differential equations

$$-sA_1 + A_o = (2w_{AB} + 2w_{AD})A_1 - 2w_{AB}B_1 - 2w_{AD}D_1 \quad (5.44a)$$

$$-sB_1 = -w_{AB}A_1 + (w_{AB} + 2w_{AD})B_1 - 2w_{AD}G_1 \quad (5.44b)$$

$$-sA_2 = -2w_{AB}B_2 + (2w_{AB} + w_{AD})A_2 - w_{AD}D_1 \quad (5.44c)$$

$$-sB_2 = -w_{AB}A_2 + (w_{AB} + w_{AD})B_2 - w_{AD}G_1 \quad (5.44d)$$

$$-sD_1 = -w_{AD}A_1 - w_{AD}A_2 + (2w_{AB} + 2w_{AD})D_1 - 2w_{AB}E_1 \quad (5.44e)$$

$$-sE_1 = -w_{AB}D_1 + (w_{AB} + 2w_{AD})E_1 - w_{AD}N_1 - w_{AD}N_2 \quad (5.44f)$$

$$-sG_1 = -w_{AD}B_1 - w_{AD}B_2 + (2w_{AB} + 2w_{AD})G_1 - 2w_{AB}I_1 \quad (5.44g)$$

$$-sI_1 = -w_{AB}G_1 + (w_{AB} + 2w_{AD})I_1 - w_{AD}O_1 - w_{AD}O_2 \quad (5.44h)$$

$$-sN_1 = -2w_{AD}E_1 + (2w_{AB} + 2w_{AD})N_1 - 2w_{AB}S_1 \quad (5.44i)$$

$$-sO_1 = -2w_{AD}I_1 + (2w_{AB} + 2w_{AD})O_1 - 2w_{AB}U_1 \quad (5.44j)$$

$$-sN_2 = -w_{AD}E_1 + (2w_{AB} + w_{AD})N_2 - 2w_{AB}S_2 \quad (5.44k)$$

$$-sO_2 = -w_{AD}I_1 + (2w_{AB} + w_{AD})O_2 - 2w_{AB}U_2 \quad (5.44l)$$

$$-sS_1 = -w_{AB}N_1 + w_{AB}S_1 \quad (5.44m)$$

$$-sU_1 = -w_{AB}O_1 + w_{AB}U_1 \quad (5.44n)$$

$$-sS_2 = -w_{AB}N_2 + w_{AB}S_2 \quad (5.44o)$$

$$-sU_2 = -w_{AB}O_2 + w_{AB}U_2 \quad (5.44p)$$

The 16x16 matrix is then formed from these equations in a manner exactly analogous to that for the 2-trimer model discussed above. Due to restrictions of space, it is not written explicitly here. The corresponding population as a function of time is then obtained using matrix inversion and inverse Laplace transforms exactly as before.

Again, many trimers share the same orientation. Table I shows the grouping according to orientation along with orientational terms for each

Table I. Orientational grouping for 27-trimer calculation

Group	$\langle\mu_{Ax}^2\mu_{?x}^2\rangle$	$\langle\mu_{Ax}^2\mu_{?x}^2\rangle$	Subunits	i
1	1/5	1/15	$A_i, P_i, Q_i, S_i, U_i, \Phi_i, \Pi_i$	1,2,3
2	$(1-2\gamma^2+3\gamma^4)/10$	$(7+6\gamma^2-9\gamma^4)/60$	$B_i, C_i, N_i, M_i, O_i, R_i, T_i, V_i, W_i, X_i, Y_i, Z_i, \Delta_i, \Sigma_i$	1,2,3
3	$(3-8\gamma^2+8\gamma^4)/15$	$(1+4\gamma^2-4\gamma^4)/15$	D_i, J_i, K_i	1,2
4	$(3+2\gamma^2+\gamma^4)/10$	$(7-2\gamma^2-\gamma^4)/60$	$E_i, F_i, G_i, H_i, I_i, L_i$	1,2

group for parallel ($\langle \mu_{Ax}^2 \mu_{?x}^2 \rangle$) and perpendicular ($\langle \mu_{Ax}^2 \mu_{?y}^2 \rangle$) polarizations. Note that although there are six unique orientations in the BChl a-protein crystal, there are only 4 orientational groups. This is because subunit pairs such as B,C and E,F share the same orientational terms although they are differently oriented (see Eqs. 5.19 and 5.40b).

Literature Review of Photosystem I

The introduction in Chapter I outlined briefly the experiments of Emerson and Arnold, in which they deduced that ~2400 Chl molecules interact in the evolution of one molecule of O_2. In order to relate this result to the size of the photosynthetic unit, it was necessary to determine the minimum number of photons required to produce a molecule of O_2. The basic reaction of photosynthesis, $H_2O + CO_2 \rightarrow (CH_2O) + O_2$, is a 4-electron exchange; the discovery that there are two photosystems which act in series [43] makes oxygen evolution an 8-photon event. This implies an overall size of ~300 Chl for the photosynthetic unit of green plants and algae.

Green plants and algae differ from photosynthetic bacteria in that they contain two different types of reaction centers (one in each photosystem), as well as in their ability to produce oxygen. The two photosystems, designated photosystem (PS) I and PS II, act in series through a complex set of electron and hydrogen carriers. PS II uses excitation energy from light absorption to produce a strong oxidant which is able to split electrons from water, while PS I generates a strong reductant which is eventually used to reduce CO_2. Each photosystem is

associated with its own set of antenna, and they are in general located in different areas of the chloroplast; PS I is associated with the stroma lamellae region, while PS II is located in the stacked granal region.

Several groups have studied the excitation dynamics in whole chloroplasts [44-50] by time-resolved fluorescence techniques. The excitation decay in all cases is highly nonexponential and faster than in monomeric Chl due to trapping at reaction centers. The experimental fluorescence decay is fit to a sum of exponentials with each component assigned to PS I or PS II. Due to the complexity of the photosynthetic apparatus, this procedure has a considerable margin of error. One of the major problems is that it is difficult to experimentally resolve multiple component decays in which the lifetimes are of the same order of magnitude [51], even with the high data quality available with single photon counting. The shape of the decay could also be affected by "spillover", where excess excitation energy in PS II antenna can be transferred to PS I [49,52]. In order to improve the ability to resolve complex decays, some groups have used global fitting techniques, in which a series of fluorescence decays collected at various emission wavelengths are fit simultaneously [49]. The assumption is that the observed lifetimes are independent of emission wavelength; only the pre-exponential factors change. In effect, this constitutes a mapping of the fluorescence intensity in a two-dimensional time-wavelength space. A related technique is the collection of time-resolved fluorescence spectra [46]. With this method, one is able to follow the appearance or disappearance of different fluorescence bands, and therefore the transfer of excitation energy between pigments responsible for each band.

It is also common to measure fluorescence parameters with the sample at low (cryogenic) temperatures. This has the effect of sharpening absorption and fluorescence bands and (sometimes) of slowing the rate of EET. The latter effect can be explained on the basis of the spectral overlap integral in Eq. 1.27; if the spectral bands are sharpened, then the overlap would be expected to decrease. An exception could be the situation of downhill transfer; this process requires only the emission of a phonon, and could be independent of temperature. A detailed experimental investigation of the temperature dependence of EET between molecules relevant to photosynthetic antennae has not been undertaken.

Each of the above techniques are useful in obtaining data on excitation dynamics in chloroplasts, but assignment of each component of the complex decay to PS I or PS II remains as a major problem. Toward that end, it is desireable to measure the fluorescence decay of the two photosystems separately. (This is particularly true in the case of PS I, since the quantum yield of fluorescence in PS II is much higher [53].) However, the thylakoid proteins are highly hydrophobic, which makes extraction difficult and the extraction conditions rather harsh. Major Chl complexes separated from the thylakoid with various detergent solutions fall into three major groups: 1) Chl-protein complexes containing the PS I reaction center and associated antenna, 2) Chl-protein complexes containing PS II reaction center and its antenna, and 3) light-harvesting chlorophyll (LHC) protein complexes with molar ratios of Chl a/Chl b of ~3.

Photosystem I complexes isolated by varying techniques have yielded a wide array of different preparations; the most common of these have been

summarized by Dunahay and Staehelin [54]. Many of the complexes differ only in the presence or absence of polypeptides in the 8-25 kD range which do not bind Chl and are likely associated with secondary electron acceptors; all photosystem I preparations contain P700, the primary electron donor of PS I. Depending on the separation method, complexes can be isolated with various antenna sizes as measured by the total number of Chl per P700. The "native" PS I particle has often been considered as containing ~110 Chl/P700 [55], with about half the Chl contained in LHC Ia (~23-24 kD) and LHC Ib (~20-21 kD) proteins, which have the characteristic LHC Chl a/b ratio of ~3. With a selective choice of detergent, the LHC proteins can be stripped away, leaving a PS I-65 complex. This preparation contains no Chl b, and the remaining Chl a and P700 are bound to 82-83 kD proteins; it retains full photochemical activity. Further treatment produces a preparation with 40 Chl a/P700, often called CP I. This is the most stable preparation [56], which retains photochemical activity even in the presence of sodium dodecyl sulfate (SDS), a usually denaturing detergent. In the effort to isolate the PS I reaction center, still smaller particles with ~10 Chl a/P700 have been isolated through the use of ether extraction [57]. In particles of this size, it is unclear what fraction of the remaining Chl a is contained in the reaction center, and how many molecules (if any) are antenna Chl.

It is reasonable to expect that the successive extraction procedures applied to the "native" particle each remove a particular protein component. The nomenclature that has developed is that the "peripheral antennae" are removed when the particle size is reduced from 110 to 65

Chl; reduction from 65 to 40 Chl/P700 removes the "internal antennae", leaving the "core antennae" intact. It is interesting to note that if the reaction center polypeptide is considered as containing 15 Chl/P700 (such a particle has been isolated [58]), then each antenna group contains ~25 Chl or a multiple thereof.

In addition to these common particle sizes, PS I preparations have been made with varying Chl/P700 ratios of ~20 to 55 [59]. If the structure of the PS I antennae were similar to that of the BChl a-protein from P. aestuarii, such variable antenna size would be difficult to explain; the size would be expected to step in increments of 21. However, ultraviolet CD spectra indicate that while the protein of P. aestuarii forms antiparallel β layers which enclose the chromophores [18], the polypeptides in PS I antennae contain parallel α/β domains [60]. The Chl chromophores are probably located between or on the exterior of such domains, at least partially exposed to the solvent. This is consistent with the severely hydrophobic nature of the PS I proteins, and allows one to visualize how progressively harsher detergent treatment could remove a variable number of chromophores. If each Chl is individually exposed to the solvent, then it would be expected that each would have a different binding affinity and be released under different extraction conditions. In such a picture of Chl-protein arrangement, it is important to consider the effect of detergent on the complex and the integrity (as compared to in vivo) of the various particles. This is particularly true in light of the large amount of free pigment released in the initial solubilization of thylakoids [54]. It has been shown that for isolated LHC complexes, the energy transfer dynamics depend on

detergent concentration [61]. Nechushtai et al. [62] found that the fluorescence maximum of PS I-65 particles shifted dramatically depending on the identity of the detergent; while the fluorescence maximum was located at about 670-685 nm in the presence of SDS or Triton X-100, it appeared at 721-725 nm when using dodecyl maltoside. However, it has been shown on the basis of low-temperature LD and fluorescence experiments that the isolation of complexes as small as 65 Chl/P700 do not alter the intrinsic orientation of pigments inside the complexes [63]. In addition, particles of PS I-110 have been isolated without the use of detergents [64]. Although the excitation dynamics in this preparation appear the same as in those obtained using detergents, the fluorescence spectrum of the latter particle shows a component not found in the detergent-free particle [65].

Although PS I-110 is often called the "native" particle, it is possible to prepare photosystem I complexes with as many as 200 Chl/P700 [66]. These particles contain additional LHC proteins, and contain considerable Chl b. PS I-200 is likely the naturally-occurring complex, since its size seems to match ~125 Å particles observed in electron micrographs of thylakoid membranes [67]. By contrast, micrographs of PS I-110 particles reconstituted in phosphatidyl choline vesicles showed images 106 Å in diameter [68]. Assuming approximately spherical complexes, these results give similar chromophore densities, with an average Chl-Chl separation of ~18 Å; such estimates using smaller particles may be inaccurate due to the enrichment in proteins which do not bind Chl.

As mentioned above, PS I complexes (regardless of size) show several

fluorescence bands, which indicates inhomogeneous antenna structure. Although they are more difficult to distinguish, the absorption spectrum also contains several bands. The correlation between absorption and fluorescence maxima seem to be generally agreed upon, but there is some disagreement as to the interpretation of each band. Major fluorescence peaks have been observed at ~690 nm, and 720 nm, with a minor component sometimes occurring at 735 nm [69]. (The 735 band has only been observed in particles with >65 Chl/P700, and is seen in green plants, but not algae.) These three peaks appear to correlate with absorption peaks centered at about 675, 690, and 705 nm respectively [65]. Although these are the most commonly observed Q_y bands, others have reported as many as five components [46,68,70,71]. Identification of fluorescence bands is complicated by the fact that steady-state spectra are strongly dependent of temperature [72,73] and on detergent as mentioned above. In addition, steady-state fluorescence spectra are very sensitive to the presence of impurities (solubilized Chl and denatured complexes) because the fluorescence quantum yield is much lower for functional PS I than for nonfunctional impurities.

The fluorescence excitation dynamics of PS I has been the subject of a considerable amount of study. It has become evident that PS I preparations with more than 65 Chl/P700 require at least three exponentials to describe the fluorescence decay [46,74-76]; experiments on mutant strains of C. reinhardtii which lack the PS II give very similar decays [74,75], indicating that isolation procedures do not significantly alter the dynamics in PS I preparations. The multicomponent decays invariably show a dominant fast component

(τ ~ 50 ps), one or two intermediate components with lifetime(s) in the hundreds of picoseconds, and a very small amplitude long component (τ ~ 2.2 ns). The long component is possibly due to a small number of PS I complexes which lack a trap, since the 2.2 ns lifetime is similar to that observed in a C. reinhardtii mutant lacking both PS I and PS II [75].

In smaller PS I particles (40 Chl a/P700 or less) the intermediate lifetime components disappear, and only a short (τ < 40 ps) component and a long, ~6 ns component are observed [76-79]. (This immediately implies that the intermediate lifetimes observed in larger particles correspond to transfer from the peripheral to the core antenna.) The long component typically contributes less than 5% of the amplitude of the decay, and is likely due to impurities; its lifetime is similar to that observed for detergent-solubilized Chl a [80]. The fast lifetime has been attributed to efficient trapping by the PS I reaction center. This is supported by time-resolved absorption, which shows a 15-30 ps risetime for $P700^+$ formation [81]. The lifetime of this fast component has been shown to depend linearly on the size of the PS I antenna [77]. This result was interpreted in terms of a random walk across a uniform lattice using a theory developed by Pearlstein [82]. This analysis of the data indicated that the average single-step transfer time is 0.2 ps, which is reasonably close to estimates from Förster weak-coupling theory for Chl a molecules separated by ~18 Å (see above). The average transfer time was also reported to be relatively insensitive to the structure of the array (square vs. cubic); this observation is important since the chromophore positions are unlikely to correspond to a perfect lattice. Although the PS I core contains several spectral forms, analysis in terms of a lattice

model assumes a homogeneous array of Chl a. The observed linear dependence of trapping time on core antenna size therefore seems in conflict with the "funnel" description of EET [83], but would indicate that any intermediate traps (long-wavelength forms of Chl a) would have to be randomly distributed among the core. This is in agreement with observations that the shape of the absorption spectrum is independent of core antenna size [79]. In this type of arrangement, one would expect that at room temperature excitations would be rapidly homogenized among all spectral forms in the core antenna [79]. However, at low temperatures long-wavelength antenna forms become energy "sinks" because they are unable to undergo uphill transfer to surrounding (shorter wavelength) forms. Searle et al. [84] recently performed an analysis of the temperature dependence of excitation decay in PS I-40 particles. They found that the fluorescence lifetime measured at 720 nm (emitted by the C690 absorption component) slows from ~30 ps at 270 K to ~190 ps at 10 K. The lifetime of the C675 fluorescence component (F690), however, was relatively independent of temperature, indicating that transfer from this component is not inhibited by temperature. The behavior of both components was interpreted in terms of a kinetic model in which both components may exchange energy with each other or with P700; no evidence of energy funnel behavior was detected. This kinetic model shows significant differences from a model used by Wittmershaus [65], in which the excitation must pass through the C690 component before being trapped by P700. This arrangement was suggested by a fast risetime in the long-wavelength fluorescence, matching the decay of the short-wavelength component [85].

In the above discussion of absorption and fluorescence components, the precise identity of each component was not considered. In terms of the antenna Chl, there are two possibilities: the different components are due to Chl molecules in different environments (and therefore energetically shifted), or different bands arise from excitonic interaction between chromophores. These two explanations are not mutually exclusive, nor is there a sharp distinction between them; unlike the BChl a-protein discussed above, the components in the Q_y spectrum are unresolved. Since the chromophore positions and orientations are unknown, the chromophore interaction energies cannot be explicitly calculated. However, an estimate of the average coupling energy may be inferred in the point dipole approximation using the 18 Å separation mentioned above. A quantitative equivalent of Eq. 1.16 (with $\mu_a = \mu_b = \mu$) is [86]

$$U = (5.04\ \mu^2\ R^{-3})\kappa \tag{5.45}$$

where R is in nm, μ is in Debye, and the interaction energy U is in cm^{-1}. If the oscillator strength is taken as 5 D [86], and an "average" value of κ as $\sqrt{2/3}$, then the 1.8 nm spacing gives an interaction energy of 18 cm^{-1}. This may be regarded as a conservative estimate since the size of the particles includes contributions from proteins which do not bind Chl, and monopole effects generally increase the magnitude of U [31]; in any case, it is evident that variations of only a few angstroms from a perfect lattice could produce appreciable splitting of the absorption bands. CD spectra of isolated PS I [87] show some evidence of excitonic

interaction, but seem to indicate that not all Chl molecules participate; this is in agreement with studies of small (8-10 Chl a/P700) particles which indicate that such coupling occurs very near the reaction center [88], and with linear dichroism spectra of electric field aligned complexes [89]. Also, hole-burning studies of PS I-60 particles [90] indicate that some delocalized exciton character is present in the core antenna complex.

The presence of excitonic interactions in the antenna of PS I would not necessarily conflict with any of the experimental results discussed above. In the interpretation of the linear dependence of lifetime vs. core antenna size [77], it is important to remember that the average core size is measured, with no indication of standard deviation in the size of the particles. It is entirely possible that only two to three different sizes of core antenna exist in vitro, and the variable sizes reported are weighted averages of two distinct complexes. The measured excitation lifetime would then be a weighted average also, thus explaining the observed linear dependence. The temperature dependence of the excitation lifetime in core antennae [84] can also be explained in terms of excitonic interaction. Since the population of the exciton levels is governed by the Boltzmann distribution, at low temperatures only the lowest exciton level will be populated. If this level shows poor spectral overlap with the acceptor or low dipole moment strength, then the transfer probability would be expected to decrease with temperature, resulting in a longer excited state lifetime. It is interesting here to note the work of Pearlstein and Zuber [91], who considered the cyclic structure often observed in pigment-protein complexes. They found that

excitonic interaction in such structures can lead to low oscillator strength in the lower energy levels, producing an "exciton storage ring" effect. Although such a proposal is highly speculative, it is entirely possible that cyclic structures do exist in PS I antennae. Shubin, et al. [60] have observed that the 65 kD core proteins (variously reported as 81 kD) binds ~12 Chl a molecules, and contains 2-3 parallel α/β domains. Therefore, they have proposed clusters of 4-6 Chl a molecules in each domain; this coincides with the number of absorption bands they observe in the Q_y region.

The question of whether excitonic interaction is present in the antenna of PS I is one of many which have yet to be answered. Also largely undetermined is whether low energy forms of Chl a play a part in EET, whether the "funnel" description is valid for this system, and how the pigments are coupled to the PS I reaction center.

References

1. Jortner, J.; Michel-Beyerle, M. E. In "Antennas and Reaction Centers of Photosynthetic Bacteria"; Michel-Beyerle, M. E., Ed.; Springer-Verlag: Berlin, 1985; p. 345.
2. Clayton, R. K. "Photosynthesis: Physical Mechanisms and Chemical Patterns"; Cambridge University Press: Cambridge, 1980; p. 116.
3. Borisov, A. Yu.; Fetisova, Z. G. Mol. Biol. 1971, 5, 509.
4. Sauer, K. In "Bioenergetics of Photosynthesis"; Govindjee, Ed.; Academic Press: New York, 1975; p. 115.
5. Zuber, H. Photochem. Photobiol. 1985, 42, 821.
6. MacColl, R.; Lee, J. J.; Berns, D. S. J. Biol. Chem. 1973, 248, 7080.

7. Knox, R. S. In "Primary Processes in Photosynthesis"; Barber, J., Ed.; Elsevier: Amsterdam, 1977; Vol. 2, p. 78.

8. Olson, J. M. Int. J. System. Biol. 1978, 28, 128.

9. Holt, S. C.; Conti, S. F.; Fuller, R. C. J. Bacteriol. 1966, 91, 311.

10. Gorlenko, V. M.; Zhilina, T N. Microbiology 1968, 37, 892.

11. Staehelin, L. A.; Golicki, J. R.; Drews, G. Biochim. Biophys. Acta 1980, 589, 30.

12. Olson, J. M.; Gerola, P. D.; van Brakel, G. H. In "Antennas and Reaction Centers of Photosynthetic Bacteria", Michel-Beyerle, M. E., Ed.; Springer-Verlag: Berlin, 1985; p.67

13. Swarthoff, T.; Amesz, J. Biochim. Biophys. Acta 1979, 548, 427.

14. Braumann, T.; Vasmel, H.; Grimme, L. H.; Amesz, J. Biochim. Biophys. Acta 1986, 848, 83.

15. Gerola, P. D.; Olson. J. M. Biochim. Biophys. Acta 1986, 848, 69.

16. Olson, J. M.; Romano, C. A. Biochim. Biophys. Acta 1962, 59, 726.

17. Olson J. M. In "Methods of Enzymology", Vol. 23, Part A; San Pietro, A., Ed.; Academic Press: New York, 1971; p. 636

18. Matthews, B. W.; Fenna R. E. Acc. Chem. Res. 1980, 13, 309.

19. Olson, J. M. In "The Photosynthetic Bacteria"; Clayton, R. K.; Sistrom, W. R., Eds.; Plenum: New York, 1978; p. 105.

20. Tronrud, D. E.; Schmid, M. F.; Matthews, B. W. J. Mol. Biol. 1986, 188, 443.

21. Fenna, R. E.; Ten Eyck, L. F.; Matthews, B. W. Biochem. Biophys. Res. Commun. 1977, 75, 751.

22. Olson, J. M.; Jennings, W. H.; Hanna, C. H. Arch. Biochem. Biophys. 1969, 130, 140.

23. Fenna, R. E.; Matthews, B. W.; Olson, J. M.; Shaw, E. K. J. Mol. Biol. 1974, 84, 231.

24. Matthews. B. W.; Fenna, R. E.; Remington, S. J. J. Ultrastruc. Res. 1977, 58, 316.

25. Philipson, K. D.; Sauer, K. Biochemistry 1972, 11, 1880.

26. Olson, J. M.; Ke, B.; Thompson, K. H. Biochim. Biophys. Acta 1976, 430, 524.

27. Whitten, W. B.; Nairn, J. A.; Pearlstein, R. M. Biochim. Biophys. Acta 1978, 503, 251.

28. Whitten, W. B.; Olson, J. M.; Pearlstein, R. M. Biochim. Biophys. Acta 1980, 591, 203.

29. Tinoco, Jr., I. Advan. Chem. Phys. 1962, 4, 113.

30. Swarthoff, T.; Amesz, J.; Kramer, H. J. M.; Rijgersberg, C. P. Israel J. Chem. 1981, 21, 332.

31. Sybesma, C.; Olson, J. M. Proc. Natl. Acad. Sci. 1963, 49, 248.

32. Pearlstein, R. M.; Hemenger, R. P. Proc. Natl. Acad. Sci. USA 1978, 75, 4920.

33. Chang, J. C. J. Chem. Phys. 1977, 67, 3901.

34. Hemenger, R. P. J. Chem. Phys. 1977, 66, 1795.

35. Hemenger, R. P. J. Chem. Phys. 1977, 67, 262.

36. Hemenger, R. P. J. Chem. Phys. 1978, 68, 1722.

37. Lutz, M.; Hoff, A. J.; Brehamet, L. Biochim. Biophys. Acta 1982, 679, 331.

38. Olson, J. M. Biochim. Biophys. Acta 1980, 594, 33.

39. Swarthoff, T.; deGrooth, B. G.; Meiburg, R. F.; Rijgersberg, C. P.; Amesz, J. Biochim. Biophys. Acta 1980, 593, 51.

40. Whitten, W. B.; Pearlstein, R. M.; Phares, E. F.; Geacintov, N. E. Biochim. Biophys. Acta 1978, 503, 491.

41. Marion, J. B. "Classical Dynamics of Particles and Systems"; Academic Press: New York, 1965; p. 391.

42. Stehfest, H. Commun. ACM 1970, 13,47.

43. Hill, R.; Bendall, F. Nature 1960, 186, 136.

44. Gulotty, R. J.; Fleming, G. R.; Alberte, R. S. Biochim. Biophys. Acta 1982, 682, 322.

45. Reisberg, P.; Nairn, J. A.; Sauer, K. Photochem. Photobiol. 1982, 36, 657.

46. Mimuro, M.; Yamazaki, I.; Tamai, N.; Yamazaki, T.; Fujita, Y. In "Primary Processes in Photobiology"; Kobayashi, T., Ed.; Springer-Verlag: Berlin, 1987; p. 23.

47. Hodges, M.; Moya, I. Biochim. Biophys. Acta 1986, 849, 193.

48. Holzwarth, A. R.; Wendler, J.; Haehnel, W. Biochim. Biophys. Acta 1985, 807, 155.

49. Holzwarth, A. R. In "Progress in Photosynthesis Research"; Biggins, J., Ed.; Martinus Nijhoff: The Hague, 1987; Vol. I, p. 53.

50. Karukstis, K.; Sauer, K. Biochim. Biophys. Acta 1985, 806, 374.

51. James, D. R.; Ware, W. R. Chem. Phys. Lett. 1985, 120, 455.

52. Wong, D.; Merkelo, H.; Govindjee Photochem. Photobiol. 1981, 33, 97.

53. Govindjee; Govindjee, R. In "Bioenergetics of Photosynthesis"; Govindjee, Ed.; Academic Press: New York, 1975; p. 18.

54. Dunahay, T. G.; Staehelin, L. A. Plant Physiol. 1985, 78, 606.

55. Green, B. R. Photosyn. Res. 1988, 15, 3.

56. Anderson, J. M. Biochim. Biophys. Acta 1980, 591, 113.

57. Ikegami, I.; Katoh, S. Biochim. Biophys. Acta 1975, 376, 588.

58. Vacek, K.; Wong, D.; Govindjee Photochem. Photobiol. 1977, 26, 269.

59. Owens, T. G.; Webb, S. P.; Alberte, R. S.; Mets, L.; Fleming, G. R. In "Progress in Photosynthesis Research"; Biggins, J., Ed.; Martinus Nijhoff: The Hague, 1987; Vol. I, p. 83.

60. Shubin, V. V.; Karapetyan, N. V.; Krasnovsky, A. A. Photosyn. Res. 1986, 9, 3.

61. Ide, J. P.; Klug, D. R.; Crystall, B.; Gore, B. L.; Giorgi, L. B.; Kuhlbrandt, W.; Barber, J.; Porter, G. In "Progress in Photosynthesis Research"; Biggins, J., Ed.; Martinus Nijhoff: The Hague, 1987; Vol. I, p. 131.

62. Nechushtai, R.; Nourizadeh, S. D.; Thornber, J. P. Biochim. Biophys. Acta 1986, 848, 193.

63. Tapie, P.; Choquet, Y.; Breton, J.; Delepelaire, P.; Wollman, F.-A. Biochim. Biophys. Acta 1984, 767, 57.

64. Huang, C.; Berns, D. S. Arch. Biochim. Biophys. 1983, 220, 145.

65. Wittmershaus, B. P. In "Progress in Photosynthesis Research"; Biggins, J., Ed.; Martinus Nijhoff: The Hague, 1987; Vol. I, p. 75.

66. Malkin, R.; Ortiz, W.; Lam, E.; Bonnerjea, J. Physiol. Veg. 1985, 23, 619.

67. Simpson, D. Eur. J. Cell Biol. 1983, 31, 305.

68. Mullet, J. E.; Burke, J. J.; Arntzen, C. J. Plant Physiol. 1980, 65, 814.

69. Rijgerberg, C. P.; Amesz, J.; Thielen, A. P. G. M.; Swager, J. A. Biochim. Biophys. Acta 1979, 545, 473.

70. Garnier, J.; Maroc, J.; Guyon, D. Biochim. Biophys. Acta 1986, 851, 395.

71. Mimuro, M.; Tamai, N.; Yamazaki, T.; Yamazaki, I. FEBS Letters 1987, 213, 119.

72. Wachtveitl, J.; Krause, H. In "Progress in Photosynthesis Research"; Biggins, J., Ed.; Martinus Nijhoff: The Hague, 1987; Vol. I, p. 87.

73. Brown, J. S. Photochem. Photobiol. 1977, 26, 519.

74. Hodges, M.; Moya, I.; Briantais, J.-M.; Remy, R. In "Progress in Photosynthesis Research"; Biggins, J., Ed.; Martinus Nijhoff: The Hague, 1987; Vol. I, p. 115

75. Gulotty, R. J.; Mets, L.; Alberte, R. S.; Fleming, G. R. Photochem. Photobiol. 1985, 41, 487.

76. Mimuro, M.; Yamazaki, I.; Tamai, N.; Yamazaki, T.; Fujita, Y. In "Progress in Photosynthesis Research"; Biggins, J., Ed.; Martinus Nijhoff: The Hague, 1987; Vol. I, p. 91.

77. Owens, T. G.; Webb, S. P.; Mets, L.; Alberte, R. S.; Fleming, G. R. Proc. Natl. Acad. Sci. USA 1987, 84, 1532.

78. Kamogawa, K.; Morris, J. M.; Takagi, Y.; Nakashima, N.; Yoshihara, K.; Ikegami, I. Photochem. Photobiol. 1983, 37, 53.

79. Owens, T. G.; Webb, S. P.; Alberte, R. S.; Mets, L.; Fleming, G. R. Biophys. J. 1988, 53, 733.

80. Il'ina, M. D.; Borisov, A. Yu. Biochim. Biophys. Acta 1981, 637, 540.

81. Il'ina, M. D.; Krasauskas, V. V.; Rotomskis, R. J.; Borisov, A. Yu. Biochim. Biophys. Acta 1984, 767, 501.

82. Pearlstein, R. M. Photochem. Photobiol. 1982, 35, 835.

83. Seely, G. R. J. Theor. Biol. 1973, 40, 189.

84. Searle, G. F. W.; Tamkivi, R.; van Hoek, A.; Schaafsma, T. J. J. Chem Soc., Faraday Trans. 1988, 84, 315.

85. Wittmershaus, B.; Nordlund, T. M.; Knox, W. H.; Knox, R. S.; Geacintov, N. E.; Breton, J. Biochim. Biophys. Acta 1985, 806, 93.

86. van Grondelle, R.; Amesz, J. In "Light Emission by Plants and Bacteria"; Govindjee; Amesz, J.; Fork, D. C., Eds.; Academic Press: New York, 1986; p. 197.

87. Scott, B.; Gregory, R. P. F. Biochem. J. 1975, 149, 341.

88. Ikegami, I.; Itoh, S. Biochim. Biophys. Acta 1986, 851, 75.

89. Gagliano, A. G.; Geacintov, N. E.; Breton, J.; Acker, S.; Remy, R. Photochem. Photobiol. 1979, 29, 415.

90. Gillie, J. K.; Hayes, J. M.; Small, G. J.; Golbeck, J. H. J. Phys. Chem. 1987, 91, 5524.

91. Pearlstein, R. M.; Zuber, H. In "Antennas and Reaction Centers of Photosynthetic Bacteria"; Michel-Beyerle, M. E., Ed.; Springer-Verlag: Berlin, 1985; p. 53.

POLARIZED PUMP-PROBE SPECTROSCOPY OF EXCITON TRANSPORT IN BACTERIOCHLOROPHYLL A-PROTEIN FROM PROSTHECOCHLORIS AESTUARII

Timothy P. Causgrove, Shumei Yang, and Walter S. Struve

Department of Chemistry and Ames Laboratory-USDOE

Iowa State University, Ames, Iowa 50011

CHAPTER VI. POLARIZED PUMP-PROBE SPECTROSCOPY OF EXCITON TRANSPORT IN BACTERIOCHLOROPHYLL A-PROTIEN FROM PROSTHECOCHLORIS AESTUARII

Introduction

Electronic excitation transport (EET) is the first process which occurs after light absorption by antenna pigments in green photosynthetic bacteria and plants. The excitation migration is believed to proceed by an incoherent random-walk mechanism [1] arising from Förster dipole-dipole coupling [2] between molecules or aggregates containing antenna chromophores. The antenna chlorophylls in plants are complexed with proteins in units containing six or more chromophores. In Sauer's "pebble mosaic" model, the chlorophylls within such units are strongly coupled, and electronic excitation exists as exciton states which are delocalized over the clusters [3]. Chromophores belonging to different units are weakly coupled, and EET between clusters is presumed to occur by ordinary Förster hopping.

Few time-domain experiments have directly resolved the antenna EET processes in green photosynthetic organisms. Owens et al. [4] recently measured the reaction center quenching of antenna fluorescence lifetimes in photosystem I core antennae of P700 Chl a-protein complexes from barley, and in a photosynthetic mutant of Chlamydomonas reinhardtii without the photosystem II antenna/reaction center complex. The fluorescence lifetime varied linearly with core antenna size in both cases, in accordance with random walk models [5,6] in which the

chlorophylls are assumed to occupy the sites of a regular lattice. Analysis of the fluorescence profiles in terms of the lattice models yielded a calculated single-step EET time of between 0.1 and 0.2 ps in the core antenna of photosystem I. Excitation migration was found to be nearly diffusive, with photoconversion in the reaction center occurring on the average of once per 2.4 excitation hops from the core antenna.

In our EET program, systems excited with linearly polarized laser pulses have been studied by analyzing the time-dependent fluorescence profiles $I_{\parallel}(t)$, $I_{\perp}(t)$ polarized parallel and perpendicular to the laser polarization [7,8]. Unlike reaction center trapping of antenna fluorescence, this technique's sensitivity is specific to fluorescence depolarization attending single excitation hops from the laser-excited chromophore. However, the instrument function of ~45 ps FWHM [8] in our current time-correlated single photon counting apparatus is far too slow for direct characterization of single-step EET in green photosynthetic antennae. We have therefore resorted to polarized pump-probe spectroscopy. The relationships between the polarized optical density components $A_{\parallel}(t)$, $A_{\perp}(t)$ and time-resolved observables in EET are analogous to those for fluorescence intensity components, but the time resolution is laser pulse-limited. In separate experiments [9], we probed EET in glycerol solutions of rhodamine 640 at concentrations between 3.4 μM and 1.4 mM, using both time-correlated single photon counting (to evaluate $I_{\parallel}(t)$ and $I_{\perp}(t)$) and pump-probe techniques (which yielded $A_{\parallel}(t)$ and $A_{\perp}(t)$). The transport was found to be well described by a two-particle theory [10] for the time-dependent probability that the excitation resides on the laser-pumped molecule. Optimized Förster parameters from nonlinear

least-squares fits of the two-particle theory to the polarized profiles from both photon counting and pump-probe experiments proved to be congruent to within data scatter, ensuring that our pump-probe techniques furnish a valid test of transport in this prototype system.

For our initial study of EET in photosynthetic antennae, we elected the bacteriochlorophyll (BChl) a-protein from the green sulfur bacterium Prosthecochloris aestuarii -- the only bacterial antenna system whose 3-dimensional structure is known [11]. Photon absorption in such bacteria occurs in the chlorobium chlorophyll system, which comprises some 10^3 BChl c, d, or e molecules per reaction center. Excitation is channeled to a BChl a-protein complex containing ~10^2 chromophores, which in turn funnels the excitation to the reaction center. The basic structural unit in BChl a-protein is a trimer of subunits containing 7 BChl a molecules each. The nearest-neighbor Mg-Mg separations for BChl a chromophores within a subunit range from 11.3 to 14.4 Å [11]. The BChl a-protein crystallizes in either the $P6_3$ (hexagonal) or $P6_1$ (trigonal) space group [12]; there are no Mg-Mg separations shorter than 24 Å (30 Å) for chromophores in different subunits in crystals of $P6_3$ ($P6_1$) symmetry [11]. (Tronrud et al. [13] have recently refined the x-ray structure of the BChl a-protein; they concentrated on the protein sequence and BChl a conformations, and did not report the chromophore orientations or positions.) Hence, BChl a-protein from P. aestuarii presents a possible realization of the "pebble mosaic" model, in which EET (whose rate scales as R^{-6} for chromophores separated by R) is expected to be far more rapid within subunits than among subunits. Absorption and circular dichroism spectra of the BChl a-protein in a triglycerophosphate buffer show strong evidence for exciton

interactions in both the Q_y absorption system at 809 nm and in the Q_x system at 603 nm [14]. The observed splittings in the Q_y system are comparable to off-diagonal resonance dipole interaction energies (up to ~250 cm^{-1}) calculated [15] by a transition monopole method [16]. However, attempts to simulate the absorption and CD spectra based on the known BChl a-protein geometry have not been successful.

In this work, we have performed pump-probe experiments on the BChl a-protein Q_x band system at wavelengths between 598 and 609 nm. The long-time behavior of $A_{\parallel}(t)$ and $A_{\perp}(t)$ varies with probe wavelength and is related to the projection of the probed transition moment along the crystal c-axis. The time-resolved data are analyzed using a kinetic model derived from the geometry of the BChl a-protein.

Experimental

The BChl a-protein solution in triglycerophosphate buffer [14,17] was generously provided by R. E. Fenna. For most experiments, it was concentrated to ~5.0 optical density for 1 cm path length at 809 nm; its room temperature absorption spectrum between 590 and 840 nm matched published spectra [17,18]. Such solutions contain BChl a-protein crystallites with a mean particle size of at least 30 trimers [19]. Samples were housed between $\lambda/4$ fused silica flats separated by a 800 μm teflon spacer; they were rotated at 12 Hz to minimize photooxidation by the laser beams during pump-probe scans.

A multiline argon ion laser with 6 W plasma tube pumped a passively mode-locked dual-jet rhodamine 590-DQOCI laser [20] to produce vertically

polarized pulses between 598 and 609 nm with ~50 mW average power at 125 MHz repetition rate. Real-time autocorrelation traces [21] exhibited ~1.5 ps FWHM. The output beam was divided into pump and probe beams, which were modulated at 5.0 and 0.5 MHz respectively with ~80% modulation depth using Isomet 1206C acoustooptic modulators. The variably delayed pump beam was reflected by a BK-7 corner cube prism mounted on a Micro-Controle UT10050PP translation stage (0.1 μm/step, 5 cm range). The beam polarizations were selected using identical calcite Glan-Thompson polarizers; the probe polarization was fixed at 45° from the laser polarization, and the pump polarization was varied. A 7.3 cm f. l. lens focussed both beams to ~20 μm diameter in the rotating sample. The average incident power was <5 mW in each beam. The transmitted probe beam was collected by an EG&G FOD-100 photodiode, and phase-locked single-sideband detection was achieved at 5.5 MHz using a modified Drake R-7A radio receiver [22]. The receiver's signal-bearing 50 kHz intermediate frequency (IF) was tapped and routed to a Stanford Research Systems SR510 lock-in amplifier (LIA) and was demodulated using the receiver reference IF output. Data were transmitted during pump-probe sweeps from the LIA via an RS-232 port to a DEC MINC-23 computer operating in a TSX-Plus multiuser environment. Pump-probe scans were normalized to the instantaneous square of the laser intensity by deflecting part of the laser beam into another FOD-100 photodiode, processing the signal in a current-to-voltage converter and RC filter, and transmitting the digitized signal through the LIA RS-232 port to the computer.

Results and Discussion

A typical pump-probe profile obtained at 603 nm (the Q_x band maximum) with the probe polarization rotated 54.7° from the pump polarization is shown in Fig. 6-1. The observed decay, which corresponds to ground state repopulation in the BChl *a*-protein, is highly nonexponential; it is well described by the biexponential law P(t) = 0.41exp(-t/14.6 ps) + 0.59exp(-t/52.4 ps). These time constants are some two orders of magnitude shorter than intrinsic Q_y lifetimes of BChl *a* chromophores [23]. The isotropic decay obtained with the average power halved in both beams is very similar (P(t) = 0.43exp(-t/17.0 ps) + 0.57exp(-t/68.6 ps)). The rapid decay is therefore not primarily a consequence of exciton annihilation, which would be important if far more intense laser pulses were used; typical pulse energies were ~0.05 nJ at 603 nm.

In Figure 6-2, we show the polarized pump-probe transients $A_{\parallel}(t)$ and $A_{\perp}(t)$ at 603 nm and at 598 nm. They are dominated by coherent coupling artifacts [24] during the first ~1.5 ps. These can be removed in principle by data antisymmetrization [25]; this procedure is useful only for data with higher S/N, which is limited here by the available concentrations of BChl *a*-protein. The transients were fitted instead with convolutions of the laser autocorrelation function with the phenomenological expressions

$$A_{\parallel}(t) = P(t)\{1 + 0.8[(1-a)\exp(-t/\tau) + a]\}$$
$$A_{\perp}(t) = P(t)\{1 - 0.4[(1-a)\exp(-t/\tau) + a]\} \qquad (6.1)$$

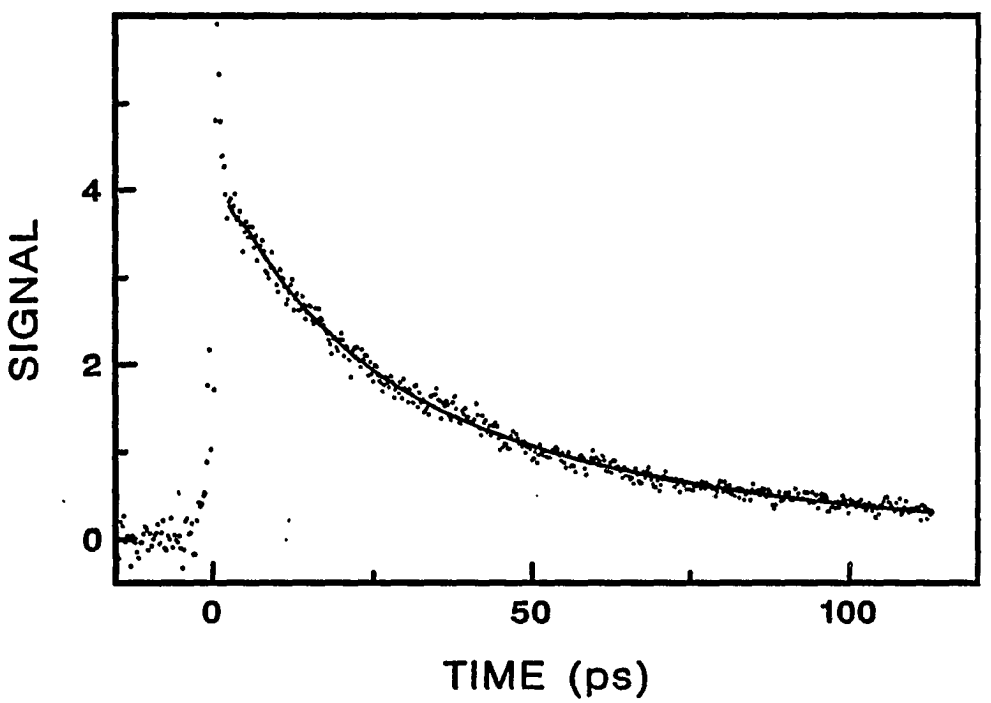

Figure 6-1. Photobleaching transient of triglycerophosphate buffer solution of BChl a-protein from P. aestuarii, obtained using 603 nm pump and probe polarizations 54.7° apart. Continuous curve gives convolution of laser autocorrelation function with biexponential decay law P(t) = 0.41exp(-t/14.6ps) + 0.59exp(-t/52.4ps).

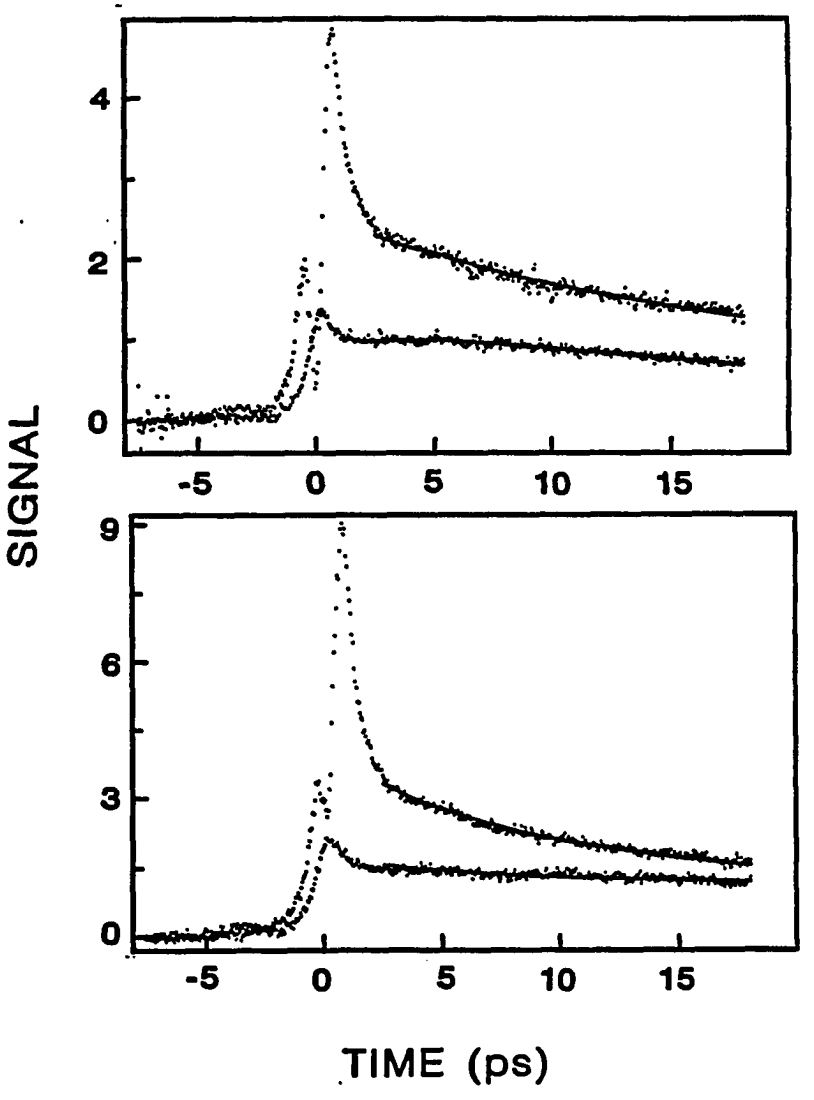

Figure 6-2. Polarized pump-probe transients for BChl a-protein at 603 nm (upper panel) and at 598 nm (lower panel). In each panel the upper and lower traces correspond to $A_{\parallel}(t)$ and $A_{\perp}(t)$, respectively. Continuous curves show convolutions of laser autocorrelation function with Eqs. 6.1, with lifetime and anisotropy parameters optimized as described in text. Note the slower depolarization timescale at 598 nm.

beginning with the data channel corresponding to 2.5 ps past the coherent coupling peak. The isotropic decay function P(t) was expressed as a biexponential function with parameters fixed at values obtained by fitting isotropic decays analogous to that shown in Figure 6-1. The polarized profiles $A_{\parallel}(t)$ and $A_{\perp}(t)$ were fitted simultaneously in a linked deconvolution procedure [26] which minimized the combined sum of residuals for both profiles with respect to the parameters $\underline{a}$ and τ. The results of such analyses are given for several pump-probe experiments at 609, 603, and 598 nm in Table I. Nonzero values of the parameter $\underline{a}$ are required to simulate the polarized photobleaching decays at 609 and 603 nm: analyses of pump-probe scans obtained over 125 ps windows (not shown in Fig. 6-2) confirm that $A_{\parallel}(t)/A_{\perp}(t)$ does not approach unity at long times, and they yield fitting parameters similar to those derived from the shorter scans, which were limited to 25 ps windows.

To model the depolarization due to EET in BChl $\underline{a}$-protein, we consider the $P6_3$ crystal structure shown in Fig. 6-3. The unit cell contains two trimers [11,13] which are labelled ABC and DEF. Trimer ABC is located in an ab-plane which is displaced by 49.3 Å along the c-axis from the plane occupied by trimers DEF, GIJ, and HKL. Because spectroscopic evidence supports the existence of strong exciton interactions between BChl $\underline{a}$ chromophores inside a subunit [14,15], our model presumes that Förster excitation hopping occurs between exciton states which are delocalized over tightly coupled groups of seven BChl $\underline{a}$ molecules. Creation of an exciton state in subunit A may be followed by migration to exciton states centered on other subunits. We arbitrarily restrict EET to hopping between neighboring subunits, and we distinguish two kinds of contiguous

Table I. Fitting parameters for polarized pump-probe profiles in BChl *a*-protein from *P. aestuarii*

Wavelength, nm	Scan duration, ps	a	τ, ps
609	125	0.497	3.48
609	125	0.485	1.47
603	25	0.530	3.50
603	25	0.435	5.65
603	25	0.468	4.74
603	25	0.422	5.12
603	125	0.467	9.44
603	125	0.537	5.28
598	25	0.0[a]	20.9
598	25	0.0[a]	18.3
598	125	0.034	32.9

[a]Parameter held fixed at 0.0.

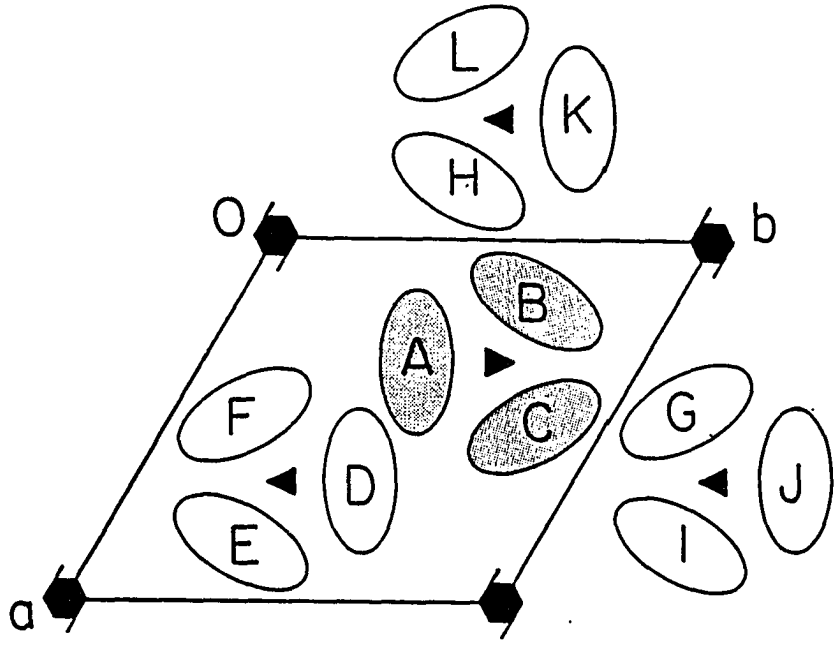

Figure 6-3. Schematic diagram of $P6_3$ (hexagonal) unit cell of BChl *a*-protein from *P. aestuarii*. Unit cell dimensions are a = b = 111.9 Å, c = 98.6 Å [11]. Trimers ABC and DEF are separated by 49.3 Å along the c-axis.

subunit pairs. The first kind is an adjacent pair of subunits within the same trimer, typified by A-B or D-E. The second kind is a pair of neighboring subunits belonging to different trimers, such as A-D or B-H. The Förster hopping rate between subunits $\underline{i}$ and $\underline{j}$ will scale approximately as

$$w_{ij} = R_{ij}^{-6}\kappa_{ij}^2 \tag{6.2}$$

where R_{ij} is the separation between subunits. The orientational factor κ_{ij} is given in terms of the transition moment orientations $\hat{d}_i$, $\hat{d}_j$ in the lowest-energy exciton component of the Q_y state by

$$\kappa_{ij} = \hat{d}_i \cdot \hat{d}_j - 3(\hat{d}_i \cdot \hat{R}_{ij})(\hat{d}_j \cdot \hat{R}_{ij}) \tag{6.3}$$

If a subunit centroid is defined as the mean Mg atom position inside that subunit, and if one associates R_{ij} with the separation between centroids of subunits $\underline{i}$ and $\underline{j}$, the distances R_{AB} and R_{AD} pertinent to the first and second kinds of hopping are 33.1 and 61.5 Å, respectively. Equation 6.2 then implies that the relative transition rates will be given by $w_{AD}/w_{AB} \sim 0.024\ \kappa_{AD}^2/\kappa_{AB}^2$. Owing to the crystal symmetry, the orientational factors can be compactly expressed in terms of the transition moment orientation $\hat{d}_A = (\rho, \sigma, \upsilon) \equiv (\rho, \sigma, \sqrt{1-\rho^2-\sigma^2})$ in subunit A; they are

$$\kappa_{AB} = 1 - \frac{9}{4}\rho^2 + \frac{3}{4}\sigma^2 \tag{6.4}$$

$$\kappa_{AD} = \frac{3}{4}\rho^2 + \frac{1}{4}\sigma^2 - \rho\sigma\sqrt{3}/2 - 1 \tag{6.5}$$

The ratio $\kappa_{AD}^2/\kappa_{AB}^2$ is a slowly varying function of the (unknown) transition moment components ρ, σ in the ab-plane for most $\rho^2 + \sigma^2 < 1$; typical values range between 0.0 and 2.0. The function $\kappa_{AD}^2/\kappa_{AB}^2$ is singular at special combinations of ρ and σ where κ_{AB} vanishes (e.g., ρ~0.7 and σ~0.3, Eq. 6.4). The ratio w_{AD}/w_{AB} of intertrimer to intratrimer hopping will consequently be small for most orientations $\hat{d}_A$; it only becomes large for the singular orientations corresponding to very slow hopping rates w_{AB} between subunits in the same trimer. The qualitative migration patterns for $w_{AD}/w_{AB} >> 1$ and $w_{AD}/w_{AB} << 1$ are illustrated in Fig. 6-4.

Prior to modelling EET for general w_{AD}/w_{AB}, we treat the limiting case where $w_{AD}/w_{AB} << 1$ (cf., Fig. 6-4b). The depolarization at early times following excitation of subunit A will then be dominated by hopping among subunits A, B, and C; negligible exciton populations will be found in subunits D through L. The time-dependent probabilities A(t), B(t), C(t) of finding excitation in subunits A, B, C are then given by solutions to the kinetic equation

$$-\frac{dA}{dt} = w_{AB}(2A - B - C) \tag{6.6}$$

under the initial conditions

$$A(0) = A_0 \tag{6.7}$$

$$B(0) = C(0) = 0 \tag{6.8}$$

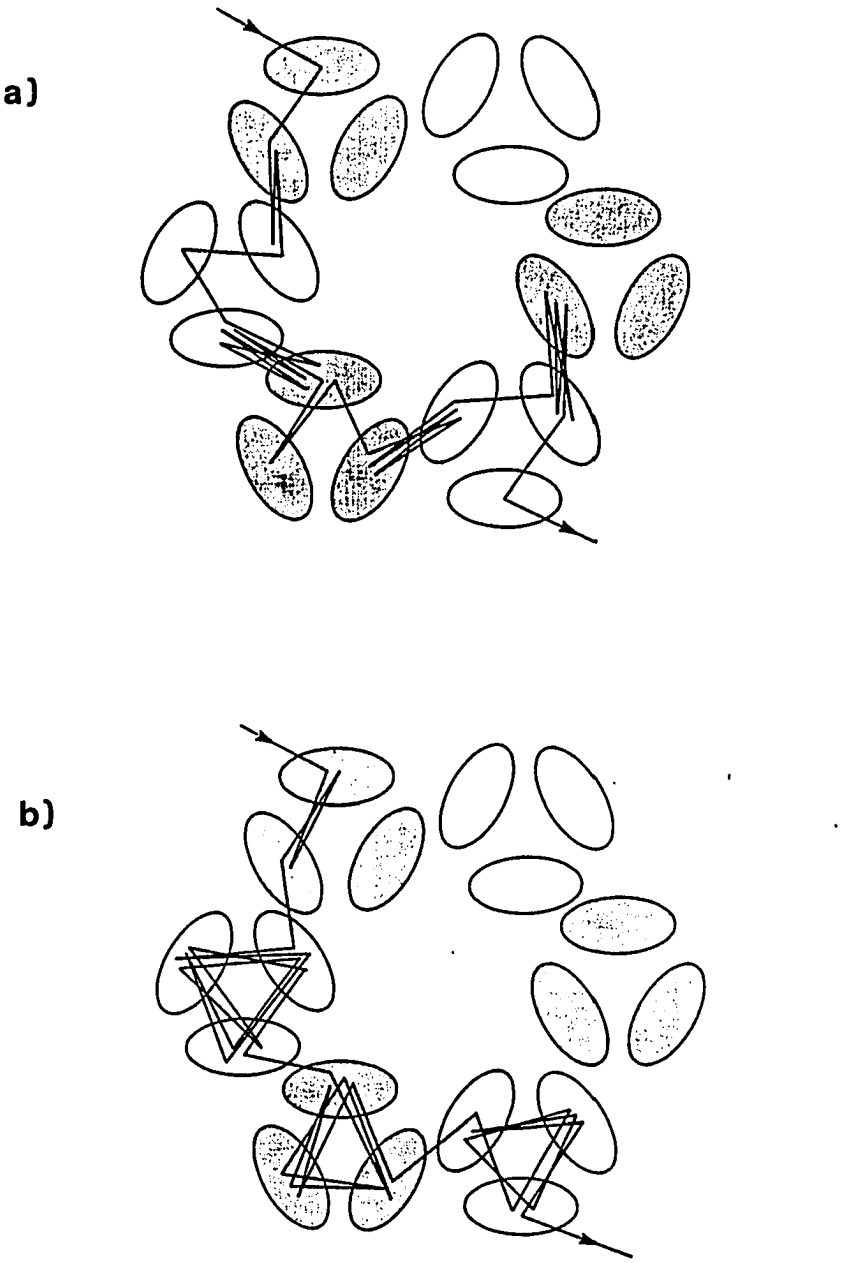

Figure 6-4. Excitation migration patterns for a) $w_{AD} >> w_{AB}$ and b) $w_{AD} << w_{AB}$.

The solutions are

$$A(t) = A_0[1 + 2\exp(-3w_{AB}t)]/3 \tag{6.9}$$

$$B(t) = C(t) = A_0[1 - \exp(-3w_{AB}t)]/3 \tag{6.10}$$

We next consider an idealized pump-probe experiment in which subunit A is excited in a trimer having the specific orientation shown in Fig. 6-5. The pump pulse is polarized along the laboratory-fixed x-axis, and pulses which probe $A_{\parallel}(t)$ and $A_{\perp}(t)$ are polarized along the x- and y-axes respectively. The trimer ab-plane is parallel to the xy-plane. The exciton transition moment for subunit A at the probe wavelength has components $\mu^o_{Ax} = \alpha$, $\mu^o_{Ay} = \beta$, $\mu^o_{Az} = \gamma$; these components are normalized so that $\alpha^2 + \beta^2 + \gamma^2 = 1$. By symmetry, the transition moments for the same exciton transition in subunits B and C are

$$\mu^o_{Bx} = -\alpha/2 - \beta\sqrt{3}/2 \tag{6.11a}$$

$$\mu^o_{By} = \alpha\sqrt{3}/2 - \beta/2 \tag{6.11b}$$

$$\mu^o_{Bz} = \gamma \tag{6.11c}$$

$$\mu^o_{Cx} = -\alpha/2 + \beta\sqrt{3}/2 \tag{6.11d}$$

$$\mu^o_{Cy} = -\alpha\sqrt{3}/2 - \beta/2 \tag{6.11e}$$

$$\mu^o_{Cz} = \gamma \tag{6.11f}$$

For a trimer whose orientation is displaced from that in Fig. 6-5 by

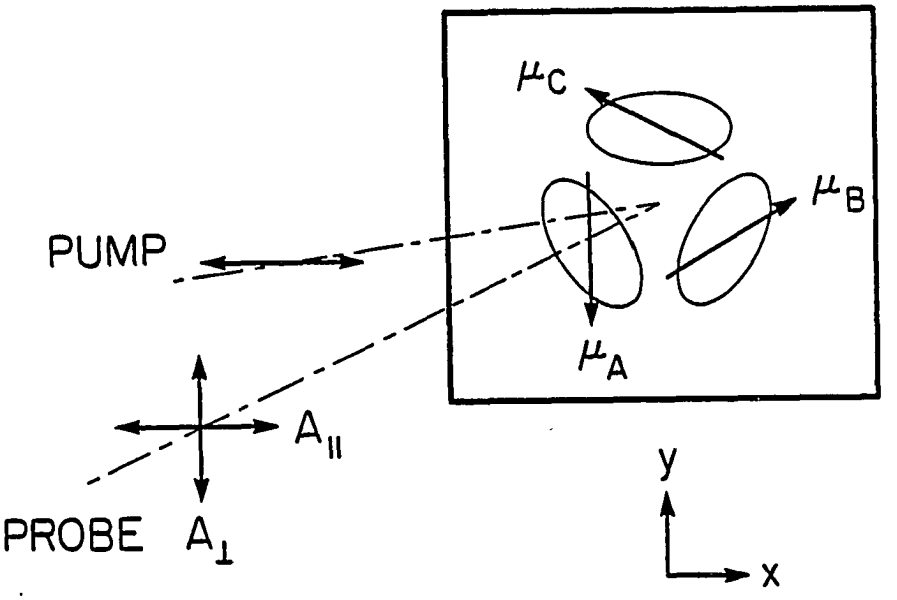

Figure 6-5. Pump-probe beam geometry and exciton transition moment orientations used in derivation of Eqs. 6.11 through 6.13.

arbitrary Euler angles ϕ, θ, χ, the transition moments in the laboratory system may be expressed using the pertinent rotation matrix $\underline{\underline{\lambda}}$ [27],

$$\begin{aligned} \mu_A &= \underline{\underline{\lambda}} \cdot \mu_A^o \\ \mu_B &= \underline{\underline{\lambda}} \cdot \mu_B^o \\ \mu_C &= \underline{\underline{\lambda}} \cdot \mu_C^o \end{aligned} \tag{6.12}$$

Rotational averaging over the random BChl $\underline{a}$-protein crystallite orientations in the solution then yields

$$\begin{aligned} A_{\parallel}(t) &= P(t)\left[\langle\mu_{Ax}^4\rangle A(t) + \langle\mu_{Ax}^2\mu_{Bx}^2 + \mu_{Ax}^2\mu_{Cx}^2\rangle B(t)\right] \\ A_{\perp}(t) &= P(t)\left[\langle\mu_{Ax}^2\mu_{Ay}^2\rangle A(t) + \langle\mu_{Ax}^2\mu_{By}^2 + \mu_{Ax}^2\mu_{Cy}^2\rangle B(t)\right] \end{aligned} \tag{6.13}$$

Substitution of Eqs. 6.9-6.12 into Eqs. 6.13 then leads to expressions for $A_{\parallel}(t)$, $A_{\perp}(t)$ which are identical to the phenomenological Eqs. 6.1 if one makes the associations

$$\tau = 1/3w_{AB} \tag{6.14}$$

and

$$a = (3\gamma^2 - 1)^2/4 \tag{6.15}$$

According to this model, the observed depolarization lifetime τ is shorter than the exciton hopping time w_{AB}^{-1} by a factor of three. The form of the

residual anisotropy parameter a, which depends on the projection γ of the exciton moment along the trimer symmetry axis, is reminiscent of intrinsic fluorescence depolarization observed in solutions of molecules in which the fluorescence transition moment is inclined at an angle $\cos^{-1}\gamma$ from the absorption moment [28].

Extension of this kinetic model to general w_{AB}/w_{AD} requires *ad hoc* assumptions about the crystal boundaries. To test the effects of crystal size on the calculated absorption transients, we compared the EET simulated in $P6_3$ crystallites containing 7 trimers and 27 trimers. In the first type of calculation, excitation in the initially excited subunit A was allowed to migrate to subunits in the six trimers adjacent to trimer ABC. (These six trimers coincide with trimers DEF, GIJ, and HKL in the projection of Fig. 6-3, and they occupy ab-planes located 49.3 Å above and 49.3 Å below the plane of trimer ABC.) Only six of the 21 subunit exciton populations in this 7-trimer calculation are independent by symmetry. Their Laplace transforms a(s) through i(s) obey

$$(2w_{AB} + 2w_{AD} + s)a(s) - 2w_{AB}b(s) - 2w_{AD}d(s) = A_0 \qquad (6.16a)$$

$$-w_{AB}a(s) + (w_{AB} + 2w_{AD} + s)b(s) - 2w_{AD}g(s) = 0 \qquad (6.16b)$$

$$-w_{AD}a(s) + (2w_{AB} + w_{AD} + s)d(s) - 2w_{AB}e(s) = 0 \qquad (6.16c)$$

$$-w_{AB}d(s) + (w_{AB} + s)e(s) = 0 \qquad (6.16d)$$

$$-w_{AD}b(s) + (2w_{AB} + w_{AD} + s)g(s) - 2w_{AB}i(s) = 0 \qquad (6.16e)$$

$$-w_{AB}g(s) + (w_{AB} + s)i(s) = 0 \qquad (6.16f)$$

The seven determinants required for computation of the six Laplace transforms were evaluated numerically, and the inverse transforms A(t) through I(t) were obtained using the Stehfest algorithm [29]. Using equations for the 7-trimer system analogous to Eqs. 6.11 and 6.13, the polarized absorption transients $A_{\parallel}(t)$ and $A_{\perp}(t)$ were computed for given hopping rates w_{AB}, w_{AD} and probed exciton moment projection γ along the c-axis. In the 27-trimer calculation, the kinetic model included three trimers coinciding with ABC in the projection of Fig. 6-3, located at c=0 and ±98.6 Å; the two trimers superimposed on each of DEF, GIJ, and HKL and located at c = ±49.3 Å; and 18 peripheral trimers having subunits whose ab-projections are contiguous to those of subunits E, F, I, J, K, and L, located at c = 0 and ±98.6 Å. The anisotropy functions $r(t) = 2.5(A_{\parallel}-A_{\perp})/(A_{\parallel}+2A_{\perp})$ yielded by 7-trimer and 27-trimer calculations are compared for several combinations of w_{AB} and w_{AD} in Fig. 6-6. The 7-trimer and 27-trimer calculations produce virtually identical results for large w_{AB}/w_{AD}, e.g., for $w_{AB}/w_{AD} = 3$ in the top plot in Fig. 6-6. The effect of finite crystal size becomes apparent when intertrimer EET becomes more rapid than intratrimer transport, as shown for $w_{AB}/w_{AD} = 1/3$ in the bottom plot of Fig. 6-6. In the limit where $w_{AB}/w_{AD} \gg 1$, the depolarization dynamics are controlled by the first few migration steps, and are relatively insensitive to details of EET on the periphery. The anisotropy function in this limit approaches the single-exponential form $r(t) = (1-\underline{a})\exp(-t/\tau)+\underline{a}$, with the parameters τ and $\underline{a}$ given by Eqs. 6.14 and 6.15. The opposite limit $w_{AB}/w_{AD} = 0$ is a somewhat artificial case ($\kappa_{AB} = 0$) in which the excitation equilibrates between two parallel stacks of subunits whose projections coincide with A and D in Fig. 6-3. The

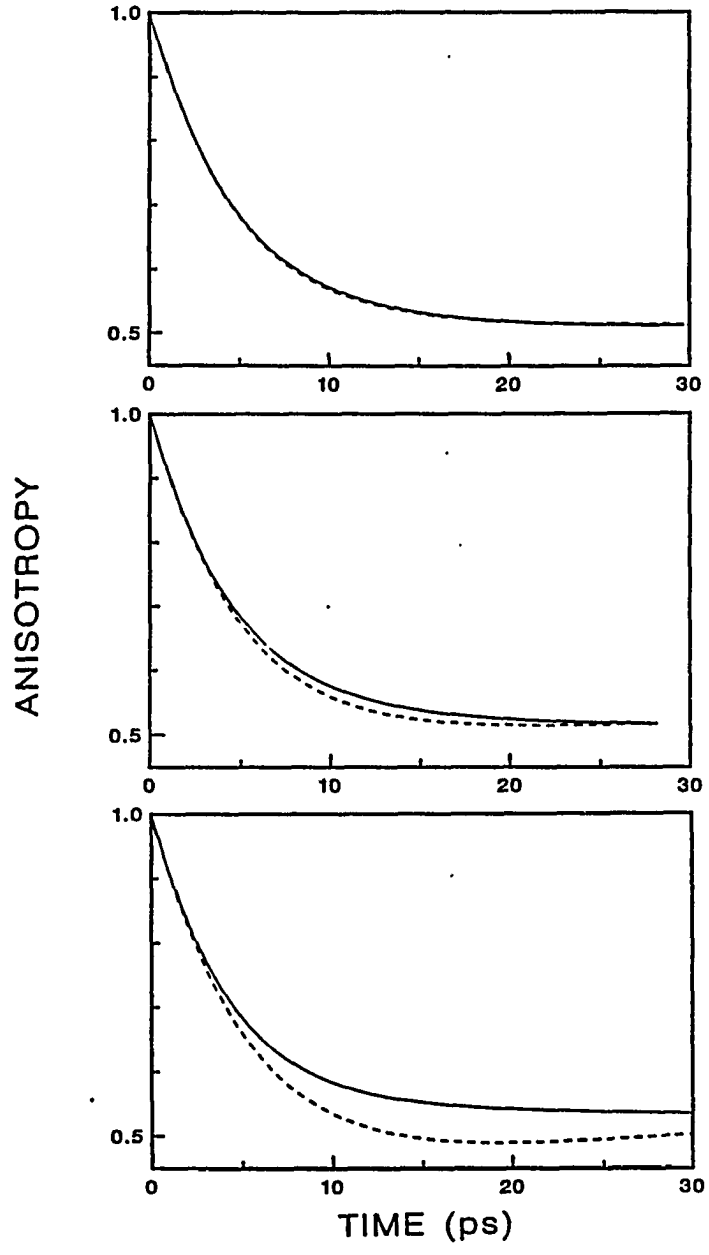

Figure 6-6. Calculated anisotropy functions r(t) from EET simulations in BChl a-protein for (top) w_{AB} = (20.2 ps)$^{-1}$, w_{AD} = (60.7 ps)$^{-1}$; (center) $w_{AB} = w_{AD}$ = (28.5 ps)$^{-1}$; (bottom) w_{AB} = (66.0 ps)$^{-1}$, w_{AD} = (22.0 ps)$^{-1}$. Dashed and continuous curves are 7-trimer and 27-trimer simulations, respectively.

anisotropy decay here becomes single-exponential in a 7-trimer calculation with lifetime $\tau = (3w_{AD})^{-1}$, and biexponential with lifetimes $(1.38w_{AD})^{-1}$ and $(3.62w_{AD})^{-1}$ in a 27-trimer calculation. For general combinations of w_{AB}, w_{AD} the anisotropy decay is nonexponential, with $r(\infty) = \underline{a}$ given by Eq. 6.15.

Most of the pump-probe profiles were obtained at 603 nm, the peak absorption wavelength in the room-temperature Q_x system. The 603 nm depolarization times τ obtained by fitting $A_{\parallel}$, $A_{\perp}$ with convolutions of Eqs. 6.1 with the laser autocorrelation function are distributed about a 4.78 ps mean with 0.76 ps standard deviation. We plot in Fig. 6-7 the anisotropy functions r(t) yielded by 27-trimer calculations for (a) $w_{AB} \neq 0$, $w_{AD} = 0$, (b) $w_{AB} = 3w_{AD}$, (c) $w_{AB} = w_{AD}$, and (d) $w_{AB} = w_{AD}/3$. The c-component γ of the probed exciton transition moment was fixed at 0.9, corresponding to a residual anisotropy parameter $\underline{a} = 0.511$ similar to the 603 nm experimental values (Table I). In each case, the values of w_{AB} and w_{AD} (Table II) were scaled to render the 1/e decay time in r(t) equal to 4.78 ps. The 4.78 ps single-exponential decay time in case (a) corresponds to the hopping rates $w_{AB} = 1/3\tau = (14.3\ \text{ps})^{-1}$ and $w_{AD} = 0$. While the anisotropy decays in cases (b) and (c), $w_{AB} = 3w_{AD}$ and $w_{AB} = w_{AD}$, are (strictly speaking) nonexponential, they are nearly indistinguishable from the single-exponential decay in case (a). Hence, Figure 6-7 emphasizes that the observed decay will be essentially single-exponential in our model for $w_{AB}/w_{AD} \geq 1$, and that a continuum of combinations of the hopping rates can account for the observed decay. Discernible nonexponentiality sets in for $w_{AB}/w_{AD} = 1/3$ (case (d)) in Fig. 6-7, but the displayed differences between this and the near-exponential

Table II. Förster transition rates from 27-trimer simulation of EET in BChl a-protein from P. aestuarii

Case	w_{AB}/w_{AD}	w_{AB}^{-1}, ps	w_{AD}^{-1}, ps	$w_{AB} + w_{AD}$, ps^{-1}
a	∞	14.3	∞	0.070
b	3	20.2	60.7	0.066
c	1	28.5	28.5	0.070
d	1/3	66.0	22.0	0.061

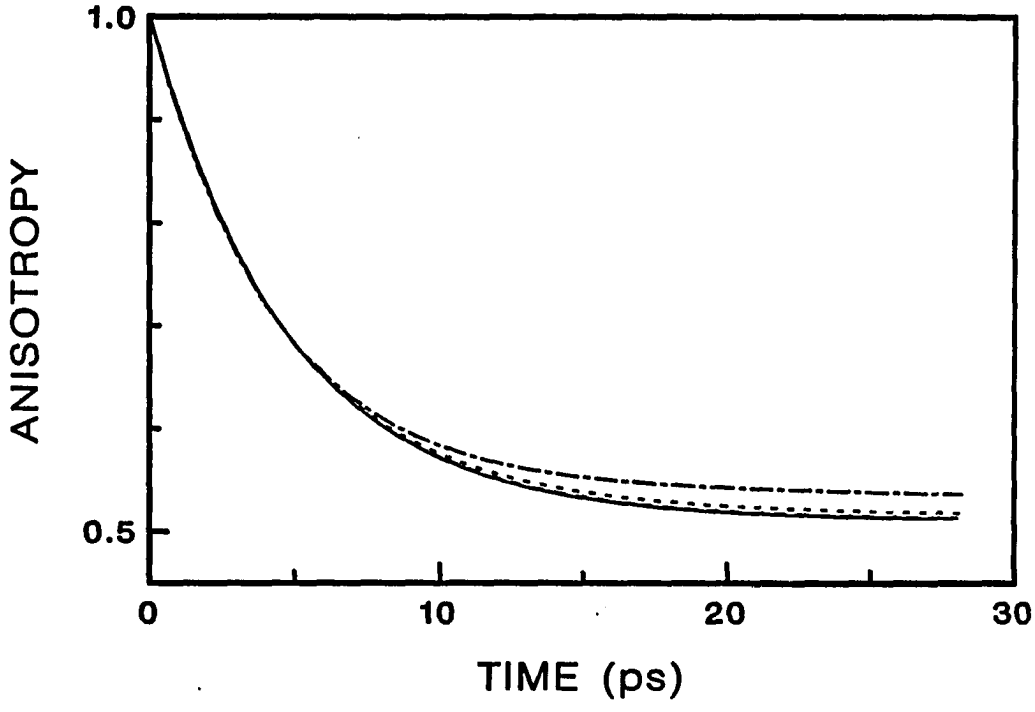

Figure 6-7. Calculated anisotropy functions r(t) from 27-trimer EET simulations, scaled to exhibit same decay time (4.78 ps) as the experimental mean from fits of 603 nm profiles using Eqs. 6.1. Anisotropy decays for cases (a) and (b), corresponding to $w_{AB}/w_{AD} = \infty$ and 3, are essentially congruent and are given by continuous curve. Cases (c) and (d), corresponding to $w_{AB}/w_{AD} = 1$ and 1/3, are given by dotted and dot-dashed curves respectively.

cases are too small for detection under current S/N in polarized pump-probe experiments. In summary, our 603 nm data establish a well-defined timescale for EET depolarization in the BChl a-protein. In the context of our kinetic model (which assumes migration only occurs between proximate subunits), they are consistent with the ranges of hopping timescales $0 < w_{AB}, w_{AD} \leq (15\ ps)^{-1}$ in combinations typified by Table II. Figure 6-7 shows that depolarization studies alone cannot prove whether one of the migration patterns illustrated in Fig. 6-4 dominates EET; independent knowledge of the pertinent orientational factors (e.g., from polarized single-crystal absorption studies of the 809 nm Q_y system or from successful modeling of exciton structure in the Q_y absorption and CD spectra) is required.

The 609 nm profiles are considerably noisier (S/N ~4) than those shown for 598 and 603 nm in Fig. 6-2. Their depolarization lifetimes, 3.48 and 1.47 ps, agree with the 603 nm mean (4.78 ps) within data scatter. The mean anisotropy parameter $\underline{a} = 0.477$ at 603 nm agrees well with the values $\underline{a} = 0.497$ and 0.485 obtained at 609 nm. This nominally corresponds to a Q_x exciton transition moment inclined 27° from the crystallite c-axis (Eq. 6.15). However, the P. aestuarii exciton bands overlap appreciably due to thermal broadening at 300K [7], and two distinct electronic transitions (2-1* and 1-2* in the notation of Petke et al. [30]) contribute to the Q_x system. More than one exciton band may therefore contribute to the observed anisotropy.

At 598 nm, the depolarization lifetime (24 ps mean, Table I) and lack of anisotropy contrast with the behavior exhibited at longer wavelengths. Wavelength variations in the anisotropy parameter a are easily

rationalized in terms of contrasting exciton transition moment orientations within the Q_x system. Our model cannot account for the observed disparity in depolarization lifetime, however, because EET should occur in the lowest-energy exciton component in the 809 nm Q_y system irrespective of excitation wavelength. In separate experiments, we obtained polarized Q_y fluorescence profiles from similar BChl _a_-protein solutions using a time-correlated single photon counting apparatus with 300 ps instrument function [7,8]. Under this resolution, profiles excited at 609 and 603 nm proved to be completely depolarized at all times, while discernible anisotropy ($I_\perp > I_\parallel$) appeared during the first few tens of ps in profiles excited at 593 nm. This behavior is consistent with the observed pump-probe depolarization timescales. These results suggest that some species other than BChl _a_-protein trimers contributes to the absorption at shorter wavelengths. Since the trimers cannot be dissociated into subunits without separating the BChl _a_ from the protein [31], the impurity species may be randomly oriented BChl _a_ molecules. This would explain the observed lack of anisotropy ($\underline{a} = 0$) at 598 nm; the observed negative polarization ($I_\parallel - I_\perp < 0$) at 593 nm would be a consequence [32] of the perpendicular Q_x and Q_y transition moments exhibited by BChl _a_ monomers. (The Q_x and Q_y transition moments are not generally orthogonal in BChl _a_-protein, owing to exciton interactions.) Furthermore, the Q_x spectrum of BChl _a_ monomers in solution peaks to the blue (573 nm in ether [14]) of the BChl _a_-protein spectrum. The difficulty experienced in simulating the Q_y absorption and CD spectra of similar BChl _a_-protein solutions may stem in part from such inhomogeneity.

In principle, crystallite orientational diffusion could contribute to

the observed depolarization. The linear dichroism of electric field-aligned BChl a-protein particles exhibits a decay time of ~140 μs [19]. Particle reorientation is thus far too slow to account for our depolarization timescale, as would be expected for BChl a-protein aggregates containing several tens of trimers. The magic-angle photobleaching decay (Fig. 6-1) may be attributed to excitation trapping at defect sites in the interior and on the surface of the BChl a-protein particles. Its nonexponentiality is logically a consequence of dispersion in the aggregate size and random walk length. The dominant long-component lifetime (52.4 ps) of the biexponential fit to the magic-angle decay in Fig. 6-1 is equivalent to ~3.7 excitation hops between neighboring subunits. It is consistent with the 55.1 ps dominant component lifetime which we find in the magic-angle Q_y fluorescence profile excited at 603 nm: a triexponential fit to this profile yields the decay law $I(t) = 0.816\exp(-t/55.1\ \text{ps}) + 0.073\exp(-t/507\ \text{ps}) + 0.121\exp(-t/2247\ \text{ps})$.

Acknowledgements

We are indebted to Professor R. E. Fenna for the donation of the BChl a-protein. We are grateful to W. E. Catron for supporting one of us (T. P. C.) through a Research Fellowship. The Ames Laboratory is operated for the U. S. Department of Energy by Iowa State University under Contract No. W-7405-Eng-82. This work was supported by the Office of Basic Energy Sciences.

References

1. Geacintov, N. E.; Breton, J. CRC Crit. Rev. Plant Sci. 1987, 5, 1.
2. Förster, Th. Discuss. Faraday Soc. 1959, 27, 7.
3. Sauer, K. In "Bioenergetics of Photosynthesis"; Govindjee, Ed.; Academic Press: New York, 1975.
4. Owens, T. G.; Webb, S. P.; Mets, L.; ALberte, R. S.; Fleming, G. R. Proc. Natl. Acad. Sci. USA 1987, 84, 1532.
5. Hemenger, R. P.; Lakatos-Lindenburg, K.; Pearlstein, R. M. J. Math. Phys. 1972, 13, 1056.
6. Pearlstein, R. M. Photochem. Photobiol. 1982, 35, 835.
7. Hart, D. E.; Anfinrud, P. A.; Struve, W. S. J. Chem. Phys. 1987, 86, 2689.
8. Anfinrud, P. A.; Struve, W. S. J. Chem. Phys. 1987, 87, 4256.
9. Causgrove, T. P.; Bellefeuille, S. M.; Struve, W. S. J. Phys. Chem., in press.
10. Huber, D. L.; Hamilton, D. S.; Barnett, B. Phys. Rev. B. 1977, 16, 4642.
11. Fenna, R. E.; Ten Eyck, L. F.; Matthews, B. W. Biochem. Biophys. Res. Commun. 1977, 75, 751.
12. Olson, J. M. Biochim. Biophys. Acta 1980, 594, 33.
13. Tronrud, D. E.; Schmid, M. F.; Matthew, B. W. J. Mol. Biol. 1986, 188, 443.
14. Philipson, K. D.; Sauer, K. Biochemistry 1972, 11, 1880.
15. Pearlstein, R. M.; Hemenger, R. P. Proc. Natl. Acad. Sci. USA 1978, 75, 4920.
16. Chang, J. C. J. Chem. Phys. 1977, 67, 3901.
17. Whitten, W. B.; Nairn, J. A.; Pearlstein, R. M. Biochim. Biophys. Acta 1978, 503, 251.
18. Lutz, M.; Hoff, A. J.; Brehamet, L. Biochim. Biophys. Acta 1982, 679, 331.

19. Whitten, W. B.; Pearlstein, R. M.; Phares, E. F.; Geacintov, N. E. Biochim. Biophys. Acta 1978, 503, 491.

20. French, P. M. W.; Taylor, J. R. In "Ultrafast Phenomena V"; Fleming, G. R.; Siegman, A. E., Eds.; Springer-Verlag: Berlin, 1986; p. 11.

21. Yasa, Z. A.; Amer, N. M. Opt. Commun. 1981, 36, 406.

22. Anfinrud, P.; Struve, W. S. Rev. Sci. Instrum. 1986, 57, 380.

23. van Grondelle, R.; Amesz, J. In "Light Emission by Plants and Bacteria"; Govindjee; Amesz, J.; Fork, D. C., Eds.; Academic Press: New York, 1986.

24. Fleming, G. R. "Chemical Applications of Ultrafast Spectroscopy"; Oxford University Press: New York, 1986.

25. Engh, R. A.; Petrich, J. W.; Fleming, G. R. J. Phys. Chem. 1985, 89, 618.

26. Anfinrud, P. A.; Hart, D. E.; Hedstrom, J. H.; Struve, W. S. J. Phys. Chem. 1986, 90, 2374.

27. Marion, J. B. "Classical Dynamics of Particles and Systems"; Academic Press: New York, 1965; p. 391.

28. Chuang, T. J.; Eisenthal, K. B. J. Chem. Phys. 1972, 57, 5094.

29. Stehfest, H. Commun. ACM 1970, 13, 47.

30. Petke, J. D.; Maggiora, G. M.; Shipman, L.; Christofferson, R. E. Photochem. Photobiol. 1979, 30, 203.

31. Matthews, B. W.; Fenna, R. E. Acc. Chem. Res. 1980, 13, 309.

32. Seely, G. R.; Connolly, J. S. In "Light Emission by Plants and Bacteria"; Govindjee; Amesz, J.; Fork, D. C., Eds.; Academic Press: New York, 1986.

ELECTRONIC EXCITATION TRANSPORT IN CORE ANTENNAE OF ENRICHED PHOTOSYSTEM I PARTICLES FROM SPINACH CHLOROPLASTS

Timothy P. Causgrove, Shumei Yang, and Walter S. Struve
Department of Chemistry and Ames Laboratory-USDOE
Iowa State University, Ames, Iowa 50011

and

John H. Golbeck
Department of Chemistry, Portland State University
Portland, Oregon 97207

CHAPTER VII. ELECTRONIC EXCITATION TRANSPORT IN CORE ANTENNAE OF ENRICHED PHOTOSYSTEM I PARTICLES FROM SPINACH CHLOROPLASTS

Introduction

Electronic excitation transport (EET) in antenna chlorophyll complexes of green photosynthetic organisms has been extensively modeled by theoreticians [1-7]. Singlet excitation, created by photon absorption in light-harvesting antenna complexes, is believed to migrate by an incoherent random-walk mechanism until it is trapped at a reaction center complex. The excitation hopping is governed by a resonance dipole-dipole interaction [8] which produces transition rates varying with chromophore separation as R^{-6}. Little structural information exists concerning the chlorophyll organization in green plant antennae; EET in such systems is frequently treated under the assumption that the chromophores occupy sites on a regular lattice [2,3]. It is now recognized that antenna chlorophyll molecules are complexed with proteins into clusters of six or more chromophores [7,9]. In Sauer's "pebble mosaic" model [9], electronic excitation is rapidly delocalized within such clusters, and migrates relatively slowly between clusters. Calculations which contrast the EET dynamics in a regular lattice with those in model systems containing strongly interacting clusters of five molecules [2] predict similar timescales in both cases for excitation trapping at reaction centers. Kinetic measurements of antenna fluorescence quenching by reaction centers therefore cannot easily differentiate between the regular lattice model and the pebble mosaic model for antenna EET.

Owens et al. [10] recently studied antenna fluorescence lifetimes in photosystem I core antennae of P700 Chl a-protein complexes from barley, and in a photosynthetic mutant of Chlamydomonas reinhardtii without the photosystem II antenna/reaction center complex. They determined that the fluorescence lifetime varied linearly with core antenna size in both species, in accordance with random walk models [11,12] in which the Chl a chromophores occupy sites in a regular lattice. Further analysis of the fluorescence profiles yielded a single-step EET time of 0.1 - 0.2 ps between chromophores in photosystem I core antennae. The excitation migration was found to be nearly diffusive, and photoconversion in the reaction center occurred on an average of once per 2.4 excitation visits from the core antenna.

In a separate work [13], we performed a polarized pump-probe study with ~1.5 ps resolution on the structurally well-characterized BChl a-protein from the green photosynthetic bacterium Prosthecochloris aestuarii. Solutions of the BChl a-protein in triglycerophosphate buffer were excited in the Q_x system with linearly polarized pulses between 598 and 609 nm, and probed with pulses polarized parallel or perpendicular to the pump polarization. The resulting transient photobleaching profiles $A_{\parallel}(t)$, $A_{\perp}(t)$ were fitted with convolutions of the laser autocorrelation function with the expressions

$$A_{\parallel}(t) = P(t)\{1 + 0.8[(1-a)\exp(-t/\tau) + a]\}$$
$$A_{\perp}(t) = P(t)\{1 - 0.4[(1-a)\exp(-t/\tau) + a]\} \qquad (7.1)$$

The isotropic function P(t), which describes ground-state recovery in BChl a-protein if the Q_x and Q_y excited states do not absorb at the probe wavelength, was determined from magic-angle profiles obtained with the probe polarization rotated by 54.7° from the pump polarization. The time-dependent depolarization implicit in Eqs. 7.1 describes the reorientation in the probed transition moment accompanying EET. Such pump-probe experiments therefore focus on the initial steps following laser excitation, rather than on overall random walk duration. At 603 nm, the mean depolarization lifetime τ for BChl a-protein was 4.78 ps. The depolarization dynamics were analyzed with a kinetic model [13] based on the crystal structure [14] of BChl a-protein, in which the basic structural unit is a trimer of subunits containing 7 BChl a molecules each. Spectroscopic evidence [15,16] suggests that strong exciton interactions exist between BChl a chromophores inside a subunit; the model therefore assumed that Förster excitation hopping occurred between exciton states delocalized inside subunits. EET was arbitrarily restricted to migration between neighboring subunits, and two kinds of hopping were distinguished. The first kind occurred with transition rate w_{AB} between subunits in the same trimer (e.g., A→B or D→E in the projection of the BChl a-protein $P6_3$ crystal structure shown in Fig. 7-1). The second kind occurred with rate w_{AD} between subunits in different trimers (e.g. A→D or B→H). The 4.78 ps depolarization lifetime observed at 603 nm proved to be consistent with combinations of w_{AB} and w_{AD} satisfying $(w_{AB} + w_{AD})^{-1} \approx$ 15 ps. In the limiting case where $w_{AB}/w_{AD} \gg 1$ (i.e., where intratrimer transport occurs far more rapidly than intertrimer transport), the theoretical expressions for $A_{\parallel}(t)$, $A_{\perp}(t)$ become identical to Eqs. 7.1; the

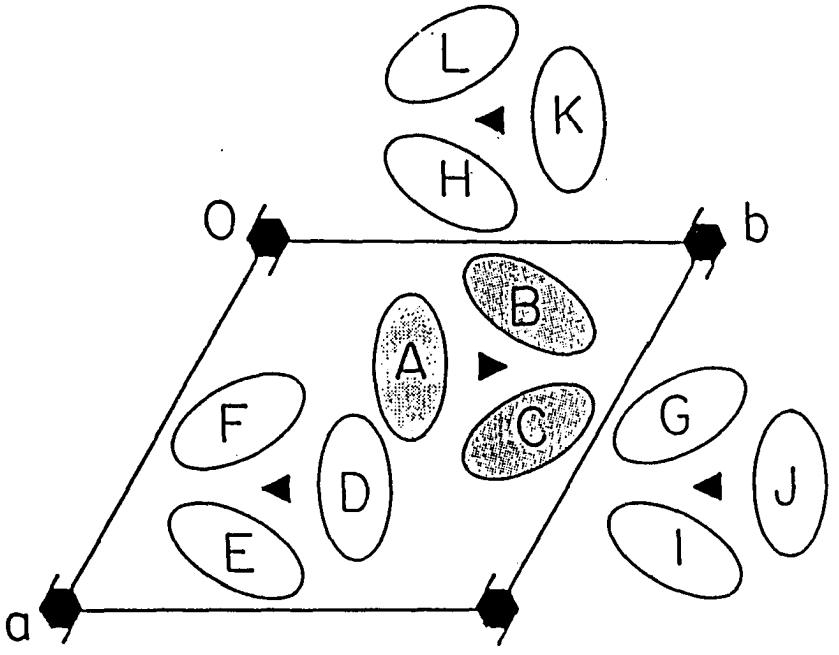

Figure 7-1. Schematic projection upon the ab-plane of the $P6_3$ crystal structure of BChl a-protein from Prostecochloris aestuarii, the only bacterial antenna system whose 3-dimensional structure is known. Unit cell dimensions are a = b = 111.9 Å, c = 98.6 Å [14]. Trimers DEF, GIJ, and HKL are separated from trimer ABC by 49.3 Å along the c-axis.

observed depolarization lifetime τ is then related to the intratrimer hopping rate w_{AB} by $w_{AB} = (3\tau)^{-1}$. In such a case, the transition rate w_{AB} consistent with $\tau = 4.78$ ps would be $(14.3 \text{ ps})^{-1}$. Nonzero values of the residual anisotropy parameter a were required to fit most polarized pump-probe profiles using Eqs. 7.1, owing to the nonrandom chromophore orientations in BChl a-protein. For the trimer packing geometry illustrated in Fig. 7-1, the parameter a is related to the direction cosine γ of the probed exciton transition moment along the trimer symmetry axis by [13] $a = (3\gamma^2 - 1)^2/4$.

In the present work, the pump-probe experiments have been extended to the Chl a-protein core antenna complex in enriched photosystem I particles from spinach chloroplasts. The antenna Chl a-protein architecture is unknown in spinach (as in other plants), and these experiments offer clues on the Chl a chromophore organization. The present pump and probe wavelengths (665 - 681 nm) overlap the lowest-energy band in the Q_y system of the enriched PS I particles (Fig. 7-2), providing direct excitation and monitoring of the singlet electronic state involved in transport. (This configuration contrasts with the BChl a-protein work [13] in which Q_y transport was monitored following excitation of the Q_x system.) The polarized profiles $A_{\parallel}(t)$, $A_{\perp}(t)$ from spinach PS I core antennae are remarkably similar to those obtained from P. aestuarii, and their isotropic decays P(t) yield direct information concerning the excitation trapping at the reaction centers.

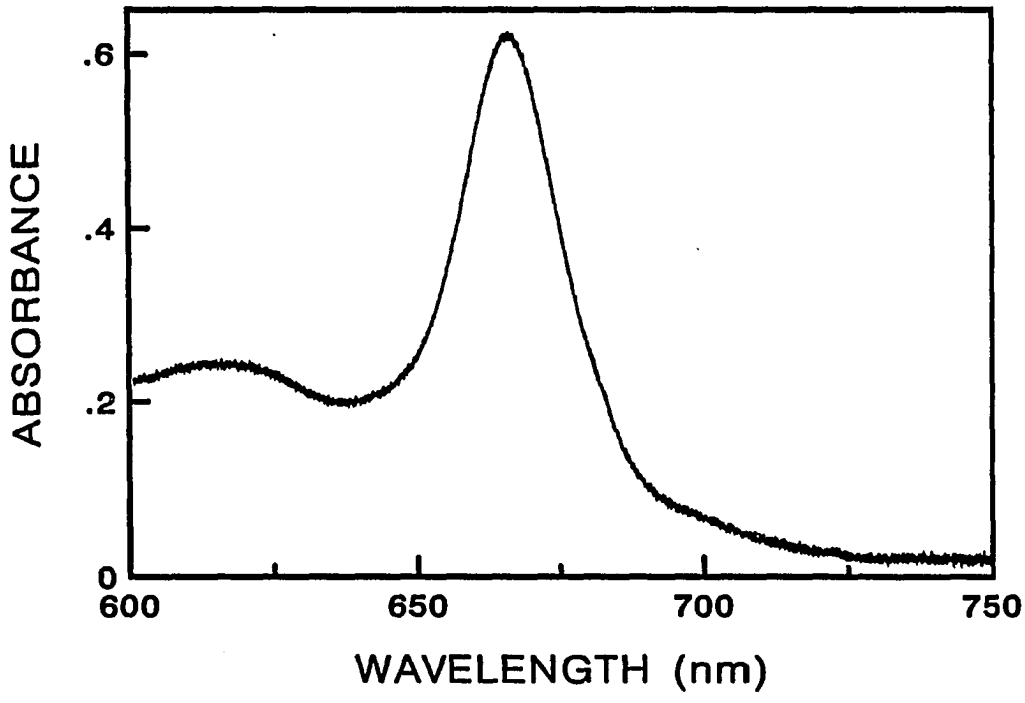

Figure 7-2. Absorption spectrum of PS I-60 particles from spinach at 1.6°K.

Experimental

For experiments performed between 665 and 681 nm, a multiline Ar^+ laser with 6 W plasma tube pumped a passively mode-locked dual-jet DCM/DDCI dye laser to produce vertically polarized pulses with ~40 mW average power at 125 MHz repetition rate. Autocorrelation traces at these wavelengths displayed FWHM ranging from 1.75 ps to 2.15 ps. The output beam was split into pump and probe beams, which were modulated at 5.0 and 0.5 MHz respectively with ~80% modulation depth using Isomet 1206C acousto-optic modulators. The pump beam delay was varied by reflection from a translatable BK-7 corner cube prism mounted on a Micro-Controle UT10050PP translation stage. The beam polarizations were defined using calcite Glan-Thompson prism polarizers; the probe polarization was fixed at 45° from the laser polarization, while the pump polarization was varied. Both beams were focussed to ~10 μm diameter in the sample using a 7.3 cm f.l. lens, and the average incident power was ~5 mW in each beam. The probe beam was monitored by an EG&G FOD-100 photodiode, and phase-locked single-sideband detection was performed at 5.5 MHz using a modified Drake R-7A radio receiver [17]. The receiver's signal-bearing 50 kHz intermediate frequency was tapped and demodulated in a Stanford Research Systems SR510 lock-in amplifier (LIA). Pump-probe data were transmitted from the LIA through an RS-232 port to a DEC MINC-23 computer operating in a TSX-Plus multi-user environment, where they were normalized to the square of the instantaneous laser intensity detected by a second EG&G FOD-100 monitor photodiode.

The PS I-60 sample preparation, which extracts solutions of highly

purified reaction center particles enriched in iron-sulfur protein and P700 from spinach chloroplasts, has been described previously [18]. A PS I-60 particle contains an 82-83 kDa reaction center Chl a-protein complex (CP I), along with 6 to 8 polypeptides (8-25 kDa) which are not complexed with chlorophyll and are termed Subunits II-VIII [19]. CP I and Subunits II-VIII contain two 2Fe-2S centers and two 4Fe-4S centers, respectively; the 43-45 kDa light-harvesting Chl a/Chl b antenna complex (LHC I) present in PS I-110 particles [19] are absent in PS I-60. The particles are largely free of Chl b, cytochromes f, b_6, and b-559; their β-carotene content is considerably reduced. PS I-60 solutions in water, glycerol, Tris buffer, and Triton X-100 exhibited ~2.5 optical density at 675 nm in a 1 cm cell. Samples were housed between λ/4 fused silica flats separated by an 800 μm teflon spacer, and were rotated at 12 Hz during pump-probe scans to minimize photooxidation by the laser beams. All experiments were performed at room temperature.

Results

Close similarities appear among the PS I-60 magic-angle photobleaching profiles obtained at 665, 670, 675, and 681 nm, wavelengths which lie near the peak of the main Chl a Q_y absorption band of the core antenna (Fig. 7-2). The isotropic decay at these wavelengths is nonexponential; a typical 675 nm magic-angle profile is shown in Fig. 7-3. Each of the magic-angle profiles was fitted for times later than ~1.5 ps with a convolution of the laser autocorrelation function with a biexponential decay law; the resulting optimized parameters are listed in Table I. Two

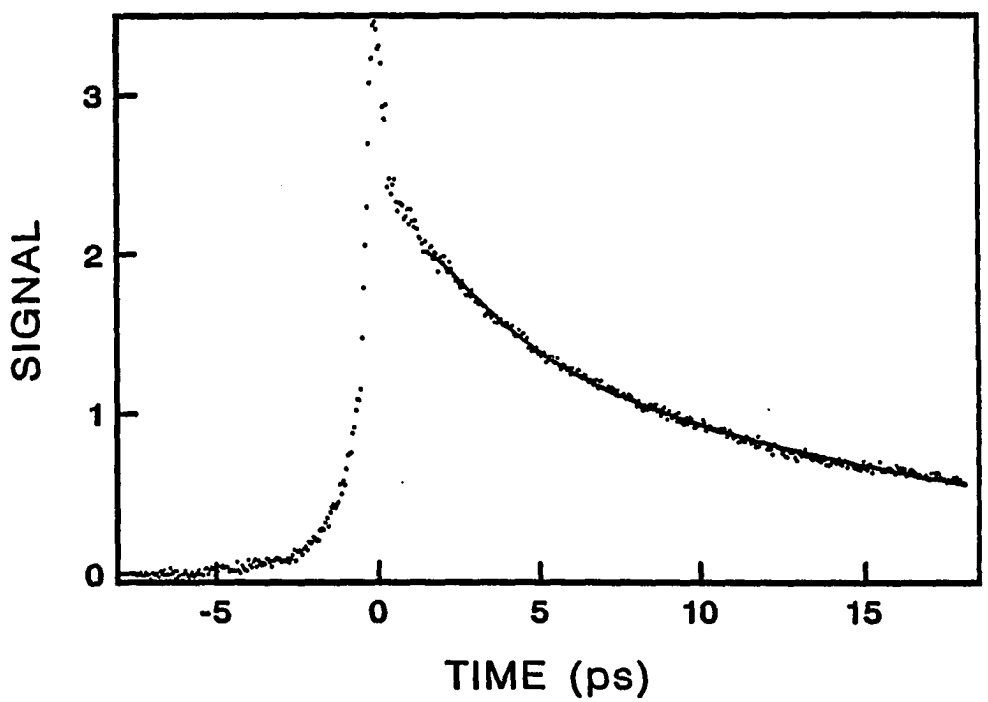

Figure 7-3. Magic-angle profile for PS I-60 particles at 675 nm. Continuous curve is convolution of laser autocorrelation function with biexponential decay law $P(t) = 0.534\exp(-t/1.99\ \text{ps}) + 0.466\exp(-t/16.8\ \text{ps})$.

Table I. Biexponential fitting parameters for magic-angle profiles from spinach photosystem I particles

Wavelength, nm	Scan duration, ps	A_1	τ_1, ps	A_2	τ_2, ps
665	25	0.725	1.41	0.275	18.7
	25	0.781	1.10	0.219	17.2
	25	0.744	1.25	0.256	16.8
	25	0.712	1.29	0.288	17.0
	50	0.678	3.94	0.322	36.8
	50	0.699	2.78	0.301	28.2
670	25	0.597	1.64	0.403	17.6
	25	0.599	1.69	0.401	17.8
	25	0.624	1.69	0.376	18.2
	25	0.615	1.47	0.385	16.5
	50	0.630	4.39	0.370	29.8
	50	0.634	4.38	0.366	31.8
675	25	0.520	2.00	0.480	15.8
	25	0.534	1.99	0.466	16.8
	25	0.570	2.99	0.430	19.9
	50	0.665	5.97	0.335	33.0
	50	0.672	6.06	0.328	32.5
	50	0.632	5.67	0.368	31.9
681	25	0.551	3.38	0.449	19.7
	25	0.506	2.83	0.494	17.9
	50	0.613	6.47	0.387	23.2
	50	0.460	4.90	0.540	18.5
	50	0.541	5.69	0.459	22.8
	50	0.568	6.00	0.432	22.7
	50	0.544	6.13	0.456	22.9
	50	0.629	5.60	0.371	29.1
	50	0.603	5.64	0.397	25.9

pump-probe scan durations were used (25 and 50 ps); the final biexponential parameters depend on the duration selected, in consequence of the multi-exponential character of the isotropic decays. The profiles accumulated using 25 ps sweeps invariably show a dominant short component with average lifetime between 1.26 ps (665 nm) and 3.11 ps (681 nm); the long component lifetimes are distributed about a mean of 17.8 ps with a standard deviation of 1.2 ps. The short component tends to exhibit a somewhat larger preexponential factor at 665 nm than at 670, 675, or 681 nm. There is little else to distinguish among the isotropic decays at these four wavelengths. Nearly identical magic-angle profiles were obtained when the pump and probe beams were both attenuated by 50%; exciton annihilation is not a major component of the isotropic decay. A caveat should be attached to the present use of the 125 MHz laser repetition rate, which corresponds to 8 ns pulse spacing. While the intersystem crossing quantum yield in Chl *a* is low, sufficiently high repetition rates can build up appreciable triplet state populations to introduce artifacts into the absorption transients. Cavity-dumped pump-probe experiments testing the effects of variable repetition rate are planned in our laboratory.

Polarized transient profiles $A_{\parallel}(t)$ and $A_{\perp}(t)$ are shown in Fig. 7-4 for 675 and 681 nm. Such profiles were fitted with convolutions of the autocorrelation function with Eqs. 7.1 using a linked convolute-and-compare algorithm described previously [20]. The biexponential parameters in the isotropic decay $P(t)$ were held at the optimized values obtained from deconvolution of the corresponding magic-angle profiles (Table I);

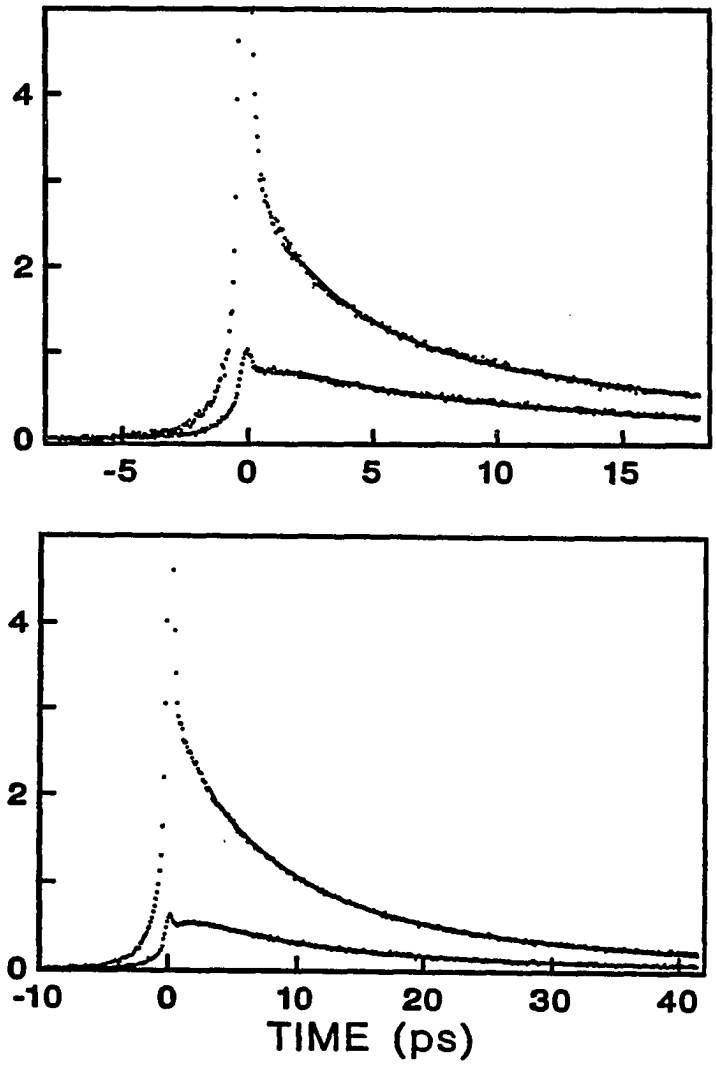

Figure 7-4. Polarized pump-probe transients for PS I-60 particles at 675 nm (upper panel) and at 681 nm (lower panel). In each panel, the upper and lower traces correspond to $A_{\parallel}(t)$ and $A_{\perp}(t)$ respectively. Continuous curves show convolutions of laser autocorrelation function with Eqs. 7.1, with lifetime and anisotropy parameters as described in text. Parameters for displayed profiles are τ = 2.90 ps, $\underline{a}$ = 0.458 (675 nm), and τ = 2.91 ps, $\underline{a}$ = 0.636 (681 nm).

Table II. Fitting parameters for polarized pump-probe profiles from photosystem I particles from spinach

Wavelength, nm	Scan duration, ps	a	$\bar{a}$	τ, ps	$\bar{\tau}$, ps
665	25	0.489	0.625	4.36	6.59
	25	0.658		7.73	
	25	0.677		7.02	
	25	0.402		6.77	
	50	0.687		0.92	
	50	0.837		12.8	
670	25	0.427	0.466	5.00	3.65
	25	0.409		2.79	
	25	0.409		3.31	
	25	0.489		2.88	
	50	0.651		5.54	
	50	0.412		2.43	
675	25	0.460	0.431	2.47	2.85
	25	0.458		2.91	
	25	0.446		2.01	
	50	0.313		2.33	
	50	0.492		3.72	
	50	0.419		3.64	
681	25	0.542	0.627	3.37	3.47
	50	0.636		2.91	
	50	0.621		2.68	
	50	0.671		5.51	
	50	0.674		4.19	
	50	0.725		3.00	
	50	0.522		2.66	

the phenomenological depolarization lifetime τ and the residual anisotropy parameter $\underline{a}$ were varied. The final parameters from these linked deconvolutions are listed in Table II. Since $A_{\parallel}(t)/A_{\perp}(t)$ do not tend to unity at long times (cf., Fig. 7-4), nonzero anisotropy parameters were generally required to fit the polarized transients. (According to Eqs. 7.1, this ratio approaches $(1 + 0.8\underline{a})/(1 - 0.4\underline{a})$ as $t \to \infty$.) Moreover, the anisotropy parameter depends on the wavelength probed. The difference between the average anisotropy parameters $\underline{a} = 0.431$ and 0.627 at 675 and 681 nm, respectively, is significantly larger than their standard deviations, 0.062 and 0.069. This wavelength variation is also reflected in Fig. 7-4, in which the profiles exhibit contrasting asymptotic ratios $A_{\parallel}(t)/A_{\perp}(t)$ at 675 and 681 nm. The average depolarization lifetimes $\bar{\tau}$ range from 6.59 ps at 665 nm to 2.85 ps at 675 nm. This depolarization timescale is similar to that found in BChl $\underline{a}$-protein from $\underline{P}$. $\underline{aestuarii}$ [13], and the residual anisotropy in PS I-60 is also reminiscent of the behavior exhibited that system. The former observation is pertinent to the physical interpretation of the transient depolarization in $\underline{P}$. $\underline{aestuarii}$, since those experiments probed photobleaching in the Q_x rather than the Q_y system of the BChl $\underline{a}$-protein [14]. The similarity of the depolarization timescales in the two species corroborates the attribution of the BChl $\underline{a}$-protein depolarization to EET, rather than to nonradiative processes such as $Q_x \to Q_y$ internal conversion.

Discussion

Owens et al. [10] recently reported that the fluorescence decay of P700 Chl a-protein preparations with Chl a/P700 ratios <40 exhibits a dominant component with lifetime between 15 and 30 ps. This order of magnitude is commensurate with our PS I-60 isotropic long-component decays ($\bar{\tau}$ = 17.8 ps) in Table I, and suggests that our isotropic decay mechanism for 665 nm < λ < 681 nm is efficient excitation trapping at the P700 reaction center. The short components in Table I typically contribute <15% of the integrated photobleaching decay, and would escape detection under the 60-80 ps instrument function [10] in time-correlated single photon counting.

While much is now known about the 3-dimensional structure of BChl a-protein from P. aestuarii [14], the light-harvesting Chl a/b-protein complex of photosystem II [21], and the light-harvesting C-phycocyanin biliprotein from the blue-green alga Mastigocladus laminosus [22], we are unaware of similar data on the structure of photosystem I core antennae. The oligomers in the well-characterized pigment-containing proteins in photosynthetic systems have all proven to be trimers, perhaps because three-fold symmetry is the minimum required for isotropic absorption of light polarized in a plane perpendicular to the oligomer's symmetry axis [14]. We therefore consider kinetic depolarization models similar to one proposed earlier [13] for EET in BChl a-protein. Closed-form expressions for $A_{\parallel}(t)$ and $A_{\perp}(t)$ are obtained when the intratrimer transition rate w_{AB} is assumed to be much faster than the intertrimer transition rate w_{AD}. Under these conditions, the exciton state populations A(t), B(t), C(t) in

subunits A, B, and C following creation of an exciton state in subunit A evolve as [13]

$$A(t) = A_0[1 + 2\exp(-3w_{AB}t)]/3$$
$$B(t) = C(t) = A_0[1 - \exp(-3w_{AB}t)]/3 \qquad (7.2)$$

where k is the rate constant for hopping between adjacent subunits. The corresponding expressions for the polarized transient components are

$$A_{\parallel}(t) = P(t)[\langle\mu_{Ax}^4\rangle A(t) + \langle\mu_{Ax}^2\mu_{Bx}^2 + \mu_{Ax}^2\mu_{Cx}^2\rangle B(t)] \qquad (7.3a)$$

$$A_{\perp}(t) = P(t)[\langle\mu_{Ax}^2\mu_{Ay}^2\rangle A(t) + \langle\mu_{Ax}^2\mu_{By}^2 + \mu_{Ax}^2\mu_{Cy}^2\rangle B(t)] \qquad (7.3b)$$

Here μ_A, μ_B, μ_C are the exciton transition moments in subunits A, B, C; the laboratory-fixed x and y axes are oriented along the parallel and perpendicular probe polarizations, respectively. EET between adjacent subunits in a trimer rotates the probed exciton transition moment by $2\pi/3$ about the trimer symmetry axis. Rotational averaging of Eqs. 7.3 over the random BChl a-protein crystallite orientations in solution then leads to Eqs. 7.1 for the polarized transients $A_{\parallel}(t)$ and $A_{\perp}(t)$, provided that $\tau = 1/3w_{AB}$ and $\underline{a} = (3\gamma^2 - 1)^2/4$. We may also consider dimers (n=2) and tetramers (n=4) as possible oligomeric forms a priori (Fig. 7-5). Exciton migration between adjacent subunits with rate constant w_{AB} rotates the probed exciton transition moment by $2\pi/n$ about the oligomer symmetry axis. For dimers, our kinetic model again leads to Eqs. 7.1 for $A_{\parallel}(t)$ and $A_{\perp}(t)$,

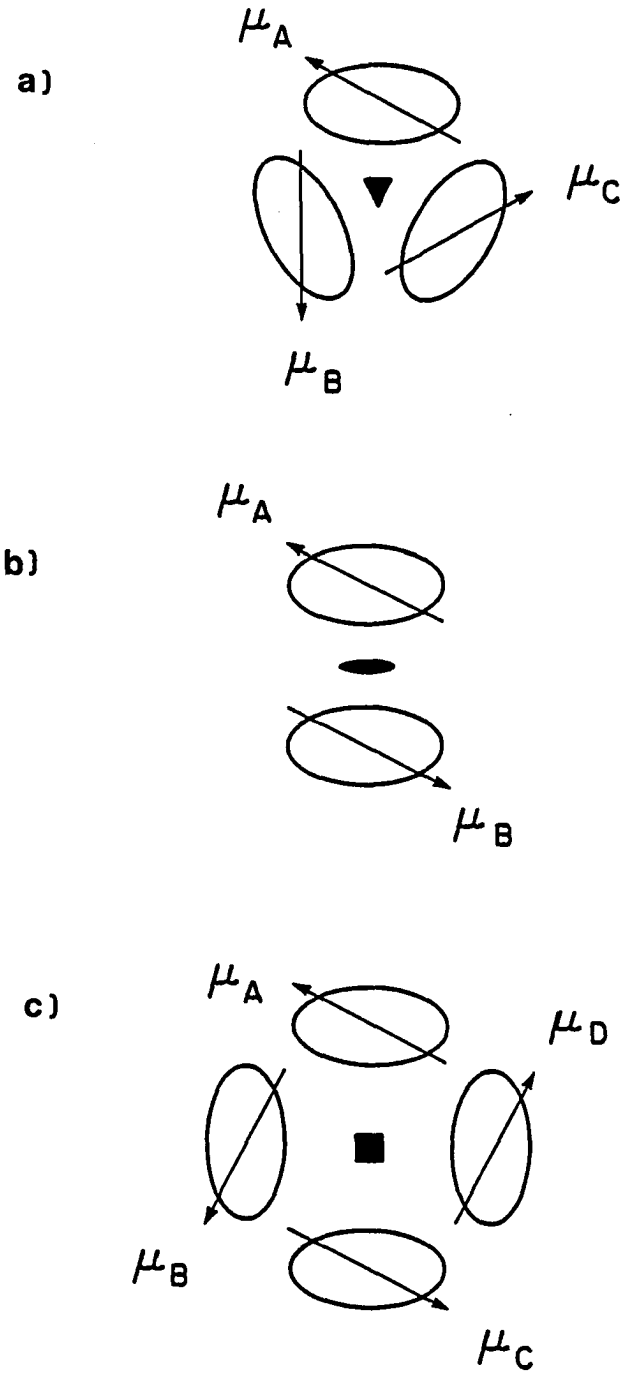

Figure 7-5. Oligomeric Chl a-protein models for interpretation of time-dependent depolarization due to EET: a) trimer, as in BChl a-protein from P. aestuarii; b) dimer; and c) tetramer.

with the depolarization lifetime and residual anisotropy parameter given by $\tau = 1/2w_{AB}$ and $\underline{a} = 1 - 3\gamma^2 + 3\gamma^4$. For tetramers, the model leads to more complicated expressions with three depolarization lifetimes,

$$A_{\parallel}(t) = P(t)\{(2-2\gamma^2+3\gamma^4) + (1+2\gamma^2-3\gamma^4)\exp(-4kt) + 2(\gamma^2-\gamma^4)[\exp(-2kt) - \exp(-6kt)]\} \quad (7.4a)$$

$$A_{\perp}(t) = P(t)\{(3+2\gamma^2-3\gamma^4) + (3\gamma^4-2\gamma^2-1)\exp(-4kt) - 2(\gamma^2-\gamma^4)[\exp(-2kt) - \exp(-6kt)]\}/2 \quad (7.4b)$$

While these do not exhibit the form of Eqs. 7.1, the asymptotic depolarization at long times may be described for tetramers using an effective anisotropy parameter $\underline{a} = 2.5[A_{\parallel}(\infty) - A_{\perp}(\infty)]/[A_{\parallel}(\infty) + 2A_{\perp}(\infty)] = (3\gamma^2 - 1)^2/4$. Generalization of these kinetic models to include EET between subunits belonging to different oligomers would require knowledge of the oligomer packing in photosystem I core antennae; this architecture has not been characterized.

All of these models generally predict a nonvanishing anisotropy parameter $\underline{a}$ in consequence of the nonrandom chromophore organizations in the oligomers. The observation of $\underline{a} \neq 0$ in Table II establishes for the first time that local ordering exists in the Chl _a_-protein core antenna of PS I-60, irrespective of the oligomer model assumed. Polarized photobleaching decays exhibiting the form of Eqs. 7.1 are consistent with either dimers of trimers as basic Chl _a_-protein structural units. In our judgement, the present time resolution and profile S/N (cf., Fig. 7-4) are not sufficient to differentiate between the single-exponential

polarization decay predicted for dimers and trimers (Eqs. 7.1) and the multiexponential decay expected in higher oligomers (e.g., Eqs. 7.4) and in more sophisticated kinetic models incorporating transport between oligomers. This question may be resolved by performing similar pump-probe experiments with a high-power, low-noise Nd:YAG-pumped dye laser. If the oligomers are assumed to be trimers of Chl _a_-protein subunits, the average depolarization lifetimes $\bar{\tau}$ = 6.59 and 2.85 ps at 665 and 675 nm (Table II) correspond to rate constants w_{AB} = $(19.8\ ps)^{-1}$ and $(8.6\ ps)^{-1}$ respectively for hopping between adjacent subunits. The fractional scatter in depolarization lifetimes τ is considerably larger than that in the anisotropy parameters _a_, because the depolarization timescale exceeds the laser pulse FWHM by less than an order of magnitude.

The depolarization timescale in PS I-60 is more than an order of magnitude slower than the 0.2 ps hopping time of Owens et al. [10] using a regular lattice model for EET in P700 Chl _a_-protein complex preparations. A logical rationalization for the comparatively long depolarization lifetimes τ in Table II is that they arise from EET between clusters of Chl molecules, rather than between individual chromophores. On the basis of spectral hole-burning experiments on PS I core antenna complexes, Gillie et al. [23] have already pointed out that the antenna protein structure may endow EET with some delocalized exciton character. In this interpretation, the wavelength variation in the residual anisotropy parameter would stem from contrasting directions of transition moments in different exciton components of the Chl _a_-protein Q_y system. A more detailed rationalization of time-domain experiments like ours awaits better structural characterization of the Chl _a_-protein complexes.

Acknowledgements

We are grateful to W. E. Catron for supporting one of us (T. P. C.) through a Research Fellowship. We thank Professor John Golbeck for providing the PS I-60 preparations, and we thank Mr. J. Kevin Gillie for obtaining the PS I-60 absorption spectrum in Fig. 7-2. We are indebted to Professors Gerald Small and Kenneth Sauer for illuminating discussions. The Ames Laboratory is operated for the U. S. Department of Energy by Iowa State University under Contract No. W-7405-Eng-82. This work was supported by the Office of Basic Energy Sciences.

References

1. Knox, R. S. In "Bioenergetics of Photosynthesis"; Govindjee, Ed.; Academic Press: New York, 1975.

2. Knox, R. S. In "Primary Processes of Photosynthesis", Vol. 2; Barber, J., Ed.; Elsevier: Amsterdam, 1977.

3. Pearlstein, R. M. In "Photosynthesis: Energy Conversion by Plants and Bacteria", Vol. 1; Govindjee, Ed.; Academic Press: New York, 1982.

4. Paillotin, G. J. Theor. Biol. 1972, 36, 223.

5. Paillotin, G. J. Theor. Biol. 1976, 58, 219.

6. van Grondelle, R. Biochim. Biophys. Acta 1985, 811, 147.

7. Geacintov, N. E.; Breton, J. CRC Crit. Rev. Plant Sci. 1987, 5, 1.

8. Förster, Th. Discuss. Faraday Soc. 1959, 27, 7.

9. Sauer, K. In "Bioenergetics of Photosynthesis"; Govindjee, Ed.; Academic Press: New York, 1975.

10. Owens, T. G.; Webb, S. P.; Mets, L.; ALberte, R. S.; Fleming, G. R. Proc. Natl. Acad. Sci. USA 1987, 84, 1532.

11. Hemenger, R. P.; Lakatos-Lindenburg, K.; Pearlstein, R. M. J. Math. Phys. 1972, 13, 1056.

12. Pearlstein, R. M. Photochem. Photobiol. 1982, 35, 835.

13. Causgrove, T. P.; Yang, S.; Struve, W. S. J. Phys. Chem., in press.

14. Matthews, B. W.; Fenna, R. E. Acc. Chem. Res. 1980, 13, 309.

15. Philipson, K. D.; Sauer, K. Biochemistry 1972, 11, 1880.

16. Pearlstein, R. M.; Hemenger, R. P. Proc. Natl. Acad. Sci. USA 1978, 75, 4920.

17. Anfinrud, P.; Struve, W. S. Rev. Sci. Instrum. 1986, 57, 380.

18. Golbeck, J. H. Methods Enzymol. 1980, 69, 129.

19. Green, B. R. Photosyn. Res. 1988, 15, 3.

20. Anfinrud, P. A.; Hart, D. E.; Hedstrom, J. H.; Struve, W. S. J. Phys. Chem. 1986, 90, 2374.

21. Lyon, M. K.; Unwin, P. N. T. Photochem. Photobiol. 1988, 47, 30S (Abstracts of the 16th Annual Meeting for the American Society for Photobiology, March 13-17, 1988).

22. Schirmer, T.; Bode, W.; Huber, R.; Sidler, W.; Zuber, H. J. Mol. Biol. 1985, 184, 257.

23. Gillie, J. K.; Hayes, J. M.; Small, G. J.; Golbeck, J. H. J. Phys. Chem. 1986, 90, 3795.

POLARIZED PUMP-PROBE SPECTROSCOPY OF PHOTOSYSTEM I ANTENNA EXCITATION TRANSPORT

Timothy P. Causgrove, Shumei Yang, and Walter S. Struve

Department of Chemistry and Ames Laboratory-USDOE
Iowa State University, Ames, Iowa 50011

CHAPTER VIII. POLARIZED PUMP-PROBE SPECTROSCOPY OF PHOTOSYSTEM I ANTENNA EXCITATION TRANSPORT

Introduction

The structure and electronic excitation transport (EET) dynamics in photosystem I core and peripheral antennae of green plants have been extensively studied by protein/pigment characterization [1-5], absorption and circular dichroism (CD) spectra [6-8], and subnanosecond fluorescence [8-15] and picosecond absorption [16-19] spectroscopy. The PS I core antenna contains some 25-30 Chl a molecules [6] that are complexed with the P700 reaction center by two polypeptides, whose molecular weights have been variously reported as in the 60-70 kD range [20, 21] and as 82, 83 kD [1]. The peripheral antenna comprises Chl a and Chl b chromophores complexed with several smaller (19-25 kD) polypeptides [4, 5, 22, 23]. Recent CD studies of the molecular organization in the PS I core antenna [6, 7] suggest that the chlorophylls are grouped in clusters of 5-7 molecules, which is reminiscent of the known chromophore grouping in the bacteriochlorophyll a-protein from the green sulfur bacterium Prosthecochloris aestuarii [24, 25].

It has long been recognized that the 670-680 nm Chl a core antenna Q_y absorption band encompasses several spectrally distinguishable Chl a excited states [26]. These may arise a priori from exciton interactions among strongly coupled chromophores, from localized excitations on spectrally different Chl a molecules (e.g., due to contrasting porphyrin conformations occasioned by nonuniform protein environment), or from

both. Such spectral inhomogeneity raises two major issues concerning the antenna structure and transport kinetics in PS I. The first of these deals with the spatial organization of the spectral Chl a forms and its bearing on the EET dynamics. Enriched PS I particles with contrasting core antenna sizes including particles with Chl a/P700 ratio as low as 8-10 [27] exhibit very similar absorption spectra [8]. Hence, removal of antenna chlorophylls in preparations yielding different core antenna sizes does not alter the proportions of Chl a species responsible for various Q_y subbands. This appears to be inconsistent with the "funnel" model [28] for antenna structure, in which the shorter wavelength Chl a species are visualized at the periphery and the longer-wavelength species are proximate to the reaction center. Alternatively, the Chl a spectral forms may be randomly distributed about the reaction center, so that the statistical ratios of spectral forms left intact in solutions of PS I particles with decreasing antenna size are invariant. Finally, the spectral Chl a forms in the core antenna may be complexed into identical protein subunits containing identical, inhomogeneous sets of chromophores; detergent fractionation may then reduce the antenna size in quantum steps of one subunit, automatically preserving the species population ratios. Owens et al. [8] showed that the time-resolved core antenna excitation and fluorescence spectra of PS I core antennae are independent of antenna size. Their time-resolved spectra indicated that the emitting Chl a species are not limited to the long-wavelength form(s), but are "nearly homogenized" over all of the spectral forms present throughout the emission lifetime. This rapid "homogenization" of core antenna excitation argues against the "funnel" model (in which

excitation transport occurs sequentially from short-wavelength to long-wavelength components); it is consistent with randomly distributed spectral forms, and with spectral forms organized into essentially identical subunits.

The second issue is the extent of excitonlike (delocalized) character of PS I antenna excitations. Owens et al. [9] measured fluorescence lifetimes in PS I core antennae of P700 Chl a-protein complexes from barley, and in a photosynthetic mutant of Chlamydomonas reinhardtii without the PS II antenna/reaction center complex. The lifetime of the fast fluorescence component varied linearly with core antenna size in both species, in agreement with random walk models [29, 30] in which the excitations were assumed to be localized on Chl a chromophores occupying sites on a regular lattice. Analysis of the fluorescence profiles yielded a single-step EET time of 0.1-0.2 ps between chromophores. The excitation migration was found to be nearly diffusive, and photoconversion in the reaction center typically occurred once per 2.4 excitation visits from the core antenna. More recently [31], we obtained polarized photobleaching profiles through pump-probe spectroscopy on PS I-60 particles enriched in iron-sulfur protein and P700 (Chl a/P700 ratio ~60). At the wavelengths 665, 670, 675, and 681 nm, the photobleaching polarization decayed with mean lifetimes between 2.9 and 6.6 ps. This comparatively slow timescale suggested that the depolarization accompanied EET between clusters of Chl a chromophores, rather than between individual nearest-neighbor chromophores. Considerable residual anisotropy appeared in the photobleaching profiles at long times, proving that local ordering exists in the Chl a-protein

core antenna complex of PS I-60.

In order to clarify the relationship between the pump-probe depolarization dynamics [31] and the numerous PS I antenna fluorescence studies [8-15], we have extended our work to PS I-200 particles (Chl a/P700 ~ 200) from spinach chloroplasts. Details of the magic-angle Chl a photobleaching decay observed in this work between 660 and 681 nm closely parallels the multiexponential fluorescence decays reported elsewhere [8,9] for particles of similar size. At shorter wavelengths (645-655 nm), the magic-angle decay is dominated by a fast (~5 ps lifetime) component that is likely associated with excitation migration from Chl b. The observed Chl a depolarization lifetime between 660 and 681 nm exhibits marked wavelength dependence, behavior which was masked by the lower S/N and narrower wavelength range accessible in our earlier PS I-60 work. This wavelength dispersion in depolarization lifetime is consistent with predictions of Förster excitation transport rates based on published PS I core antenna absorption and fluorescence spectra [7,8]. Our results point to a PS I core antenna model in which the excitations are thermalized spectrally less than 1 ps, but require considerably more time (several ps) for spatial homogenization. This model is consistent with Sauer's "pebble mosaic" model [32], in which electronic excitation is rapidly delocalized within clusters of chlorophyll chromophores, and migrates relatively slowly between clusters.

Experimental

The PS I-200 particles (Chl/P700 ratio ~ 200) were isolated from spinach chloroplasts following the procedure of Mullet et al. [22]. Such native PS I particles retain all of the polypeptides which bind the light-harvesting antenna, core antenna, P700 reaction center, and associated electron acceptors [33]. The Chl a/Chl b ratio in the light-harvesting complex is ~3.5, and contains some 100 chromophores [4, 34, 35]; the overall Chl a/Chl b ratio for PS I-200 particles is ~6 [34, 35]. PS I-200 particles exhibit the structural and functional properties of PS I in thylakoids [34]. Particles were stored at 77 K in a buffered glycerol-water mixture (pH = 8.3) with 0.1% Triton X-100. In contrast, the PS I-60 particles used in earlier work [31] were largely free of Chl b, cytochromes f, b_6, and b-559, and their β-carotene content was considerably reduced [36]. They contained the 82, 83 kD reaction center Chl a-protein complex, together with 6 to 8 polypeptides (8-25 kD) which are not complexed with chlorophyll. The light-harvesting Chl a/Chl b antenna complex present in PS I-200 particles was absent in PS I-60. Samples were housed between λ/4 fused silica flats separated by an 800 μm teflon spacer, and were rotated at 12 Hz during pump-probe experiments to minimize photooxidation by the laser beams. All experiments were performed at room temperature.

The pump-probe apparatus and optics were identical to those used previously [31]. The multiline Ar^+ laser used for pumping the passively mode-locked dye laser was superseded by a Coherent Antares 76-s Nd:YAG cw mode-locked laser, which generated 532 nm SH pulses with ~2 W average

power at 76 MHz repetition rate. The SH pulse width was ~70 ps FWHM. The hybrid mode-locked dye laser contained two jets (DCM lasing dye, DDCI saturable dye) and yielded vertically polarized pulses at wavelengths between 645 and 681 nm. A Coherent Model 7210 cavity dumper head driven by a Coherent Model 7200 driver reduced the natural 76 MHz pulse repetition rate to values as low as 1 MHz to check for effects of long-lived excited state buildup on the Chl a/b photobleaching transients. Autocorrelation traces taken between 645 and 681 nm typically exhibited ~1.5 ps fwhm. The pump and probe beams were modulated at 3.0 and 0.5 MHz respectively using Isomet 1206C acoustooptic modulators. A BK-7 corner cube prism mounted on a Micro-Controle UT10050PP translation stage delayed the pump beam. Beam polarizations were selected by calcite Glan-Thompson prism polarizers; the probe polarization was maintained at 45° from the vertical laser polarization, while the pump polarization was alternatively parallel to, perpendicular to, or displaced 54.7° from the probe polarization. The two beams were focussed into the sample using a 7.3 cm f.l. lens. The probe beam was monitored by an EG&G FOD-100 photodiode, and phase-locked single-sideband detection was achieved at the 3.5 MHz sum frequency using a modified Drake R-7A radio receiver [37]. The receiver's internal 50 kHz signal-bearing frequency was demodulated in a Stanford Research Systems SR510 lock-in amplifier. Pump-probe data were transmitted to a DEC MINC-23 computer, where they were normalized to the square of the instantaneous laser intensity detected by a second EG&G FOD-100 monitor photodiode.

Results

Isotropic photobleaching decay

A perspective display of the wavelength dependence of the PS I-200 magic-angle photobleaching decay (obtained with the pump and probe polarizations 54.7° apart) is given in Fig. 8-1. The coherent coupling artifact at very early times [38] is a consequence of the single wavelength pump-probe technique used; the relative S/N ratios obtained at different wavelengths reflect on the available laser power as well as on the photobleaching action spectrum (vide infra). The continuous curves in Fig. 8-1 show the optimized convolutions of the laser autocorrelation functions (obtained with a KDP SHG crystal in place of the sample) with a single-exponential decay law (645 nm), biexponential decay laws (650 and 655 nm), and triexponential decay laws (660 through 681 nm). The final fitting parameters for all analyzed magic-angle profiles are listed in Table I. At wavelengths between 660 and 681 nm, a minimum of three exponentials is required to describe the decay. The first component τ_1 in Table I, with lifetime typically 1 to 2 ps, has no counterpart in the fluorescence decays observed in PS I core antennae [8-15], because photon counting instrument functions are limited to $\gtrsim$45 ps fwhm. Similar short-lifetime components were observed in our PS I-60 pump-probe experiments between 665 and 681 nm [31]. The optimized values of the second and third component lifetimes τ_2 and τ_3 depend on the duration selected for pump-probe scans. The second-component lifetimes τ_2 derived from the longer (250 ps) scans in Table I are generally 25-40 ps, times which resemble the "fast" fluorescence components reported by Owens et

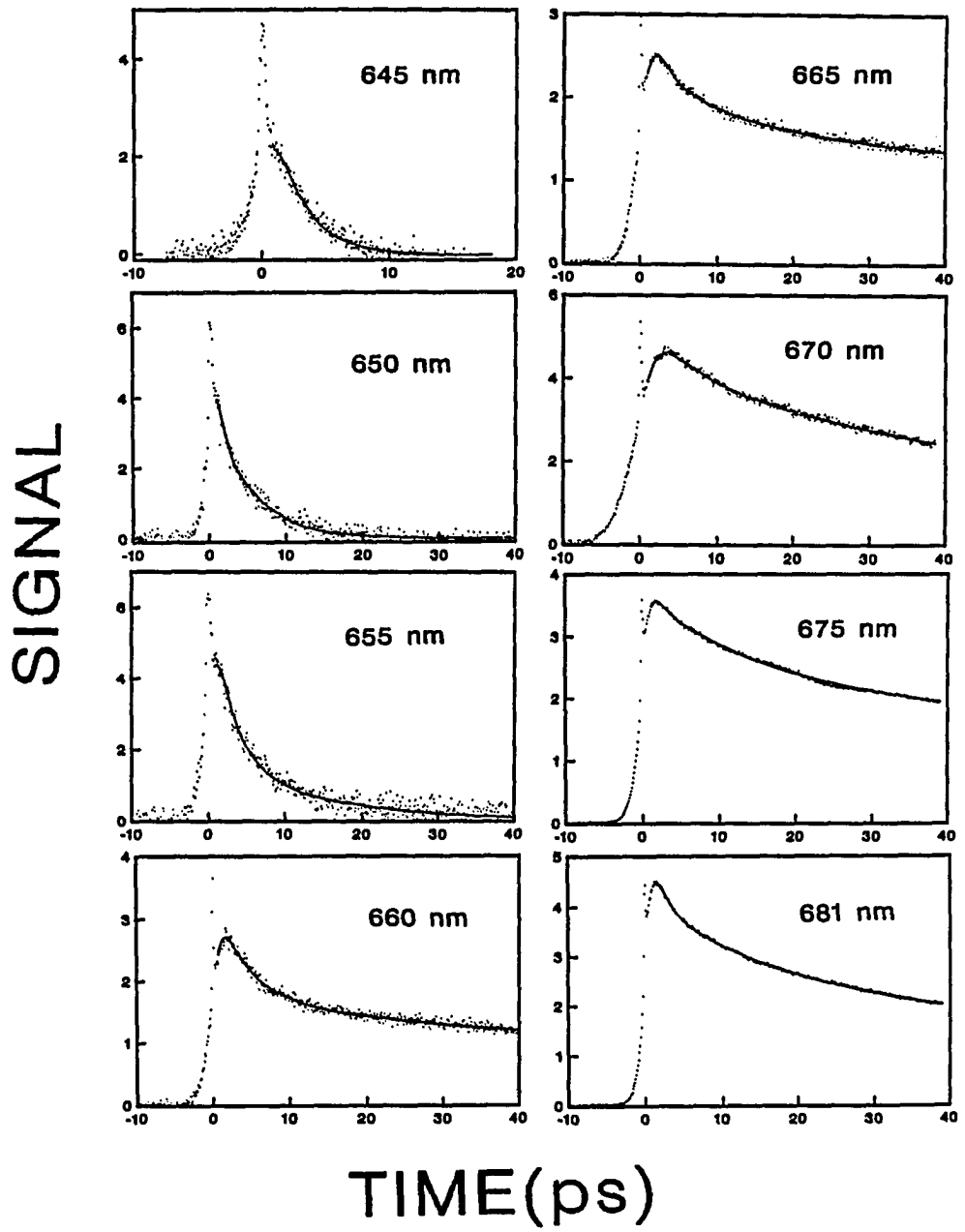

Figure 8-1. Magic-angle photobleaching transients for PS I-200 particles at eight wavelengths from 645 to 681 nm. The pump and probe wavelengths are identical. Continuous curves are optimized convolutions of laser autocorrelation functions with bi-exponential decay law (645-655 nm) and triexponential decay law (660-681 nm). Note different time scale used at 645 nm.

Table I. Multiexponential fitting parameters for magic-angle profiles for PS I-200 particles from spinach

$$P(t) = A_1\exp(-t/\tau_1) + A_2\exp(-t/\tau_2) + A_3\exp(-t/\tau_3)$$

Wavelength nm	A_1	τ_1, ps	A_2	τ_2, ps	A_3	τ_3, ps
645	1.000	2.00				
	1.000	2.04				
	0.713	2.11	0.287	2.11		
650	0.506	0.765	0.494	4.54		
	-0.131	1.64	0.869	2.24		
	-0.231	3.12	0.769	3.21		
	0.753	0.393	0.247	4.86		
	0.727	0.267	0.273	2.76		
	0.679	1.60	0.321	7.95		
655	0.776	2.43	0.224	13.9		
	0.810	2.67	0.190	24.1		
	0.869	2.84	0.131	29.2		
	0.807	2.81	0.193	25.9		
	0.829	2.81	0.171	39.6		
660	0.448	2.56	0.227	12.6	0.325	250
	0.367	1.32	0.294	7.94	0.339	250
	0.436	3.50	0.182	15.7	0.382	250
	0.472[a]	2.20	0.286	33.6	0.242	250
665	0.342	1.92	0.263	14.2	0.395	250
	0.493	1.19	0.180	11.5	0.327	250
	0.426	1.47	0.205	11.4	0.369	250
	0.458[a]	1.43	0.344	34.8	0.198	250

[a]Magic angle profiles obtained from 250 ps scans. All other profiles were obtained using 50 ps sweeps.

Table I. (continued)

Wavelength nm	A_1	τ_1, ps	A_2	τ_2, ps	A_3	τ_3, ps
670	0.489	1.11	0.240	14.9	0.271	250
	0.433	1.72	0.302	21.8	0.265	250
	0.317[a]	3.67	0.421	37.0	0.262	250
675	0.413	1.34	0.175	24.5	0.412	194
	0.563	0.500	0.128	16.0	0.309	194
	0.564	0.557	0.173	16.0	0.263	194
	0.339[a]	3.21	0.241	39.0	0.420	254
	0.330[a]	4.23	0.257	44.7	0.413	255
	0.342[a]	2.42	0.210	29.8	0.448	215
681	0.340	1.23	0.224	12.3	0.436	179
	0.377	0.225	0.206	13.1	0.416	179
	0.329	1.65	0.222	13.5	0.445	179
	0.340	1.23	0.224	12.3	0.436	179
	0.358[a]	4.15	0.243	38.1	0.399	234
	0.576[a]	1.48	0.163	26.9	0.261	213
	0.558[a]	2.36	0.182	23.9	0.260	212

al. [8] for photosystem I particles with Chl/P700 ratios ≳40; they are also similar to the fast PS I fluorescence decay times reported for chloroplasts and intact algae [39]. Third-component lifetimes τ_3 obtained from 250 ps scans at 675 and 681 nm (Table I; not shown in Fig. 8-1) are clustered around 200 to 250 ps; these are similar to the "intermediate" fluorescence components characterized in PS I preparations with Chl a/P700 ratios greater than 65 [8, 40, 41]. This decay component was not observed in our PS I-60 pump-probe experiments [31]. Less accurate values for τ_3 are obtained in triexponential fits of magic-angle profiles obtained with 50 ps scans (cf., Fig. 8-1), whose durations are considerably shorter than τ_3 values derived from 250 ps scans. (The 50 ps scans were accumulated for purposes of modeling the isotropic decay function for analysis of the polarized photobleaching decays, because the depolarization timescale proved to be much faster than τ_3.) The 660-681 nm magic-angle decays monitored using 50 ps time windows were therefore fitted with a triexponential model function in which τ_3 was fixed at 250 ps, and the other five triexponential parameters were floated. We do not attach physical significance to the final parameters for triexponential fits to these 50 ps magic-angle profiles, which are used only to separate the isotropic and anisotropic portions of the polarized photobleaching profiles.

While the magic-angle profiles for 660-681 nm in Fig. 8-1 superficially appear to exhibit risetimes (i.e., rising portions following the coherent spikes at t=0), the convolute-and-compare analysis shows that this phenomenon is entirely a consequence of the broad wing on the laser pulse shape autocorrelation. The unusually broad "risetime"

feature in the 670 nm panel of Fig. 8-1, for example, is accompanied by a visibly broadened rising (t<0) edge in the profile. Deconvolution of these profiles with triexponential model functions uncovered no evidence for any risetime components (negative preexponential factors); we estimate that any risetimes present would be much shorter than 1 ps.

In preliminary PS I-200 magic-angle profiles taken at 675 and 681 nm, the third-component lifetime τ_3 was found to be ~170 ps. Reduction of the laser power in the pump and probe beams yielded τ_3 in the 200-250 ps range reported in Table I; the isotropic decay in the earlier profiles was accelerated by exciton annihilation. The laser power employed in the earlier profiles had been shown to be sufficiently low to avoid annihilation effects in photobleaching decay of PS I-60 particles, and so the PS I-200 profiles which exhibited τ_3 ~ 170 ps indicate that the effective domain size [42] in 660-681 nm photobleaching is significantly larger in PS I-200 than PS I-60 particles.

The 250 ps maximum time window of our pump-probe scans was insufficiently wide to verify the presence of the 5-6 ns "long" decay component observed by Owens et al. in PS I antenna fluorescences [8, 9]. The PS I-200 isotropic photobleaching signal typically decayed to ~15% of the initial amplitude by 250 ps, so the upper limit on the preexponential factor for such a component is conservatively estimated to be less than 0.1.

At the three shortest wavelengths (645, 650, and 655 nm) the 200-250 ps decay component is absent, and the decay is well represented within noise by a biexponential law. The isotropic decay accelerates toward shorter pump-probe wavelengths, and exhibits ~2 ps lifetime at 645 nm.

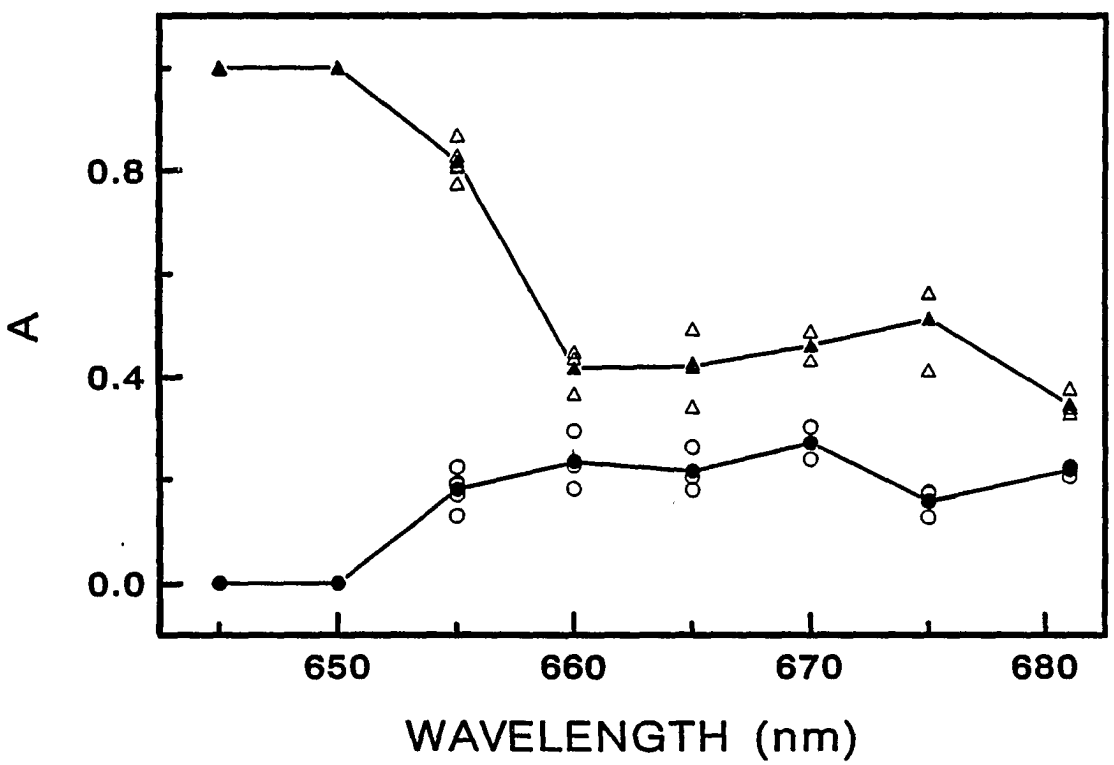

Figure 8-2. Wavelength dependence of preexponential factors A_1, A_3 for triexponential fits to PS I-200 magic-angle photobleaching decays, $P(t) = A_1\exp(-t/\tau_1) + A_2\exp(-t/\tau_2) + A_3\exp(-t/\tau_3)$. The sum of preexponential factors is normalized to unity at each wavelength.

Figure 8-2, which plots the wavelength dependence of preexponential factors A_1 and A_3 for the first and third triexponential decay components, emphasizes this trend toward more rapid magic-angle decay in the blue portion (645-655 nm) of the spectrum.

The majority of these pump-probe profiles were accumulated with the dye laser cavity dumper repetition rate at 9.5 MHz. In separate experiments, isotropic photobleaching profiles were obtained for PS I-60 particles at several repetition rates down to 1 MHz; the profiles were not materially changed by such reductions in repetition rate. This fact, coupled with the similarity in PS I antenna excited state lifetime parameters found here and in the fluorescence studies [8-15], is convincing evidence that artifacts arising from long-lived excited state buildup are not present in this work. Our previous experience with pump-probe spectroscopy of EET in alcohol solutions of rhodamine 640 [43] has shown that accurate isotropic and anisotropic photobleaching profiles are readily obtainable even when the laser pulse spacing is considerably shorter than the T_1 state lifetime.

Anisotropic photobleaching decay

Representative anisotropic pump-probe profiles, generated using parallel and perpendicular pump-probe polarizations, are shown for PS I-200 particles at 665 and 675 nm in Fig. 8-3. The simplest time-dependent functions capable of modeling these and the other anisotropic profiles obtained at 660 through 681 nm have the form

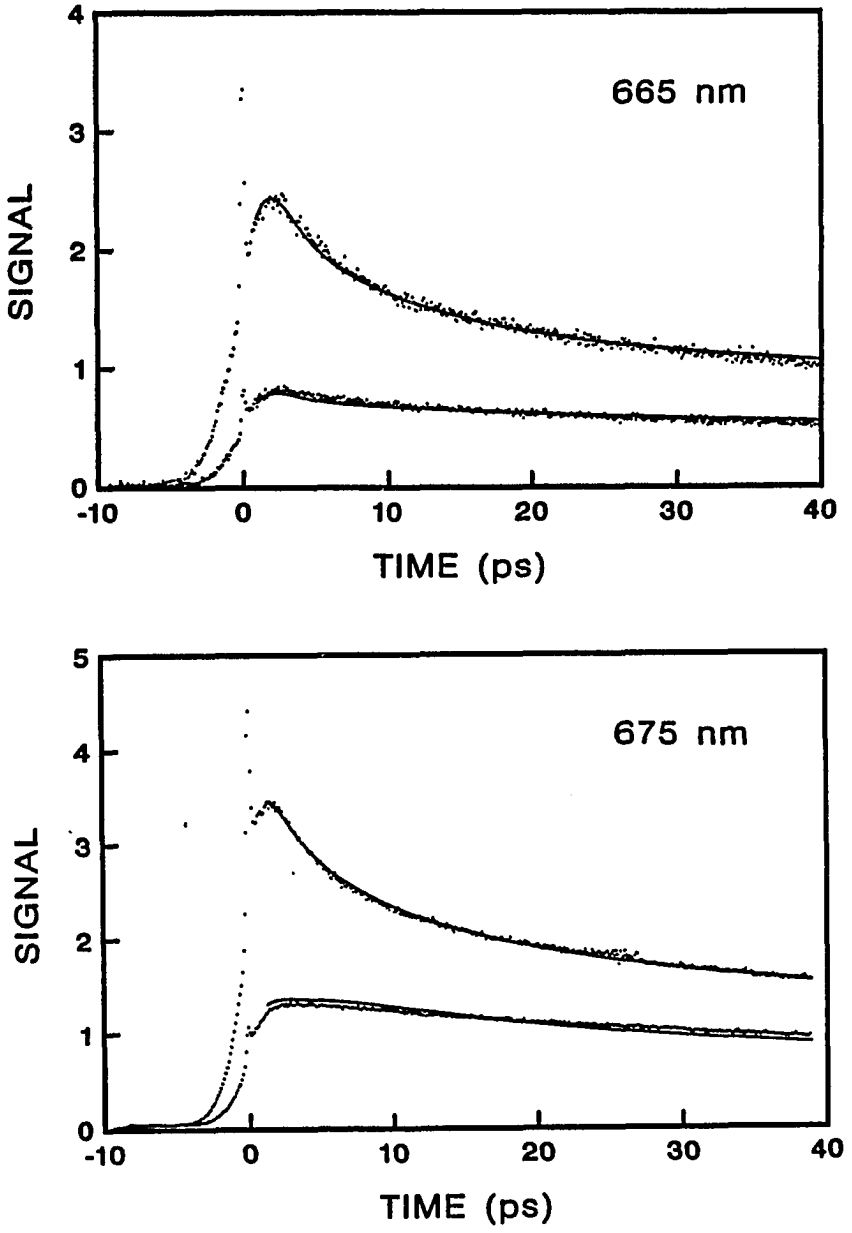

Figure 8-3. Anisotropic photobleaching transients for PS I-200 particles at 665 and 675 nm. At each wavelength, the upper (lower) profile was obtained using parallel (perpendicular) pump and probe polarizations. Continuous curves are optimized convolutions of Eqs. 8.1 with the laser pulse autocorrelation functions. At 665 nm, τ = 11.1 ps and a = 0.469; at 675 nm, τ = 4.87 ps and a = 0.429.

$$A_{||}(t) = P(t)\{1 + 0.8[(1-a)r(t) + a]\}$$
$$A_{\perp}(t) = P(t)\{1 - 0.4[(1-a)r(t) + a]\} \quad (8.1)$$

Here $P(t)$ is the magic-angle photobleaching decay measured with pump and probe polarizations separted by 54.7°. $r(t)$ is an anisotropy decay function, initialized to unity at zero time, which tends to zero at long times. The presence of the residual anisotropy parameter $\underline{a} \neq 0$ is necessitated by the fact that $A_{||}/A_{\perp}$ does not approach unity at long times (cf., Fig. 8-3)

$$A_{||}(\infty)/A_{\perp}(\infty) = (1 + 0.8a)/(1-0.4a) \quad (8.2)$$

or

$$a = 2.5[A_{||}(\infty) - A_{\perp}(\infty)]/[A_{||}(\infty) + 2A_{\perp}(\infty)] \quad (8.3)$$

Pairs of anisotropic profiles $A_{||}(t)$, $A_{\perp}(t)$ were deconvoluted from the laser pulse autocorrelation function using a linked convolute-and-compare scheme [44] in which the six triexponential parameters in the isotropic decay function $P(t)$ were frozen at the values found in the magic-angle profile analyses (Table I). The anisotropy decay function $r(t)$ was phenomenologically modeled as single-exponential, although some evidence for nonexponentiality surfaced in the anisotropic profiles with higher S/N (e.g., bottom half of Fig. 8-3) and such nonexponentiality can be expected theoretically (see Discussion). The final depolarization lifetimes τ (based on $r(t) = \exp(-t/\tau)$) and residual anisotropy parameters $\underline{a}$ yielded by the linked deconvolutions are listed in Table II. These

Table II. Anisotropic fitting parameters for anisotropic profiles for PS I-200 particles from spinach

$$A_{\parallel}(t) = P(t)\{1 + 0.8[(1-a)\exp(-t/\tau) + a]\}$$

$$A_{\perp}(t) = P(t)\{1 - 0.4[(1-a)\exp(-t/\tau) + a]\}$$

Wavelength, nm	τ, ps	a
660	13.3	0.612
	15.8	0.342
	11.3	0.605
	11.9	0.369
665	8.79	0.468
	7.81	0.413
	11.1	0.469
	10.7	0.523
670	3.82	0.336
	6.34	0.321
	7.48	0.293
675	4.50	0.337
	4.26	0.366
	6.37	0.620
681	6.99	0.528
	7.82	0.556
	5.67	0.476

depolarization lifetimes are plotted in Fig. 8-4 (open circles), along with their averages (closed circles), as a function of pump-probe wavelength. Other symbols represent calculations which will be discussed below. The depicted trend, hinted at in our earlier PS I-60 work in which our DCM dye lasing bandwidth was limited to wavelengths greater than 665 nm, clearly shows that the depolarization lifetime increases from ~4 ps to ~13 ps as the pump-probe wavelength is tuned toward the blue from 675 to 660 nm.

At the three shortest wavelengths (645, 650, and 655 nm) where the isotropic decay is dominated by components with <5 ps lifetime (Table I), no evidence was found for depolarization on the timescale of several ps. Gillbro et al. [45] recently observed polarized photobleaching decays in the light-harvesting Chl a/b complex from photosystem II. They found that rapid energy transfer occured from Chl b to Chl a (6 ± 4 ps), and that no depolarization appeared in the Chl b photobleaching during the lifetime of Chl b excitation. However, they found evidence for excitation redistribution (~20 ps timescale) between differently oriented Chl a chromophores. Since the Chl b absorption in PS I is concentrated at the shorter wavelengths studied here (645-655 nm) and the antenna Chl a absorption system is centered at 670-680 nm (Discussion section), the LHC II depolarization behavior reported by Gillbro et al. qualitatively parallels that observed here in PS I-200.

Photobleaching action spectra

The wavelength dependence of the pump-probe signals between 655 and 692 nm was evaluated by measuring the signals at 100 ps and 7 ps and

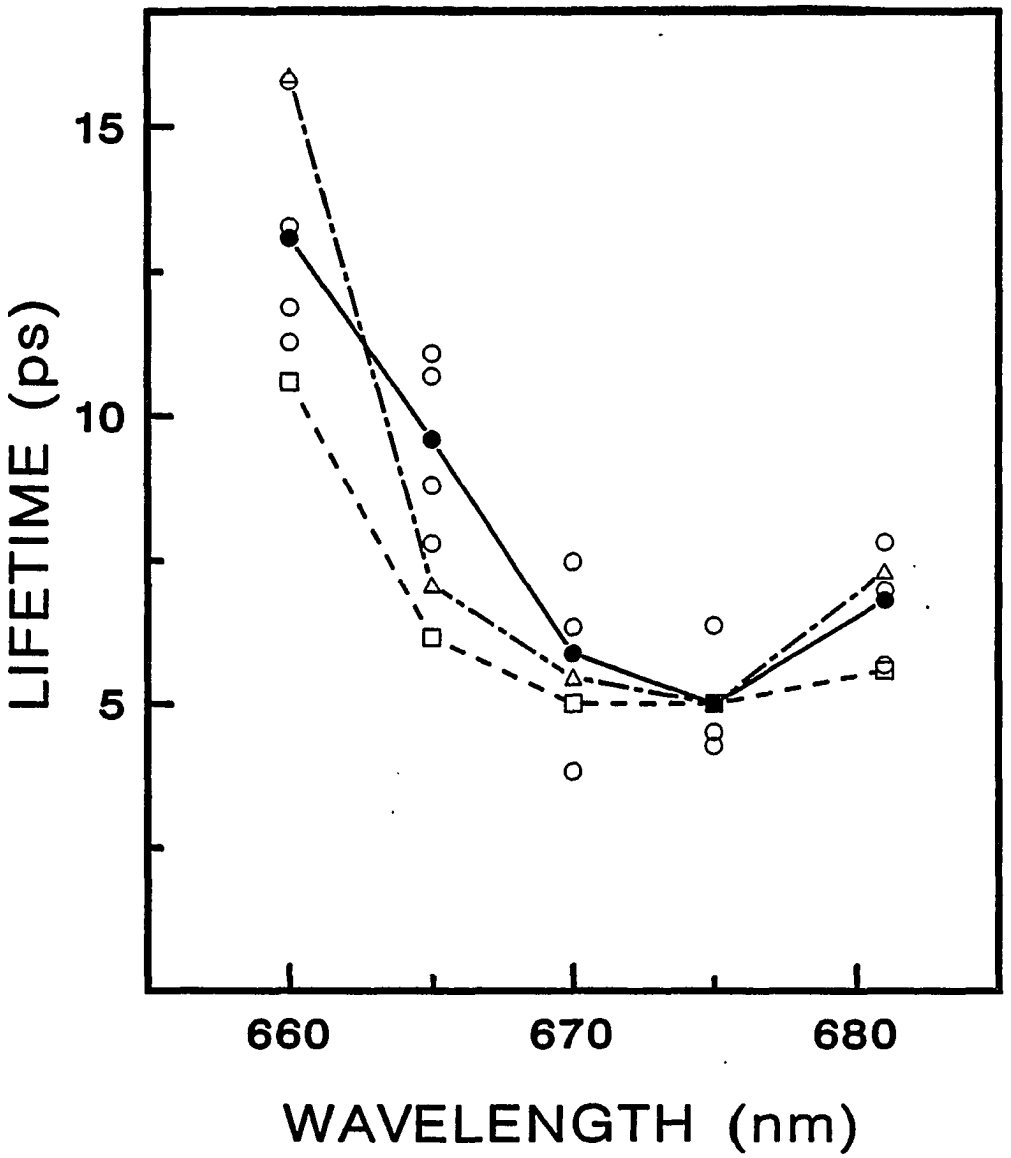

Figure 8-4. Pump-probe wavelength variation of depolarization lifetimes τ from deconvolution of anisotropic transients using Eqs. 8.1 with $r(t) = \exp(-t/\tau)$. Open circles are lifetimes derived from single pairs of profiles $A_{\parallel}(t)$, $A_{\perp}(t)$; filled circles are averaged values. Calculated lifetimes from deconvolution of PS I-13 and PS I-200 absorption spectra are given by squares and triangles, respectively.

normalizing them to the square of the incident laser power at the pertinent wavelength. In Fig. 8-5, we show the action spectrum of the 100 ps signal (which is a measure of the intensity of the third photobleaching component with lifetime τ_3 ~ 200-250 ps), the 7 ps signal, and the difference between the 7 ps signal and the 100 ps signal extrapolated back to 7 ps using the lifetimes τ_3 in Table I. The latter difference yields an estimate of the action spectrum of the second photobleaching component, with lifetime τ_2 in the tens of ps. For comparison, the PS I-200 steady-state absorption spectrum [46] is also shown. The action spectra peak well to the red (~680 nm) of the PS I-200 Chl a steady-state absorption band maximum at ~670 nm. This situation contrasts with fluorescence excitation spectra reported for a PS I preparation with Chl a/P700 = 33 [8], which closely approximate the steady-state absorption spectrum.

Discussion

Many of the PS I-200 pump-probe phenomena reported here have been anticipated in earlier accounts of PS I time-resolved fluorescence experiments [8-15] and in our polarized pump-probe studies of PS I-60 particles [31]. Aside from an ultrafast component (τ_1 ~ 1-3 ps) which overlaps the coherent spike, the multiexponential isotropic decays at 660-681 nm are dominated by components with lifetimes τ_2 = 25-40 ps and τ_3 = 200-250 ps. These coincide with the "fast" and "intermediate" fluorescence lifetime components observed by Owens et al. [8] for PS I particles with Chl a/P700 ratios ≥65. No isotropic photobleaching

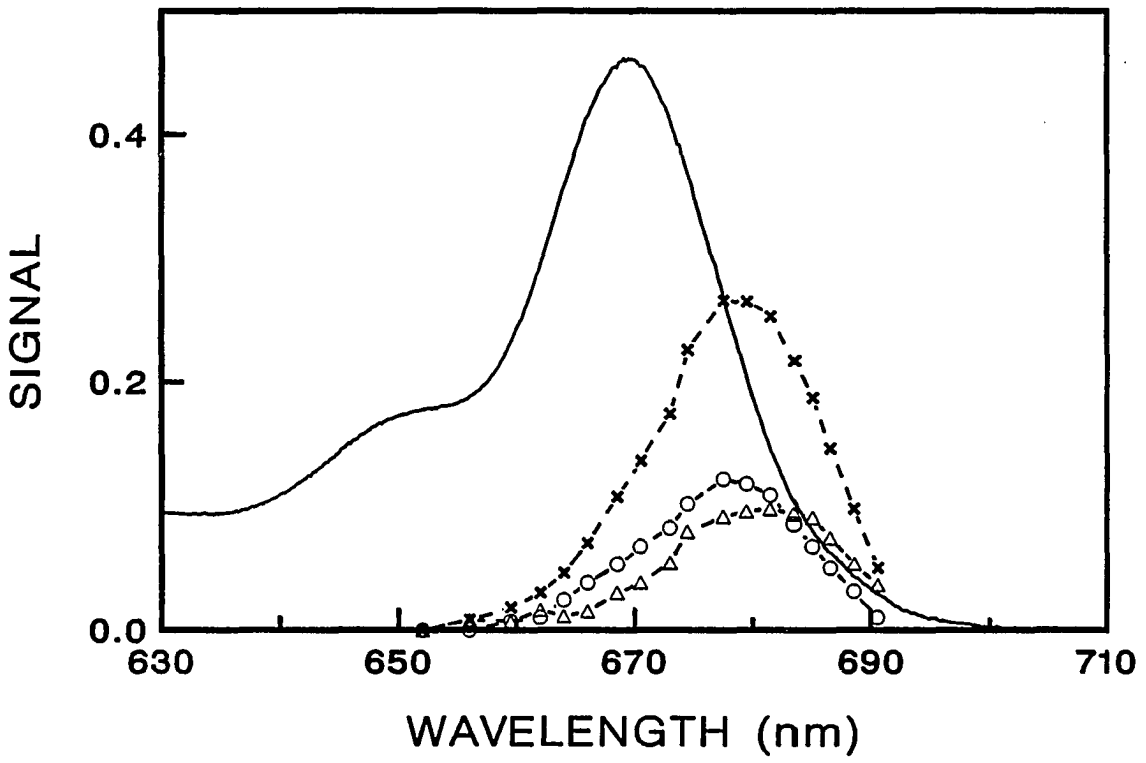

Figure 8-5. Photobleaching signal normalized to the square of incident laser power at 7 ps (crosses), 100 ps (circles), and the difference between the 7 ps normalized signal and the 100 ps normalized signal extrapolated back to 7 ps using the lifetimes τ_3 in Table I (triangles). Continuous curve is low temperature steady-state absorption spectrum of PS I-200.

component with lifetime $\gtrsim$ 20 ps was found in our PS I-60 work [31], in agreement with earlier reports [8, 9] that the "intermediate" component is absent in PS I particles with Chl *a*/P700 < 65. The pump-probe depolarization timescales found between 665 and 681 nm (Fig. 8-4) are commensurate with those seen in PS I-60 [31]. All of these correspondences between our data and the earlier time-resolved PS I experiments confirm that while these pump-probe studies are potentially subject to artifacts from long-lived excited state buildup, exciton annihilation, and variations in PS I fractionation techniques, they do furnish an accurate probe of antenna excited state dynamics in particles kinetically similar to those studied by other groups.

Several investigators have analyzed the static absorption spectra of PS I core antennae by simulating them as sums of Gaussian components [7, 8]. Owens et al. decomposed the Chl *a* Q_y spectrum of particles with Chl *a*/P700 = 43 into three components centered at 667, 677, and 685 nm with ~20 nm (450 cm^{-1}) bandwidth [8]; Ikegami and Itoh simulated the Q_y spectrum of highly enriched PS I particles as a sum of six Gaussians at 650, 660, 669, 675, 684, and 698 nm, with 1/e bandwidths of 400-600 cm^{-1} [7]. Proposed models for the nature of EET between the different spectral forms of Chl *a* have included the "funnel model" [28], in which excitation migrates sequentially downhill and becomes concentrated in the long-wavelength Chl *a* species, and a more recent model [8] in which excitation becomes rapidly "homogenized" among the different spectral forms. We are unaware of published time-resolved data which support the funnel model for PS I antennae. The PS I fluorescence spectra reported by Owens et al. [8] lend considerable support to the homogenization

scenario, because substantial fluorescence is emitted by Chl a spectral forms other than the lowest-energy form. An unequivocal test of these models would be a dual-wavelength pump-probe experiment in which antenna Chl a absorption is probed at ~660 nm following excitation at ~685 nm: resolvable uphill EET from the 685 to 660 nm spectral forms in a "homogenization" process would be signalled by a 685 nm photobleaching risetime if excited state absorption is absent. We now analyze whether such risetime behavior would be detectable in the present single-wavelength pump-probe experiments as well. In particular, we consider photobleaching monitored at some wavelength λ_m in a region of spectral overlap between adjacent forms of Chl a, such as Chl a-684 and Chl a-675 in the simulation of ref. [7]. The ratio N^0_{675}/N^0_{684} of initial excited state populations in the two spectral forms will be given by the ratio $\varepsilon_{675}/\varepsilon_{684}$ of their absorption coefficients at λ_m in the Beer's law limit of low excitation power. At early times where negligible excitation trapping has occurred at P700, equilibration of excitation between the spectral forms with uphill and downhill rates k_u and k_d yields the time-dependent excited state populations

$$N_{675}(t) = \frac{k_u(N^0_{675} + N^0_{684})}{k_u + k_d}\left[1 - e^{-(k_u+k_d)t}\right] + N^0_{675}e^{-(k_u+k_d)t}$$

$$N_{684}(t) = \frac{k_d(N^0_{675} + N^0_{684})}{k_u + k_d}\left[1 - e^{-(k_u+k_d)t}\right] + N^0_{684}\,e^{-(k_u+k_d)t} \qquad (8.4)$$

The observed photobleaching signal at λ_m is then proportional to

$$D(t) = \Delta\varepsilon_{675}N_{675}(t) + \Delta\varepsilon_{684}N_{684}(t)$$

$$= A[1 - e^{-(k_u + k_d)t}] + Be^{-(k_u + k_d)t} \qquad (8.5)$$

where $\Delta\varepsilon_{675}$ and $\Delta\varepsilon_{684}$ are the (ground state - Q_y) differential absorption coefficients at the respective wavelengths. In view of Eqs. 8.4, the difference between the coefficients A and B for the rise and decay contributions to D(t) is then

$$A - B = k_d\varepsilon_{675}\Delta\varepsilon_{684} + k_u\varepsilon_{684}\Delta\varepsilon_{675} - k_u\varepsilon_{684}\Delta\varepsilon_{684} - k_d\varepsilon_{675}\Delta\varepsilon_{675} \qquad (8.6)$$

If the excited state absorption is small ($\Delta\varepsilon \approx \varepsilon$) the condition for observation of risetime behavior ($A - B > 0$) becomes

$$1 < \frac{\varepsilon_{684}}{\varepsilon_{675}} < \frac{k_d}{k_u} \qquad (8.7)$$

The funnel model arises in the special case of essentially irreversible downhill EET, $k_d >> k_u$. In this limit, risetime behavior will be observed in single-wavelength pump-probe experiments at virtually all wavelengths λ_m for which $\varepsilon_{684} > \varepsilon_{675}$. In the contrasting limit where $k_d/k_u = 1$, the excited state populations of the two spectral forms tend toward parity ("homogenization") at equilibrium, and no risetime will be observed at any wavelength according to Eq. 8.7. No risetime components are in fact observed in any of the isotropic profiles at the wavelengths of strong Chl a absorption (660-681 nm) in Table I, and hence we find no evidence of funnel-type EET in the photosystem I core antenna. However,

we cannot rule out unresolvably fast irreversible downhill EET (<< 1 ps) on the basis of our data alone; dual-wavelength femtosecond pump-probe studies will help to resolve this question. Gaussian simulations of the Chl *a* Q_y core antenna absorption spectrum predict that the absorption peaks of the various spectral forms are spaced ~150-200 cm^{-1} apart, irrespective of how many Gaussian components are used [7, 8]. This spacing is considerably narrower than the bandwidths (typically 400 cm^{-1}) of the fitted absorption [7, 8] and fluorescence [8] components. Consequently, while the Förster formulation of the EET transition rates between two adjacent Chl *a* spectral forms in terms of an overlap integral involving their absorption and fluorescence spectra [47] predicts that the downhill transition rate will exceed the uphill rate, it does not project that $k_d >> k_u$ in the spirit of irreversible downhill transport.

The rapid (<5 ps) isotropic decays observed at 645-655 nm (Fig. 8-1) indicate that the excited state probed at these wavelengths is dynamically different from the state(s) probed at 660-681 nm, where the isotropic decay is found to be fairly uniform with components of 25-40 ps and 200-250 ps. Since the Chl *b* Q_y transition begins to dominate in this wavelength regime, these ultrafast decays may be associated with excitation migration from Chl *b* to the lower-energy Chl *a* species. Such decays are not readily resolved by time-correlated photon counting (≳ 45 ps instrument function); the fluorescence decay kinetics in *C. reinhardtii* mutants without the PS II reaction center were reported to be insensitive to excitation wavelength even when 95% of the absorption occurred in Chl *b* [12]. Similarly, the fluorescence decay was indistinguishable under 652 and 680 nm excitation of PS I particles

containing Chl b [8]. Hence, EET from Chl b to the core antenna is much more rapid than core antenna excitation decay. Our ultrafast 645 nm isotropic decays (Fig. 8-1 and Table I) serve to lower the upper time limit on excitation migration from Chl b to ~2 ps. Furthermore, while the 645-655 nm decays are fast, they are not laser pulse-limited, as is clear from the asymmetry of the profiles (Fig. 8-1); the Chl b deexcitation timescale does not appear to be much less than the laser pulse width.

The depolarization lifetimes derived from anisotropic profiles (Fig. 8-4) shows that while excitation may equilibrate rapidly over all of the Chl a spectral forms as suggested by Owens et al. [7], such equilibration does not extend spatially over the entire core antenna. In a scenario consistent with this observation, the core antenna chlorophylls are organized into (nearly) identical subunits, each containing a full complement of spectral forms of Chl a. Rapid equilibration of excitation occurs among the Chl a species inside a subunit, causing the antenna chlorophyll fluorescence spectrum and dynamics to be essentially independent of excitation wavelength [8]. Slower EET (manifested by the depolarization lifetimes in Fig. 8-4 and Table II) occurs between spectrally similar subunits with different orientations. The subunit orientations cannot be random, because the measured anisotropy parameters a in Table II are nonzero. This model is consistent with the conclusion of Shubin et al. [6] that the PS I core antenna contains several identical clusters of six to eight Chl a pigments each.

The wavelength dependence of the depolarization lifetime was phenomenologically modeled by applying Förster theory [47] to the problem

of incoherent EET between like subunits. For definiteness, six Chl *a* spectral forms were assumed, having Gaussian absorption bands $\varepsilon_i(\omega)$ with positions, bandwidths, and peak heights listed in ref. [7]. The fluorescence spectrum $f_i(\omega)$ of each Chl *a* species i was similarly modeled as Gaussian, with peak height and bandwidth proportional to and identical to the peak height and bandwidth respectively of the corresponding absorption component $\varepsilon_i(\omega)$. The fluorescence peak in $f_i(\omega)$ was arbitrarily shifted 3 nm to the red from the absorption peak in $\varepsilon_i(\omega)$. The rate R_{ij} of excitation migration from spectral component i in a subunit to spectral component j in a different subunit was evaluated using [47]

$$R_{ij} = \int f_i(\omega)\varepsilon_j(\omega)\,d\omega/\omega^4 \tag{8.8}$$

and the resulting excitation decay from component i was computed as

$$P_i(t) = \exp[-t\Sigma_{j=1}^{6} R_{ij}] \tag{8.9}$$

For each pump-probe wavelength $\lambda_m = 1/\omega$, the overall excitation migration rate from the initially pumped subunit then assumes the multiexponential form

$$P(\omega,t) = \Sigma_{i=1}^{6} \varepsilon_i(\omega) P_i(t) \tag{8.10}$$

These computed decays were then fitted with the single-exponential model

function $Aexp(-t/\tau)$ to compute a theoretical depolarization lifetime τ. The results are representd by squares in Fig. 8-4, where the theoretical lifetime at 675 nm has been normalized to the average experimental lifetime at that wavelength. Similar calculations using parameters resulting from a deconvolution of the PS I-200 absorption spectrum are represented by triangles in Fig. 8-4. The theoretical lifetimes reproduce the qualitative trend of slower depolarization at shorter wavelengths, principally because the absorption coefficients of the components absorbing at the shorter wavelengths (650, 660 nm) are considerably smaller than those of the components absorbing at the longer wavelengths (669, 675, 684 nm). Excessive significance should not be attached to this calculation, owing to the crude assumptions made. The unknown dipole-dipole orientational factors [47] were not considered; the use of Eqs. 8.8-8.10 implicitly assumed that each pigment species i in one subunit is spatially equidistant from all of the pigment species j in the other subunit, so that the transition rates R_{ij} depend only on the pertinent absorption and fluorescence spectra. The physical nature of the Chl a spectral forms (exciton states versus spectrally distinct monomers with different conformations, etc.) was also ignored. Nevertheless, this phenomenological calculation does mimic the essential features of Fig. 8-4, in which the average depolarization lifetime at each wavelength correlates inversely with the static absorption coefficient at that wavelength (Fig. 8-5).

Acknowledgements

We are grateful to W. E. Catron for supporting one of us (T.P.C.) through a Research Fellowship. We thank Professor John Golbeck for isolating the PS I-200 preparations, and we thank Mr. J. Kevin Gillie for evaluating the PS I-200 absorption spectrum in Fig. 8-5. We are indebted to Professors Gerald Small, Kenneth Sauer, John Golbeck, and Graham Fleming for valuable discussions. The Ames Laboratory is operated for the U. S. Department of Energy by Iowa State University under Contract No. W-7405-Eng-82. This work was supported by the Office of Basic Energy Sciences.

References

1. Green, B. R. Photosyn. Res. 1988, 15, 3.
2. Golbeck, J. H. Biochim. Biophys. Acta, submitted to reviews in Bioenergetics
3. Wollman, F.-A.; Bennoun, P. Biochim. Biophys. Acta 1982, 680, 352.
4. Haworth, P.; Watson, J. L.; Arntzen, C. J. Biochim. Biophys. Acta 1983, 724, 151.
5. Anderson, J. M.; Brown, J. S.; Lam, E.; Malkin, R. Photochem. Photobiol. 1983, 38, 205.
6. Shubin, V. V.; Karapetyan, N. V.; Krasnovsky, A. A. Photosyn. Res. 1986, 9, 3.
7. Ikegami, I.; Itoh, S. Biochim. Biophys. Acta 1986, 851, 75.
8. Owens, T. G.; Webb, S. P.; Alberte, R. S.; Mets, L.; Fleming, G. R. Biophys. J. 1988, 53, 733.
9. Owens, T. G.; Webb, S. P.; Mets, L.; Alberte, R. S.; Fleming, G. R. Proc. Natl. Acad. Sci. USA 1987, 84, 1532.

10. Gulotty, R. J.; Mets, L.; Alberte, R. S.; Fleming, G. R. Photochem. Photobiol. 1985, 41, 487.

11. Kyle, D. J.; Baker, N.; Arntzen, C. J. Photobiochem. Photobiophys. 1983, 5, 11.

12. Owens, T. G.; Webb, S. P.; Eads, D. D.; Alberte, R. S.; Mets, L.; Fleming, G. R., In "Progress in Photosynthesis Research"; Biggins, J., Ed.; Martinus Nijhoff: The Hague, 1987; Vol. I, p. 83.

13. Lotshaw, W. T.; Alberte, R. S.; Fleming, G. R. Biochim. Biophys. Acta 1982, 682, 75.

14. Searle, G. F. W.; Tamkivi, R.; van Hoek, A.; Schaafsma, T. J. J. Chem. Soc., Far. Trans. 1988, 84, 315.

15. Wittmershaus, B. P.; Berns, D. S.; Huang, C. Biophys. J. 1987, 52, 829.

16. Shuvalov, V. A.; Nuijs, A. M.; van Gorkum, H. J.; Smit, J. W. J.; Duysens, L. M. N. Biochim. Biophys. Acta 1986, 850, 319.

17. Il'ina, M. D.; Kravsauskas, V. V.; Rotomskis, R. J.; Borisov, A.-Y. Biochim. Biophys. Acta 1984, 767, 501.

18. Borisov, A.-Y.; Darelius, P. V.; Il'ina, M. D.; Kravsauskas, V. V.; Piskarskas, A. S.; Razjuim, A. P.; Rotomskis, R. J. Mol. Biol. (Moscow) 1985, 19, 636.

19. Nuijs, A. M.; Shuvalov, V. A.; van Gorkum, H. J.; Plijter, J. J.; Duysens, L. N. M. Biochim. Biophys. Acta 1986, 850, 310.

20. Bengis, C.; Nelson, N. J. Biol. Chem. 1975, 250, 2783.

21. Takahashi, Y.; Hirota, K.; Katoh, S. Photosyn. Res. 1985, 6, 183.

22. Mullet, J. E.; Burke, J. J.; Arntzen, C. J. Plant Physiol. 1980, 65, 814.

23. Ish-Shalom, D.; Ohad, I. Biochim. Biophys. Acta 1983, 722, 498.

24. Matthews, B. W.; Fenna, R. E. Acc. Chem. Res. 1980, 13, 309.

25. Tronrud, D. E.; Schmid, M. F.; Matthews, B. W. J. Mol. Biol. 1986, 188, 443.

26. Shiozawa, J. A.; Alberte, R. S.; Thornber, J. P. Arch. Biochem. Biophys. 1974, 165, 388.

27. Ikegami, I. Biochim. Biophys. Acta 1976, 449, 245.

28. Seely, G. R. J. Theor. Biol. 1973, 40, 189.

29. Pearlstein, R. M. Photochem. Photobiol. 1982, 35, 835.

30. Hemenger, R. P.; Lakatos-Lindenberg, K.; Pearlstein, R. M. J. Math. Phys. 1972, 13, 1056.

31. Causgrove, T. P.; Yang, S.; Struve, W. S. J. Phys. Chem. 1988, 92, 0000.

32. Philipson, K. D.; Sauer, K. Biochemistry 1972, 11, 1880.

33. Golbeck, J. H. J. Membrane Sci. 1987, 33, 151.

34. Malkin, R.; Ortiz, W.; Lam, E.; Bonnerjea, J. Physiol. Veg. 1985, 23, 619.

35. Lam, E.; Ortiz, W.; Mayfield, S.; Malkin, R. Plant Physiol. 1984, 74, 650.

36. Golbeck, J. H. Methods Enzymol. 1980, 69, 129.

37. Anfinrud, P., Struve, W. S. Rev. Sci. Instrum. 1986, 57, 380.

38. Fleming, G. R. "Chemical Applications of Ultrafast Spectroscopy"; Oxford University Press: London, 1986; p. 66.

39. Geacintov, N. E.; Breton, J. CRC Crit. Rev. Plant Sci. 1987, 5, 1.

40. Holzwarth, A. R.; Haehnal, W.; Wendler, J.; Suter, G.; Ratajczak, R. In "Advances in Photosynthesis Research"; Sybesma, C., Ed.; Martinus Nijhoff: The Hague, 1984; p. 73.

41. Kamagawa, K.; Morris, J. M.; Takagi, Y.; Nakashima, N.; Yoshihara, K.; Ikegami, I. Photochem. Photobiol. 1983, 37, 207.

42. van Grondelle, R.; Amesz, J. In "Light Emission by Plants and Bacteria"; Govindjee; Amesz, J.; Fork, D. C., Eds.; Academic Press: New York, 1986; p. 213.

43. Causgrove, T. P.; Bellefeuille, S. M.; Struve, W. S. J. Phys. Chem. 1988, 92, 0000.

44. Anfinrud, P. A.; Hart, D. E.; Hedstrom, J. F.; Struve, W. S. J. Phys. Chem. 1986, 90, 2374.

45. Gillbro, T.; Sandstrom, A.; Spangfort, M.; Sundstrom, V.; van Grondelle, R. "Technical Digest", Sixth International Conference on Ultrafast Phenomena, Mt. Hiei, Kyoto, Japan, July 1988.

46. Gillie, J. K.; Small, G. J.; Golbeck, J. H. J. Phys. Chem., in press.

47. Shipman, L. L.; Housman, D. L. Photochem. Photobiol. 1979, 29, 1163.

CHAPTER IX. SUMMARY

Initial experiments were performed on rhodamine 640 chromophores distributed on ZnO and fused silica surfaces. This study indicated that fast energy transfer could occur from photoexcited dye molecules into semiconductor surface modes, a decay route not available for dyes on fused silica. The coverage-dependent decay on fused silica pointed to another problem, that of energy transport among chromophore molecules. This subject was addressed further in experiments on rhodamine 640 randomly distributed in glycerol solutions. In a homogeneous system such as this, depolarization techniques must be used to measure the rate of EET. The energy transfer parameters (specifically, the critical transfer distance R_0) were measured using both fluorescence depolarization via time-correlated single photon counting and absorption depolarization via pump-probe spectroscopy. The conclusion was that the two techniques quantitatively matched the predictions of the simple two-particle theory; deviations from the theory had been observed for DODCI in glycerol. Although the timescales covered were quite different, both techniques were able to accurately measure the critical transfer distance. This study established the reliability and validity of EET studies using pump-probe spectroscopy.

Because pump-probe absorption depolarization allows the resolution of much faster events than single photon counting, the technique was applied to photosynthetic antenna systems, where EET is expected to be extremely rapid. The first system studied was the BChl a-protein from P. aestuarii, for which the three-dimensional structure has been determined

by x-ray diffraction. The absorption polarization was found to decay to a constant, nonzero value with a time constant of ~5 ps. The observed decay was interpreted in terms of the known trimeric structure, and pointed to the existence of strong coupling of clusters of seven molecules; the clusters were found to be weakly coupled to each other as in the "pebble mosaic" model of photosynthetic antennae. The residual polarization at long times was related to the projection of the probed exciton transition moment on the three-fold symmetry axis.

The pump-probe depolarization was then extended to PS I of green plants, for which the three-dimensional structure is not known. The results indicated that an oligomeric form also exists in PS I antennae, with Förster hopping between small clusters of molecules. The timescale of transport indicates that the clusters should be separated by distances on the order of 30-40 Å, similar to that in the BChl _a_-protein. The data also shows some evidence of inhomogeneity in the PS I antenna as indicated by a wavelength dependent depolarization lifetime; the exact cause of the wavelength dependence was not well determined. These studies represent the first time that local ordering has been established for the antenna system of a green plant.

Future studies which could provide informative results include pump-probe depolarization in the Q_y band of the BChl _a_-protein. The studies in Chapter VI suffered from poor signal-to-noise due to the low absorption coefficient of the Q_x band of BChl _a_, and contributions to the depolarization lifetime may have occurred due to $Q_x \rightarrow Q_y$ internal conversion. In addition, pump-probe experiments of Q_y transport as a function of temperature in this system would be particularly interesting,

since it would allow an unambiguous characterization of the temperature dependence of EET in photosynthetic systems. Such characterization could be very important in bridging the results of transport and trapping experiments at low temperature with those at room temperature.

Since there are many unanswered questions about the nature of EET in PS I antennae, there are many different experiments which could be performed. One of the most informative would be two-color pump-probe experiments in the PS I core antenna. Such experiments could provide a definite determination of whether energy "funnelling" is an important process in energy transport and trapping. In a two-color experiment, one could use a pump wavelength of ~675 nm and probe at ~690 nm. If C675 and C690 are due to different molecules, one would expect to see a risetime of photobleaching at 690 nm corresponding to excitation transfer to this component. The risetime, when compared to the single-step hopping time measured by depolarization at 675 nm, would indicate the number of steps required to reach C690. If the calculated number of steps is ~1, then it could be concluded that C690 is located among the C675; larger numbers would indicate that C690 in located near the reaction center, and the excitation must pass through several C675 to reach it.

Such a two-color experiment could also provide data on whether excitonic interactions are present in the system. If the C690 component is a lower-energy exciton level of C675, then no risetime would be expected; excitation of C675 would constitute excitation of C690 as well. In addition, reversal of pump and probe wavelengths could provide data on whether "uphill" transfer, either among the core antenna or from antenna chromophores to P700, is important in the excitation trapping process.

ACKNOWLEDGEMENTS

I would of course like to thank my research advisor, Prof. Walter Struve, for his guidance and support (psychological, monetary, etc.) throughout this project. Although at times it seems to have been a long, strange trip, I have never regretted choosing Dr. Struve as my major professor. The work contained here is certainly more a product of his efforts than of mine.

I would also like to thank members of the group who have gone before me, in particular Philip Anfinrud. In addition to teaching me what to do (and what not to do) in a laboratory, Phil was kind enough to leave behind several pieces of home-built equipment without which these experiments would not have been possible. Other former members, Bob Crackel, Dave Hart, and Jack Hedstrom, were pleasurable co-workers who made it much easier to get through those days when experiments refused to work.

I would also like to recognize the current group members with whom much of this work was done, Shumei Yang and Sandy Bellefeuille; I wish both of them the best of luck in completing their degrees and in their future careers. A half thank-you also goes to the latest half group member, Paul Lyle.

In the experiments dealing with photosynthetic systems, I would like to acknowledge Kevin Gillie for help with handling the samples and for supplying copies of many relevant papers (a well as for using me as lead-off hitter).

Finally, I thank my mother for emphasizing academics through grade

school and high school, supporting my undergraduate education, providing encouragement during graduate school, and, well, everything.

APPENDIX A. TRANSLATION CONTROL PROGRAM

The following program was written to run on a Commodore 64 computer to provide for control of the translation stage used for the variable delay in pump-probe experiments. The main program provides five basic functions: 1) Move (relative), 2) Move (absolute), 3) Home, 4) Reset zero, and 5) Exit program. Option 1 asks the user to input the number of steps to be taken from the present position, while option 2 provides essentially a "go to" the given position. Both will later prompt the user for the desired speed and the number of steps per channel, a variable explained in Chapter II. Option 3 sends the delay stage to its zero position at maximum speed; option 4 resets the current position to be the zero position.

The program uses several machine language subroutines, the first of which is entered at line 340. All motion control takes place from the machine language subroutines; a glossary of the storage locations accessed in these routines is given in Table I. Finally, it should be noted that there is no explicit entry to the subroutines at addresses 49300 and 49800. The former is entered on a nonmaskable interrupt (NMI) which occurs when the number of steps limit is reached; the subroutine at 49800 is entered at a fixed rate of 60 Hz (the interrupt request, or IRQ rate) while the machine language subroutines are active.

Table I. Variable storage locations used in machine language subroutines

Address: Decimal	Address: Low Byte	High Byte	Description
49286	134	192	Timer A low byte after ramp down
49287	135	192	Timer A high byte after ramp down
49288	136	192	Diagnostic
49289	137	192	Diagnostic
49290	138	192	Timer A low byte after NMI
49291	139	192	Timer A high byte after NMI
49292	140	192	Timer B low byte after NMI
49293	141	192	Timer B high byte after NMI
49294	142	192	Number of steps necessary to ramp to given speed
49295	143	192	Bit 7: Ramping necessary flag Bit 6: Unused Bit 5: Unused Bit 4: Ramp up complete flag Bit 3: Ramp down complete flag Bit 2: Ramp up in progress flag Bit 1: Ramp down in progress flag Bit 0: Currently in ramp mode flag
49296	144	192	Keyboard character hit (0=no key)
49297	145	192	NMI contents .AND. 3
49298	146	192	Ramp counter
49299	147	192	Number of NMI interrupts
49300-49386	148	192	NMI interrupt routine
49500-49544	92	193	Set-up subroutine
49600-49631	192	193	Keyboard scan subroutine
49700-49747	36	194	Termination subroutine

Table I. (continued)

Address: Decimal	Address: Low Byte	Address: High Byte	Description
49800- 49880	136	194	IRQ ramping subroutine
49900- 49981	236	194	KBD triggered ramp down
52736- 52991	0 255	206 206	Low bytes of SID frequencies used during ramping
52992- 53247	0 255	207 207	High bytes of SID frequencies used during ramping

```
01    REM ---STEPPER MOTOR CONTROL PROGRAM---
10    DIM XTRA(256)
15    POKE 53280,9:POKE 53281,0
20    CD=0:PRINT
30    S=54272:T=56576:GOSUB2000
40    FORJ=49500 TO 49544:READ A%:POKE J,A%:NEXT
50    FORJ=49600 TO 49631:READ A%:POKE J,A%:NEXT
60    FORJ=49700 TO 49747:READ A%:POKE J,A%:NEXT
70    FORJ=49300 TO 49386:READ A%:POKE J,A%:NEXT
80    FORJ=49800 TO 49880:READ A%:POKE J,A%:NEXT
90    FORJ=49900 TO 49981:READ A%:POKE J,A%:NEXT
110   FOR I=49280 TO 49299:POKE I,0:NEXT
120   FOR L=S TO S+24:POKE L,0:NEXT
130   POKE S+5,0:POKE S+6,240
140   POKE S+2,0:POKE S+3,8
150   POKE S+24,15
160   GOSUB 6000
165   PRINT "[CLR]"
166   IF OP%>5 OR OP%<1 GOTO 160
170   ON OP% GOTO 600,700,800,900,900
180   PRINT
200   IF D%<>1 AND D%<>0 GOTO 160
250   FR = RATE/.06097
260   FHI% = INT(FR/256):FLO% = INT(FR-256*FHI%)
262   IF RATE>200 GOTO 270
264   BHI% = INT((NS-1)/256):BLO% = NS-1-256*BHI%
266   NS = BHI%*256 + BLO% +1
270   POKE 251,0:POKE 253,0
280   POKE 252,206:POKE 254,207
290   POKE T+4,P2%:POKE T+5,P1%
300   POKE T+6,BLO%:POKE T+7,BHI%
305   IF RATE>200 GOTO 320
310   POKE S+1,FHI%:POKE S,FLO%
320   POKE S+24,15:POKE 56589,127
330   POKE T+3,65:POKE T+1,D%
331   TT = NS*PC/RATE
332   RG = 2/3*NS*PC/1000
335   IF RATE>200 THEN GOSUB 3000
336   TT = INT(TT*100.)/100.
337   RG = INT(RG*100.)/100.
338   PRINT:PRINT "TRAVEL TIME = ";TT;" SECONDS"
339   PRINT:PRINT "SCAN RANGE = ";RG;" PICOSECONDS"
340   SYS 49500
350   ALO% = PEEK(49290):AHI% = PEEK(49291)
360   BLO% = PEEK(49292):BHI% = PEEK(49293)
370   IF PEEK(49299)>0 GOTO 440
380   DIST = NS*PC - (BHI%*256+BLO%+1)*PC + PC - 1 - (256*AHI%+ALO%)
390   GOTO 410
400   DIST = NS*PC + PC - 1 - (256*AHI%+ALO%)
410   IF PEEK(49295)<128 GOTO 440
```

```
420   DIST = DIST + 65535 - (256*PEEK(49287)+PEEK(49286))
440   IF D% = 1 THEN DIST = -DIST
450   CD = CD + DIST
460   PRINT:PRINT:PRINT
470   PRINT "PRESENT COORDINATE = ";CD
480   FOR I=1 TO 2000:NEXT
490   GOTO 110
600   GOSUB 4500
610   INPUT "[DOWN]NUMBER OF STEPS";NS
612   IF NS<0 OR NS>500000 GOTO 610
620   GOSUB 4000
630   GOSUB 5000
640   GOTO 180
700   INPUT "[DOWN]COORDINATE";AM
710   NS = CD - AM:D%=1
720   IF NS<0 THEN D%=0
730   NS = ABS(NS)
735   IF NS<0 OR NS>500000 GOTO 700
740   GOSUB 4000
750   GOSUB 5000
760   GOTO 180
800   NS = ABS(CD):D%=1
810   IF CD<0 THEN D%=0
820   FOR I= 1 TO 256
830   IF NS<2*XTRA(I) GOTO 860
840   NEXT
850   RATE = 3500:GOTO 870
860   RATE = (256*PEEK(52992+I) + PEEK(52736+I))*.06097
865   IF RATE<0 OR RATE >3590 THEN INPUT "RATE";RATE
870   PC = 0:GOSUB 4005
880   PRINT "NUMBER OF STEPS/SECOND =";RATE
890   GOTO 180
900   IF CD = 0 GOTO 940
905   PRINT "[DOWN][DOWN][RGHT][RGHT][RGHT][RVON] WARNING:COORDINATE WILL
BE LOST [RVOF]"
910   INPUT "[DOWN][DOWN][RGHT][RGHT] ARE YOU SURE? ";Q3$
920   IF Q3$ = "N" GOTO 160
930   IF Q3$ <> "Y" AND Q3$ <> "N" GOTO 910
940   ON OP% GOTO 160,160,160,950,999
950   CD = 0:PRINT "[DOWN][DOWN][DOWN] PRESENT COORDINATE = ";CD
960   FOR I=1 TO 2000:NEXT
970   GOTO 160
999   END
1100  DATA 120,169,130,141,13,221,169,148
1110  DATA 141,24,3,169,192,141,25,3
1120  DATA 169,136,141,20,3,169,194
1130  DATA 141,21,3,169,77
1140  DATA 141,15,221,169,35,141,14,221
1150  DATA 169,65,141,4,212,88,76,192,193
1199  REM END OF SUBROUTINE AT 49500
1200  DATA 234,234,234,173,143,192
1210  DATA 41,8,208,17,32,159,255
```

```
1220  DATA 32,228,255,201,0,240,237
1230  DATA 141,144,192,76,236,194,234,234,234
1240  DATA 76,36,194
1299  REM END OF SUBROUTINE AT 49600
1300  DATA 169,0,141,1,212,141,0,212,141
1310  DATA 24,212,141,14,221,141,15,221
1320  DATA 173,4,221,141,134,192
1330  DATA 173,5,221,141,135,192
1340  DATA 173,6,221,141,140,192
1350  DATA 173,7,221,141,141,192
1360  DATA 32,132,255,96,234,234,234
1399  REM END OF SUBROUTINE AT 49700
1400  DATA 120,173,13,221,41,3,141,145,192
1410  DATA 41,2,240,53,238,147,192
1420  DATA 173,4,221,141,138,192
1430  DATA 173,5,221,141,139,192
1440  DATA 173,143,192,41,128,240,41,169,147
1450  DATA 141,143,192,169,0,141,142,192,141,14,221
1460  DATA 169,255,141,4,221,141,5,221,169,39,141,14,221
1470  DATA 169,0,88,64,234,234,234
1480  DATA 238,146,192,169,0,88,64
1490  DATA 234,234,234,169,8,141,143,192
1495  DATA 169,0,88,64
1499  REM END OF SUBROUTINE AT 49300
1500  DATA 173,143,192,41,1,208,3,76,49,234
1510  DATA 172,146,192,177,251,141,0,212
1520  DATA 177,253,141,1,212,173,143,192
1530  DATA 41,4,240,16,238,146,192
1540  DATA 173,146,192,205,142,192,208,5
1550  DATA 169,144,141,143,192
1560  DATA 173,143,192,141,136,192,41,2,208,3
1570  DATA 76,49,234,206,146,192
1580  DATA 173,146,192,205,142,192,240,3
1590  DATA 76,49,234,169,136,141,143,192,76,49,234
1599  REM END OF SUBROUTINE AT 49800
1600  DATA 173,143,192,201,147,240,51
1610  DATA 120,173,4,221,141,138,192
1620  DATA 238,137,192
1630  DATA 173,5,221,141,139,192
1640  DATA 173,143,192,41,128,240,42
1650  DATA 169,147,141,143,192,169,0
1660  DATA 141,142,192,141,14,221,169,255
1665  DATA 141,4,221,141,5,221,169,33
1670  DATA 141,14,221,88,234,234,234
1680  DATA 173,143,192,41,8,240,247
1690  DATA 76,36,194,234,234,234
1695  DATA 169,8,141,143,192,88,76,36,194
1699  REM END OF SUBROUTINE AT 49900
1999  END
2000  FB = 20:FT = 3590:XTRA(0) = FB/60.
```

```
2010  PS = (FT-FB)/255:FQ = FB-PS
2020  FOR I=0 TO 255
2030  FQ = FQ + PS
2040  IF I=0 THEN 2060
2050  XTRA(I) = XTRA(I-1) + FQ/60.
2060  FR = FQ/.06097
2070  FHI% = INT(FR/256)
2080  FLO% = INT(FR-256*FHI%)
2090  POKE 52992+I,FHI%:POKE 52736+I,FLO%
2100  NEXT
2110  RETURN
3000  FA = RATE/FT:FM% = INT(FA/255)
3020  XS% = INT(XTRA(FM%))
3030  TT = FM%/60.*2 + (NS*PC-2*XS%)/RATE
3050  NS = NS - XS%/PC
3060  BHI% = INT((NS-1)/256):BLO% = NS-1-256*BHI%
3070  NS = BHI%*256 + BLO% + 1
3080  RG = 2./3.*(NS*PC+XS%)/1000.
3090  POKE T+6,BLO%:POKE T+7,BHI%
3100  POKE S,1:POKE S+1,72:POKE S+24,15
3110  POKE 49294,FM%:POKE 49295,133
3120  RETURN
3995  NS = NS*PC
4000  INPUT "[DOWN]NUMBER OF STEPS/CHANNEL";PC
4005  IF PC<1 THEN PC=10
4010  P1% = INT((PC-1)/256):P2% = INT((PC-1)-256*P1%)
4020  PC = (256*P1% + P2% +1):NS = NS/PC
4025  IF NS>65535 GOTO 3995
4030  FPC = 2./3.*PC:FPC = INT(FPC*1000.)/1000.
4035  IF OP% = 3 GOTO 4050
4040  PRINT "[DOWN]FEMTOSECONDS/CHANNEL = ";FPC
4050  RETURN
4500  PRINT "INPUT DIRECTION OF TRAVEL"
4510  PRINT "0 = MORE OPTICAL DELAY"
4520  PRINT "1 = LESS OPTICAL DELAY"
4530  INPUT D%:PRINT
4540  IF D%<>1 AND D%<>0 GOTO 4500
4550  RETURN
5000  INPUT "[DOWN]NUMBER OF STEPS/SECOND ";RATE
5010  IF RATE<0 OR RATE>3590 GOTO 5000
5020  RETURN
6000  PRINT "[CLR][DOWN][DOWN][DOWN][DOWN][RGHT][RGHT][RGHT][RGHT][RGHT]
       [RGHT][RGHT][RGHT][RGHT][RGHT][RGHT][RGHT]CONTROL OPTIONS"
6010  PRINT "[DOWN][DOWN][RGHT][RGHT]1)MOVE(RELATIVE)[RGHT][RGHT]4)RESET
       COORDINATE"
6020  PRINT "[DOWN][DOWN][RGHT][RGHT]2)MOVE(ABSOLUTE)[RGHT][RGHT]5)EXIT
       PROGRAM"
6030  PRINT "[DOWN][DOWN][RGHT][RGHT]3)HOME"
6040  PRINT "[DOWN][DOWN][DOWN][DOWN]COORD = ";CD
6060  OP% = 0
6070  PRINT [UP][UP][UP][UP][UP][UP][RGHT][RGHT]":INPUT "OPTION ";OP%
6080  RETURN
```

```
SUBROUTINE AT 49500 - SETUP

SEI             120             Set interrupt disable status
LDA #130        169,130         Set NMI control register to gen-
STA 56589       141,13,221        erate NMI on timer B underflow
LDA #148        169,148
STA 792         141,21,3        Change NMI interrupt vector
LDA #192        169,192              to address 49300
STA 793         141,25,3
LDA #136        169,136
STA 788         141,20,3        Change IRQ hardware interrupt
LDA #194        169,194            vector to address 49800
STA 789         141,21,3
LDA #77         169,77          Start timer B, count timer A
STA 56591       141,15,221         underflows
LDA #39         169,39          Start timer A, count
STA 56590       141,14,221         external CNT2 transitions
LDA #65         169,65          Start SID chip, generate
STA 54276       141,4,212          pulse waveform
CLI             88              Clear interrupt disable status
JMP 49600       76,192,193      Go to 49600

SUBROUTINE AT 49600 - KEYBOARD SCAN AND WAITING LOOP

NOP NOP NOP     234,234,234
LDA 49295       173,143,192     Check for ramp down completed
AND #8          41,8                signal (bit 3 = 1)
BNE +17         208,17          Branch on ramp down complete
JSR SCNKEY      32,159,255      Look for key hit on keyboard
JSR GETIN       32,228,255      Load key hit into accumulator
CMP #0          201,0           If acc. = 0 then no key was hit
BEQ -19         240,237         Cycle back on no key hit
STA 49296       141,144,192     Store ASCII code of key hit
JMP 49900       76,236,194      Go to 49900 on key hit
NOP NOP NOP     234,234,234
JMP 49700       76,36,194       Go to 49700 on ramp down complete

SUBROUTINE AT 49700 - TERMINATION SEQUENCE

LDA #0          169,0
STA 54273       141,1,212
STA 54272       141,0,212       Stop SID chip
STA 54296       141,24,212
STA 56590       141,14,221      Stop Timer A
STA 56591       141,15,221      Stop Timer B
LDA 56580       173,4,221       Store Timer A low byte
STA 49286       141,134,192        final value
LDA 56581       173,5,221       Store Timer A high byte
STA 49287       141,135,192        final value
```

```
LDA 56582          173,6,221          Store Timer B low byte
STA 49292          141,140,192           final value
LDA 56583          173,7,221          Store Timer B high byte
STA 49293          141,141,192           final value
JSR IOINIT         32,132,255         Re-init. I/O devices to allow
                                         cassette use
RTS                96                 Return to BASIC main program
NOP NOP NOP        234,234,234
```

SUBROUTINE AT 49300 - NON-MASKABLE INTERRUPT (NMI) HANDLING ROUTINE

```
SEI                120                Set interrupt disable status
LDA 56589          173,13,221         Load NMI int. register contents
AND #3             41,3               Mask all but Timer A,B NMI's
STA 49297          141,145,192        Diagnostic
AND #2             41,2               Check if NMI from Timer B
BEQ +53            240,53             If not a Timr B NMI, branch
INC 49299          238,147,192        Count Timer B underflows
LDA 56580          173,4,221          Store current Timer A
STA 49290          141,138,192           low byte value
LDA 56581          173,5,221          Store current Timer A
STA 49291          141,139,192           high byte value
LDA 49295          173,143,192        Check if ramping
AND #128           41,128               is necessary (rate < 200 Hz)
BEQ +41            240,41             If ramping is unnecessary, branch
LDA #147           169,147            Store signal to start ramp
STA 49295          141,143,192           down (bit 1 = 1)
LDA #0             169,0              Let ramp down
STA 49294          141,142,192           count down to zero
STA 56590          141,14,221         Stop timer A
LDA #225           169,255            Reset Timer A to count number
STA 56580          141,4,221             of steps taken during ramp
STA 56581          141,5,221             down; start at maximum
LDA #39            169,39             Start Timer A
STA 56590          141,14,221            counting CNT transitions
LDA #0             169,0              Zero accumulator before returning
CLI                88                 Clear interrupt disable status
RTI                64                 Return from interrupt
NOP NOP NOP        234,234,234
INC 49298          238,146,192        Count non-Timer B interrupts
LDA #0             169,0              Zero accumulator before returning
CLI                88                 Clear interrupt disable status
RTI                64                 Return from interrupt
NOP NOP NOP        234,234,234
LDA #8             169,8              Store ramp down complete
STA 49295          141,143,192           signal to exit waiting loop
LDA #0             169,0              Zero accumulator before returning
CLI                88                 Clear interrupt disable status
RTI                64                 Return from interrupt
```

SUBROUTINE AT 49800 - INTERRUPT REQUEST (IRQ) RAMPING ROUTINE

```
LDA 49295          173,143,192        Check if currently in
AND #1             41,1                  ramp mode
BNE +3             208,3              If not ramping,
JMP $EA31          76,49,234             do normal IRQ routine
LDY 49298          172,146,192        If ramping, load # steps taken
LDA (251),Y        177,251            Change SID frequency
STA 54272          141,0,212             low byte
LDA (253),Y        177,253            Change SID frequency
STA 54273          141,1,212             high byte
LDA 49295          173,143,192        Check if ramping up is
AND #4             41,4                  currently in progress
BEQ +16            240,16             If not ramping up, branch
INC 49298          238,146,192        If ramping up, count this step
LDA 49298          173,146,192        Check if ramp up
CMP 49294          205,142,192           is complete
BNE +5             208,5              If not complete, branch
LDA #144           169,144            If complete, store
STA 49295          141,143,192           ramp up over signal
LDA 49295          173,143,192        Check if ramping down is
STA 49288          141,136,192        (diagnostic)
AND #2             41,2                  currently in progress
BNE +3             208,3              If not ramping down,
JMP $EA31          76,49,234             do normal IRQ routine
DEC 49298          206,146,192        If ramping down, count this step
LDA 49298          173,146,192        Check if ramp down
CMP 49294          205,142,192           is complete
BEQ +3             240,3              If not complete,
JMP $EA31          76,49,234             do normal IRQ routine
LDA #136           169,136            If ramp down is complete,
STA 49295          141,143,192           ramp down over signal
JMP $EA31          76,49,234          Do normal IRQ routine
```

SUBROUTINE AT 49900 - KEYBOARD INTERRUPT ROUTINE

```
LDA 49295          173,143,192        Check if already in
CMP #147           201,147               ramp down sequence
BEQ +51            240,51             If in ramp down, branch
SEI                120                Set interrupt disable status
LDA 56580          173,4,221          Store current Timer A
STA 49290          141,138,192           low byte value
INC 49289          238,137,192        (diagnostic)
LDA 56581          173,5,221          Store current Timer A
STA 49291          141,139,192           high byte value
LDA 49295          173,143,192        Check if ramping is
AND #128           41,128                necessary (bit 7 = 1)
BEQ +42            240,42             If ramping is unnecessary, branch
LDA #147           169,147            If ramping is necessary, store
```

```
STA 49295          141,143,192          ramp down in progress signal
LDA #0             169,0                Count down to zero
STA 49294          141,142,192             during ramp down
STA 56590          141,14,221           Stop Timer A
LDA #255           169,255              Reset Timer A to count number
STA 56580          141,4,221               of steps during ramp down;
STA 56581          141,5,221               count down from maximum
LDA #33            169,33               Restart Timer A counting
STA 56590          141,14,221              CNT2 transitions
CLI                88                   Clear interrupt disable status
NOP NOP NOP        234,234,234
LDA 49295          173,143,192          Check for ramp down
AND #8             41,8                    complete signal
BEQ -9             240,247              If not complete, check again
JMP 49700          76,36,194            If complete, go to term. sequence
NOP NOP NOP        234,234,234
LDA #8             169,8                If ramping unnecessary, store
STA 49295          141,143,192             ramp down complete signal
CLI                88                   Clear interrupt disable status
JMP 49700          76,36,194            Go to terminations sequence
```

APPENDIX B. DATA ACQUISITION PROGRAM

The following program was written in FORTRAN to run on a DEC PDP 11/23 computer under the TSX-Plus operating system. The program receives interrupts via a DRV-11 card which are interpreted as "collect data" commands. The program makes extensive use of three subroutine packages; ALEDA, which provides connection to RS232 devices from FORTRAN; TSXLIB, which allows access to TSX system parameters from user programs; and HGRAPH, a data plotting subroutine package. The subroutines from these packages which are accessed in the program are listed in Table I. The basic logic of the program suspends operation at the CALL SUSPND line until an interrupt is received. At this time, control is forwarded to subroutine CPLRTN, which resumes program operation (CALL RESUME). A data point is then read from the SR510 lock-in amplifier via RS232 and plotted on the screen. If this is not the final (512^{th}) data point, the program cycles back to the CALL SUSPND line. This cycle is repeated until 512 data points have been collected, at which time the data may be normalized to the square of the laser power (if the user so chooses) and is then written to a disk file.

Table I. Subroutines used program LOCKIN from commercial subroutine packages ALEDA, TSXLIB, and HGRAPH

Package	Subroutine	Description
ALEDA	LENABL	Enable device for transfer
	LERROR	Output to console ALEDA error messages
	LPUTLN	Output characters to specified device
	LRECEV	Initiate transfer of characters from device
	LGETLN	Access device for transfer of characters
	LPUTST	Output string to console
	LDSABL	Disable device for transfer
HGRAPH	INIPLT	Initialize plotting
	ERASE	Erase the terminal screen
	WINDOW	Define size of window in inches
	SCALE	Define axis range
	AXIS	Draw and label axes
	MOVETO	Draw a line to the given point
	DMPPLT	Empty the terminal buffer
	ENDPLT	Deselect terminal for plotting
TSXLIB	BRKCTL	Connect subroutine to specified keystroke
	ISTPRV	Set current priority value
	ICNINT	Connect interrupt vector to user subroutine
	IBISIO	Set interrupt enable bit
	IBICIO	Clear interrupt enable bit

```
C
C     PROGRAM LOCKIN----------------------------------------
C
C     This program takes data from the SRS 510 lock-in amplifier when an
C     interrupt signal from the Commodore 64 is received.  A total of
C     512 data points are taken and stored on disk.  The data may be
C     normalized to the square of the laser power.  For more information
C     on the subroutines used, see the HGRAPH, TSXLIB, and ALEDA manuals.
C
C
      EXTERNAL CPLRTN,BRKRTN
      COMMON NTIMES
      BYTE FILNAM(16),BUF(40),LINE(12),TERM(2),REQDAT(2),BUF2(40)
      BYTE GETGN(2),YSCALE(2),GTPHAS(2),GETADC(3)
      DIMENSION DATA(512),ADCDAT(512)
      INTEGER*2 RTNCOD,RESET,NPTS,GAIN,POWER
      DATA TERM/1,13/          !Define one terminator which is carr. ret.
      DATA RESET/"1000/
      DATA REQDAT/81,13/       !Send ASCII "Q" (81) to request data
      DATA GETGN/71,13/        !Send ASCII "G" (71) to get sensitivity
      DATA GTPHAS/80,13/       !Send ASCII "P" (80) to get phase setting
      DATA GETADC/88,49,13/    !Send ASCII "X1" to get laser power
      TYPE 75                  !Ask for name of output file
      ACCEPT 900,FILNAM
      TYPE 15                  !Ask if data is to be normalized
      ACCEPT 910,NORM
      DO 5 I=1,512
5       DATA(I)=0.
      NPTS=0
      IF (LENABL(0, , ,RTNCOD)) GO TO 10      !Enable console input
      IF (LENABL(1, , ,RTNCOD)) GO TO 10      !Enable console output
      GO TO 20
10    CALL LERROR(RTNCOD,10,'Console failed to enable.',25)
      STOP
20    IF (LENABL(6,BUF,40,RTNCOD).NE.0) GO TO 30  !Enable lockin input
      IF (LENABL(7,BUF2,40,RTNCOD).NE.0) GO TO 30 !Enable lockin output
      GO TO 35
30    CALL LERROR(RTNCOD,20,'Lock-in enable failed.',22)
      STOP
35    CALL LPUTLN(7,GETGN,2,RTNCOD,9,TERM)     !Ask for gain setting
      IF (RTNCOD.LT.0) CALL LERROR(RTNCOD,35,'  LPUTLN error.',15)
      CALL LRECEV(6, , ,RTNCOD,RESET)
      IF (RTNCOD.LT.0) CALL LERROR(RTNCOD,35,'  LRECEV error.',15)
      CALL LGETLN(6,LINE,4,RTNCOD,1,TERM)      !Receive gain setting
      IF (RTNCOD.LT.0) CALL LERROR(RTNCOD,35,'  LGETLN error.',15)
      NCHARS=RTNCOD
      DECODE(NCHARS-1,25,LINE) GAIN
      GAIN=GAIN+3
      SENS=FLOAT(GAIN)/9.
      IF (SENS.LT.3.05) YSCALE(1)='m'          !'m' for millivolt scales
      IF (SENS.LT.2.05) YSCALE(1)='u'          !'u' for microvolt scales
```

```
      IF (SENS.LT.1.05) YSCALE(1)='n'          !'n' for nanovolt scales
      YSCALE(2)='V'
      IF (YSCALE(1).EQ.'m') FACTOR=1000.
      IF (YSCALE(1).EQ.'u') FACTOR=(1000.)**2
      IF (YSCALE(1).EQ.'n') FACTOR=(1000.)**3
      SENS=(SENS-AINT(SENS-.1))*3.
      POWER=INT(SENS-.1)
      DIGIT=SENS-.1-FLOAT(POWER)
      IF (DIGIT.LT.0.95) MULT=5
      IF (DIGIT.LT.0.65) MULT=2
      IF (DIGIT.LT.0.3) MULT=1
      SENS=FLOAT(MULT)*10**POWER               !SENS ranges from 1 to 500
      CALL LPUTLN(7,GTPHAS,2,RTNCOD,9,TERM)    !Ask for phase setting
      IF (RTNCOD.LT.0) CALL LERROR(RTNCOD)
      CALL LRECEV(6, , ,RTNCOD,RESET)
      IF (RTNCOD.LT.0) CALL LERROR(RTNCOD)
      CALL LGETLN(6,LINE,8,RTNCOD,1,TERM)      !Receive phase setting
      IF (RTNCOD.LT.0) CALL LERROR(RTNCOD)
      NCHARS=RTNCOD-1
      DECODE(NCHARS,27,LINE) PHASE
      CALL INIPLT(7,10.2,7.2)
      CALL ERASE
      CALL WINDOW(1.4,9.8,.9,7.1)
      CALL SCALE(0,512.,0.,SENS)                !Set up for plotting
      SENSNG=SENS/5.
      NYFORM=2-POWER
      CALL AXIS(50.,SENSNG,'CHANNEL',7,2,0,'SIGNAL',6,2,NYFORM)
      CALL MOVETO(0.,0.,0,0)
      CALL DMPPLT                               !Empty the plotter buffer
      IBRKCH=3
      CALL BRKCTL(IBRKCH,BRKRTN)                !Go to BRKRTN on Control/C
      CALL ISTPRV(127)                          !Set priority to 127
      CALL ICNINT( "360,CPLRTN,7,IERR)          !Go to CPLRTN on interrupt
      IF (IERR.GE.0) STOP 'Error connecting to interrupt'
      IERR=IBISIO("167750,"100)                 !Set interrupt enable bit
      IF (IERR.GE.0) STOP 'Error setting interrupt enable'
60    CALL SUSPND                               !Wait for int. from C64
      CALL LPUTLN(7,REQDAT,2,RTNCOD,9,TERM)     !Ask for data point
      IF (RTNCOD.LT.0) GO TO 45
      GO TO 55
45    CALL LERROR(RTNCOD,35,'  LPUTLN error.',15)
      STOP 'Error receiving data'
55    CALL LRECEV(6,BUF,40,RTNCOD,RESET)
      IF (RTNCOD.LT.0) CALL LERROR(RTNCOD,55,'  LRECEV error.',15)
      CALL LGETLN(6,LINE,12,RTNCOD,1,TERM)      !Receive data point
      IF (RTNCOD.LT.0) CALL LERROR(RTNCOD,55,'  LGETLN error.',15)
      NCHARS=RTNCOD
      DECODE(NCHARS-1,70,LINE) DATA(NPTS+1)   !Convert data, byte to real
      CALL LPUTLN(7,GETADC,3,RTNCOD,9,TERM)
      IF (RTNCOD.LT.0) GO TO 46
      GO TO 56
```

```
46    CALL LERROR(RTNCOD,35,'  LPUTLN error.',15)
      STOP 'Error receiving ADC data'
56    CALL LRECEV(6,BUF,40,RTNCOD,RESET)
      IF (RTNCOD.LT.0) CALL LERROR(RTNCOD,55,'  LRECEV error.',15)
      CALL LGETLN(6,LINE,12,RTNCOD,1,TERM)      !Receive data point
      IF (RTNCOD.LT.0) CALL LERROR(RTNCOD,55,'  LGETLN error.',15)
      NCHARS=RTNCOD
      DECODE(NCHARS-1,69,LINE) ADCDAT(NPTS+1) !Convert data, byte to real
      NPTS = NPTS+1
      POINT=FACTOR*DATA(NPTS)        !FACTOR = 1E3(mV),1E6(uV), or 1E9(nV)
      CALL MOVETO(FLOAT(NPTS),POINT,1,0)        !Plot data point
      CALL DMPPLT
      IF (NPTS.LT.512) GO TO 60              !Check if last point
      IERR=IBICIO("167750,"100)              !Clear interrupt enable bit
      IF (IERR.GE.0) STOP 'Error clearing interrupt enable'
      CALL BRKCTL(0,0)                    !Return Ctrl/C to normal oper.
      CALL ENDPLT
50    CALL LPUTST('Data transfer completed.\',RTNCOD)
      CALL LDSABL(6)
      CALL LDSABL(7)
      CALL LDSABL(0)
      CALL LDSABL(1)
      CALL ISTPRV(50)                             !Reset priority to 50
      DO 80 I=1,NPTS
80       DATA(I)=DATA(I)*FACTOR*10000./SENS     !Scale to 10000=full scale
      IF (NORM.EQ.'Y') CALL PWRNRM(DATA,ADCDAT) !Normalize: (power)**2
84    OPEN(UNIT=1,NAME=FILNAM,TYPE='NEW',ERR=82)
      DO 90 I=1,NPTS-1,8
90    WRITE (1,92) I,(DATA(I+J),J=0,7)     !SENS ranges 1 to 500
      WRITE (1,95) SENS,YSCALE,PHASE
      CLOSE(UNIT=1)
      STOP 'End of program'
82    TYPE 75
      ACCEPT 900,FILNAM
      GO TO 84
      STOP
15    FORMAT(/'$Do you want to normalize the data? ')
25    FORMAT(I3)
27    FORMAT(F7.2)
69    FORMAT(F10.4)
70    FORMAT(E11.5)
75    FORMAT(/'$Name of output file? ')
92    FORMAT(X,I4,X,8F7.0)
95    FORMAT(' SENS = ',F6.2,2A1,'   PHASE = ',F7.2,' degrees')
900   FORMAT(16A1)
910   FORMAT(1A1)
      END
```

```
C
C     Subroutine to normalize data to the square of the laser power--
C
      SUBROUTINE PWRNRM(DATA,ADCDAT)
      DIMENSION DATA(512),ADCDAT(512)
      DO 80 I=1,512
80       DATA(I)=DATA(I)*50./(ADCDAT(I)*ADCDAT(I))   !ADCDAT should
      RETURN                                          !be about 7
      END
C
C     Timing subroutine entered on interrupt------------------
C
      SUBROUTINE CPLRTN
      COMMON NTIMES
      NTIMES=NTIMES+1        !For debugging purposes
      CALL RESUME
      RETURN
      END
C
C     Break sentinel control subroutine-----------------------
C
      SUBROUTINE BRKRTN
C     This subroutine is executed when a Control/C character is pressed
C     on the keyboard.  The subroutine releases the interrupt enable so
C     that an interrupt occurring after Ctrl/C does not crash the system
C
      IERR=IBICIO("167750,"100)                   !Disable interrupt
      IF (IERR.GE.0) STOP 'Error clearing interrupt enable'
      CALL ERASE                                  !Clear the screen
      CALL DMPPLT
      CALL ENDPLT                                 !Terminate plotting
      CALL ISTPRV(50)                             !Reset priority to 50
      STOP 'Program aborted by Control/C'         !Terminate the program
      RETURN
      END
```